Unsteady Loading on Floating Horizontal axis Tidal Turbine

Mohamad Hasif Bin Osman
St Edmund Hall College
University of Oxford

A thesis submitted for the degree of
Doctor of Philosophy
Michaelmas Term 2022

Acknowledgement

I would like to thank my supervisor, Prof. Richard Willden, for his guidance and support throughout this project. It has been a privilege to work with and learn from him, and I feel I have gained valuable experience for my future career. I would also like to thank Dr Christopher Vogel and Dr James McNaughton for all their help in reviewing the thesis. Secondly, I wish to express my gratitude to my colleagues in the tidal energy research group Aidan, Bowen, Federico, and Steven for their valuable ideas and help in reviewing the thesis. Thank you also to my other colleagues in the tidal energy research group, for many useful discussions and encouragement, in particular Subash, Taka, and Ahmad. Additionally, I would like to thank my friends and colleagues in the wider Civil Engineering Group.

I would like to formally acknowledge colleagues with whom I worked in developing the fully coupled model (aside from my supervisor), Dr Edward Ransley and Dr Scott Brown from the University of Plymouth. Many of the simulations reported in this thesis were run on high-performance computing clusters managed by Advanced Research Computing at the University of Oxford, and I would like to acknowledge the help of their staff. To my wife Sofia and my son Musa, thank you so much for being there for me, for the love and support, and for giving me the purpose in completing this thesis. Thank you to my good friends, Adli, Omar, James, Jaezah, Rabeah, Mahmud, Aliff, and Iskandar for their company, friendship, and support over the last couple of years. Finally, I would like to thank my parents Rozilawati and Osman, and my brothers Hafiz and Naqib.

Abstract

Floating tidal turbines (FTT) are gaining popularity in the field of tidal energy these past few years due to some advantages they had when compared to the bottom fixed devices. However, the floating motion of an FTT, due to waves and tidal current, leads to unsteady loadings on the rotor. This motivates the present study to pursue this topic to further understand and characterize the hydrodynamic of an FTT. To conduct a study on a device scale, a floating tidal turbine undergoing single degrees of freedom (DoF) is preferable to isolate the effect of each motion on the device performance. Blade resolved computational fluid dynamic (CFD) simulations of floating tidal turbines undergoing surge, heave, and pendulum (pitch) motions were carried out over a range of motion's amplitude and frequency and also using multiple rotor rotational speeds. The present study seeks to determine the effect of each motion on the floating turbine's performance. The rotor goes into stall at higher motion amplitude and frequency for the surge and pendulum motions. The mean power decrease while the mean thrust increase as the motion amplitude and frequency is increased, due to the loss in the lift at the maximum apparent velocity which increases the angle of attack on the blade, causing the flow to separate, thus stalling the rotor. This can be minimized when operating the rotor at a higher rotational speed, i.e., using speed control to reduce the stalling effect. A floating tidal turbine undergoing the heave motion can be viewed as a dynamic yawing motion case; there is evidence of the advancing and retreating phases and wake skewness formation at every heave motion cycle. The added mass and damping forces are calculated based on the blade resolved CFD results, which can be used as standardized hydrodynamic coefficients to be included in a simplified model, such as an actuator disc, for a fully coupled model simulation. Modifications to include the added mass and damping forces into an existing fully coupled model are presented in this thesis. The result shows good improvement from the original model when verified against the blade resolved simulations. The model is then tested under various wave frequencies, including the combined wave-current conditions. The present model increases the mean thrust on the rotor while decreasing the loading amplitude compared to the original model.

Contents

References

Nomenclature

Symbol	Unit	Definition
A^*	-	Amplitude ratio
A_0	m	Prescribe motion amplitude
A_D	m^2	Rotor swept area
a	-	Induction factor
B	-	Blockage ratio
C_{P}	-	Power coefficient
C_{T}	-	Thrust coefficient
C_{pre}	-	Pressure coefficient
c	m	Chord length
C_L	-	Lift coefficient
C_D	-	Drag coefficient
C_X	N	Axial aerodynamic forces
C_Y	N	Tangential aerodynamic forces
$C'_{A,i}$	-	Non-dimensional forces in phase with the turbine's acceleration
$C'_{V,i}$	-	Non-dimensional forces in phase with the turbine's velocity
$\bar{C}_{T,i}$	-	Mean thrust coefficient

Symbol	Unit	Definition
D	m	Rotor diameter
$\mathbf{d}_0$	m	Translational displacement
d_Z	m	Vertical displacement
F_ax	N/m	Axial force profile
F_tan	N/m	Tangential force profile
F_X	N	Axial structural loads
F_Z	N	Vertical structural load
$F_{T,i}$	N	Fluctuating thrust force
$F_{TA,i}$	N	Force component in phase with the turbine's acceleration
$F_{TV,i}$	N	Force components in phase with the turbine's velocity
$\bar{F}_{T,i}$	N	Mean force component
$\hat{F}_{A,i}$	kg	Magnitude of the added mass associated with the rotor acceleration
$\hat{F}_{V,i}$	kg/s	Magnitude of the added damping associated with the rotor velocity
GR	-	Growth rate
$\mathbf{g}$	m/s^2	Acceleration due to gravity
h	m	Length from the centre of rotation to the rotor hub
H	m	Wave height
I	%	Turbulence intensity
k	m^2/s^2	Turbulent kinetic energy
L	m	Length
LE	m	Leading edge cell size

Symbol	Unit	Definition
N_{cell}	-	Number of cells
P_R	-	Power output ratio
P_D	W	Power extracted by the turbine
P_T	W	Total available power in the flow
R	m	Rotor radius
r	m	Local rotor radius
Re	-	Reynolds number
t	s	Time
TE	m	Trailing edge cell size
T_r	s	Period of one revolution of the rotor
T_R	-	Thrust ratio
T	N	Rotor thrust
$\Delta\bar{T}_i$	N	Difference between the mean thrust of the stationary and oscillating turbines
t_R	m	Blade thickness
U_∞	m/s	Free-stream velocity
U_{ap}	m/s	Apparent velocity
U_Z'	m/s	Vertical flow velocity
U_Z	m/s	Vertical rotor velocity
u_i	m/s	Induced velocity
U_R	m/s	Effective relative free stream velocity
U_T	m/s	Local instantaneous velocity
u_R	m/s	Surge motion velocity
V_C	m/s	Inflow velocity normal to the rotor plane

Symbol	Unit	Definition
$\mathrm{v_h}$	m/s	Induce velocity in ‘hover’
V	$\mathrm{m^3}$	Volume
W	m/s	Resultant velocity relative to the blade
$\mathbf{x}$	m	Coordinate vector in the moving reference frame
X	m	Local chord length
$x_{1,3,5}$	m	Displacement of prescribed motions. Subscript 1,3,5 refers to surge, heave, and pitch motions
x, y, z	m	Cartesian coordinates
α	°	Angle of attack
α_S	°	Static stall angle
β	°	Rotor blade twist angle
$\delta_{A,i}$	kg/s	Added damping
ε	$\mathrm{J\ kg^{-1}\ s^{-1}}$	Turbulence dissipation rate
γ	°	Inflow angle
λ	-	Tip-speed ratio
λ'	m	Wavelength
$\mathcal{M}_{A,i}$	kg	Added mass
ω^*	-	Frequency ratio
ω_0	rad/s	Prescribe motion frequency
ω_r	rad/s	Rotor rotational speed
ω	$\mathrm{s^{-1}}$	Specific dissipation rate
θ	rad	Angular displacement
θ_{pen}	°	Instantaneous angular (pendulum) motion
ρ	$\mathrm{kg/m^3}$	Fluid density

Symbol	Unit	Definition
η_P	-	Power efficiency
η_T	-	Thrust efficiency
$\eta_{1,3,5}$	-	Non-dimensional displacement of prescribed motions. Subscript 1,3,5 refers to surge, heave, and pitch motions
ϕ	°	Resultant flow angle
ψ	°	Azimuth angle

Abbreviations

Abbreviation	Meaning
AMI	Arbitrary mesh interface
BEMT	Blade element momentum theory
CFD	Computational fluid dynamics
CPU	Computing
COR	Centre of rotation
DoF	Degrees of freedom
FTT	Floating tidal turbines
FOWT	Floating offshore wind turbines
FVM	Free Vortex method
GDW	General dynamic wake
HATT	Horizontal axis tidal turbine
IRF	Inertial reference frame
LES	Large Eddy Simulation
LPT	Linear Potential Theory
MRF	Moving reference frame
NREL	National Renewable Energy Laboratory
RANS	Reynolds-averaged Navier-Stokes
RAO	Response amplitude operator
SST	Shear stress transport

Abbreviation	Meaning
TLP	Tension leg platform
TSR	Tip-speed ratio
UBEMT	Unsteady blade element momentum theory
VOF	Volume of fluid
VRS	Vortex ring state
WInDS	Wake Induced Dynamics Simulator

Chapter 1

Introduction

The topic of renewable energy has become popular over the past decade. Several motives have driven scientists worldwide to pursue the development of renewable energy due to several issues, mainly environmental (i.e., climate change) and economic issues (Jing et al., 2017). One of the main reasons for climate change is the constant use of fossil fuels. Fossil fuels are used as the main energy source for transportation, industrial, and agricultural sectors throughout the world. The negative effect of climate change can be reduced by substituting the use of fossil fuel with renewable energy. Moreover, this is one of the promising sectors to develop for a country such as the UK, which has a vast renewable energy resource (DECC, 2009).

Generally, there are a variety of renewable energy resources, such as solar, wind, and geothermal, which can be exploited and put to good use. One of the most reliable renewable energy sources is the ocean. Marine energy, such as tidal current flows, waves, thermal and salinity gradients, are considered to have vast potential energy resources which can be utilized to fulfil the ever-increasing energy demand (Uihlein & Magagna, 2016; Nachtane et al., 2020).

Many countries have begun developing technologies to harness marine energy resources. One of the more promising fields is the development of tidal energy devices (Jing et al., 2017). Tidal energy is not a new topic and many have developed and deployed tidal stream turbines (although most of them are prototypes), most of them are fixed in one position i.e., fixed turbines piled on the seabed (McAdam et al., 2010; Draper & Nishino, 2014; Wimshurst & Willden, 2016; Nachtane et al., 2020). Recently, floating tidal turbines (FTT) are gaining popularity due to some advantages when compared to the bottom fixed devices (Ransley et al., 2016; Brown et al., 2020):

- They can be easily installed or removed from the site;
- Does not require any specific sea bed geometry condition, like bottom-fixed tidal turbines where it is desirable to have a flat (or minimal slope) and even sea bed;
- Easier to do routine maintenance since they are located nearer to sea surface;
- More suitable for deepwater operations;
- Presuming a shear flow profile, the velocity of an open channel is highest near the water surface; therefore they will be able to capture higher power since they are located nearer to the water surface; and
- Has minimal impact on marine life since they often used mooring lines anchored to the seabed to keep the turbine in place, instead of using a monopile or a gravity-based foundation. The latter can quickly impact the morphology and ecosystem of marine life.

In 2018, an FTT prototype SR1-2000 by Orbital Marine Power Limited (then Scotrenewables Tidal Power) managed to extract more energy in a year (3 GWh per year) than the entire wave and tidal devices in Scotland in 12 years (Orbital Marine Power Ltd., 2018). However, the floating motion of an FTT, which originates from the combined waves and tidal current, leads to unsteady loadings on the rotor. The fluctuating loads will increase the fatigue on the rotor blades. This motivates the author to pursue this topic to further understand and characterize the hydrodynamic of an FTT. Another good example is the Platform for Inshore energy (PLAT-I) floating tidal turbine system by Sustainable Marine Energy Limited. The system consists of a three-hull floating support structure with a mounting system that connects the four tidal turbines underneath the platform, which can raise the rotor above the water surface for inspection and maintenance. SCHOTTEL SIT250 turbines, with a selection of two diameters of 4 and 6.3 m, were attached to the platform. Field testing of the system has been documented in Starzmann et al. (2018) and Jeffcoate & Cresswell (2018) at the Falls of Lora in Scotland and has been validated with numerical models. Based on the analyses presented in these papers, this floating turbine system has a high potential for further deployment and commercialization.

1.1 Research on floating turbines

Even though floating tidal turbine technology has been around for more than a decade, the availability of scientific literature surrounding this topic is not widely available compared to floating wind turbines. However, many studies have been conducted on floating offshore wind turbines (FOWT). Some of the research focuses on the instability of the device performance under various wind and waves conditions. Others look at the unsteady loading and motion response using different support platforms, where the most common are spar-buoy, barge, and semi-submersible (Bagbanci, 2011; Sebastian and Lackner, 2013). Besides this, much research investigates floating wind turbines operating under prescribed single DoF motions or fully coupled fluid-structure interaction models (Jonkman et al., 2007; Wen et al., 2017). The difference between wind and tidal turbines is the fluid density flowing through these devices. A tidal turbine tends to be bulkier than a wind turbine to withstand the tidal flow, and blockage effects are more significant in the tidal stream due to the limitation provided by the water surface (Wimshurst & Willden, 2016). Although not entirely correct, the mechanics behind wind and tidal turbines are deemed similar. Therefore, some of the literature on floating wind turbines can be used as references to conduct a floating tidal turbine study.

Generally, for a floating wind or tidal turbine operating at sea, they will experience six degrees of freedom (DoF) motion due to the platform interaction with waves, wind, and tidal current. Based on the literature, the two most significant motions contributing to the unsteady loading on a floating turbine are surge and pitch motions (Tran & Kim, 2015; Micallef & Sant, 2015; Shen et al., 2018). Although the impact is minimal, the heave motion can be considered important since the vertical motion can increase the fatigue damage to the rotor blades, and it is difficult to mitigate this effect through any seakeeping technique. Therefore, it is essential to look into more detail on these three motions on a floating tidal turbine.

Several studies have been conducted to understand the dynamics of floating wind and tidal turbines undergoing these individual motions. Whelan et al. (2009) carried out experiments on a horizontal-axis tidal turbine in unsteady flow conditions to study the effects of the added mass on the rotor. A 0.56 m diameter turbine rotor was attached to an oscillating motorized carriage mounted on a towing tank. The experiments were conducted under constant inflow by towing using a constant speed while oscillating the turbine back and forth to simulate the unsteady loading on the rotor. Morison's equation was used to determine the added mass and damping coefficients in the study. The main contributor to the axial force on the rotor was found to be the damping term, while the added mass term was shown to be small. They have reported that the small added mass might be due to the occurrence of Seich waves during the oscillating motion of the turbine inside the towing tank. This results in corrections to the velocity calculation due to Seiche wave excitation during the stream-wise oscillation. Other than that, hesitation occurred at the motorized carriage damping system where the machine cannot continuously oscillate. These errors cause the small added mass productions during the measurements and calculations of the experiments.

Another experimental study on a floating horizontal-axis tidal turbine had been conducted by Shirasawa et al. (2016) inside a laboratory and on-site (sea) testing. A 2 m diameter prototype floating tidal turbine with a float attached at the top and a counterweight attached to the bottom to balance the buoyancy effects when the device was towed. Unlike the typical HATT design, the rotor was located at the back of the nacelle. The turbine was tested inside a towing tank with a constant towing speed and was tested on-site by dragging the device in the open sea using a boat moving at a constant velocity to simulate the ocean current. Cables were attached to the turbine nacelle and the top floater during the experiments. The experiment shows that other than the rotor, other components such as floater and counterweight also produce drag force which will affect the performance of the turbine. The drag force can influence the platform motions and thus, the unsteady loading on the rotor. Therefore, it is important to study the platform motion response as it can alter the turbine performance. Building and testing a turbine in experimental work, although essential in understanding the dynamics of a floating turbine, is considered very expensive (Sant et al., 2006; Rockel et al., 2014; Xie et al., 2019; Brown et al., 2021). Therefore, most researchers prefer using numerical simulations since it is relatively cheaper. For a floating turbine undergoing a single DoF motion, computationally cheaper engineering code, such as the dynamic inflow coupled with lifting-line or free-wake method, or the blade element momentum theory (BEMT), such as the NREL FAST code, are preferable (Bagbanci, 2011; Sebastian & Lackner, 2013; Wen et al., 2017; Shen et al., 2018; Lienard et al., 2019).

To improve the accuracy of quasi-steady models, such as BEMT or lifting line, correction methods such as Prandtl’s tip loss or Galuert correction methods, need to be applied to a quasi-steady model, such as BEMT or lifting-line methods, to improve its accuracy. Besides this, to model unsteady inflow conditions, empirical models, such as the dynamic inflow method, are needed. These models can only be applied to a small range of dynamic cases since they are based on certain assumptions (Shen et al., 2018). Quasi-steady models tend to overpredict the aerodynamic calculation due to the assumptions, which are considered a limitation for such a model (Tran et al., 2014; Leble & Barakos, 2016). For example, BEMT does not include the effects of viscosity since it is a potential-based method. Besides this, BEMT models often neglect the blade-vortex interaction due to the floating turbine motion, which is an important aspect in simulating a transient case (Liu et al., 2017). It also cannot model complex flow such as the turbulent wake state or the vortex ring state, which occurs around the turbine plane when it oscillates downstream due to the platform motion (Wen et al., 2018). Other than BEMT, the lifting-line method is also unable to model the effects of viscosity accurately since it is based on the potential flow theory. Therefore, flow separation in a highly turbulent flow also cannot be accurately predicted. This model tends to suffer from instability when tip vortices become close to each other (Liu et al., 2017). CFD, on the other hand, is able to predict detailed fluid flow surrounding the rotor blade; able to accurately model blade-vortex interaction; able to capture specific flow detail around the rotor plane for a floating wind turbine (Shen et al., 2018). The downside of CFD modelling is that it requires a huge computational cost, particularly when more than one case needs to be simulated (Wen et al., 2018). However, computational capabilities have been significantly improved over the last decade. Therefore, a more robust numerical method, such as CFD, is preferred among researchers and engineers in studying transient cases such as floating wind or tidal turbines.

1.2 Problem statement

There are a few challenges in modelling a floating tidal turbine. Most numerical models used to simulate floating tidal turbines come from studies of floating wind turbines. Models such as the standard blade element momentum (BEMT) or the actuator disc model, the lifting line method, or the dynamic inflow model, were initially developed for wind turbines (Burton et al., 2001; Sebastian & Lackner, 2012; Micallef & Sant, 2015). Even though it is acceptable to use such models to simulate floating tidal turbines, a few aspects need to be considered.

For a fully coupled model, most studies have not considered the added mass and damping effect (Vaal et al., 2006; Wen et al., 2018; Lienard et al., 2019). Although this can be neglected in floating wind turbine simulations, it must be considered when modelling a floating tidal turbine since the fluid density is significantly higher (Jing et al., 2017; Sun et al., 2017; Guo et al., 2018). When the rotor accelerates (in any DoF motion) inside the high-density fluid of water, some mass (of water) will also accelerate with the moving device (Bonfiglio et al., 2011; Chen & Christensen, 2016). This additional mass is considered crucial in understanding the hydrodynamics of a floating tidal turbine since it adds to the unsteady forces. However, this effect can be neglected when the rotor is accelerating inside the low-density fluid of air. Therefore, there is a need to improve some existing models to include this effect for a floating tidal turbine.

In determining the dynamic forces, one needs to calculate the hydrodynamic coefficients (added mass and damping) from a more accurate model to improve the calculation accuracy, such as from blade resolved simulations, rather than imposing assumptions based on specific shapes, which is widely considered to be the standard method for this type of study (Javanmard et al., 2020). Therefore, it is preferable to conduct an experimental or numerical study to determine these coefficients. However, there is a gap in understanding the transient nature of floating tidal turbines since only a small number of research was conducted on floating tidal turbines. Therefore, analyzing this problem on a device scale, operating under single degrees of freedom (DoF) motion, is considered an important process in order to fully understand the hydrodynamic nature of a floating tidal turbine.

1.3 Aims of study

Since relatively little literature exists on floating tidal turbines, understanding the unsteady hydrodynamics of a floating tidal turbine is limited. Besides this, it is less accurate to assume that floating wind and tidal turbine dynamics are similar since the fluid density is different, introducing additional forces to the turbine. These additional forces are the added mass and damping produced from the inertia of the moving rotor inside a high-density fluid. Three degrees of freedom (DoF) motions, surge, heave, and pitch, will be considered in the present study to understand the unsteady loading of these motions on a floating tidal turbine on a device scale. The surge and pitch motions are the two most significant degrees of freedom that contribute to the unsteady loading of a floating tidal turbine. Therefore it is important that these two motions are included in the present study to understand the dynamics of a floating tidal turbine. The heave motion was also chosen because, to the author's knowledge, on a device scale, there is no research done on this particular motion due to the small impact it has on a floating turbine. However, some interesting physics is presented in this thesis regarding the heave motion, particularly its contribution to fatigue damage. Therefore, the present study aims to improve the understanding of the hydrodynamic forces of a floating tidal turbine undergoing these motions.

Based on these single DoF motions, the added mass and damping forces are calculated. These dynamic forces are important in studying a floating tidal turbine since they count for one of the two major components of the force acting on the floating device (another one being the mean force component). Therefore, the present study aims to produce standardized hydrodynamic coefficients to be included in a simplified model (such as an actuator disc) of a fully coupled floating tidal turbine model.

The availability of literature on floating tidal turbines undergoing prescribed motions (single DoF) and fully coupled models (multi-DoF) is very limited. Thus, this thesis can add to the literature in this field of study. The present study focus on developing a numerical model of a floating tidal turbine. A few good models have been developed throughout the years; however, most of them are simplified models which did not account for the added mass and damping. Therefore, the present study aims to improve an existing numerical model to include the added mass and damping forces into the calculation.

1.4 Thesis outline

Chapter 2 presents the analysis of a floating tidal turbine undergoing a surge motion. A literature review on this topic is presented at the beginning of the chapter, followed by the numerical method used for the surge motion and some model validation. Unsteady loading under various surge amplitude and frequency is analyzed; some result shows a similar trend in the literature while others show contrast the present work. This chapter also looks into various rotor rotational speeds on a surging turbine. Chapter 3 presents the analysis of a floating tidal turbine undergoing a pendulum (pitch) motion. Just like previous chapters, literature reviews on this topic are presented at the beginning. The pendulum motion uses a different mesh and numerical method from the previous chapters, which will be shown in the methodology section. Similar to previous chapters, the dynamics of the floating tidal turbine are analyzed under various motion amplitude and frequency, and also using various rotor rotational speeds. This chapter also compares the unsteady loading of a turbine oscillating in the surge and pendulum motions.

Chapter 4 presents the findings of a floating tidal turbine undergoing a heave motion. Since there is no available literature on this particular topic (not even on floating wind turbines), literature reviews on yawing turbines are presented instead. This is because a heaving turbine can be viewed as a turbine having a dynamic yawing inflow, which will be further explained later in the chapter. The numerical method used for the heave motion will be described briefly, followed by a model verification test. Analyses of the dynamics of a heaving turbine over a range of amplitude and frequency are presented, followed by different rotor rotational speeds on a heaving turbine. Chapter 5 explains the derivation of the added mass and damping forces from the individual DoF blade resolved simulations from previous chapters. Results of the added mass and damping over a range of motion amplitude and frequency are also presented.

Chapter 6 presents the findings of a fully coupled model of a floating tidal turbine. The literature review on this topic is presented at the beginning of the chapter, followed by the numerical method and the model optimization study. Comparison between the present study's modified actuator disc model with the blade resolved and the original model of Brown et al. (2020) is also given in the chapter. The effect of waves only and combined wave-current cases are analyzed. Chapter 7 summarizes the analysis of each chapter, including key findings and discussion on future work.

Chapter 2

Dynamic loading of a floating tidal turbine undergoing surge motion

2.1 Introduction

There are many studies done on stationary tidal turbines operating under different flow and operating conditions. However, little has been done on floating tidal turbines (FTT). However, a large number of scientific literature on floating offshore wind turbine's (FOWT) is available which can be used in understanding methodologies and analyses of FTT. Therefore, this chapter will begin with reviews of some of the literature on FOWT before going into the FTT.

Bagbanci (2011) conducted a numerical study of a FOWT using a fully-coupled model NREL FAST code, developed by Jonkman & Buhl (2007). The NREL 5-MW baseline turbine is used in the study, where comparisons between the stationary turbine (i.e., using a monopile support) and floating turbines supported using three types of platforms: spar buoy, barge, and semi-submersible. The hydrodynamic added mass and damping of each platform are generated using WAMIT, a numerical code that is based on potential flow theory which can model and analyze floating structures under waves conditions. The result shows that the response of each degree of freedom (DoF) varies between platforms. However, the surge and pitch motions were shown to have the highest motion response (amplitude and mean values) for all platform types used in the study. Therefore, it is necessary to include these two motions to study the dynamics of a floating turbine. For the present study, the surge motion is considered in this chapter to develop the methodology properly. The analyses can be isolated to only this motion as a preliminary step before going into other motions.

Wen et al. (2017) conducted a numerical study on a FOWT undergoing a prescribed surge motion using the Free Vortex method (FVM). FVM uses the lifting line method to model the rotor blade and uses a combination of the Kutta-Joukowski theorem and the Blade element momentum theory (BEMT) to calculate the vorticity around the rotor blade. They model the surging motion by changing the frame of reference. The turbine remains stationary (i.e., not physically moving in the surge motion) while a dynamic inflow model is applied at the rotor boundary to simulate a surging turbine. The NREL 5-MW baseline turbine was used in the study. They validated their model against other studies, which used the BEMT, a combined FAST and General dynamic wake (GDW), combined FAST-BEMT, actuator disc theory, and an experimental result. The model shows good agreement with the literature. They simulated a surging turbine oscillating over a range of motion amplitude and frequency. They found that the surge motion affects the change in the angle of attack on the rotor blade. The increase in surge amplitude and frequency increases the loading variation. The study shows that the mean thrust decreases while the mean power increases as they increase the motion amplitude and frequency. The study also investigates surging turbines rotating at different rotational speeds, and they found that the power and thrust variations increases as they increase the rotational speed. A similar study was conducted by Shen et al. (2018) using a modified version of FVM on a FOWT undergoing surge motion. From these two literature, the motion amplitude and frequency, and the rotor rotational speed are essential parameters that need to be considered in investigating a surging turbine. The concept of changing the frame of reference that was used in the study is also a promising method. The computational cost of simulating a surging turbine can be significantly reduced by not having to move the mesh in the surge direction.

Lienard et al. (2019) carried out a computational fluid dynamic (CFD) study of a FOWT undergoing prescribed pitch and surge motions. The overset grid method was used to simulate the pitching and surging motions of the floating turbine. They also used the FVM method to calculate some of the data which the CFD cannot produce, such as the local velocity and angles of attack at the rotor plane. The NREL 5-MW baseline turbine was used in the study. They validated their model on a non-oscillating turbine, with NREL's thrust and power curves (which were calculated using FAST) and a numerical work by Kirby et al. (2017). The model agrees reasonably well with the studies in the literature. The parameter space considered in the study is relatively small compared to literature, with just a variation of two pitch and surge amplitudes. There are no variations in the motion frequency and the rotor rotational speed. The results show similar trends as previous literature presented in this chapter. The mean thrust decreases, and mean power increases for both surging and pitching turbines as the motion amplitude increases. However, they pointed out that the turbine switch from a rotor state to a propeller state, where the thrust and power are negative. They also introduce an analysis based on a helicopter notation, where the turbine enters the vortex ring state, which was related to the switch into the propeller state. This is an interesting view on the problem as not many studies involving floating turbines investigate the matter.

Tran & Kim (2016) conducted a comparative study between CFD and BEMT on a floating wind turbine oscillating under prescribed surge motion. The NREL 5-MW baseline wind turbine was used in the study. The FAST-GDW (generalized dynamic wake) and the AeroDyn module, originally developed based on the BEMT theory, were used in the study. They also include an in-house code based on the unsteady blade element momentum theory (UBEMT) in the comparative study. The details on the setups of all three models can be found in the paper. The surging motion of the turbine was simulated using the overset grid mesh method for the CFD modelling. Typical results were shown, where the loading variation increases as the motion amplitude and frequency are increased. At low motion amplitude, BEMT models overpredict the loading variation when compared to CFD. A similar trend is shown even when the motion frequency is increased while using the same motion amplitude. BEMT models overpredict the loading variation at high motion amplitude when compared to CFD, but only at lower motion frequency. These models begin to underpredict the loading as the motion amplitude is increased. This is shown in their results where BEMT models underpredict the loading at the maximum relative velocity (i.e., at the peak of each cycle of power and thrust coefficients time histories, which is at the maximum loading). They found that in modelling a turbine oscillating in surge motion, BEMT models are only accurate when the axial induction factor is below 0.5. Besides that, the result shows that flow separation occurs at higher motion amplitude cases at the outboard section of the blade ($r/R > 7.5$). This might be due to the unsteady local flow velocity during the surge motion. Flow separation is a sign that the rotor goes into stall at higher instantaneous local flow velocity. Flow separation is also one of the unsteady effects of the floating turbine undergoing a prescribed motion.

Jing et al. (2017) conducted a CFD study on an FTT undergoing a surge motion. An in-house rotor mesh was used in the study; a 2-bladed 0.7 m diameter horizontal axis rotor. The mesh is divided into three sections: the rotor section, the middle section, and the outer section. They simulate the surging motion by deforming the outer section to keep the rotor and middle sections free from mesh skewness. This is to maintain the accuracy of the simulation. The model was validated against an experimental result for a stationary (non-surging) case. The model agrees well with the experiment. The turbine oscillated under various surge motion amplitude and frequency, and rotor rotational speeds. Typical results were presented, where the loading variation increases as the motion amplitude and frequency are increased. The loading variation also increases as the rotor rotational speed is increased. However, the interesting part of the study is the added mass and damping calculations. They extracted the hydrodynamic coefficients using a least-square fitting method. This is quite useful since the added mass and damping coefficients can be used on a quasi-steady model, such as an actuator disc model, to simulate a fully coupled model of an FTT by introducing the additional forces that cannot be captured properly by such a model. Therefore, we can minimize the computational cost by using a simpler model than a blade resolved simulations. Similar studies have been done on yawing (Wang et al., 2016) and rolling (Sun et al., 2017) tidal turbines by the same research group using a similar rotor design and methodology.

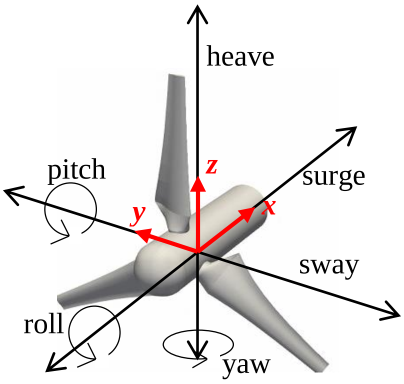

Figure 2-1 Diagram of 6 DoF motions. Translational motion: surge, sway, and heave. Rotational motion: roll, pitch, and yaw.

The present study aims to look at the performance of FTT oscillating in surge motion and the characterization of the hydrodynamics of the turbine. The present study used the moving reference frame to simulate the surging motion of the turbine to minimize the computational cost while maintaining accuracy by not deforming the mesh when surging the rotor. The surge amplitude and frequency will be presented as dimensionless parameters, which are the amplitude ratio $A^* = A_0/R$ and frequency ratio $\omega^* = \omega_0/\omega_r$. A_0 is the surge amplitude (m), R is the blade radius (m), ω_0 is the surge frequency (rad/s) and ω_r is the rotor rotational speed (rad/s).

2.2 Performance metrics

This section provides definitions of parameters used throughout this thesis, including some which are typically used in the field of wind and tidal turbines. Other parameters which are only used in certain sections of the thesis will be defined later in their respective topic of discussion.

In literature, the power and thrust coefficients are the typical parameters used to measure the performance of a tidal turbine. Based on the wind energy handbook by Burton et al. (2001) the power coefficient for a stationary tidal turbine can be defined as the ratio of power extracted by the turbine, P_D, over the total available power, P_T,

$$C_P = \frac{P_D}{P_T} = \frac{P_D}{\frac{1}{2}\rho U_\infty^3 A_D} \qquad (2.1)$$

where ρ is the fluid density, U_∞ is the free stream velocity, and A_D is the swept area of the rotor. The thrust coefficient can be defined as

$$C_T = \frac{T}{\frac{1}{2}\rho U_\infty^2 A_D} \qquad (2.2)$$

where T is the rotor thrust. Since this thesis covers the topic of floating tidal turbines, another set of definitions for these parameters is needed to account for the effect of varying instantaneous velocity. For a turbine moving under a prescribed motion, it will have varying P_D and P_T over time. So, the apparent velocity U_{ap} is used instead of U_∞ to define P_D and P_T. Since U_{ap} varies over time, the definition in equation 2.1 cannot be called power coefficient; rather, it can be called the power efficiency. Applying the same concept for thrust, the power and thrust efficiencies can be presented, respectively, as

$$\eta_P = \frac{P_D(t)}{\frac{1}{2}\rho U_{ap}(t)^3 A_D} \qquad (2.3a)$$

$$\eta_T = \frac{T(t)}{\frac{1}{2}\rho U_{ap}(t)^2 A_D} \qquad (2.3b)$$

where $T(t)$ and $P_D(t)$ are, respectively, the thrust and power extracted by a floating turbine undergoing prescribed motions.

Other than that, the term tip speed ratio is often used to describe the efficiency of a (stationary) turbine. In Burton et al. (2001), the rotor tip speed ratio is defined as the ratio between the rotational speed at the blade tip to the free stream velocity.

$$\lambda = \frac{\omega_r R}{U_\infty} \qquad (2.4)$$

ω_r and R are the rotor rotational speed and rotor radius, respectively. The term λ used to define the tip speed ratio should not be confused with the term wavelength λ', which will be introduced later in Chapter 6.

In this chapter, and in Chapter 4, comparisons in the methodology used to model the prescribed motion (surge and heave) were done using a moving cylinder. Therefore, different terminology is needed to define the loading on the moving cylinder. In this thesis, the axial and vertical structural loadings were chosen to represent the loading on the moving cylinder, based on a numerical study by Meneghini & Bearman (1995) on a cylinder oscillating in the cross-flow direction, where they define the structural loading coefficients for a moving cylinder as

$$C_X' = \frac{F_X}{\frac{1}{2}\rho U_\infty^2 D^2} \qquad (2.5a)$$

$$C_Z' = \frac{F_Z}{\frac{1}{2}\rho U_\infty^2 D^2} \qquad (2.5b)$$

where F_X and F_Z are the axial and vertical structural loads, respectively, and D is the cylinder's diameter.

2.3 Methodology

It is preferable to have a design concept of the whole system of a floating turbine before we can construct the mesh and set up the simulation. Figure 2-2 shows the schematic of the design concept of a floating tidal turbine used in the present study. A single turbine is connected by a steel mast/tower attached underneath a floating platform. Note that for the single DoF simulation (surge, heave, and pitch), dynamic effects from the floating platform, mast, mooring lines, and waves are neglected.

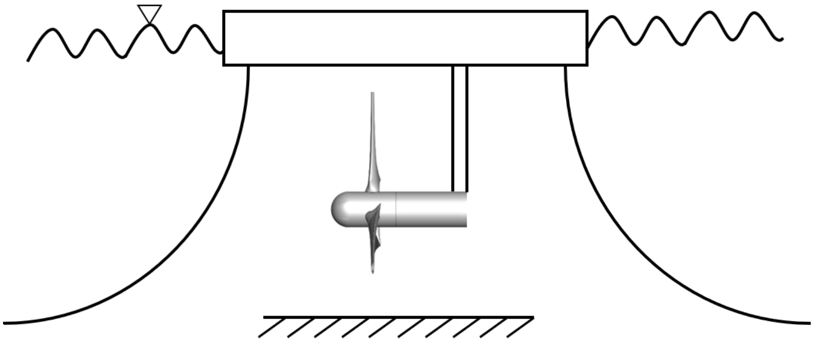

Figure 2-2 Schematic of a floating tidal turbine used in the present study. A single turbine is attached under the floating platform, operating under combined wave-current conditions.

An in-house horizontal axis tidal turbine with a diameter D = 20 m was used in the present study, originally developed by Schluntz and Willden (2015) for operation in moderate blockage levels, further developed by Wimshurst and Willden (2016) for high blockage condition operation. The rotor's blade was designed using RISØ-A1-24 aerofoil with a nacelle of 0.15*D*. The blades have a high thickness to chord ratio, which is a realistic design for a tidal turbine that operates under higher fluid density compared to wind turbines. Further details of the rotor design, which includes the solidity, twist angle, and chord length along the blade, can be found in Wimshurst and Willden (2016). The present study adopted the blocked rotor design mesh placed in the inner domain (coin-shaped mesh) area, as shown in Figure 2-3.

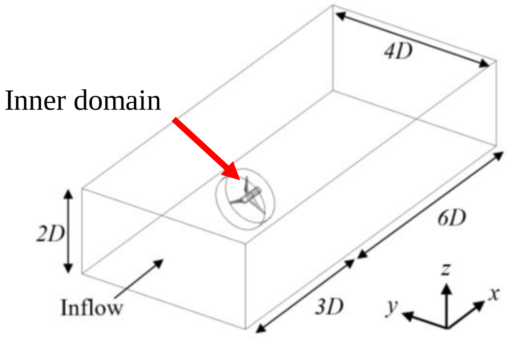

Figure 2-3 Diagram of the computational domain of the turbine. The rotor mesh (inner domain) is placed at the centre of the domain in the *y*-*z* plane.

Figure 2-3 shows the overall computational domain of the turbine. The inlet is 3*D* upstream, and the outlet is 6*D* downstream from the rotor plane. This allows the flow to properly developed before reaching the rotor plane and for the wake to properly mix with the surrounding flow downstream, following Fleming (2014) and Wimshurst & Willden (2017) for a bottom-fixed tidal turbine case. The rotor is placed in the middle of the *y*-*z* plane. The depth of the domain is 2*D* following the depth of the Fall of Warness tidal site (Anatec Ltd., 2010), making the blockage ratio $B = 0.0982$.

Velocity-inlet boundary condition was used at the inlet. Pressure-outlet boundary condition was used at the outlet, while the slip boundary condition was used at the top, bottom, and side boundaries. Slip boundaries were used to simulate a uniform flow. The wall boundary (i.e., no-slip boundary) was used at the rotor surface. The arbitrary mesh interface (AMI) was used at the interface boundaries connecting the outer and inner domains. For transient simulations, the rotor rotation was simulated via the sliding mesh method, where the inner domain is rotated without deforming the mesh.

2.3.1 Numerical method

The two most popular methods to model fluid flow are the Large Eddy Simulation (LES) and Reynolds-averaged Navier-Stokes (RANS). McNaughton (2013) explains that in LES, the fluid flow is categorized as having filtered and residual components. The filter is included inside the Navier-Stokes equation. LES filters the size of eddies inside the fluid flow, where eddies larger than the filter are resolved while smaller than the filter is modelled. Since LES is a widely known model, it will not be discussed in detail in the present study. Instead, refer to McNaughton (2013) and Ouro et al. (2017) for more information about the model. There is one major drawback to LES. It requires finer mesh near a wall boundary to be able to model the small-scale eddies. Therefore, a high-volume mesh is required to model using LES. Ouro et al. (2017) conducted a numerical study on a horizontal axis tidal turbine using an in-house code based on LES to predict the loading on a prototype turbine. The model was validated against an experimental result using a 1:30 scale commercial tidal turbine with a diameter of 0.4 m, tested in a flume tank. Further details of the turbine and the experimental work can be found in the paper. The simulations were conducted using a total of 144 cores for the validation process. The simulation was carried out for three rotor revolutions only, and it took them 31,000 CPU hours to finish simulating. Two mesh sizes were simulated with minimum cell sizes of 0.0015 m and 0.001 m near the rotor. Fine mesh sizes are required for LES simulation to capture the small-scale turbulent flow around the rotor. Even though the model agrees quite well with the experimental result (using the finer mesh), the computational cost is very high since they used 144 cores to simulate one case with only three rotor revolutions. Another factor for the simulation to be computationally expensive is due to the mesh size that was used in the study. They also mentioned that the rotor hub is modified to be shorter than the original design to minimize the computational cost. Although computational resources have increased over the last decade, which makes LES more affordable, it is still expensive if more than one case needs to be simulated.

In RANS, the flow field can be viewed as having the mean and fluctuating components. The decomposition of these components into the Navier-Stokes equations and time-averaged gives the RANS equations. OpenFOAM (version 4.1) uses the RANS equations to simulate the flow field inside the computational domain. Since this model is well established, it will not be discussed in detail in this thesis. Instead, refer to Willcox (1993) for further information on the RANS model and Jasak (1996) for the OpenFOAM model development, which includes model discretizations used in the open-source code. Afgan et al. (2013) conducted a comparative study between RANS and LES method on a horizontal-axis tidal turbine. The computational model was constructed based on an experiment. Comparison with the experimental data shows that LES is capable of producing a more accurate estimate of power coefficient for TSR from 5 to 8 while RANS shows good agreement for TSR of 6 to 8. The percentage difference is very small between both models for thrust (0.5% difference) and power coefficients (2% difference). The mean velocity profiles at 1*D*, 4*D*, and 9*D* downstream of the rotor showed good agreement with one another. The mean kinetic energy profiles at 0.4*D* downstream of the rotor were plotted at *z/D* positions of -0.5, 0, and 0.5 for both models. The result shows that the RANS model underpredicted the mean kinetic energy at all three positions compared to LES. Turbulence intensity I = 10% and 20% were plotted for *z/D* positions ranging from -1 to 1 for both models. I = 10% plot shows good agreement between the two models. For I = 20%, RANS plot shows to be consistent from *z/D* -1 to 1 while LES shows unsteady results. The study also mentioned that LES simulation uses more computational time compared to RANS. Since the present study requires more than a dozen cases to be simulated, RANS was chosen because it is computationally cheaper than LES while having a good accuracy in modelling a floating turbine undergoing prescribed motions. Tran & Kim (2016) and Lienard et al. (2019) both uses RANS for their CFD models to simulate a floating wind turbine oscillating under prescribed surge and pitch motions, respectively.

RANS model requires a turbulence closure model to calculate the Reynold-stress tensor. The $k-\omega$ SST model is one of the most popular choices in modelling turbulence. Menter (1994) improve the original $k-\omega$ model by Wilcox (1988) by combining it with the standard $k-\varepsilon$ model. A blending function is used to determine the boundary layer near the wall. The $k-\omega$ model will be used at the near wall region (i.e. sublayer and log-law) while $k-\varepsilon$ model in the far-field region. Since this is a widely-used model, it will therefore not be explained in detail in this thesis. For further information on the model, please refer to Menter (1994).

The free-stream velocity U_∞ = 2.0 m/s and the $k-\omega$ SST turbulence model with turbulence intensity I = 10% were used throughout the entire study, following the numerical setup of McNaughton (2013), Fleming (2014), and Wimshurst (2018) for turbines operating in unsteady conditions, unless otherwise specified.

2.3.2 Non-inertial (moving) frame of reference

There are a few ways to simulate a surging turbine. The deforming mesh method is one of the most straightforward ways of simulating the surge motion where the turbine moves back and forth while deforming the entire mesh. However, this method has significant drawbacks because when the mesh is deformed, the stability and accuracy of the simulation will be compromised due to the mesh skewness. Another method that can be used is the overlapping mesh (Tran & Kim, 2015) which overlaps the surging inner domain with the outer domain. However, this method requires high mesh volume at the outer domain mesh surrounding the (potential) motion area of the rotor, which increases the computational cost. In order to minimize the computational cost while maintaining the simulation accuracy, the non-inertial (moving) reference frame method was one of the best methods for this type of simulation and therefore was chosen for the present study. This method fixes the frame of reference to the rotor where the flow field moves instead of the rotor.

To model a turbine moving in the 6 DoF motion using the moving reference frame, a few additional forces need to be added on the right-hand side of the momentum equation as

$$\nabla.\mathbf{v} = 0 \qquad (2.6)$$

$$\frac{\partial \bar{\mathbf{u}}}{\partial t} + (\bar{\mathbf{u}}.\nabla)\bar{\mathbf{u}} = -\nabla\bar{p} + \nu\nabla^2\bar{\mathbf{u}} - \nabla.\overline{(\mathbf{u}'\mathbf{u}')} + \underset{(a)}{2\dot{\theta}\mathbf{v}} + \underset{(b)}{\dot{\theta}^2\mathbf{x}} + \underset{(c)}{\ddot{\theta}\mathbf{x}} - \underset{(d)}{\ddot{\mathbf{d}}_0} \qquad (2.7)$$

where θ is the angular displacement, $\mathbf{x}$ is the coordinate vector in the moving reference frame, and $\mathbf{d}_0$ is the translational displacement. The last four terms in equation 2.7 are: (a) Coriolis force; (b) centrifugal force; (c) forces due to unsteady rotational motion; and (d) forces due to unsteady translational motion. Further detail can be found in Li et al. (2002) and Speziale (1989). For the present study, only the last term on the right-hand side of equation 2.7 (the term (d)) is needed to simulate the surging motion of the turbine in the moving reference frame.

The far-field Dirichlet boundary condition needs to be modified as (Li et al., 2002)

$$U_{ap} = U_{\infty} - A_0 \omega_0 \cos(\omega_0 t) \qquad (2.8)$$

where U_{ap} is the apparent velocity (the velocity relative to the rotor) of the surge motion, U_{∞} is the free-stream velocity, A_0 is the surge amplitude, and ω_0 is the surge frequency.

2.4 Model verification

Model verification study was conducted on a 3-dimensional cylinder oscillating in surge motion. This test was to verify the moving reference frame method used in the present study under a blockage ratio *B* = 0.0982.

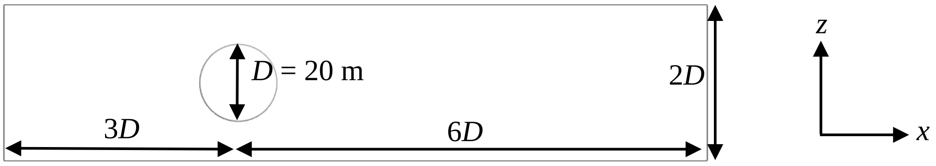

Figure 2-4 Computational domain of a cylinder undergoing the surge motion. The domain is similar to that of the rotor, with the rotor replaced by a cylinder.

Before simulating the full 3-dimensional rotor, the moving reference frame (MRF) method must be verified with an inertial reference frame (IRF) simulation. For the IRF, the present study uses the deforming/morphing mesh method, where the mesh is physically deformed around the cylinder to simulate the surging motion of an object. A 20 m diameter *D* cylinder is placed 3*D* downstream from the inlet and in the middle (vertically) of the *y*-*z* plane, as presented in Figure 2-4. The free-stream velocity U_{∞} = 2.0 m/s, turbulence intensity

I = 10% using the $k - \omega$ SST model (Menter, 1994) and a blockage ratio B = 0.0982 were adopted for the verification study, following the turbine model setup. The cylinder oscillated back and forth in surge motion of amplitude A_0 = 1.0 m and frequency ω_0 = 0.88 rad/s and the axial loading coefficients between the two methods is presented in Figure 2-5.

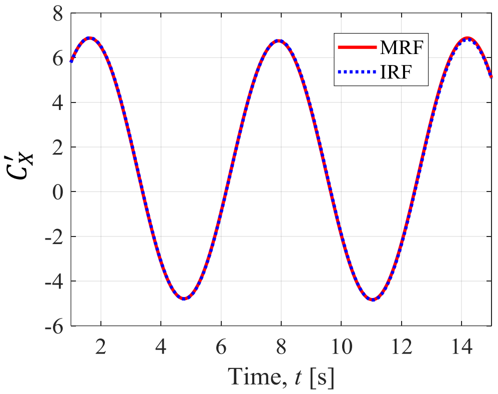

Figure 2-5 Axial loading coefficient of a cylinder undergoing surge motion using the inertial and moving reference frames, IRF and MRF, respectively.

The simulation was carried out until time step t = 15 s to get at least two motion cycles. The initial data (t < 1.0 s) was excluded to eliminate the initial transient effect. The axial load was normalized with $(1/2)\rho {U_\infty}^2 DL$ where ρ is the fluid density, D = 20 m and L = 24 m are the cylinder diameter and length, respectively. From Figure 2-5, the MRF shows good agreement with the IRF with an average percentage difference of less than 1.0%. In Figure 2-6, the vorticity magnitude flow field, which should stay the same either in inertial or non-inertial reference frames, also shows little difference between the two methods.

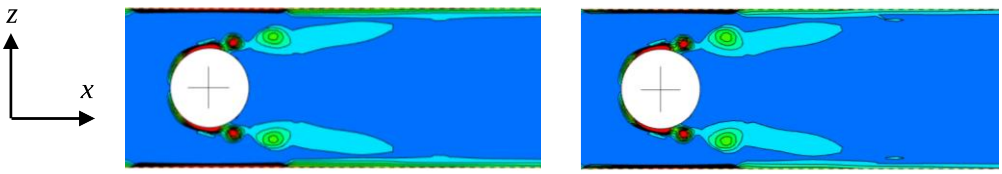

(a) t = 8.0 s (Maximum C_X')

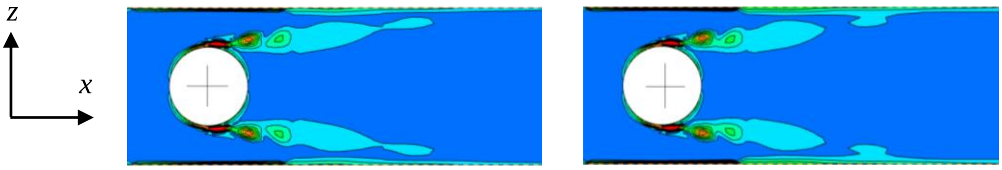

(b) t = 9.5 s

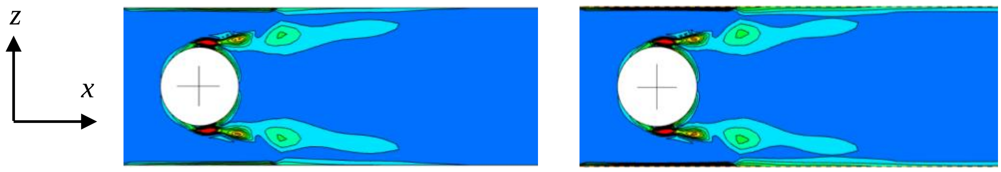

(c) t = 11.0 s (Minimum C_X')

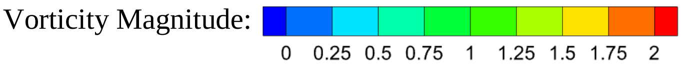

Figure 2-6 Vorticity magnitude contour plots of the wake vortex of a cylinder undergoing surge motion using the MRF (left) and IRF (right).

2.5 Model validation

In Wimshurst & Willden (2016), a mesh sensitivity test for the blocked rotor design mesh was conducted using three different mesh volumes 1.47, 2.91, and 5 million (coarse, medium, and fine meshes) in a 120° domain wedge. The loading on each rotor was compared, and they found that the percentage difference between the coarse, medium and fine meshes were low ($>$ 0.2% for C_P and C_T). Since the coarse and fine meshes agree quite well with one another (based on their result), the coarse mesh was adopted for the present study. Note that the present study did not carry out a mesh sensitivity test for the inner domain (rotor) mesh. The total number of cells for the inner domain is ∼4.4 million.

2.5.1 Mesh sensitivity test

A mesh sensitivity test was conducted using three different mesh volumes for the outer domain while using the coarse rotor mesh from Wimshurst & Willden (2016). The number of cells for the outer domain for coarse, medium, and fine meshes are 0.16, 0.55, 1.21 million, respectively. The domain mesh was refined in the crossflow direction, the radial and azimuthal directions of the O-grid mesh to generate the medium and fine meshes. Steady-state simulations were conducted using a free-stream velocity of 2.0 m/s with a blockage ratio of 9.82% and rotor tip-speed ratio of 4.4, following the optimum tip speed ratio value based on Osman et al. (2020a) (this will be shown later in Figure 2-8). The $k-\omega$ SST turbulence model was used with a turbulence intensity of 10%.

Figure 2-7 shows the axial and tangential force profiles of the three meshes. The profiles show minor differences between each mesh, spanning from the blade root until $r/R \approx 0.4$, and show good agreement towards the blade tip. The average percentage difference of the coarse and medium relative to the fine mesh around the blade tip area ($0.7 \leq r/R \leq 0.9$) is 0.11% and 0.03% for the axial force, and 0.25% and 0.07% for the tangential force profiles, respectively. The difference between coarse and medium to fine meshes around the blade root area ($0.2 \leq r/R \leq 0.4$) is 0.59% and 0.41% for the axial force, and 1.02% and 0.97% for the tangential force profiles, respectively. Since the differences are relatively low between all three meshes, the coarse mesh was adopted for all 3-dimensional rotor simulations in the present study. The present study also conducted a mesh sensitivity test using a 2-dimensional oscillating aerofoil based on Wimshurst & Willden's (2016) mesh for transient case comparison and will be presented later in this chapter.

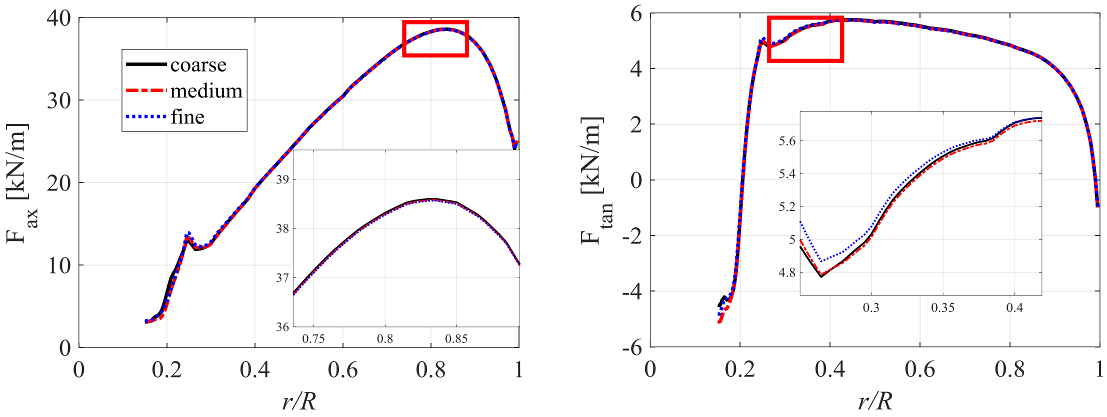

Figure 2-7 Comparison of force profiles for coarse, medium, and fine outer domain meshes. The smaller figure is a zoom-in view of the profiles near the blade tip (axial) and root (tangential).

2.5.2 *Steady-state validation*

For model validation, it is essential to validate both steady-state and transient cases. For steady-state simulation, a non-oscillating (stationary) 3-dimensional rotor was used. Comparisons of power and thrust coefficients between the present study and the result from Wimshurst & Willden (2016) are presented in Figure 2-8, where a series of steady-state multiple reference frame simulations were carried out using multiple values of tip-speed ratio λ at different blockage ratios $B = 0.0982$ and 0.01. The multiple reference frame is a steady-state simulation method where the outer domain is in the inertial reference frame, while the inner domain (rotor mesh) is rotated in a moving (rotating) reference frame. Since this is a standard method for a CFD steady-state simulation of turbomachinery, it will not be explained in detail in the present study. Instead, the reader can refer to the OpenFOAM manual for further information on the model’s discretization.

Overall, the present study agrees quite well with Wimshurst & Willden (2016) results at both blockage ratios. Estimation using polynomial curve fit was used by Wimshurst & Willden (2016) to determine the maximum C_P for the blocked rotor design (refer to their paper for more detail on the comparison between blocked and unblocked conditions). They found that maximum C_P = 0.49 occurs at tip-speed ratio λ = 4.6 for B = 0.0982. The present study found that maximum C_P = 0.52 occurs at λ = 4.4, which overestimate the maximum power by 5.8%. The difference in optimum λ and maximum C_P might be due to the aspect ratio. In Wimshurst & Willden (2016) the cross-section of the domain is a circle rather than a square. Even though the blockage ratio is the same, the aspect ratio is different. Besides this, the simulations were conducted using a 120° wedge domain, where Wimshurst & Willden (2016) use only one blade attached to one-third of a rotor hub, and they use symmetry boundary to simulate a full turbine. The difference in aspect ratio and boundary condition might cause the difference between the present study results with Wimshurst & Willden (2016).

Wimshurst & Willden (2016) found that for the blocked rotor design operating at a low blockage domain B = 0.01, the maximum $C_P = 0.479$ occurs at $\lambda = 4.18$. In the present study, the peak power coefficient $C_P = 0.463$ occurs at $\lambda = 4.2$. The percentage difference of peak power coefficient between these two studies is $\Delta C_P = 3.34\%$ although both occur at (about) similar tip speed ratio. For a stationary turbine, an increase in the blockage ratio increases the overall loading of the device, as expected based on literature (Schluntz & Willden, 2015; Wimshurst & Willden 2016).

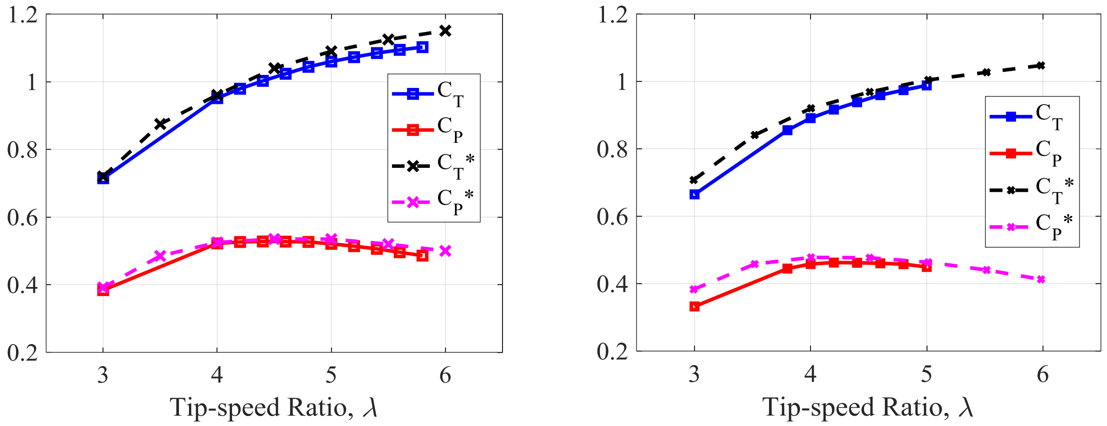

(a) $B = 0.09821$ (b) $B = 0.01$

Figure 2-8 Power and thrust coefficients for various tip speed ratios simulated using steady-state simulations for the present study and the results from Wimshurst and Willden (2016), which are marked by the asterisk, for comparison at $B = 0.09821$ (left) and 0.01 (right) at free stream velocity $U_\infty = 2.0$ m/s.

Therefore, tip-speed ratios λ = 4.4 and 4.2 with rotor rotational speeds ω_r = 0.88 and 0.84 rad/s are considered to be the optimum conditions for the present study at blockage ratios $B = 0.0982$ and 0.01, respectively. The tip-speed ratio of λ = 4.4 will be used as the optimum operating condition throughout this chapter unless otherwise specified. The tip-speed ratio λ = 4.2 will be used as the optimum operating condition later in Chapter 3 for pendulum motion (this will be explained later in the chapter).

The pressure coefficient C_{pre} of the present model was also validated with the result presented by Wimshurst et al. (2018) for $\lambda = 5.0$ using the same blocked rotor design. Two sections of blade spanwise distance $r/R = 0.60$ and 0.94 was taken from the present study and was validated with the results of Wimshurst et al. (2018), as presented in Figure 2-9. Percentage differences were calculated based on the average peak values of the pressure and suction sides of the blade cross-sections, approximately around $X/c =$ 0.2 and 0.4, respectively. The present study under predicts the pressure coefficients by 3.8% and 2.7% at $r/R = 0.60$ and 0.94, respectively.

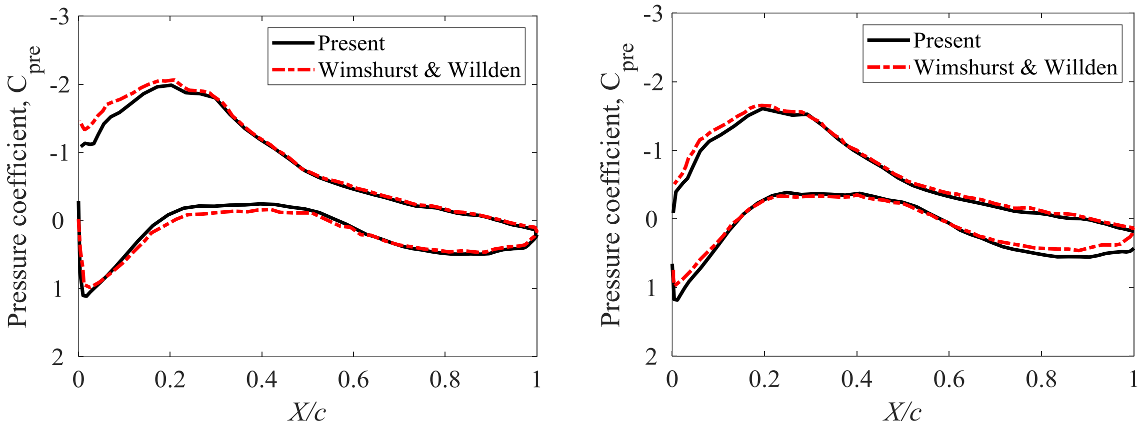

(a) $r/R = 0.60$ (b) $r/R = 0.94$

Figure 2-9 Pressure coefficients at (a) $r/R = 0.60$ and (b) $r/R = 0.94$ for the present study and the results from Wimshurst et al. (2018) simulated using steady-state simulations at $\lambda = 5.0$, $B = 1.0\%$, $U_\infty = 2.0$ m/s.

Another validation using the steady-state multiple reference frame simulation with $B = 0.197$ and a rotor tip speed ratio $\lambda = 5.0$ was carried out to validate the force profiles of the present study with the results of Wimshurst & Willden (2016), and the results are presented in Figure 2-10. The percentage difference of mean axial and tangential forces are 1.49% and 1.11%, respectively.

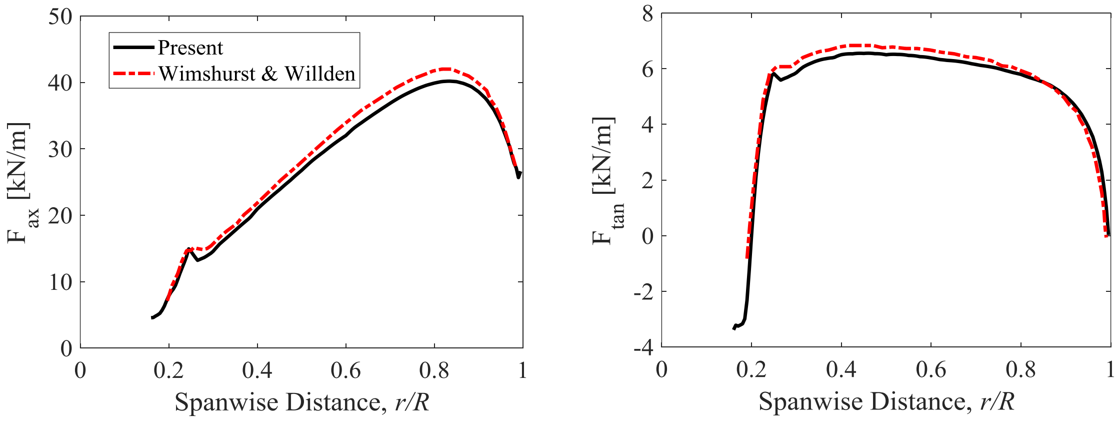

Figure 2-10 Force profiles of the present study and results from Wimshurst and Willden (2016) simulated using steady-state simulations at $\lambda = 5.0$, $B = 19.7\%$, $U_\infty = 2.0$ m/s.

2.5.3 Transient validation

This is the second part of the model validation, where a 2-dimensional RISØ A1-24 aerofoil mesh was validated for transient simulations. The aerofoil mesh was constructed based on Wimshurst & Willden (2016) and the wind turbine aerofoil catalogue by Bertagnolio et al. (2001).

Mesh sensitivity tests for oscillating aerofoil were carried out to determine the viability of using the coarse mesh from Wimshurst & Willden (2016) for the present study. Since this is a transient case, to minimize the computational cost, only 2-dimensional CFD simulations of an aerofoil with different mesh volumes were carried out, which are coarse, medium, and fine meshes. These meshes were developed based on the rotor design by Wimshurst & Willden (2016), as shown in Table 2-1.

Table 2-1 Mesh details based on Wimshurst & Willden (2016). LE and TE are cell sizes of the leading edge and trailing edge, respectively, $c_{0.8}$ = 1.23 m is the chord length at r/R = 0.8, N_{cell} is the number of cells along the chord (from leading to trailing edges), and GR is the growth rate.

Mesh	LE/$c_{0.8}$	TE/$c_{0.8}$	N_{cell}	GR
Coarse	0.0163	0.0033	58	1.2
Medium	0.0163	0.0016	78	1.1
Fine	0.0163	0.0008	98	1.075

A 2-dimensional RISØ A1-24 aerofoil was pitched at α = 6.0° ± 1.5° and 10.0° ± 1.5° with an angular velocity $\omega = 1.436$ rad/s using three different mesh sizes, and the lift and drag coefficients are presented in Figure 2-11 together with the result from Wimshurst & Willden (2016). The percentage difference of mean lift and drag coefficients between coarse and medium to fine mesh is less than 1.0%, presented in Table 2-2. Therefore, it is acceptable to use the coarse mesh of the rotor for a transient case in the present study.

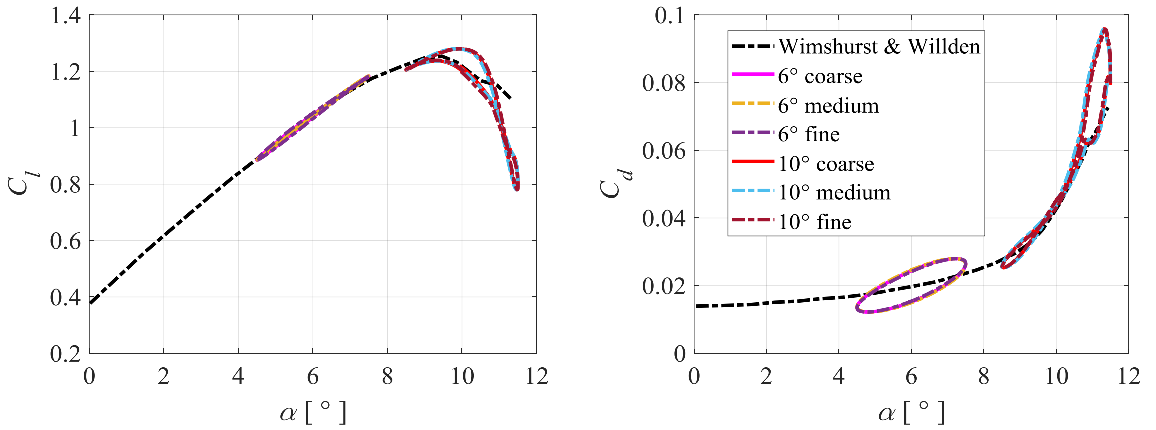

Figure 2-11 Mesh sensitivity test for a 2-dimensional RISØ A1-24 aerofoil at α = 6.0° ± 1.5° and 10.0° ± 1.5° with angular velocity ω = 1.436 rad/s, chord length c = 1.23 m and Reynolds number Re = 1.6 x 10^6.

Table 2-2 Percentage difference of lift and drag coefficients between coarse and medium to fine mesh. A negative sign shows the values of coarse and medium meshes are greater than the fine mesh.

α [°]	Mesh	$\bar{C}_L$	$\bar{C}_D$	Percentage difference $\bar{C}_L$ [%]	Percentage difference $\bar{C}_D$ [%]
6 ± 1.5	Coarse	1.0885	0.0328	0.0070	0.0102
6 ± 1.5	Medium	1.0884	0.0330	0.0169	-0.5836
6 ± 1.5	Fine	1.0886	0.0328	-	-
10 ± 1.5	Coarse	1.2257	0.0691	-0.1080	0.0183
10 ± 1.5	Medium	1.2256	0.0692	-0.0995	-0.0605
10 ± 1.5	Fine	1.2244	0.0691	-	-

A dynamic stall model study was carried out by Hansen et al. (2004) to simulate the unsteady aerodynamic loading of aerofoil sections (NACA 6315 and RISØ A1-24) undergoing prescribed pitching motion under various angles of attack. For the present study, the aerofoil was pitched at an angle α = 4.2° ± 1.5° with a reduced frequency $k_r =$

$\omega c/2U_\infty = 0.092$, an angular velocity $\omega = 1.436$ rad/s with a chord length $c = 1.448$ m and the free-stream velocity $U_\infty = 11.3$ m/s, following Hansen et al. (2004).

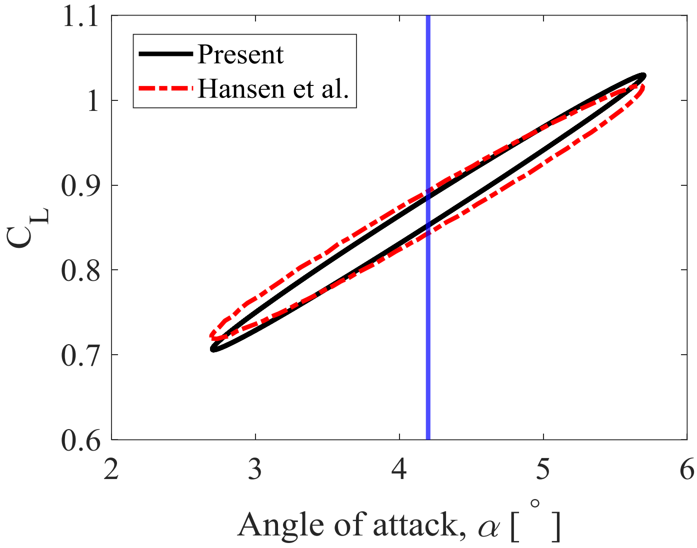

Figure 2-12 Lift coefficient over the angle of attack for a 2-dimensional RISØ A1-24 aerofoil at α = 4.2° ± 1.5° with a reduced frequency $k_r = \omega c/2U_\infty = 0.092$. The blue vertical line is at α = 4.2°.

The results were compared and presented in Figure 2-12. Only the lift coefficient data was available in Hansen et al. (2004) for the oscillating RISØ A1-24 aerofoil. The direction of the loop is counterclockwise for both plots. The overall result of the present study shows good agreement with Hansen et al. (2004), with a mean percentage difference of 0.7% and difference at maximum values at around 1.2%.

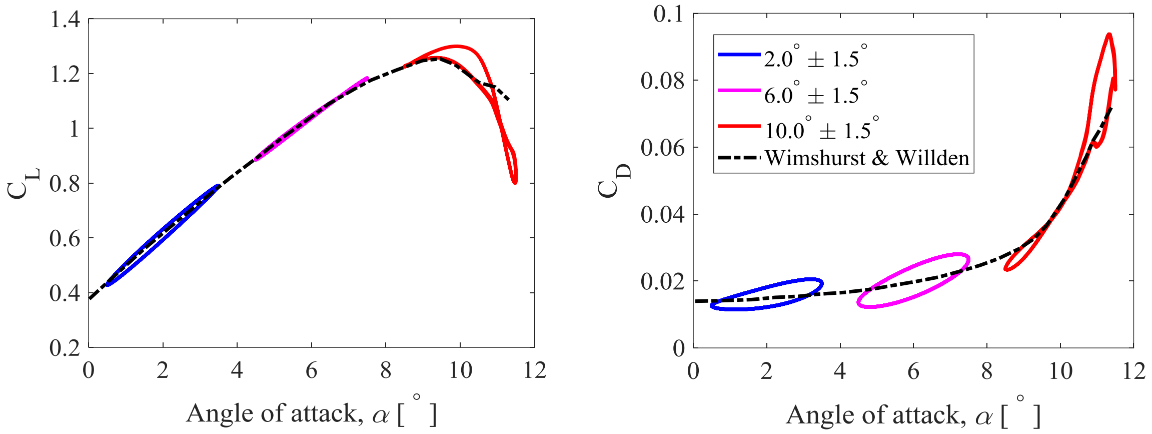

Figure 2-13 Lift and drag coefficients over the angle of attack for a 2-dimensional RISØ A1-24 aerofoil at α = 2.0° ± 1.5°, 6.0° ± 1.5°, 10.0° ± 1.5° with angular velocity ω = 1.436 rad/s, chord length c = 1.23 m and Reynolds number Re = 1.6 x 10^6.

A comparison between static (Wimshurst and Willden, 2016) and oscillating (present study) aerofoils was made, and the results are presented in Figure 2-13. The comparison with Wimshurst and Willden (2016) results can be viewed as a pseudo-validation process since data for oscillating RISØ A1-24 aerofoil are not widely available in the literature. The aerofoil oscillated at angles α = 2.0° ± 1.5°, 6.0° ± 1.5°, 10.0° ± 1.5° with an angular velocity ω = 1.436 rad/s using the chord length c = 1.23 m, based on the chord length used in Wimshurst and Willden (2016) at spanwise distance r/R = 0.8. The chord-based Reynolds number Re = 1.6 x 10^6 with turbulence intensity I = 0.7% were used for this comparison study, following Wimshurst and Willden (2016) based on the wind tunnel experiment used in Bertagnolio et al. (2001). The direction of loops in Figure 2-13 is counterclockwise. The present study (oscillating aerofoil) underpredicts $\bar{C}_L$ and $\bar{C}_D$ by 3.24% and 2.24%, respectively, at the angle α = 2.0° ± 1.5°. At the angle α = 6.0° ± 1.5° and 10.0° ± 1.5° the present study over predicts $\bar{C}_L$ by 1.54% and 5.17%, and $\bar{C}_D$ by 3.54% and 5.47%, respectively. The percentage differences were calculated based on mean values of the data. The lift and drag coefficients show irregular characteristics at α > 10.0° for the oscillating aerofoil due to flow separation.

2.6 Effect of surge motion amplitude on turbine performance

This sub-chapter investigates the effects of two surge oscillation parameters: surge amplitude and surge frequency; and rotor rotational speed, ω_r, on the floating turbine performance. First, the difference between surging and stationary (non-surging) turbines is presented to explain the dynamic effects of the surge motion. Then, the effects of surge amplitude on turbine performance are presented by investigating various surge amplitude ratios $A^* = A_0/R$, where A_0 is the surge amplitude (m), and R is the rotor radius (m). After that, the effects of surge frequency are presented using a range of frequency ratio $\omega^* = \omega_0/\omega_r$, where ω_0 is the surge frequency (rad/s) and ω_r is the rotor rotational speed (rad/s). The effects of ω_r on a surging turbine are also presented in this chapter while keeping the surge amplitude and frequency constant.

2.6.1 Surging and stationary turbines

Figure 2-14 shows the relationship between the surge displacement and the apparent velocity U_{ap} for the case of $A^* = 0.05$ and ω^* = 1.00 rotating at a constant rotational speed of 0.88 rad/s (corresponds to λ = 4.4). Note that this case will be considered for further analysis as a representative case. T_r is the period of one revolution of the rotor at the optimum λ = 4.4. Negative displacement shows the rotor moves upstream from its original position (displacement = 0) with the furthest upstream position at T_1, and positive displacement indicates the rotor moves downstream from its original position with the farthest downstream position at T_3. U_{ap} is 90° out of phase with the surge motion and is maximum when the rotor advances into the incoming flow (at V_4) and is minimum when moving away from the incoming flow (at V_2).

Figure 2-15 shows the time histories of C_P and C_T for a surging and non-surging turbine. As the rotor oscillates in the upstream direction, we observe an increase in C_P and C_T compared to the non-surging (stationary) turbine, which is partially due to the increase in U_{ap}. Conversely, C_P and C_T drop below the non-surging turbine case due to the decrease in U_{ap} when the rotor oscillates in the downstream direction. The oscillations in C_P and C_T are largely in phase with U_{ap} as the power and thrust are proportional to the velocity cubed and velocity squared, respectively.

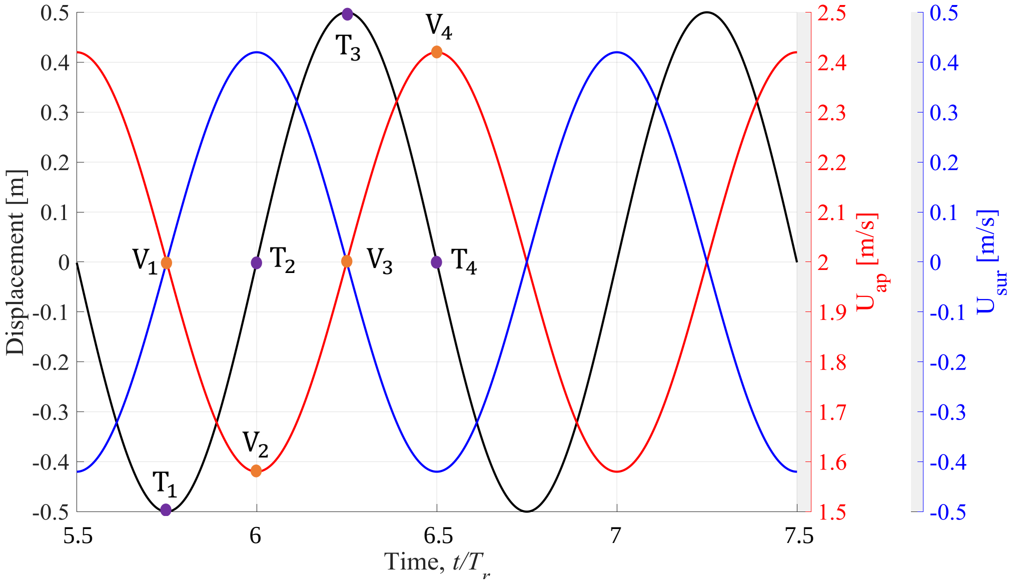

Figure 2-14 Displacement, motion velocity U_{sur}, and apparent velocity U_{ap} time histories for a turbine surging at $A^* = 0.05$ and $\omega^* = 1.00$. The turbine rotates at a constant rotational speed which corresponds to $\lambda = 4.4$. The free stream velocity $U_\infty = 2$ m/s (black dashed line).

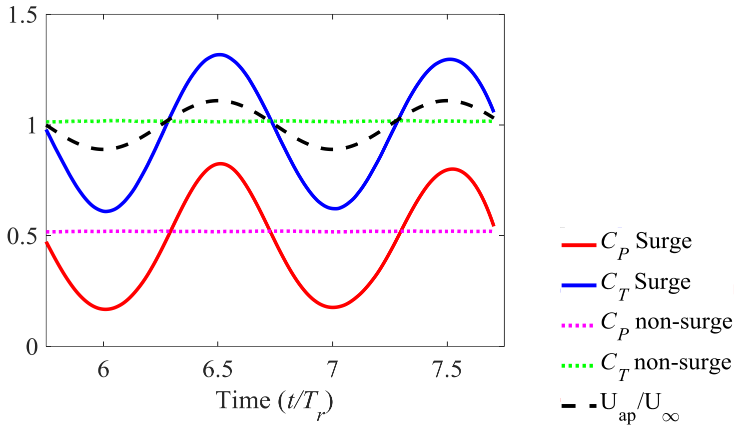

Figure 2-15 Time histories of C_P and C_T for transient blade resolved simulation of stationary (non-surge) and surging turbines at $A^* = 0.05$ and $\omega^* = 1.00$. The turbines rotate at a constant $\lambda = 4.4$. The time history of U_{ap} normalized by U_∞ is also plotted (black dashed line).

We can classify the surge motion into four stages, as shown in Figure 2-16(a). Stages 1 and 2 shows the period in which the turbine decelerates and accelerates in the downstream direction, respectively, whereas stages 3 and 4 shows the turbine accelerates and decelerates in the upstream direction, respectively.

As the power and thrust vary over time, it is informative to consider the stages in which the rotor produces the maximum and minimum power and thrust. For convenience, we define the power output ratio P_R and the thrust ratio T_R for each stage as follows:

$$P_R = \frac{\bar{C}_{P\,\mathrm{S}}}{\bar{C}_{P\,\mathrm{F}}}\ ; \quad T_R = \frac{\bar{C}_{T\,\mathrm{S}}}{\bar{C}_{T\,\mathrm{F}}} \qquad (2.4)$$

where $\bar{C}_{P\,\mathrm{S}}$ and $\bar{C}_{T\,\mathrm{S}}$ are the time-averaged values of C_P and C_T, respectively. The subscripts S and F refer to the surging and stationary (fixed) turbines, respectively. The average values of normalized power and thrust are equal to the power and thrust coefficients for the stationary turbine, respectively.

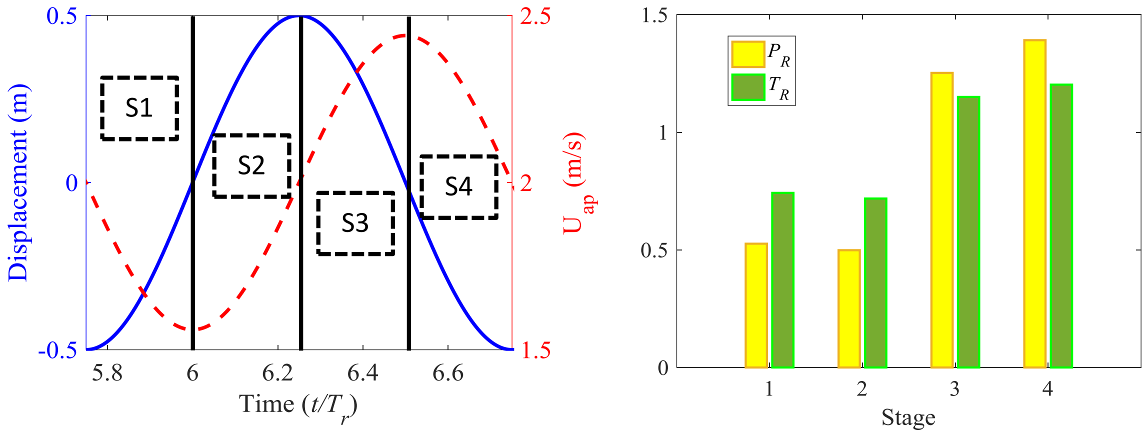

(a)

(b)

Figure 2-16 (a) Stages of the turbine in one cycle of oscillation at $A^* = 0.05$ and $\omega^* = 1.00$. (b) Power output ratio and thrust ratio of the four stages of the surging turbine.

Figure 2-16(b) shows the P_R and T_R at each stage. The minimum and maximum P_R and T_R occurs at stages 2 and 4, respectively. When the turbine moves in the upstream direction (stages 3 and 4), U_{ap} is greater than the mean velocity, leading to higher rotor power and thrust. Conversely, when the turbine moves in the downstream direction (stages 1 and 2), U_{ap} decreases, resulting in lower rotor power and thrust. Comparing stages 1 and 2, and stages 3 and 4, although the average U_{ap} is the same for both stages, P_R and T_R show slightly different values indicating dynamic effects that cannot be simply accounted for in a quasi-steady analysis. The values of P_R and T_R in each stage consequently depend on the flow conditions and wake structure developed in previous stages. In this particular case, the power production is higher than the total thrust on the rotor as the rotor moves in the upstream direction (stages 3 and 4) and shows the opposite when the rotor moves downstream (stages 1 and 2). It is advantageous to operate a surging turbine in terms of power production, where we can obtain higher power and lower thrust during the second half of a surge cycle. It will be beneficial to develop a method that can mimic this operating condition.

Figure 2-17 shows the axial and tangential force profiles along the blade for surging and non-surging turbines. Loading on the blade increase and decrease according to U_{ap} for the surging turbine case. Three points in the cycle are considered: when the turbine is advancing at T_4, leading to maximum U_{ap}; when the turbine is at the farthest upstream at T_1 and $U_{ap} \approx U_\infty$; and when the turbine is retreating at T_2, leading to minimum U_{ap}. The result shows that the spanwise force profiles of the surging turbine when $U_{ap} \approx U_\infty$ are not the same as those for the non-surging turbine, demonstrating dynamic effects associated with the acceleration and deceleration of the surging turbine. The force profiles for the surging turbines are not smooth, showing the dynamic effect associated with the unsteady vortex formation and irregular pressure along the blade, which will be explained later in Figure 2-18 and Figure 2-20. Such effects are not apparent when using a quasi-steady simulation method such as the Blade Element Momentum Theory (BEMT). Tran & Kim (2016) show that compared to CFD simulation, the BEMT model cannot capture the transient flow effect around the blades of the surging turbine correctly. This is because the annular independence assumption in BEMT does not consider the radial flow along the blade. Furthermore, wake expansion and contraction are not modelled in the original BEMT, which renders the model unable to capture the unsteady wake dynamics effects.

Comparison of the velocity magnitude contour plots between the surging turbine at $U_{ap} \approx U_\infty$ and the non-surging turbine case is presented in Figure 2-18(b) and (d), respectively, at the blade cross-section r/R = 0.8. The streamlines of the resultant velocity relative to the blade W, are superimposed onto the contour plots. For the surging turbine case, regions of swirling and reversed flow occur around the trailing edge on the suction side of the blade. These shed vortices occur due to the unsteadiness and time-dependent blade loading during surge motion. A vortex street is also observed behind the blade section in the surging turbine case (in Figure 2-18(f) and (g)). The vortex street occurs due to vortex pumping, marked by the red arrows shown in Figure 2-18(f), because of time-varying blade loading. Vortex pumping does not occur for the stationary (non-surging) turbine case, and only trailing vortices appear downstream of the blade.

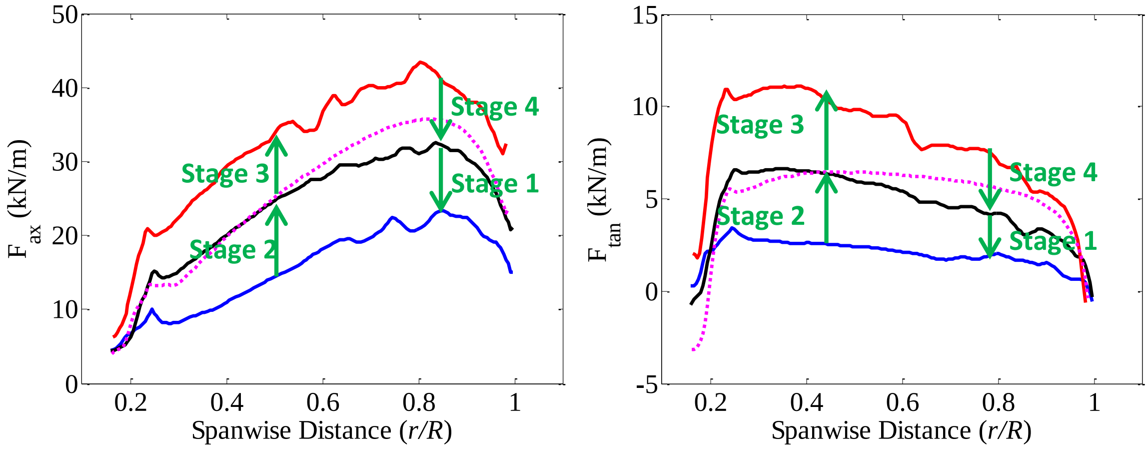

Figure 2-17 Axial and tangential force profiles along a blade for non-surging (dashed magenta line) and surging turbines at minimum U_{ap} (solid blue line), $U_{ap} \approx U_{\infty}$ (solid black line), and maximum U_{ap} (solid red line).

Looking at the Q-criterion iso-surface in Figure 2-19, the vortices are smooth for the non-surging turbine. However, there are swirling vortices at the downstream side of the rotor plane for the surging case. Although the blade-tip vortices are considered smooth for the surging case based on Figure 2-19, at other parts of the blade, the iso-surface shows a series of small swirling vortices, which corresponds to the effects on the velocity contour plots in Figure 2-18. There are also some irregularities in the force profiles (not smooth) and the pressure coefficient plots in Figure 2-17 and Figure 2-20, respectively. These are the dynamic effects associated with the surge motion acceleration, which will not be present when using a quasi-steady type simulation (Lienard et al., 2019). The surging turbine experiences time-varying velocity, which contributes to the change in the angle of attack and the tip-speed ratio of the rotor throughout the simulation. From the resultant velocity streamlines in Figure 2-18(a) to (c), the angle of attack changes according to U_{ap}, and the changes are more apparent for higher surge amplitude cases presented later in this chapter.

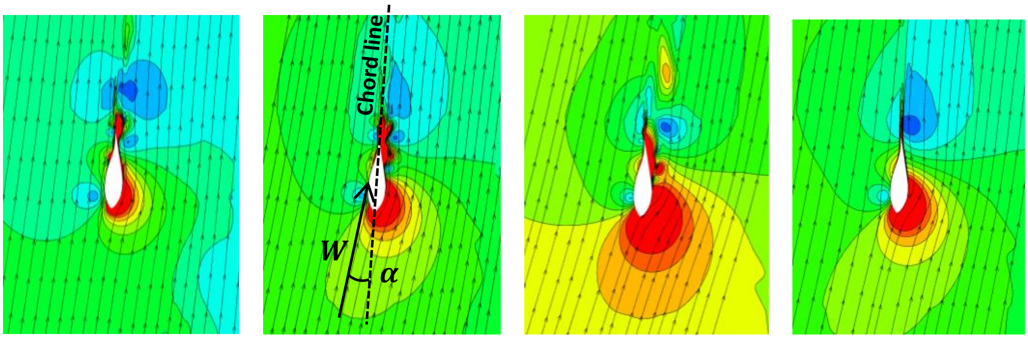

(a) Minimum U_{ap} (b) $U_{ap} \approx U_\infty$ (c) Maximum U_{ap} (d) Stationary

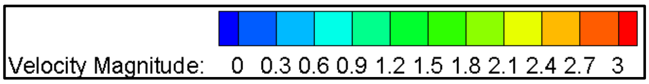

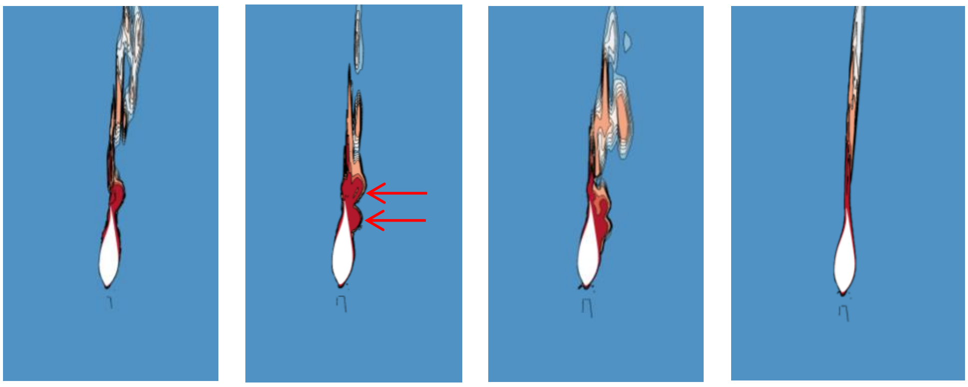

(e) Minimum U_{ap} (f) $U_{ap} \approx U_\infty$ (g) Maximum U_{ap} (h) Stationary

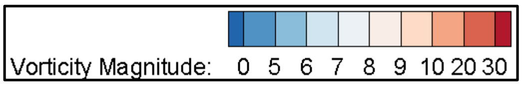

Figure 2-18 Contour plots of velocity magnitude and vorticity magnitude at spanwise distance *r/R* = 0.8 for surging and non-surging (stationary) turbines. Streamlines of the resultant velocity W are superimposed on the velocity magnitude contour plots. α is the instantaneous angle of attack.

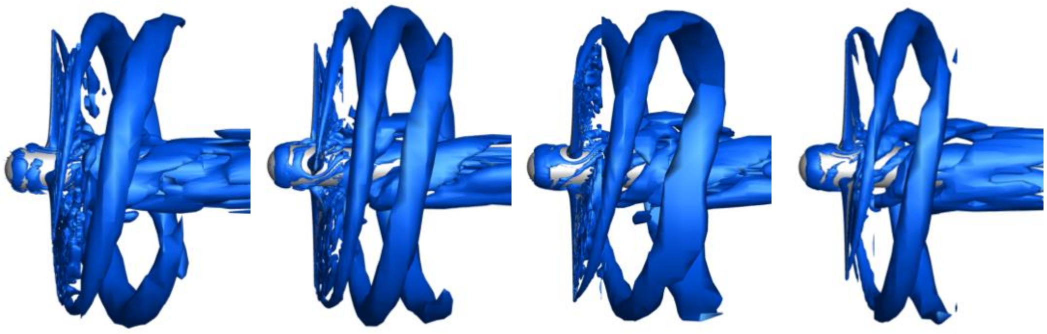

(a) Minimum U_{ap} (b) $U_{ap} \approx U_{\infty}$ (c) Maximum U_{ap} (d) Stationary

Figure 2-19 Q-criterion iso-surface for surging and non-surging (stationary) turbines.

As shown in Figure 2-20, there is little difference in the pressure distribution on the pressure side of the blade between the surging and non-surging cases. However, there are significant differences on the suction side of the blade, particularly near the trailing edge of the blade cross-section. The pressure variation is a result of vortex shedding occurring towards the trailing edge of the blade.

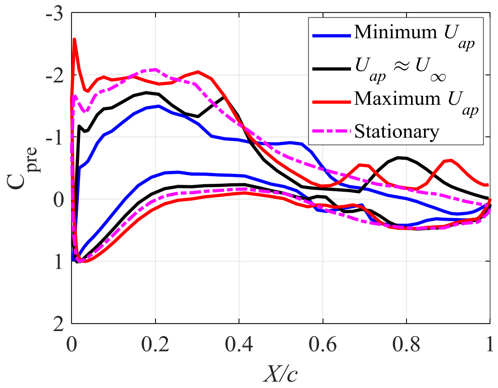

Figure 2-20 Instantaneous pressure coefficient distribution at a spanwise distance $r/R = 0.8$ for surging (A^* = 0.05 and ω^* = 1.0) and stationary turbines.

2.6.2 Effects of surge amplitude on turbine performance

Five different surge amplitude ratios, A^* = 0.025, 0.050, 0.075, 0.100, 0.150 were investigated. Throughout this investigation ω^* = 1.0 and λ = 4.4 are held constant. The values of A^* chosen for this study are based on realistic assumptions of a 20 m diameter rotor surging between 0.25 m to 1.5 m. Figure 2-21 shows the time variation of C_P and C_T for the three different surge amplitudes. Only data from the last two cycles were used for the analysis to ensure statistically converged results. The amplitude of C_P and C_T fluctuations are observed to increase as surge amplitude increases. There are asymmetries at the peak of each cycle for the cases A^* = 0.10 and 0.15, with the asymmetry most pronounced at the largest surge amplitude considered. The abrupt loss of power is a result of the rotor stalling at higher surge amplitudes.

Table 2-3 shows the percentage reduction of the mean C_P and C_T for various surge amplitudes compared to the non-surging device. The reduction in mean thrust and power is due to less optimal rotor operation due to the hydrodynamic effects associated with oscillating inflow. The mean C_P increases as the surge amplitude is increased; however, the mean C_P drops significantly for the maximum amplitude case A^* = 0.15. This happens due to the stalling effects, which can be seen in Figure 2-21, and this will be explained later in this chapter. The opposite occurs for mean C_T, where the mean C_T reduces as the surge amplitude is increased.

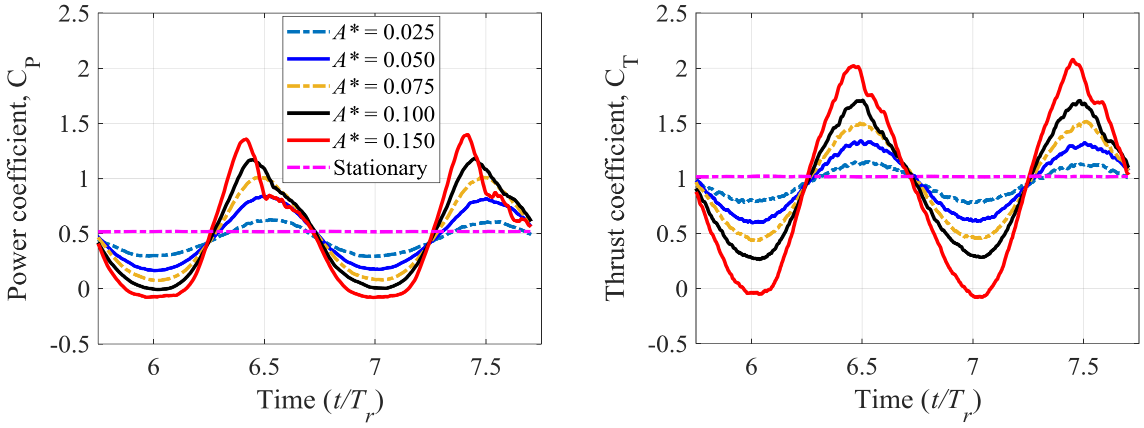

Figure 2-21 Time histories of power and thrust coefficients for non-surging and surging turbine at A^* = 0.05, 0.10, 0.15. Values of λ = 4.4 and ω^* = 1.0 were kept constant throughout the simulations.

Table 2-3 Percentage difference between mean power and mean thrust coefficients for different surge amplitudes.

A^*	$\bar{C}_P$	$\bar{C}_T$	$\Delta\bar{C}_P$ (%)	$\Delta\bar{C}_T$ (%)
Stationary	0.520	0.998	-	-
0.025	0.445	0.960	14.423	3.904
0.050	0.470	0.961	9.615	3.804
0.075	0.485	0.955	6.731	4.404
0.100	0.493	0.950	5.192	4.905
0.150	0.455	0.914	12.500	8.509

Figure 2-22 (left) shows a sketch of a 2-dimensional aerofoil section when the rotor moves upstream (at maximum U_{ap}) during the surging motion. A stationary turbine rotating at the optimum λ maintains an angle of attack α somewhat less than the static stall angle α_S (e.g. Figure 2-22 right) and the flow remains attached to the blade surface. However, when the same turbine, rotating at a constant speed, surges in the upstream direction, U_{ap}

increases, causing α to increase, and exceed α_S, causing flow separation to occur along the blade.

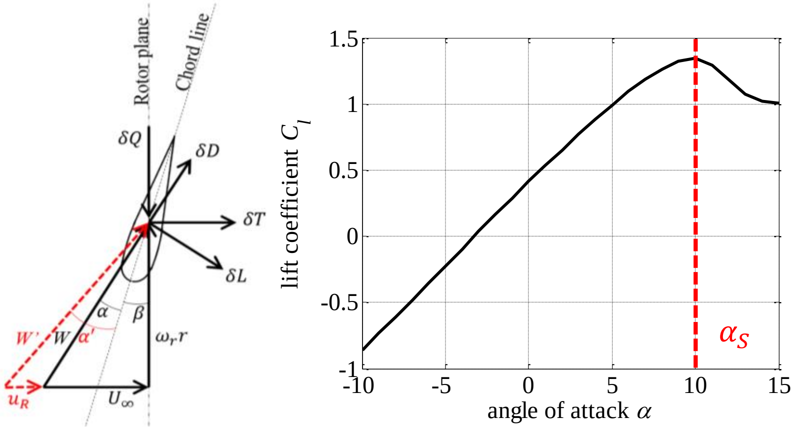

Figure 2-22 (left) 2-dimensional sketch of a blade cross-section and (right) the lift coefficient over the angle of attack curve (Wimshurst & Willden, 2012). α_S = static stall angle (red dashed line).

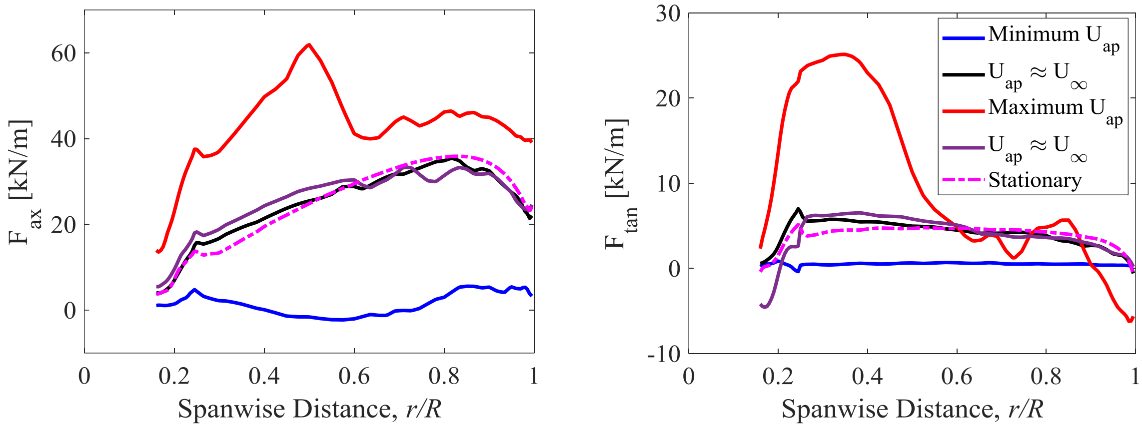

Figure 2-23 Axial and tangential force profiles along the blade for non-surging and surging turbine (A^* = 0.15) at minimum U_{ap}, $U_{ap} \approx U_\infty$, and maximum U_{ap}.

Axial and tangential force profiles for the maximum surge amplitude case (A^* = 0.15) are presented in Figure 2-23. The largest increase in both axial and tangential force occurs at a spanwise distance less than *r/R* = 0.5 when U_{ap} is maximum. The force profiles outboard of this spanwise position is reduced due to flow separation along the blade.

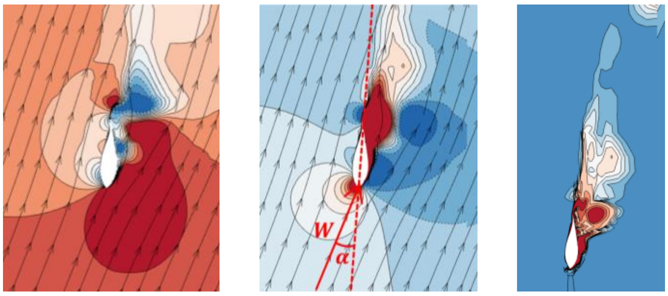

(a) Axial U_{ap} (b) Tangential U_{ap} (c) Vorticity

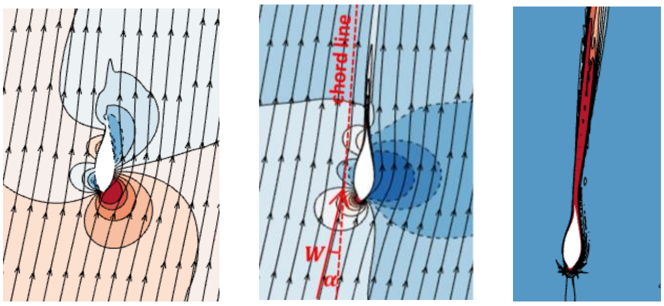

(d) Axial U_{ap} (e) Tangential U_{ap} (f) Vorticity

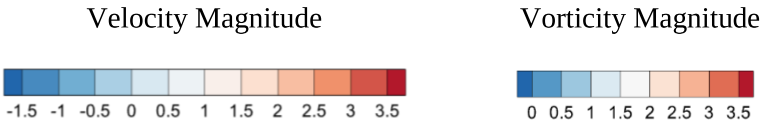

Figure 2-24 Contour plots of velocity magnitude and vorticity magnitude at *r/R* = 0.8 for surging turbine (A^* = 0.15) at maximum U_{ap} (a, b, c) and stationary turbine (d, e, f). Dashed lines indicate negative contour values. Streamlines of the resultant velocity W are superimposed on the contour plots. α is the instantaneous angle of attack.

Axial and tangential components of U_{ap} for the surging turbine around a blade cross-section at *r/R* = 0.8 are shown in Figure 2-24 for surging turbine at maximum U_{ap} and non-surging turbine. The blade angle of attack at maximum U_{ap} is increased significantly compared to the non-surging turbine, leading to a more significant drag force. The presence of separated flow is visible on the suction side of the blade, where swirling and reverse flow from trailing edge to leading edge of the aerofoil cross-section are present.

The spanwise variation in α for the stationary (non-surging) and surging turbines is shown in Figure 2-25 and shows α is increased most significantly above that for the non-surging turbine when U_{ap} for the surging turbine is maximum. The line average method presented in Jost et al. (2018) and Arcos et al. (2020) was used to extract the angle of attack α from the CFD data. This qualitatively follows the behavior results presented in the previous section, where it was found stall occurred on the blade at large values of U_{ap} which results in large angles of attack on the blade. Increasing the amplitude of oscillation for a given frequency results in higher U_{ap} and thus $\alpha > a_S$ each cycle, and consequently, the stalling effects are more significant for turbines undergoing larger surge oscillations.

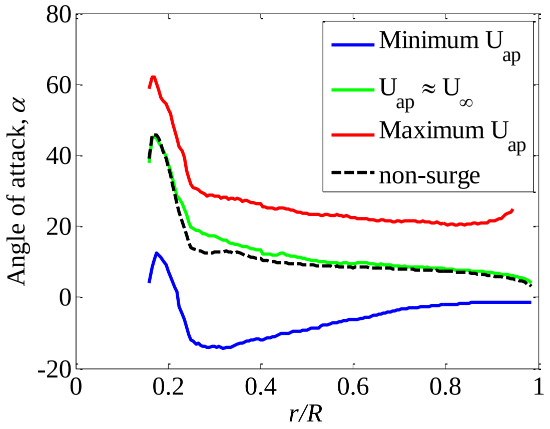

Figure 2-25 Angle of attack α profiles along the blade for stationary and surging turbine corresponding to the minimum U_{ap}, $U_{ap} \approx U_{\infty}$, maximum U_{ap}, and when the greatest flow separation occurs.

Negative values of C_P and C_T are observed in the maximum surge case when U_{ap} is minimum (see Figure 2-21), with corresponding negative axial and tangential forces along significant portions of the blade (see Figure 2-23). As shown in Figure 2-25, the low value of U_{ap} means that α are negative for most part of the blade. Recall that for these simulations the rotor rotational speed is held constant. Two situations may arise: (1) a low angle of incidence leading to a change in the drag vector, and (2) larger changes in the angle of attack which makes the lift becomes negative.

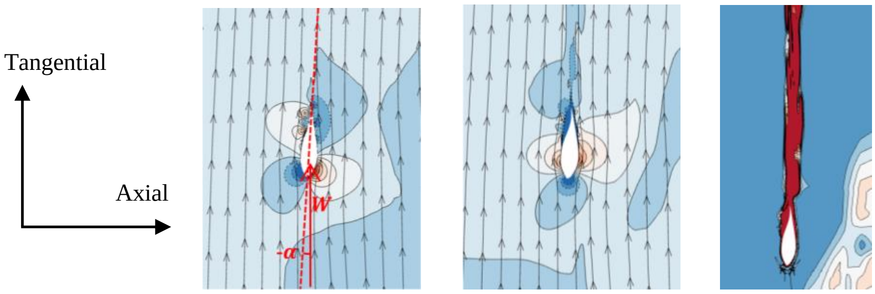

(a) Axial U_{ap} (b) Tangential U_{ap} (c) Vorticity

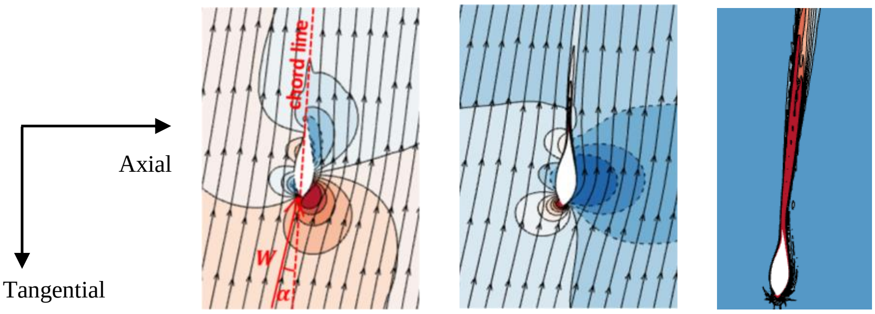

(d) Axial U_{ap} (e) Tangential U_{ap} (f) Vorticity

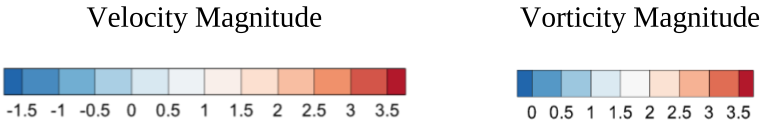

Figure 2-26 Contour plots of axial and tangential velocities relative to the blade and vorticity magnitude at *r/R* = 0.8 for surging at minimum U_{ap} (a, b, c) and non-surging turbine (d, e, f). Dashed lines indicate negative contour values. For the surging turbine, the tangential component is positive going upward. Streamlines of the resultant velocity W are superimposed on the contour plots. α is the instantaneous angle of attack.

In the first case, when α is negative and small in magnitude, the lift may still be positive, defined as the lift vector being on the suction-side of the blade (δL_1' in Figure 2-27). However, the drag will act at the pressure-side of the blade, decreasing thrust. In the second case, as α reduces further, the lift develops on the pressure side of the blade (δL_2' in Figure 2-27), causing the thrust to be negative. In this condition (i.e., thrust and power become negative), the rotor operates more like a propeller than a turbine. As shown in Figure 2-25, α is negative along much of the blade span at minimum U_{ap}. Thus, instead of extracting power from the flow, the rotor needs the power to continue rotating at the same rotational speed. Consequently, negative C_P and C_T values may arise during large surge oscillations. Note that for a real operating turbine, the C_P and C_T values will never be negative as the rotor will just stop spinning as U_{ap} goes to the minimum. This can only happen for fixed speed control; a different control system might be used to optimize the rotor operating condition better.

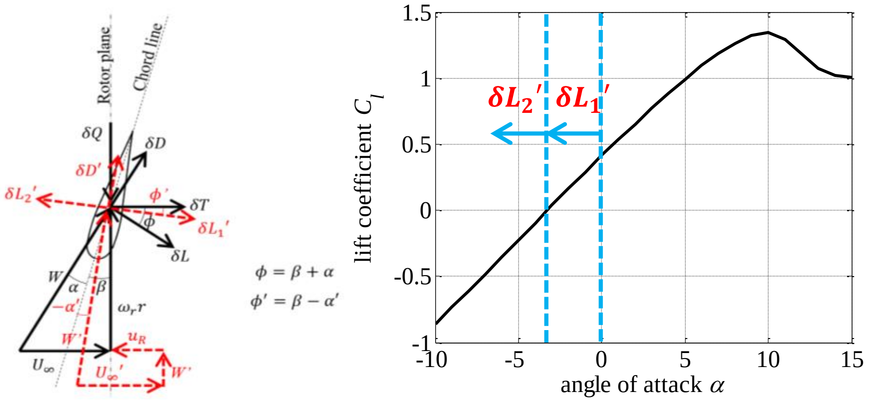

Figure 2-27 (left) 2-dimensional sketch of a blade cross-section for a surging turbine and (right) the lift coefficient over angles of attack curve (Wimshurst & Willden, 2012).

At the minimum U_{ap} for $A^* = 0.15$ case, the turbine might move into its own wake, which will cause problems to the flow around the rotor plane. To determine whether the turbine moves into the wake, also known as the vortex ring state (VRS) incident, wake visualisation and calculations based on helicopter descending flight need to be carried out. Based on Leble & Barakos (2016) and Lienard et al. (2019), for a turbine to be in the VRS, the inflow velocity ratio $V_C/\mathrm{v_h}$ needs to be in the range of $-1 \leq V_C/\mathrm{v_h} \leq 0$. Other induced velocity ratio includes the propeller state ($V_C/\mathrm{v_h} > 0$), the turbulent wake state ($-2 < V_C/\mathrm{v_h} < -1$) and the normal working state ($V_C/\mathrm{v_h} < -2$). The inflow velocity normal to the rotor plane $V_C = -U_{ap}$ where the negative sign is to agree with helicopters notation, as presented in Stewart (1959) and Johnson (2004). The induce velocity in 'hover' $\mathrm{v_h} = \sqrt{\bar{T}/2\rho A_D}$ where $\bar{T}$ is the mean thrust of the moving turbine (the term 'moving' here refers to the surge motion in this chapter, and pendulum motion in the next chapter), ρ is the fluid density (kg/m^3), and A_D is the rotor swept area (m^2). From Figure 2-28, the turbine enters the VRS at minimum U_{ap} for the case of A^* = 0.15 (only happens to the highest surge amplitude). The wake visualization iso-surface confirms this in Figure 2-29, and the vorticity magnitude contour plot in Figure 2-30, showing the turbine moves into its own wake. The range of each rotor state presented in Figure 2-28 is based on Leble & Barakos (2016). As discussed previously, the rotor becomes a propeller at minimum U_{ap} for A^* = 0.15 case. In Figure 2-28, however, it does not seem so. Lienard et al. (2019) argue that these ranges are based on the flight of a helicopter and are not exactly accurate for a turbine. For the VRS range, we can confirm that it is true based on wake visualizations. However, the range for propeller state ($V_C/\mathrm{v_h} > 0$) does not apply in the present study and in the study of Lienard et al. (2019).

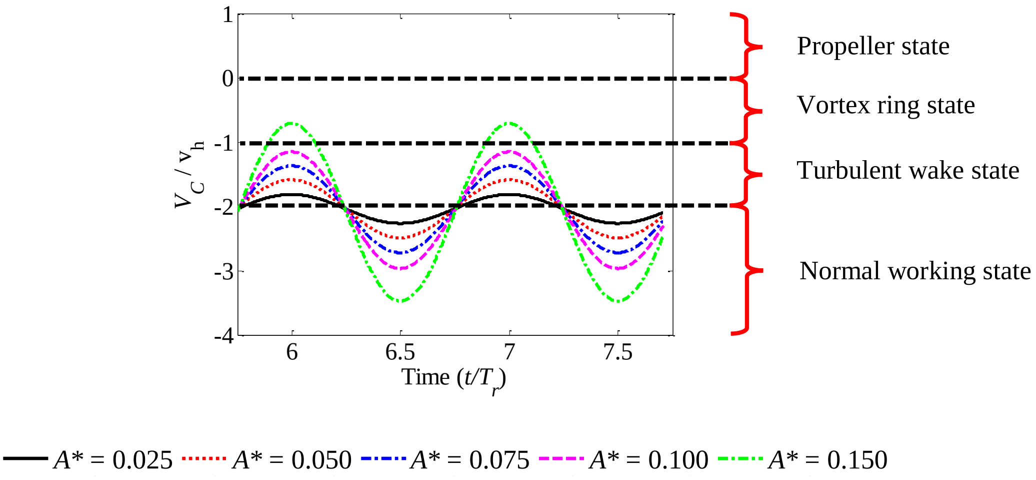

Figure 2-28 Apparent velocity ratio $V_C/\mathrm{v_h}$ time histories, showing the operating state of the turbine.

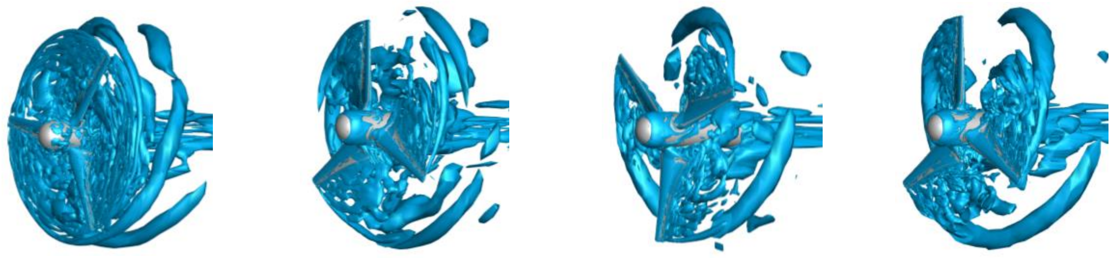

(a) Minimum U_{ap} (b) $U_{ap} \approx U_{\infty}$ (DS) (c) Maximum U_{ap} (d) $U_{ap} \approx U_{\infty}$ (US)

Figure 2-29 Q-criterion iso-surface of a floating tidal turbine undergoing the surge motion at amplitude A^{*} = 0.15. DS = downstream; US = upstream.

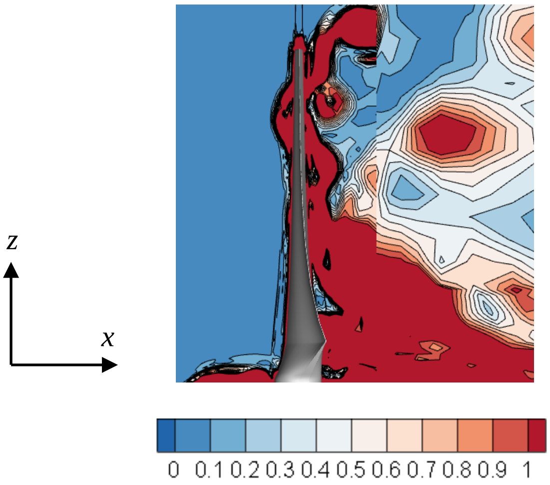

Figure 2-30 Contour plot of the vorticity magnitude at minimum U_{ap} for the case of A^{*} = 0.15.

Time histories for η_P and η_T are presented in Figure 2-31. η_P and η_T is the same as C_P and C_T for the non-surging turbine. This is because, unlike the surging turbine, the power extracted by the non-surging turbine and the total amount of power in the inflow does not vary over time (refer to equation 2.1). η_P and η_T goes near to the optimum condition (i.e., near the non-surging turbine case) twice in one complete surge cycle. This happens due to the motion of the surging turbine where it moves into the optimum position twice in one complete cycle (i.e. when $U_{ap} \approx U_{\infty}$), which can be presented as in Figure 2-31.

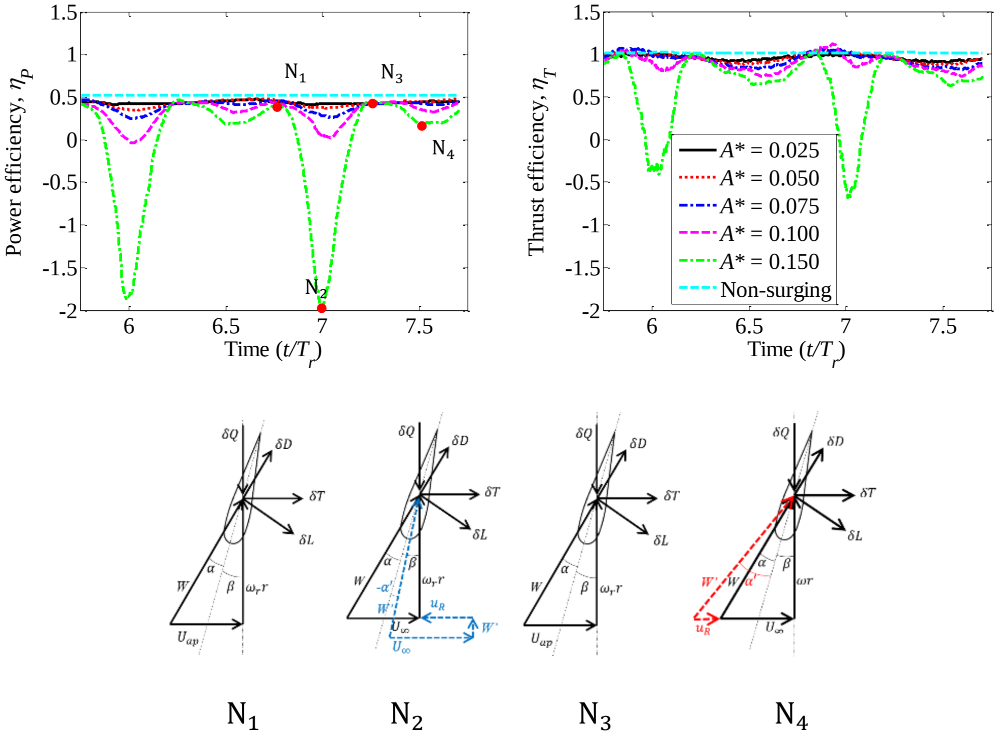

Figure 2-31 Time histories of power and thrust efficiencies for non-surging and surging turbine oscillating at various surge amplitudes.

Since all cases exhibit the same trend, it is preferable to focus on the maximum case only for better understanding. For the case of $A^* = 0.15$, although the turbine operates away from its optimum condition at both positions, the power efficiency drops quite significant at position N_2 (minimum U_{ap}) compared to the position N_4 (maximum U_{ap}). As explained previously, at position N_2 the turbine act like a propeller which needs the power to maintain a constant rotational speed. This shows that the efficiency of the turbine drops significantly low when U_{ap} goes to the minimum at higher surge amplitude.

2.7 Effects of surge frequency on turbine performance

Four cases of $\omega^* = 0.70$, 0.85, 1.00, and 1.30, were simulated to study the effects of surge frequency on the turbine performance. The A^* and λ were kept constant for all cases (0.1

and 4.4, respectively). The values of ω^* were chosen to be close to the resonant point, which lies in a sensible range of wave frequencies from The Fall of Warness tidal site (Anatec Ltd., 2010).

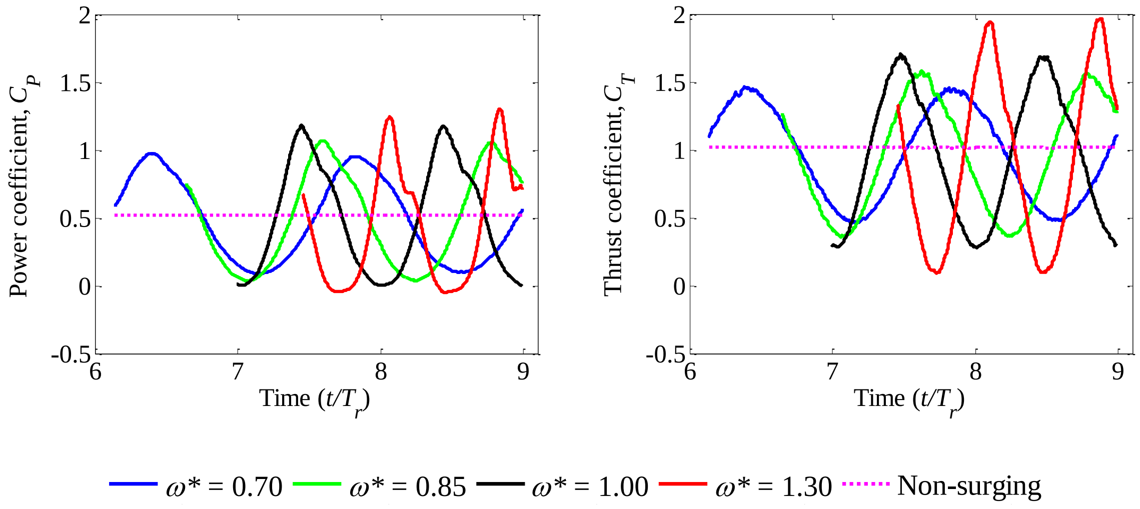

Figure 2-32 Time histories of power and thrust coefficients for non-surging and surging turbine oscillating at various surge frequencies.

Figure 2-32 shows the time histories of C_P and C_T for different surge frequencies. As explained in the previous sub-chapter, the C_P and C_T are largely in phase with U_{ap} as the power and thrust are proportional to the velocity cubed and velocity squared, respectively. From Figure 2-32, both frequency and amplitude of the fluctuating component of C_P and C_T increases as the surge frequency is increased. From equation 2.8, the rotor will have more significant motions when ω^* is increased, which also increases the velocity of the surging turbine $u_R = A_0\omega_0\cos(\omega_0 t)$. This explains why the fluctuating amplitude of C_P and C_T increases together with the frequency of oscillation. Higher oscillation frequency will cause more fatigue damage to the rotor than the increase in surge amplitude alone. The increase in both surge amplitude and frequency (together with other DoF motions) will occur in the open sea, producing even greater fatigue on the floating tidal turbine. Again, the asymmetry at the peak of each cycle occurs here for higher ω^* cases, which suggest that flow separation occurs when the surge frequency is increased.

To further investigate this matter, the axial and tangential force profiles for the maximum surge frequency case are presented in Figure 2-33. Similar to the maximum surge amplitude case presented previously, the change in the force profile is quite remarkable at the time step where the flow separation occurs most significant (from r/R = 0.5 to the blade tip), showing the rotor goes into stall at higher surge frequency.

In Figure 2-32, for the maximum surge frequency case at time step where U_{ap} is at the minimum, C_P shows negative value while C_T shows positive value. The discussion in the previous sub-chapter suggests that the rotor acts more like a propeller than a turbine when both C_P and C_T shows negative values. However, this is a different case where only C_P shows negative value. In Figure 2-33, the tangential force profile shows negative values along the entire blade at minimum U_{ap}. This means that the torque is negative at that time step, which explains the negative C_P. The axial force profile shows negative values until the mid-section of the blade at minimum U_{ap}. Since half of the blade experiences positive axial loading, the overall thrust, then, is positive. As explained previously, for a real operating turbine, the C_P values will never be negative as the rotor will just stop spinning as U_{ap} goes to the minimum. This can only happen for fixed speed control; a different control system might better optimize the rotor operating condition.

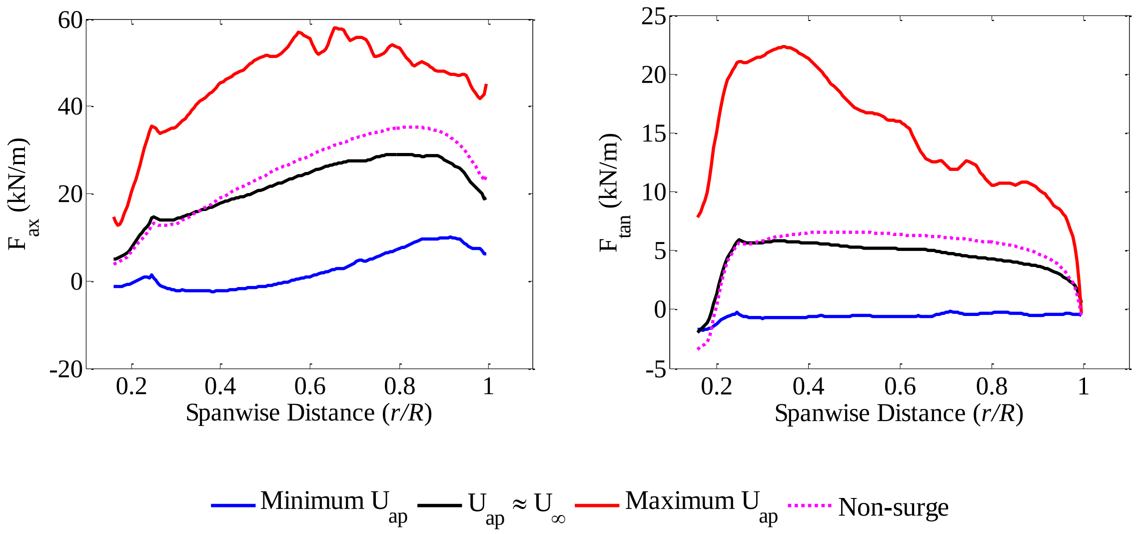

Figure 2-33 Axial and tangential force profiles along the blade for the non-surging and surging turbine at time steps correspond to the minimum U_{ap}, $U_{ap} \approx U_{\infty}$, maximum U_{ap}, and time step where flow separation occur most significantly. This result is for the maximum surge frequency case (ω^{*} = 1.3).

Table 2-4 shows the percentage change in the mean power and mean thrust coefficients for four different surge frequencies from the non-oscillating case. Wen et al. (2017) and Shen et al. (2018) conducted numerical analysis on a horizontal axis floating offshore wind turbine oscillating in surge motion using the free vortex method and lifting surface method. They found that the mean power and thrust increase as the surge amplitude and frequency is increased. Jing et al. (2017) conducted a similar numerical study using the CFD method on a horizontal axis tidal turbine. They found no change in the mean power and thrust of the surging turbine compared to the non-surging when the surge amplitude and frequency are increased. However, in the present study, it was found that the mean C_T reduced slightly when surge amplitude and frequency is increased (shown in Table 2-3 and Table 2-4). The different results from literature occurs due to the large difference in the blockage and the rotor design, but flow parameters and the change in the reference frame may also play a role. In all surging turbine cases, it was found that the mean C_P and C_T were less than the non-surging turbine case. This happened due to the time the surging rotor spends operating away from the design conditions throughout each oscillation.

Table 2-4 Mean power and thrust coefficients for surging turbine compared to non-surging for a range of surge frequencies

ω^*	$\bar{C}_T$	$\bar{C}_P$	$\Delta\bar{C}_T$ (%)	$\Delta\bar{C}_P$ (%)
Non-surging	0.998	0.520	-	-
0.70	0.959	0.484	5.703	6.923
0.85	0.952	0.487	6.391	6.346
1.00	0.950	0.493	6.588	5.192
1.30	0.927	0.438	8.850	15.769

To determine whether the turbine enters the VRS, $V_C/\mathrm{v_h}$ was plotted for all surging turbine cases in Figure 2-34. At $\omega^* = 1.3$ the rotor slightly enters the VRS, and this was confirmed based on the wake visualization in Figure 2-35, where the turbine barely enters its own wake.

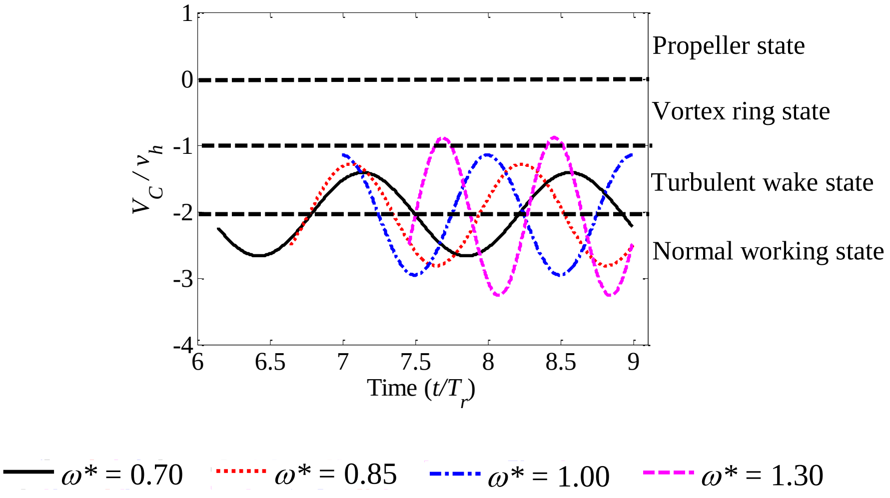

Figure 2-34 Apparent velocity ratio $V_C/\mathrm{v_h}$ time histories, showing the operating state of the turbine.

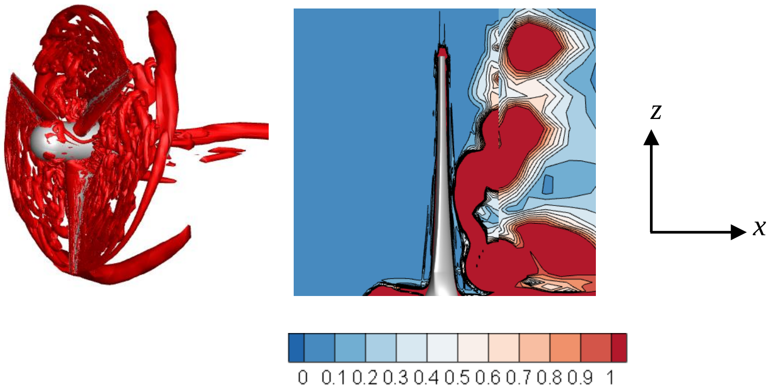

Figure 2-35 Q-criterion iso-surface and contour plot of the vorticity magnitude at minimum U_{ap} for the case of ω^* = 1.30.

2.8 Effects of rotor rotational speed on surging turbine

To study the effects of rotor rotational speed ω_r on the hydrodynamic performance of the turbine, four simulations were carried out using ω_r = 0.84, 0.88, 0.92 and 0.96 rad/s (which, in terms of a stationary turbine, corresponds to λ = 4.2, 4.4, 4.6, and 4.8, respectively) for surging and stationary (non-surging) turbine. The surge motion amplitude and frequency were kept constant at A^* = 0.1 and ω_0 = 0.88 rad/s.

The C_P and C_T time histories for all cases are presented in Figure 2-36. In this subchapter, T_r' is the period of one revolution of the rotor rotating at their respective ω_r. Note that only the data of the last two surge cycles were considered for this analysis to eliminate any discrepancies from the initial time steps. Although the surge amplitude and frequency were kept constant, the variation amplitude of C_P and C_T increase as ω_r is increase. When ω_r is increased, the relative velocity W will also increase. This will cause the lift and drag on the blade to increase, which leads to an increase in loading on the blade. Although the amplitude of variation for U_{ap} is kept constant (due to constant surge amplitude and frequency), the loads on the rotor will not be the same for every ω_r cases since W on the blade is different.

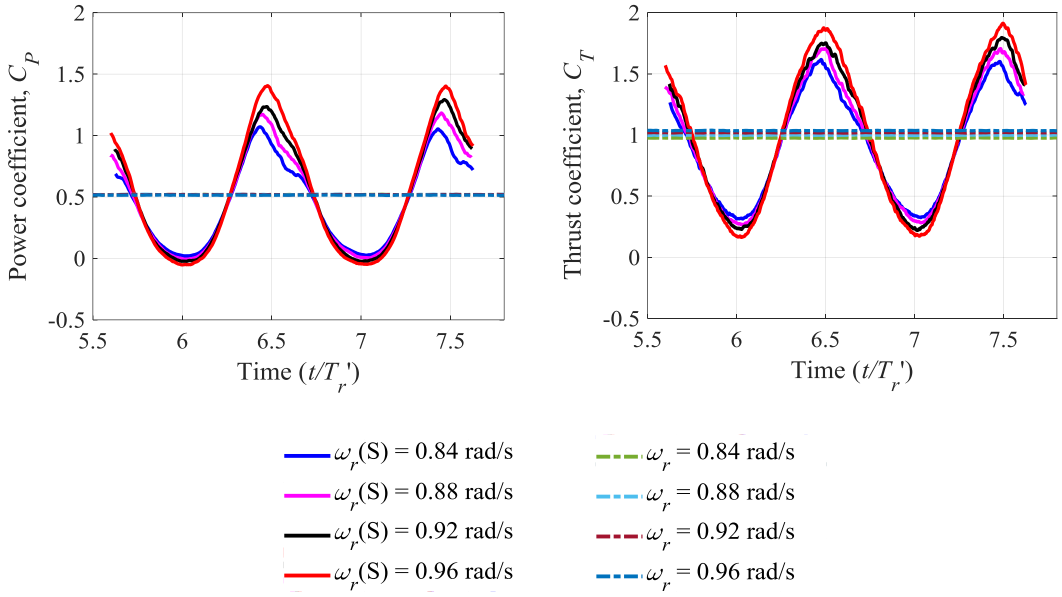

Figure 2-36 Histories of the power and thrust coefficient for four different rotor rotational speeds for the surging and stationary turbine cases. The surging turbine is labelled as (S) in the legends provided. T_r' is the period of one revolution of the rotor rotating at their respective rotational speed.

In Figure 2-36, the asymmetry at the peak of each cycle becomes less significant as ω_r is increased. This shows that the stalling effect can be minimized by operating the surging turbine at a higher ω_r, given that the surge amplitude and frequency are kept constant. To further investigate this, axial and tangential force profiles for stationary and surging turbines rotating at ω_r = 0.88 and 0.96 rad/s, which are presented in Figure 2-37, were analyzed. For surging turbine rotating at ω_r = 0.88 rad/s, the change in the force profiles for both F_{ax} and $F_{\tan}$ are quite significant compared to the stationary turbine when U_{ap} is increased. This shows that for a surging rotor operating at optimum ω_r (which is 0.88 rad/s at the tip speed ratio of 4.4 based on the stationary steady-state case presented in Chapter 2) flow separation occurs along the blade as U_{ap} increase, which causes the sudden drop of the loading along the blade. The same condition can be observed for the ω_r = 0.96 rad/s case. However, the change in the force profiles are less significant compared to ω_r = 0.88 rad/s case.

In Figure 2-38, we can see swirling and reverse flows occur at the blade's suction side. The streamlines also show that the flow is diverted and do not reattach at the suction side of the blade. This shows the occurrence of flow separation at that area of the blade cross-section. However, the flow separation is smaller as the rotor rotates at a higher rotational speed.

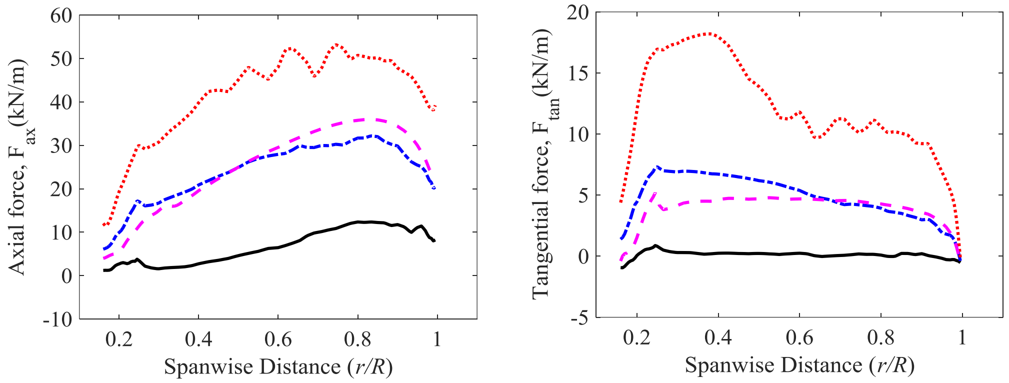

(a) ω_r = 0.88 rad/s (λ = 4.4)

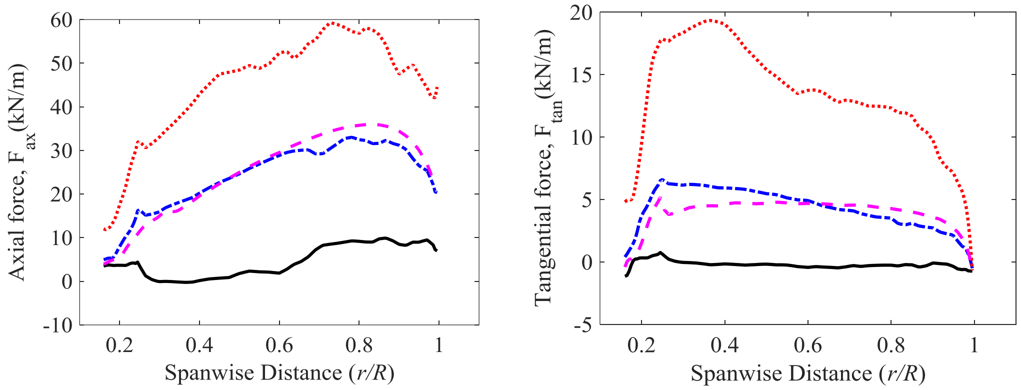

(b) ω_r = 0.96 rad/s (λ = 4.8)

Figure 2-37 Axial and tangential force profiles at minimum U_{ap}, $U_{ap} \approx U_{\infty}$, and maximum U_{ap} for ω_r = 0.88 and 0.96 rad/s (which, in terms of stationary turbines, corresponds to λ = 4.4 and 4.8, respectively).

The negative power in Figure 2-36 is caused by the fixed rotational speed of the simulation. In actual conditions, the rotor will slow down as U_{ap} goes to the minimum. In the present study, however, the rotational speed was kept constant, and the rotational speed for the case of ω_r = 0.96 rad/s is considered the highest among all cases. The power shows a negative value at minimum U_{ap} in Figure 2-36 for the highest ω_r case because at that velocity, the rotor needs power to continue rotating at the given (constant) rotational speed.

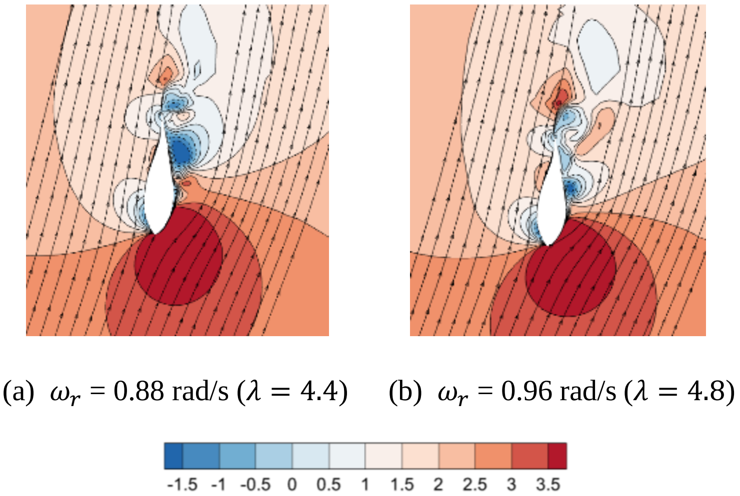
(a) ω_r = 0.88 rad/s (λ = 4.4) (b) ω_r = 0.96 rad/s (λ = 4.8)

Figure 2-38 Contour plots of velocity magnitude at *r/R* = 0.8 for surging turbine at maximum U_{ap} for ω_r = 0.88 and 0.96 rad/s. Streamlines of the resultant velocity W at the blade cross-section are superimposed on the contour plots. The axial velocity is positive from left to right, and the tangential flow is positive going downward.

In Table 2-5, the values of $\bar{C}_P$ increases until the optimum ω_r = 0.88 rad/s then decreases as the λ keep on increasing while the values of $\bar{C}_T$ keep on increasing as the ω_r increases for non-surging turbine, which is typical. The same pattern can be observed in the plots of C_P and C_T in Figure 2-36. However, the values of $\bar{C}_P$ keep on increasing as the ω_r increase for the surging turbine. This shows that for a floating offshore tidal turbine surging at a certain amplitude and frequency (A^* = 0.1 and ω_0 = 0.88 rad/s), the optimum ω_r might have increase i.e. higher than ω_r = 0.88 rad/s. And since the stalling effect can be minimize when operating the surging turbine at higher ω_r, it might be better to operate the turbine at higher

ω_r. We can extract more power while minimizing the stalling effect on the turbine. However, the load variation increases, which increases the fatigue on the rotor.

Table 2-5 Mean power and thrust coefficient for a stationary and surging turbine at different rotor rotational speeds.

ω_r [rad/s]	Stationary $\bar{C}_P$	Surging $\bar{C}_P$	Percentage difference $\bar{C}_P$ [%]	Stationary $\bar{C}_T$	Surging $\bar{C}_T$	Percentage difference $\bar{C}_T$ [%]
0.84	0.5190	0.4582	-12.4437	0.9751	0.9150	-6.3595
0.88	0.5200	0.4723	-9.6140	0.9976	0.9242	-7.7387
0.92	0.5187	0.4928	-4.9933	1.0190	0.9497	-6.8008
0.96	0.5154	0.5968	14.6377	1.0360	1.0610	2.3844

2.9 Conclusion

In conclusion, this chapter presents the analysis of the unsteady loading of a floating tidal turbine undergoing the surge motion over a range of motion amplitude and frequency, and also at different rotor rotational speeds. The surge motion was simulated using a non-inertial frame of reference (where the frame was fixed to the rotor), and the methodology has been verified using a surging cylinder. A series of model validation for steady-state and transient cases were also presented in the chapter, using both a full turbine (steady-state) and a 2-dimensional aerofoil (transient).

For a surging turbine, the loading variation increases with the increase in the motion amplitude and frequency. The overall mean power also increases while the mean thrust decreases as the motion amplitude and frequency are increased. These are typical results for a surging turbine, where a similar trend has been shown in Sebastian & Lackner (2012), Wen et al. (2017), and Lienard et al. (2019) for floating wind turbines oscillating under the surge motion. Results show that the rotor loading is directly proportional to the apparent velocity compared to other motion parameters, although this is expected based on literature (Tran & Kim, 2016; Lienard et al., 2019). The present study also analysed the power and thrust efficiencies of the surging turbine by normalizing the load with the apparent velocity. Results show that the turbine efficiency goes to the maximum twice per cycle, at around $U_{ap} \approx U_{\infty}$. This happens because the tip-speed ratio of the turbine becomes closer to the optimum condition, hence increasing the efficiency.

Flow separation occurs near the blade tip region at higher motion amplitude and frequency (stalling effect), which causes the loss in lift and therefore compromises the rotor performance. The effects of stall may be mitigated by operating the turbine at a higher rotational speed ω_r. At the highest ω_r C_P becomes negative (power loss) for a portion of the oscillation cycle. Thus, there is a compromise to be had between operating the rotor at a sufficiently high ω_r to reduce the negative effects of stall in some parts of the oscillation cycle and the loss of energy at other parts of the oscillation cycle. The rotor slightly enters the VRS at higher motion amplitude and frequency, which increases the fatigue damage to the blade from the wake interaction.

Chapter 3

Dynamic loading of a floating tidal turbine undergoing pendulum motion

3.1 Introduction

The wind energy community has extensively studied the dynamics of floating offshore wind turbines, ranging from an individual floating rotor to wind farms (Wen et al., 2017; Micallef & Sant, 2015; Castro-Santos & Diaz-Casas, 2015; Rodrigues et al., 2015). Some focus on an individual degree of freedom (DoF) motion, while others looked at a fully coupled model with 6 DoF oscillations (Tran & Kim, 2015a; Jonkman, 2009). One of the main interests of the present study is to focus on a single DoF motion of a floating tidal turbine to investigate the dynamics of the unsteady loading of the rotor. Therefore, it is essential to pick a single DoF motion that has the highest contributing factor to the loading of a floating turbine.

Sebastian & Lackner (2012) conducted a numerical study of a FOWT using the NREL 5-MW baseline turbine. Three types of platforms were used in the study to support the turbine: tension leg platform (TLP), spar buoy, and barge. An in-house code, Wake Induced Dynamics Simulator (WInDS), which is a combination of the free vortex wake and lifting-line methods, was used in the study to simulate the FOWT. However, WInDS cannot simulate the platform dynamics, which is crucial in studying a floating turbine. Therefore, the NREL FAST code, developed by Jonkman & Buhl (2007), was used to complement WInDS by providing time histories of the platform motion. They tested the FOWT under three operating conditions: below-rated, rated, and above-rated; they found that the wake formation is less stable in below-rated cases. In addition, they found variations in the bound vorticity along the blade due to the pitching motion, leading to loading variation and fatigue damage to the rotor. They demonstrate that the pitching motion is of primary interest in studying a floating turbine, where it has the most influence in the formation of wake perturbation, variations in the rotor induction (i.e., loading variation), and the angle of attack variation. In a follow-up study, Sebastian & Lackner (2013) conducted a numerical study using the FAST code to simulate a floating tidal turbine on the same three support platforms. They again tested the FOWT under three operating conditions which are below-rated, rated, and above-rated cases. They also found that the pitch DoF has the largest amplitude of motion response (followed by surge) for all three platforms tested. Besides that, the pitch DoF has the highest impact on the angle of attack variation, which can be related to the motion response of the platform. These studies show that the pitching motion is considered to have the most influence on the fluctuating rotor loading.

The same trend has been found by Bagbanci (2011) for a numerical study using FAST code and Pegalajar-Jurado et al. (2016) for an experimental study using TLP. Even though all these studies are of floating wind turbines, similar physics can be applied to tidal turbines since both wind and tidal turbines exhibit similar mechanics. Since the literature suggests that pitching motion has a significant contributing factor to the unsteady loading of a floating turbine, this motion is chosen for the present study.

Lienard et al. (2019) conducted a numerical study using CFD looking into the dynamics of a floating wind turbine oscillating in pitch and surge motions. They found that the fluctuating loading for a pitching turbine is affected by the normal inflow velocity. The mean thrust of the pitching rotor drops while the mean power increase as the motion amplitude is increased. They also found that a pitching rotor enters the vortex ring state (VRS) when it moves backwards to the downstream position at higher motion amplitude. VRS occurs when the rotor moves into its own wake as it oscillates downstream, which causes the loss in lift on the rotor blade. Besides that, the pitching turbine produces negative power when oscillating downstream at a higher pitch amplitude case. This shows that the rotor switches to the propeller state as it moves downstream. A similar trend has been demonstrated in Sebastian & Lackner (2012), where the rotor enters a propeller state, where the rotor gives energy into the flow rather than extract it, in the above-rated case. The propeller state occurs within the root and tip regions along the blade. In addition, they investigate the angle of attack variation as the rotor oscillates in the pitch motion. They found that the angle of attack varies between the upper and lower halves of the rotor. This variation depends on the effective flow velocity at the rotor plane, which varies from upper to lower halves when oscillating in the pitch motion. These are interesting analyses that need to be adopted in the present study to understand the hydrodynamic effect of a pitching motion on a floating tidal turbine.

Tran & Kim (2015) investigate the vortex-blade interaction of a floating wind turbine undergoing a pitching motion. They conducted CFD simulations that use RANS with $k-\omega$ SST turbulence closure model to simulate the fluid flow around the turbine. They use the multiple reference frame to simulate the rotation of the rotor. The multiple reference frame is where the rotor mesh is kept stationary while the surrounding fluid is rotated to simulate the rotor in a non-inertial reference frame. At the same time, the mesh outside of the rotor domain is simulated in an inertial reference frame. The deforming mesh method was used to simulate the pitching motion of the turbine, which was applied to the outer domain mesh. Besides that, they also used an in-house code based on unsteady blade element momentum theory (UBEMT) to simulate the floating wind turbine. The code uses the 3-D correction method, which includes the Prandtl tip loss and Glauert correction methods, to improve the aerodynamic force calculation from the standard BEMT method. A dynamic inflow model was applied to simulate the effect from the additional velocity contribution due to the 6 DoF platform motion. The model calculated the additional velocity locally on each blade at every time step. More details on the UBEMT model, and the CFD simulation setup, can be found in the paper. The power and thrust time histories were compared between the two models together with the FAST code. They simulated the floating turbine under various pitching motion amplitude and frequency. The overall result shows a similar trend in the literature related to this topic, where the loading variation increases as the motion amplitude and frequency increase. The UBEMT model shows a higher relative error to the CFD results compared to the FAST code, particularly at lower motion amplitude cases. They also found that each blade shows different phases to each other due to the difference in the effective azimuth velocity. Besides that, the divergence of the aerodynamic loading between CFD and the in-house UBEMT and FAST code is due to the wake interaction with the rotating blades at high motion amplitude and frequency. In addition, they found that the distance between the present and previous tip vortices is different between the top and bottom half of the wake, based on the CFD simulation results. A similar study can be found in Shen et al. (2018) of a floating wind turbine undergoing pitching motion, where they used a combination of the lifting-line and free-wake methods for the numerical method. Therefore, it is important to look into the blade-vortex interaction, aside from the multi-phase loading of individual blades, over a range of motion amplitude and frequency into the investigation of the present study.

This chapter will investigate the dynamics of a floating tidal turbine undergoing pendulum motion, which includes unsteady loading of the rotor and individual blade load variation. We will also determine the limitation of the motion amplitude when the rotor enters the vortex ring state as it moves back into the downstream direction and the stalling effect when it moves into the upstream. This chapter will present a possible way to minimize the stalling effect to leverage the advantage of using a floating tidal turbine.

3.2 Numerical method

The diagram of the present study is presented in Figure 3-1(a). The double sliding mesh method was used to model the pendulum motion while rotating the rotor. The inner domain mesh is pitching about the centre of rotation (COR) in the cross-stream (*y*-axis) direction, together with the middle domain, while the rotor rotates around its time-varying axis, as shown in Figure 3-1(b). The outer domain remains stationary throughout the entire simulation.

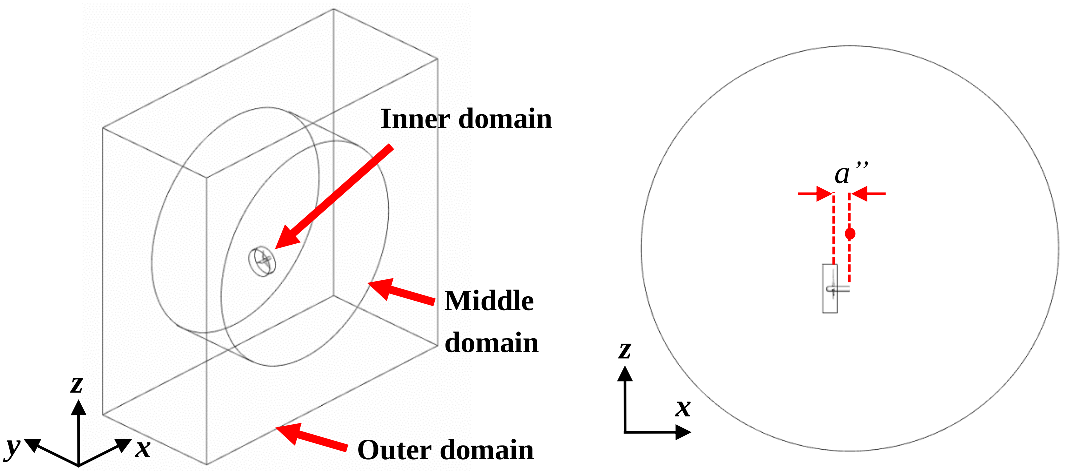

(a) Computational domain (b) Side view

Figure 3-1 Diagrams of (a) the computational domain and (b) the side view of the domain, showing the offset *a"* of the turbine plane from the COR.

The rotor plane is offset $a'' = 0.4D$ from the COR, which is located at the centre of the middle domain. The offset is to agree with the design schematics presented in Figure 2-2 in chapter 2. The nacelle centreline is located 1*D* below the COR.

No modification was made to the momentum equation as in the surge motion case since the present model uses the inertial frame of reference. The blockage ratio for the pendulum motion is $B = 0.01$. This is due to the method used in the present study to model the pendulum motion. The sliding mesh method of the middle domain and the design concept of the floating tidal turbine system requires that a larger blockage ratio needs to be used to run the simulation successfully.

3.3 Mesh sensitivity

A mesh sensitivity test was conducted using three different mesh volumes for the middle and outer domain while using the coarse rotor mesh from Wimshurst & Willden (2016). The domain mesh was refined in the crossflow direction, the radial and azimuthal directions of both O-grid meshes to generate the medium and fine mesh. Steady-state simulations were conducted using a free-stream velocity of 2.0 m/s with a blockage ratio of 1.0% and rotor tip-speed ratio of 4.2 (refer to Chapter 2 for the optimum tip-speed ratio). The $k - \omega$ SST turbulence model was used with a turbulence intensity of 10%.

The power and thrust coefficients were compared for all three meshes, as shown in Figure 3-2. The percentage difference between the coarse and medium to the fine mesh are 0.60% and 0.44% for C_{P}, and 0.49% and 0.37% for C_{T}, respectively.

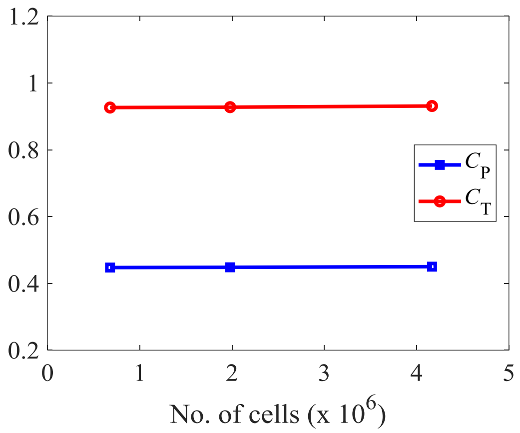

Figure 3-2 Mesh sensitivity test for coarse, medium, and fine meshes. The number of cells here refers to the cell count of the middle and outer domain mesh only.

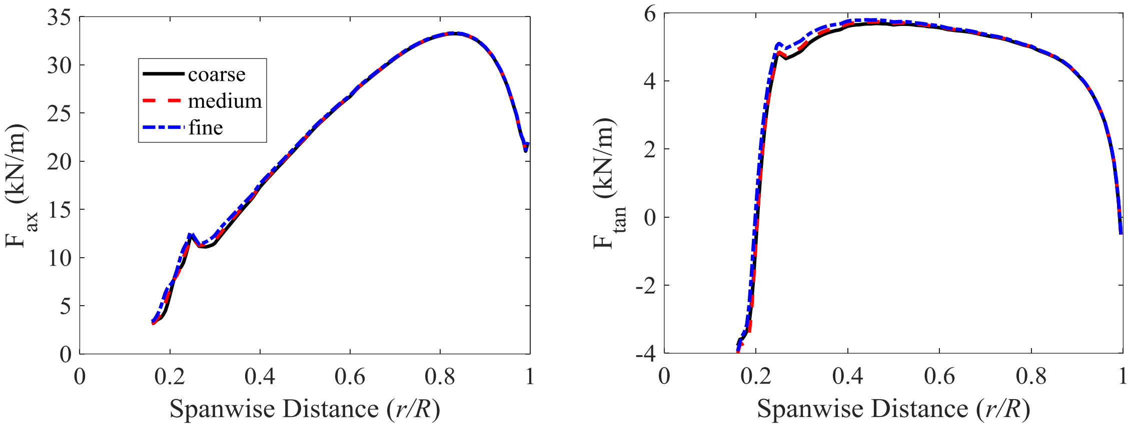

Figure 3-3 Comparison of force profiles for coarse, medium, and fine meshes.

Figure 3-3 shows the axial and tangential force profiles of the three meshes. The profiles show minor differences between each mesh, spanning from the blade root until *r/R* ≈ 0.4, and show good agreement towards the blade tip. The average percentage difference of the coarse and medium relative to the fine mesh is 0.51% and 0.25% for the axial force, and there are 1.11% and 0.53% for the tangential force profiles. Since the loadings are relatively low between all three meshes, the coarse mesh was adopted for all 3-dimensional rotor simulations in the present study.

3.4 Turbine undergoing prescribed pendulum motion

The pendulum motion amplitudes A_0 = 1.0°, 1.5°, 2.0°, 3.0°, 4.3° were chosen based on a realistic assumption of a floating 20 m diameter rotor weighing around 1.5×10^5 kg (SIMEC Atlantis Energy, 2016) oscillating in a pendulum motion. The motion frequencies ω^* = 0.6, 0.7, 0.8, 1.0, 1.3 were chosen based on the wave frequency at the Fall of Warness tidal site (Anatec Ltd., 2010), where $\omega^* = \omega_0/\omega_r$ is the non-dimensional frequency ratio, ω_0 is the frequency of oscillation (rad/s) and ω_r is the rotor rotational speed (rad/s). Tests using different tip speed ratios λ = 3.8, 4.2, 4.6 under the prescribed pendulum motion are also presented in this chapter.

The rotor's instantaneous angular motion about the centre of rotation (COR) is defined as

$$\theta_{\text{pen}}(t) = -A_0 \sin(\omega_0 t).$$

An example of the prescribed motion of a rotor oscillating with a displacement amplitude $A_0 =$ 1.5° and frequency ω^* = 1.0 is shown in Figure 3-4. The rotational displacement is negative as the turbine swings upstream and positive as it retreats downstream. The apparent velocity U_{ap}, which is the flow velocity relative to the rotor, is 90° out of phase with the turbine's rotational displacement, such that the maximum U_{ap} occur as the turbine moves back to its original position from downstream to upstream and *vice versa* for minimum U_{ap}. The apparent velocity U_{ap} was calculated, based on Lienard et al. (2019), as

$$U_{ap}(t) = U_\infty \cos\theta_{pen}(t) - \dot{\theta}_{\text{pen}}(t).h$$

where $\dot{\theta}_{\text{pen}}$ is the rotor pendulum velocity (rad/s), and h = 20 m is the rotational arm length from the centreline of the turbine nacelle to the centre of rotation.

To demonstrate the relation between the apparent velocity and the loading on the rotor, time histories of power and thrust coefficients together with U_{ap} normalized with the free stream velocity are presented in Figure 3-5. The power and thrust are largely in phase with U_{ap}. This is because the thrust is directly proportional to the velocity squared and the power to the velocity cubed.

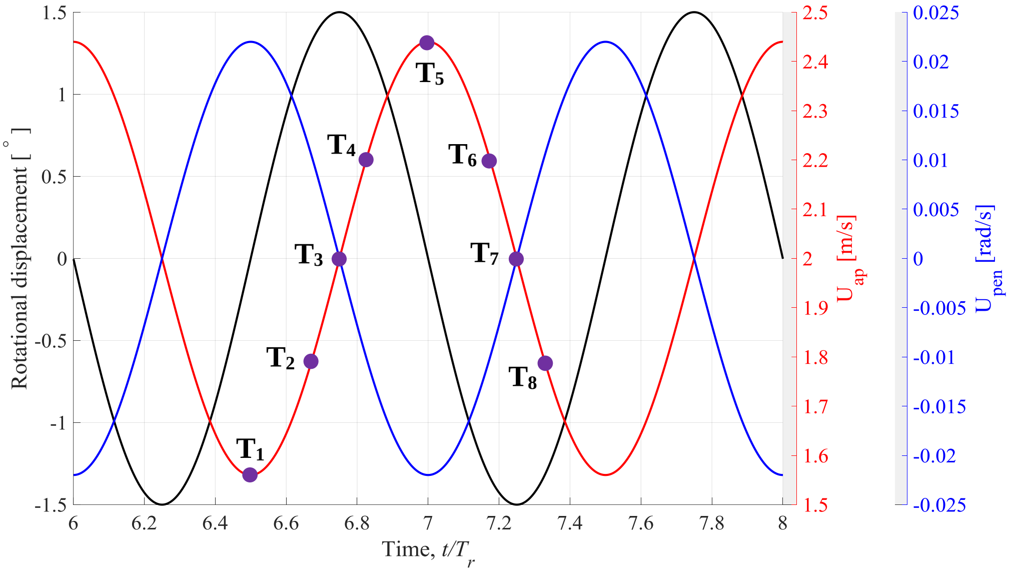

Figure 3-4 Rotational displacements, apparent velocity, and angular velocity of the pendulum motion for the case of A_0 = 1.5° with ω^* = 1.0 and λ = 4.2. The negative sign of rotational displacement shows the rotor moves forward and *vice versa* for the positive sign.

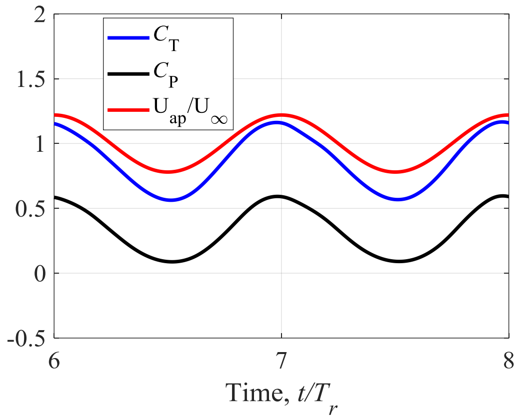

Figure 3-5 Power and thrust coefficients time histories with normalized apparent velocity for the case of A_0 = 1.5° with ω^* = 1.0 and λ = 4.2

3.5 Effect of pendulum amplitude on turbine performance

Five pendulum motion amplitudes A_0 = 1.0°, 1.5°, 2.0°, 3.0°, 4.3° were chosen based on a realistic assumption of a 20 m diameter rotor oscillating in a pendulum motion based on waves condition from the Fall of Warness tidal site (Anatec Ltd., 2010). The frequency and rotational speed of the rotor, ω^* = 1.0 and ω_r = 0.84 rad/s respectively, were kept constant for all A_0 cases. Simulations were run for ~8 rotor revolutions, and only data of the last two motion cycles of data were considered to ensure stability and convergence. Typical results of C_P and C_T time histories for a floating turbine oscillating in pendulum motion were presented in Figure 3-6, where the load variation increase as the motion amplitude is increased.

At the maximum U_{ap} (at time steps t/T_r = 6.0, 7.0, 8.0) there is an asymmetry at the peak of each cycle for higher motion amplitude cases. This happens due to the stalling effect on the rotor experiencing high local velocity. If we consider a typical velocity triangle on a rotor blade cross-section, the angle of attack α will increase pass its critical limit as the velocity is increased. This will cause the flow to detach from the blade surface (i.e., flow separation), which causes the loss in lift on the rotor, thus decreasing the load. This does not appear at lower motion amplitude cases, mainly due to small U_{ap} variation which minimally increases α.

The negative power which occurs at minimum U_{ap} (t/T_r = 6.5 and 7.5) refers to the rotor acting more like a propeller than a turbine. This means that it needs the power to continue rotating at the given rotational speed, which was kept constant throughout the simulation. However, an actual turbine will just stop spinning when the apparent velocity drops to a certain minimum value.

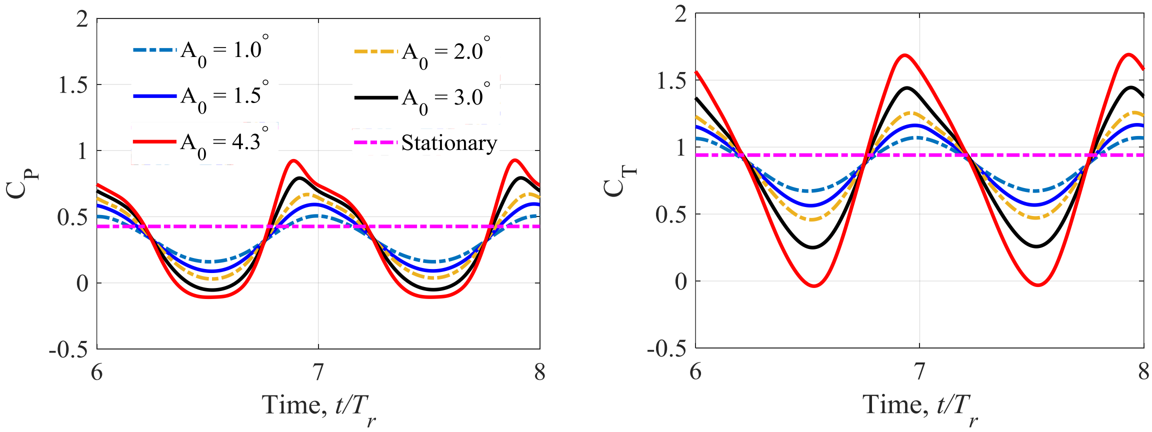

Figure 3-6 Power and thrust coefficients for a floating turbine undergoing a prescribed pendulum motion at A_0 = 1.0°, 1.5°, 2.0°, 3.0°, 4.3° with a constant ω^* = 1.0 and λ = 4.2.

Looking at the comparison in terms of the average loading between the stationary and floating turbine undergoing pendulum motion, which is presented in Table 3-1, higher motion amplitude increases the average power while decreasing the average thrust. A similar trend has been shown in Leble & Barakos (2016) and Lienard et al. (2019) for a floating wind turbine undergoing a prescribed pendulum motion. The asymmetries at the peak of each cycle (occurs at maximum U_{ap} at t/T_r = 6, 7, 8) are more significant in C_P than C_T. This happens due to the drag being more dominant than lift at maximum U_{ap}. The axial and tangential aerodynamic forces, C_X and C_Y respectively, can be presented as

$$C_L \cos\phi + C_D \sin\phi = C_X$$

$$C_L \sin\phi - C_D \cos\phi = C_Y$$

where C_L and C_D are lift and drag coefficients, respectively, and $\phi = \alpha + \beta$ is the resultant flow angle, where α is the angle of attack and β is the blade twist angle. In the above equations, thrust is calculated based on C_X while power is based on the torque, i.e., C_Y. As U_{ap} is increased, α will also increase, and it will continue increasing until it passes the static stall angle at maximum U_{ap}. When this happens, the lift will drop, but the drag will continue to increase. Therefore, at maximum U_{ap} the drag is more dominant than lift, and hence, the power coefficient will suffer a significant drop compared to thrust.

Looking at loading time histories on individual blades presented in Figure 3-7, each blade shows different loading variations and is slightly out of phase with one another. A similar trend has been shown in the literature for a floating wind turbine undergoing pendulum motion (T. Tran et al., 2014; Shen et al., 2018; Lienard et al., 2019). For the case of A_0 = 1.5°, blade 1 shows the lowest power and thrust at both minimum and maximum apparent velocities. This is because at maximum apparent velocity, blade 1 is located at its original position with azimuth angle = 0°. Due to the pendulum motion, the instantaneous velocity is larger at the bottom half of the rotor (blades 2 and 3) than the upper half (blade 1) when the rotor moves forward. The opposite will happen when the rotor swings backwards in the pendulum motion. Note that at minimum U_{ap} the rotor plane is at its original position with the azimuth angle of blade 1 is at 180°. The same behaviour can be observed for all A_0 cases.

Table 3-1 Mean power and thrust coefficients for a floating turbine undergoing a prescribed pendulum motion at A_0 = 1.5°, 3.0°, 4.3° with a constant ω^* = 1.0 and λ = 4.2. For the stationary case, the rotor tip speed ratio is also λ = 4.2.

A_0	$\bar{C}_P$	$\bar{C}_T$	Percentage difference $\bar{C}_P$ [%]	Percentage difference $\bar{C}_T$ [%]
1.0°	0.331	0.875	28.5	4.6
1.5°	0.337	0.872	27.2	4.9
2.0°	0.342	0.867	26.1	5.5
3.0°	0.344	0.853	25.7	7.0
4.3°	0.347	0.836	25.1	8.8
Stationary	0.463	0.917	-	-

Figure 3-8 shows the force profiles along each blade of a rotor undergoing a pendulum motion at A_0 = 3.0° and ω^* = 1.0 at different time step which corresponds to minimum and maximum U_{ap}, and at $U_{ap} \approx U_\infty$. As explained before, vertical variation of U_{ap} exists for a rotor undergoing a pendulum motion. At the maximum U_{ap} the local velocity is highest at the bottom and lowest at the top along the turbine plane and *vice versa* for minimum U_{ap}, where the local velocity is highest at the top and lowest at the bottom along the turbine plane. These results correspond to the result presented in Figure 3-7(b), where blade 1 has the lowest loading at both minimum and maximum U_{ap}, which happen because blade 1 is at azimuth angles of 0° and 180° at maximum and minimum U_{ap}, respectively. At the maximum U_{ap} flow separation occurs along blades 2 and 3 where there is a change in characteristics of the force profiles. This happens due to the high angle of attack on rotor blades at high U_{ap}. Although not presented here, this phenomenon does not occur at $A_0 \leq 1.5°$.

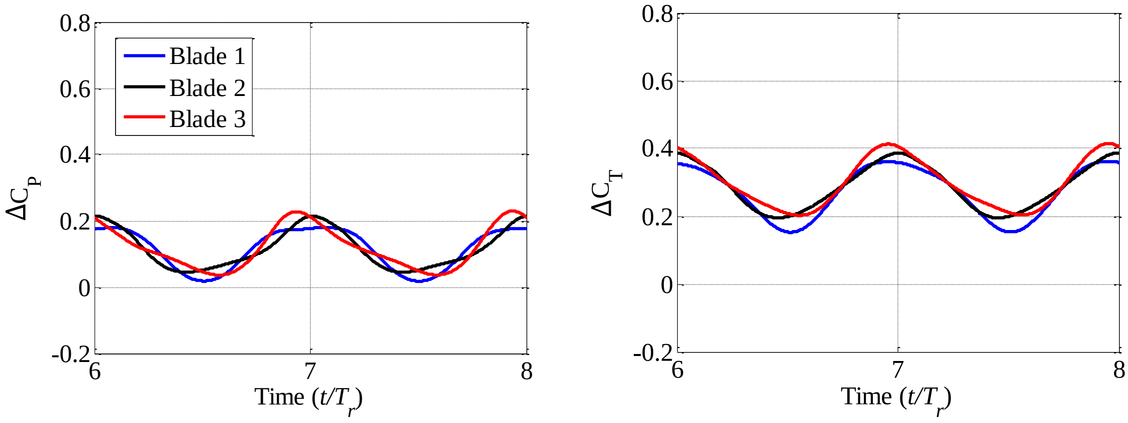

(a) A_0 = 1.5°

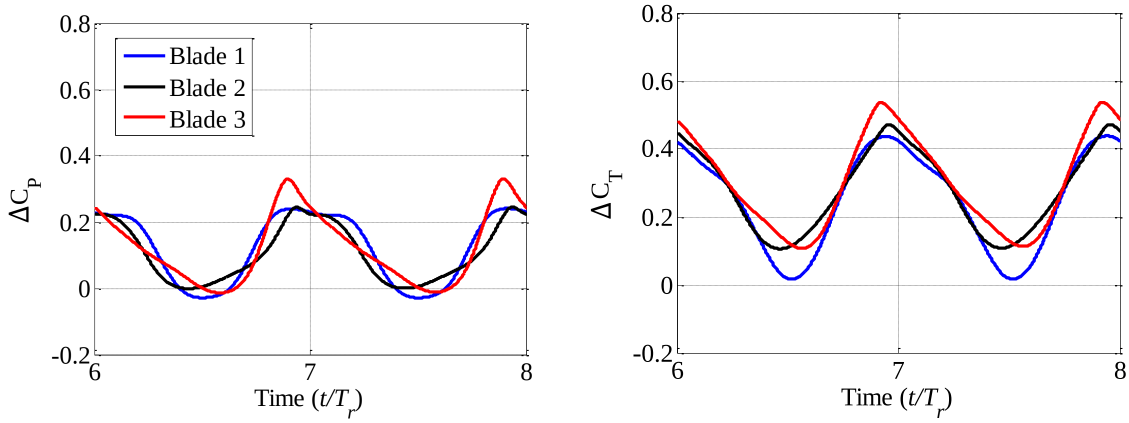

(b) A_0 = 3.0°

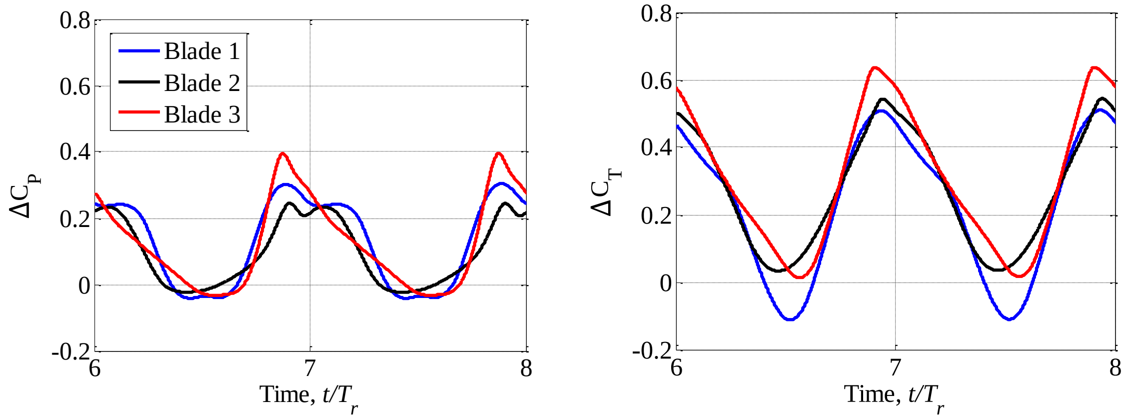

(c) A_0 = 4.3°

Figure 3-7 Power and thrust coefficients for each blade, ΔC_P and ΔC_T, respectively, for a floating turbine undergoing a prescribed pendulum motion at A_0 = 1.5°, 3.0°, 4.3° with a constant ω^* = 1.0 and λ = 4.2.

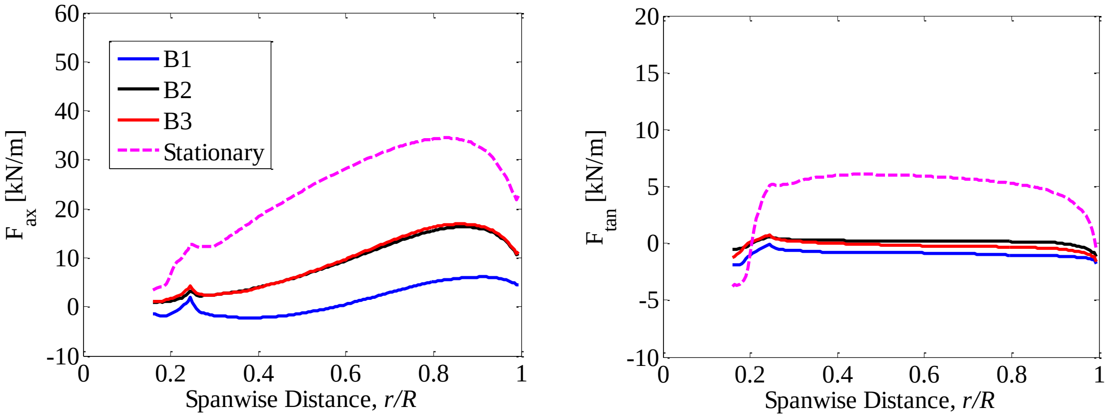

(a) minimum U_{ap}

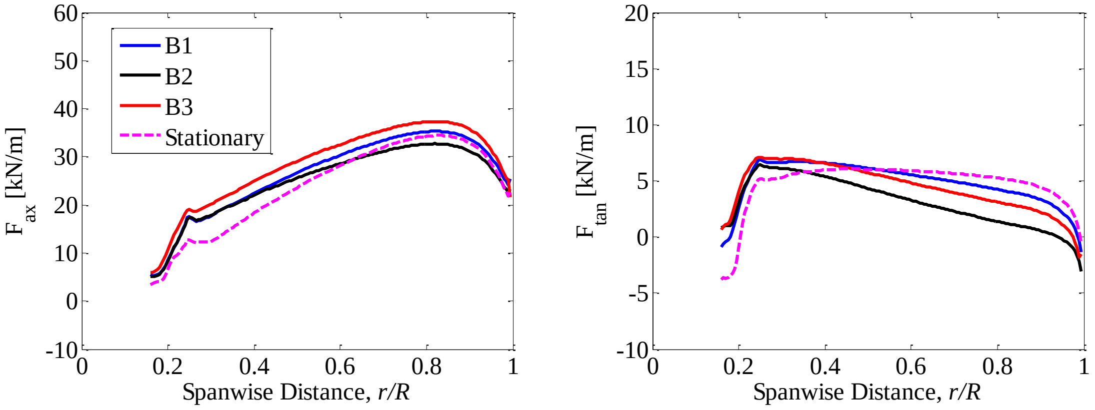

(b) $U_{ap} \approx U_{\infty}$

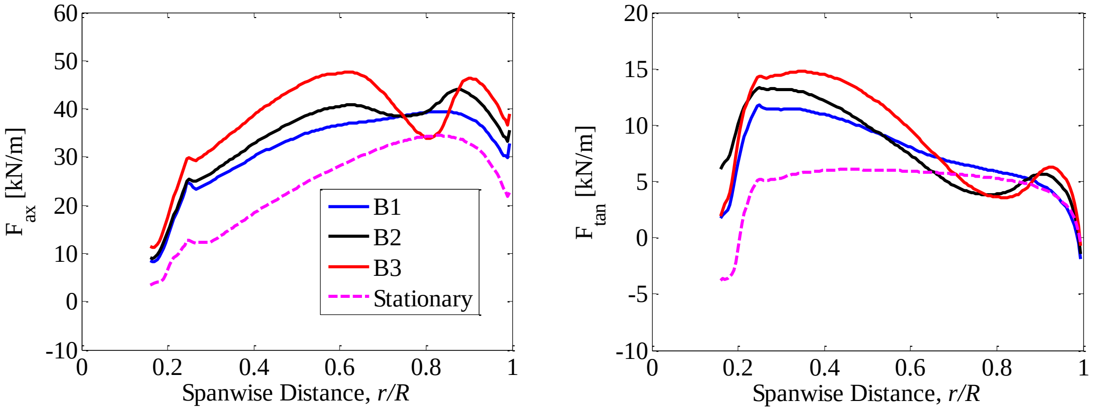

(c) maximum U_{ap}

Continue …

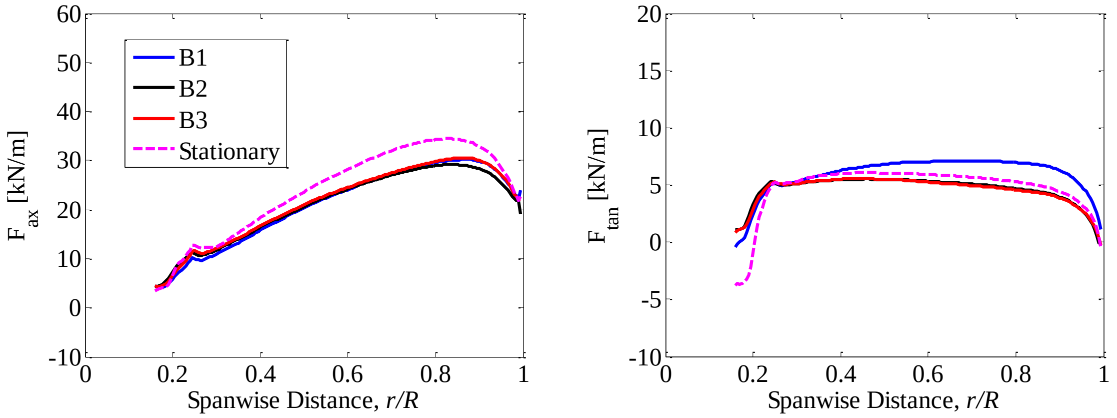

(d) $U_{ap} \approx U_{\infty}$

Figure 3-8 Force profiles for all blades at different apparent velocity conditions at A_0 = 3.0° with a constant ω^* = 1.0 and λ = 4.2.

The instantaneous velocity magnitude contour plots of blades 1 and 3 are presented in Figure 3-9 for a rotor undergoing a pendulum motion at A_0 = 3.0° and ω^* = 1.0. For the maximum U_{ap}, higher instantaneous velocity can be seen at blade 3 cross-section as compared to blade 1, which explains the higher loading in blade 3. There is also swirling flow at the suction side of blade 3, showing flow separation.

At $U_{ap} \approx U_{\infty}$ flow condition, the contour shows that the instantaneous flow field is slightly different even though the local instantaneous velocity is (assume to be) the same. This shows the dynamic effect captured by the CFD simulation, which will not be present in a quasi-steady type of simulation such as the BEMT model. Therefore, we cannot assume the forward and backward motion at $U_{ap} \approx U_{\infty}$ flow condition to be the same; even the force profiles in Figure 3-8(b) and (d) shows slight differences between the two time steps.

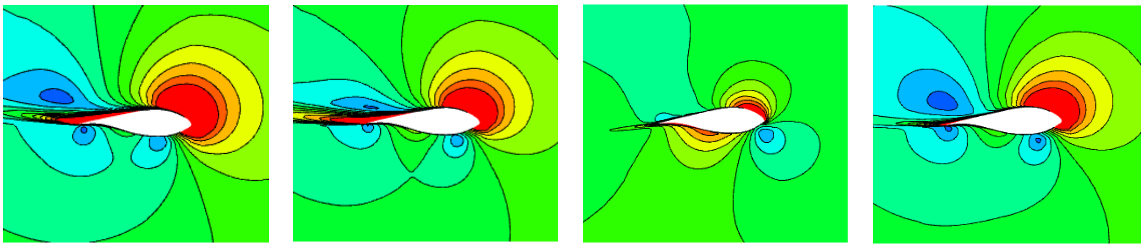

Maximum U_{ap} $U_{ap} \approx U_\infty$ Minimum U_{ap} $U_{ap} \approx U_\infty$

(a) Blade 1 at $r/R = 0.6$

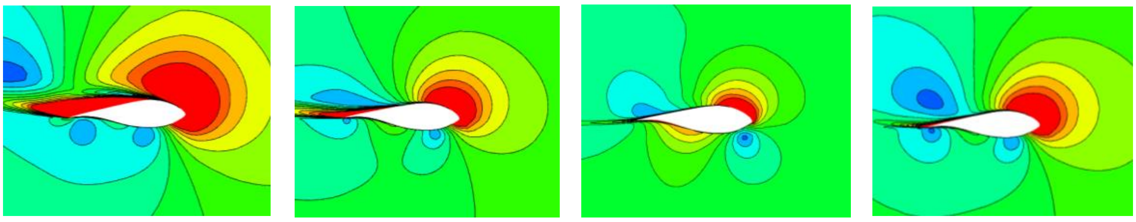

Maximum U_{ap} $U_{ap} \approx U_\infty$ Minimum U_{ap} $U_{ap} \approx U_\infty$

(b) Blade 3 at $r/R = 0.6$

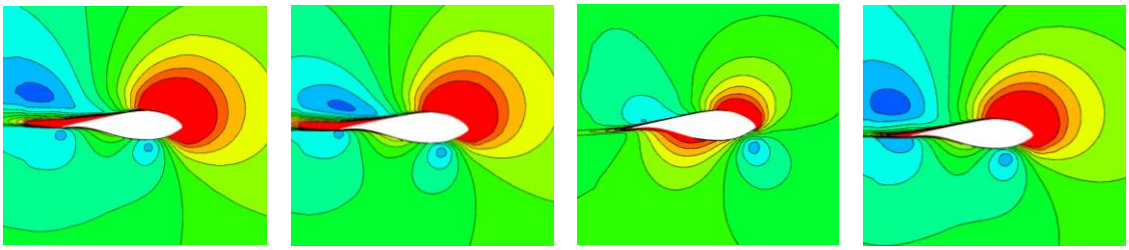

Maximum U_{ap} $U_{ap} \approx U_\infty$ Minimum U_{ap} $U_{ap} \approx U_\infty$

(c) Blade 1 at $r/R = 0.8$

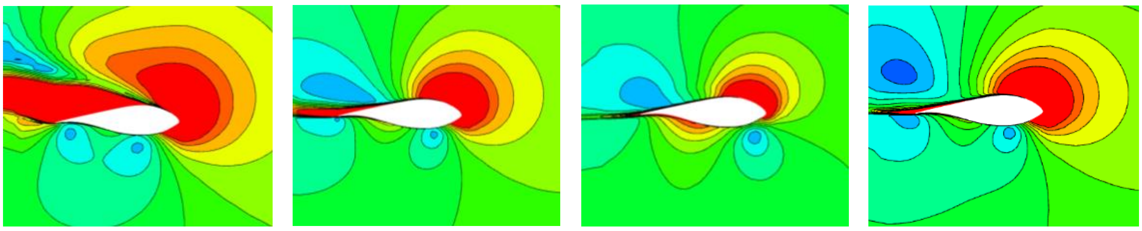

Maximum U_{ap} $U_{ap} \approx U_\infty$ Minimum U_{ap} $U_{ap} \approx U_\infty$

(d) Blade 3 at $r/R = 0.8$

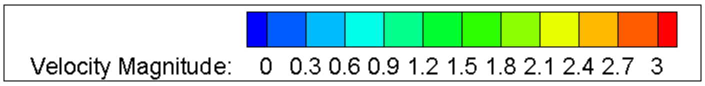

Figure 3-9 Contour plots of velocity magnitude for blades 1 and 3 of a rotor undergoing a pendulum motion at A_0 = 3.0° with ω^* = 1.0 and λ = 4.2.

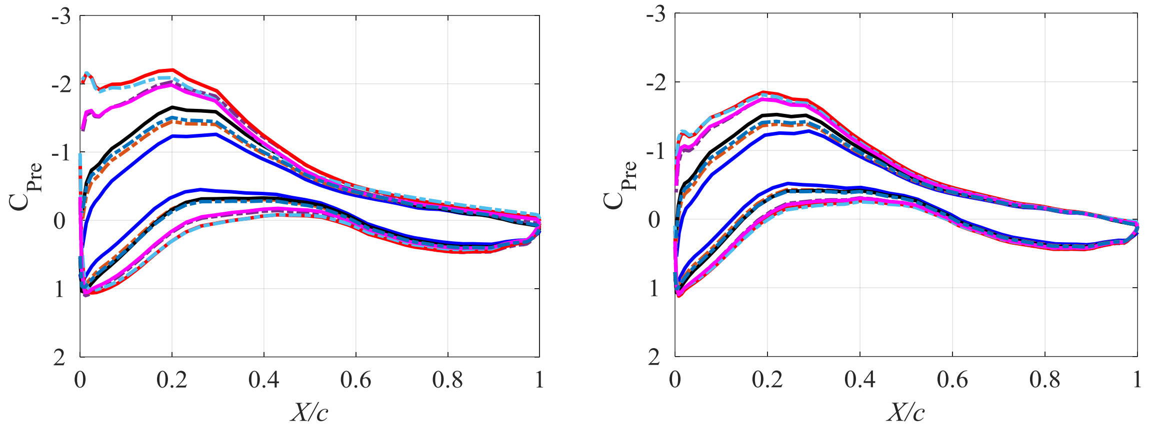

(a) A_0 = 1.5°; blade 1 at $r/R = 0.6$ (b) A_0 = 1.5°; blade 1 at $r/R = 0.8$

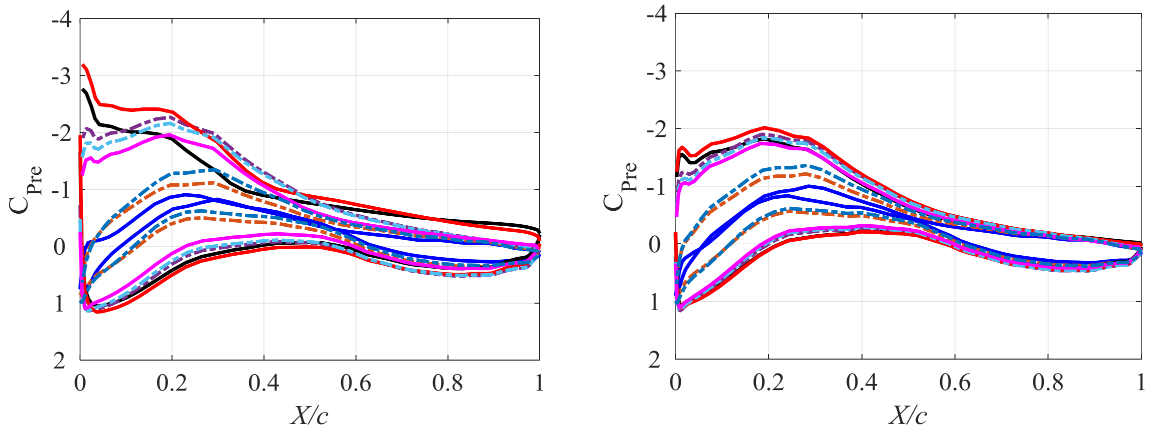

(c) A_0 = 3.0°; blade 1 at $r/R = 0.6$ (d) A_0 = 3.0°; blade 1 at $r/R = 0.8$

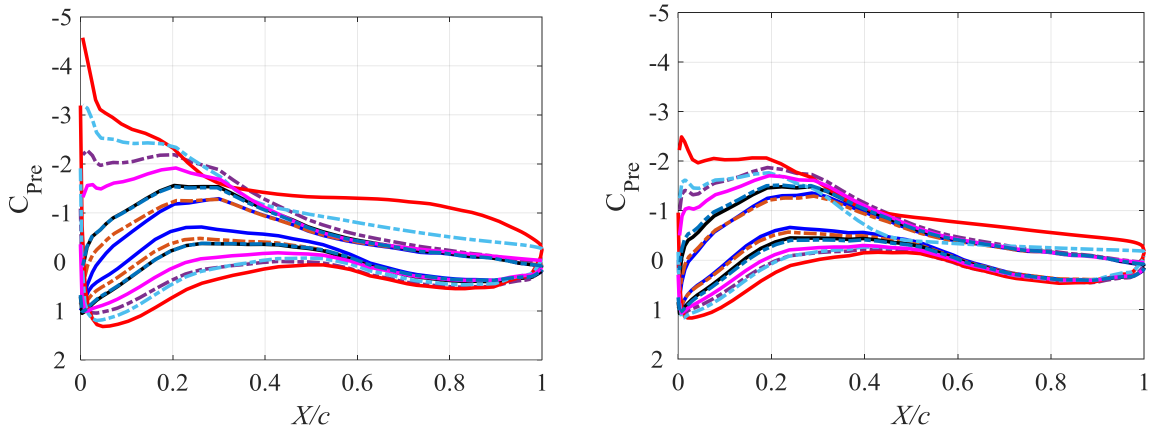

(e) A_0 = 3.0°; blade 3 at $r/R = 0.6$ (f) A_0 = 3.0°; blade 3 at $r/R = 0.8$

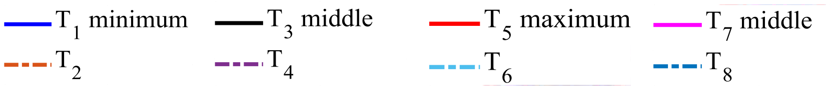

Figure 3-10 Pressure coefficient for different motion amplitudes A_0 with a constant ω^* = 1.0 and λ = 4.2. Please refer to Figure 3-4 for markers T_1 to T_8.

Figure 3-10 shows the typical results of pressure coefficients of a floating turbine undergoing pendulum motion, where the apparent velocity flow condition highly influences the pressure variation. Refer to Figure 3-4 for markers T_1 to T_8. A similar trend has been shown in literature such as Tran & Kim (2015) and Liu et al. (2017) for a floating wind turbine oscillating in a pendulum motion. At the maximum U_{ap} (T_5 and T_6) for blade 3, the flat line at the suction side towards the trailing edge of the blade section is a characteristic of flow separation. This indicates the flow separation occurs around this area, corresponding to the contour plots presented in Figure 3-9.

The power and thrust efficiencies for a turbine undergoing a prescribed pendulum motion are presented in Figure 3-11(a). It is observed that the turbine efficiencies go to the maximum twice per motion cycle. This happens because when the rotor moves into the farthest upstream and downstream, the value of apparent velocity is (almost) similar to the free stream velocity $\left(U_{ap} \approx U_{\infty}\right)$. In this condition, the turbine operates at its optimum tip speed ratio (i.e., optimum operating condition).

To describe the rotor efficiency at different apparent velocity conditions, aerofoil sketches and turbine positions are presented in Figure 3-11(b), corresponding to the markers T_1, T_3, T_5, and T_7 (refer to Figure 3-4 for markers T_1 to T_7). Although, this analysis does not consider the effects of the angle of attack on the blades relative to the position of the rotor. The rotor is slightly rotated (in the y-axis) at positions T_3 and T_7 due to the pendulum motion. This will affect the angle of the free stream flow on the rotor plane, which might affect the angle of attack on each blade.

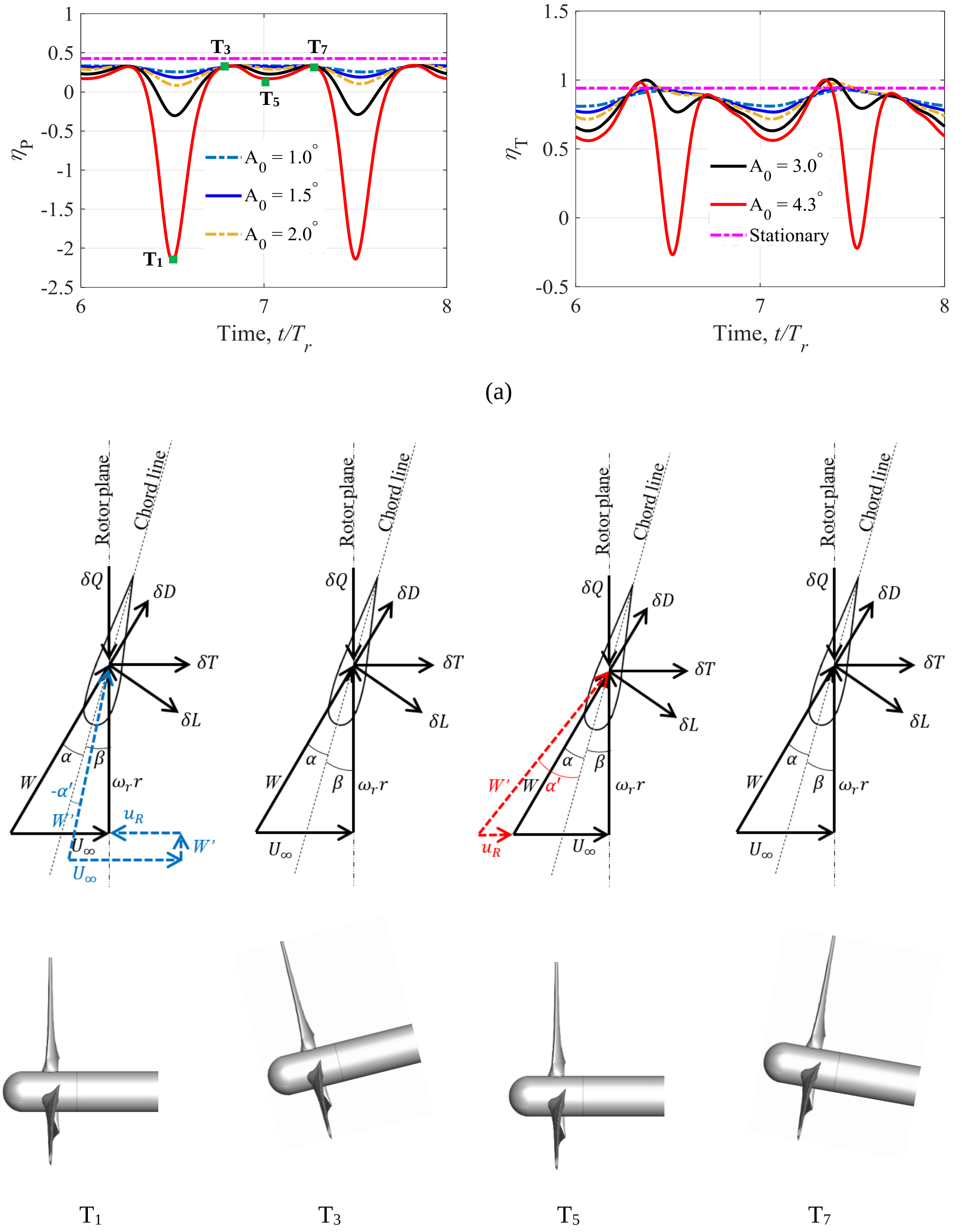

Figure 3-11 (a) Power and thrust efficiencies for a floating turbine undergoing a prescribed pendulum motion at A_0 = 1.5°, 3.0°, 4.3° with a constant ω^* = 1.0 and λ = 4.2; (b) Sketches of a blade cross section and the position of the rotor corresponds to figure (a). u_R is the additional velocity caused by the rotor's motion.

Negative efficiencies here refer to the rotor acting more like a propeller than a turbine, meaning that it needs the power to continue rotating at the given rotational speed (which is kept constant throughout the simulation). However, an actual turbine will stop spinning when the apparent velocity drops to a certain minimum value.

One of the main objectives of this study is to identify whether the turbine enters the vortex ring state (VRS). VRS is a condition used in the helicopter notation that explains the helicopter blades move into their own wake while descending and causes the loss in lift on the blades, where the helicopter will drop its altitude drastically, resulting in a crash (Stewart, 1959; Johnson, 2004). As discussed previously, flow separation will cause the rotor to stall due to the loss of lift on the turbine blades. When the rotor enters the VRS, it will cause loss in lifts on the blade, leading to the loss in power; it can also shorten the life span of the rotor due to the unsteady instantaneous flow condition. Inflow velocity ratios $V_C/\mathrm{v_h}$ of the present study are presented in Figure 3-12. The rotor slightly enters the VRS when oscillating backward at an amplitude A_0 = 4.3°.

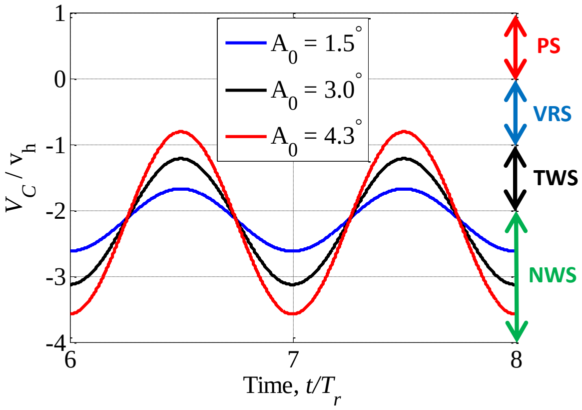

Figure 3-12 Inflow velocity ratios for a floating turbine undergoing a prescribed pendulum motion at A_0 = 1.5°, 3.0°, 4.3° with a constant ω^* = 1.0 and λ = 4.2. PS = propeller state; VRS = vortex ring state; TWS = turbulent wake state; NWS = normal working state (Leble & Barakos, 2016).

Wake iso-surface and contours are presented in Figure 3-13 and Figure 3-14 for the case of A_0 = 4.3° and ω^* = 1.0 to visualize the characteristic of the vortex ring state. Only time steps of the rotor moving backwards into the downstream direction are selected for this visualization, at T_7, T_8, T_1, T_2, T_3 (refer to Figure 3-4 for the rotor position at these time steps). From the iso-surface plots in Figure 3-13, it is unclear whether the rotor is moving into its own wake, however, the tip of the rotor blade at the bottom side of the rotor plane in Figure 3-13(c) almost get caught in the tip vortex. In Figure 3-13(d) and (e), the tip vortices can be seen attached to one another as the rotor moves further downstream. Based on Figure 3-12, these time steps are where the rotor is in the turbulent wake state, and the attachment of tip vortices is one of the characteristics of a rotor entering this vortex state (Leble & Barakos, 2016; Lienard et al., 2019).

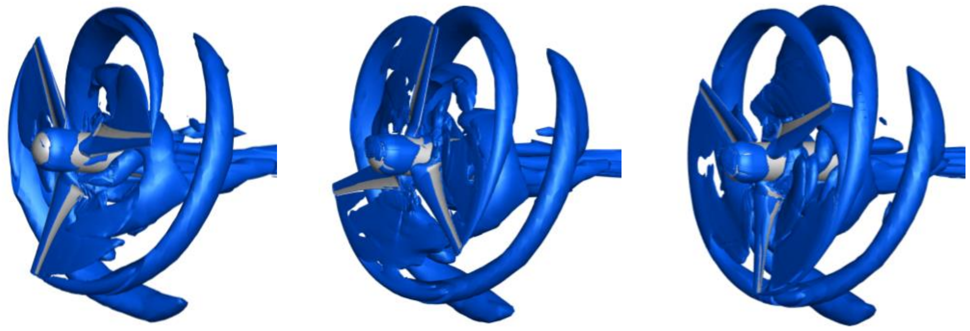

(a) $t/T_r = 7.25$ (b) $t/T_r = 7.38$ (c) $t/T_r = 7.50$ (minimum U_{ap})

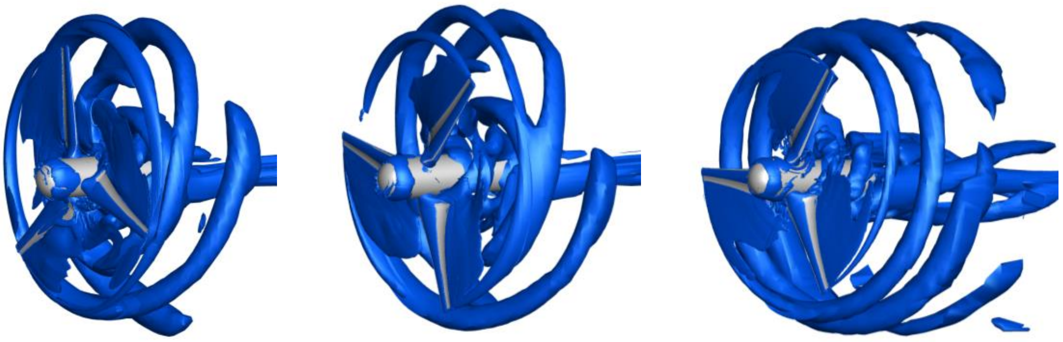

(d) $t/T_r = 7.63$ (e) $t/T_r = 7.75$ (f) Stationary

Figure 3-13 Q-criterion iso-surface plots for wake vortices visualization of the rotor undergoing a pendulum motion with A_0 = 4.3° and ω^* = 1.0 rotating at λ = 4.2.

Looking at the vorticity magnitude contour plots presented in Figure 3-14, the rotor blade (at the bottom side of the rotor plane) moves into its own wake as the rotor moves backward at minimum U_{ap} around spanwise distance $r/R \leq 0.7$. The same characteristic can be observed around $r/R \geq 0.4$ until the blade tip as the rotor moves farther downstream at $t/T_r = 7.63$. However, at the farthest downstream position at $t/T_r = 7.75$, the wake seems to have passed the rotor plane. From the wake visualizations, the rotor did enter VRS, only at the bottom side of the rotor plane due to the nature of the pendulum motion, for the highest pendulum motion amplitude case.

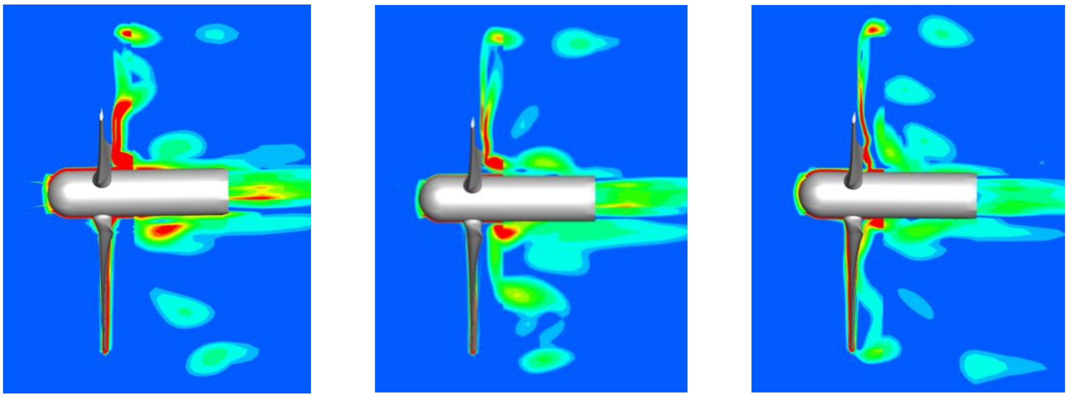

(a) $t/T_r = 7.25$ (b) $t/T_r = 7.38$ (c) $t/T_r = 7.50$ (minimum U_{ap})

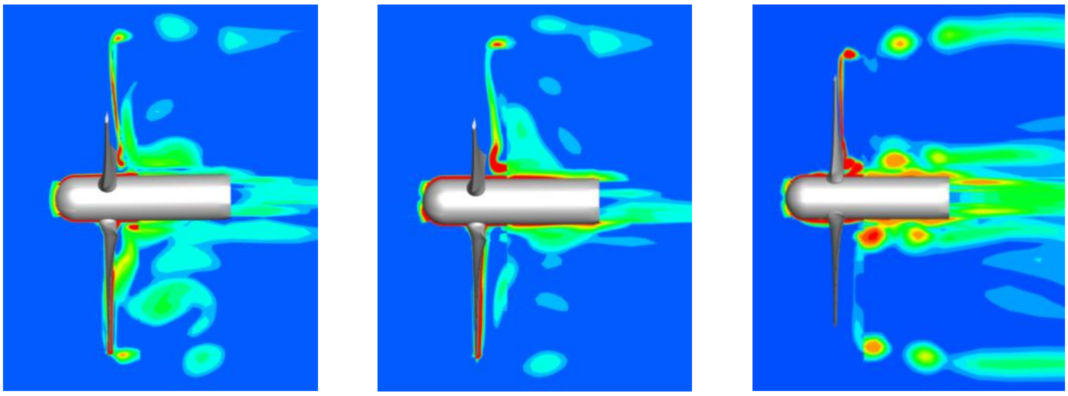

(d) $t/T_r = 7.63$ (e) $t/T_r = 7.75$ (f) Stationary

Figure 3-14 Vorticity magnitude contour plots of a rotor undergoing a pendulum motion with A_0 = 4.3° and ω^* = 1.0.

3.6 Effect of pendulum frequency on turbine performance

To broaden the aspect of analysing a floating tidal turbine undergoing pendulum motion, the present study investigates the effect of motion frequency on the rotor performance. In this subchapter, the motion amplitude and rotor rotational speed, $A_0 = 3.0°$ and $\omega_r = 0.84$ rad/s respectively, were kept constant. The range of motion frequency, $\omega^* = 0.6, 0.7, 0.8, 1.0, 1.3$, used in this study are based on the wave frequency at the Fall of Warness tidal site (Anatec Ltd., 2010).

The power and thrust coefficients time histories are presented in Figure 3-15, where T_r is the period of one revolution of the rotor. Only data from the last two cycles were considered in the present study to ensure convergence of each simulation. Figure 3-15 shows typical results for a floating turbine undergoing prescribed motion for various motion frequencies. A similar trend has been demonstrated in the literature (Vaal et al., 2006; T. T. Tran & Kim, 2016; Jing et al., 2017). The highest frequency case shows significant asymmetry at the peak of each cycle, showing that the rotor goes into stall at higher pendulum motion frequency. The stalling effect is smaller for a rotor oscillating at a lower motion frequency.

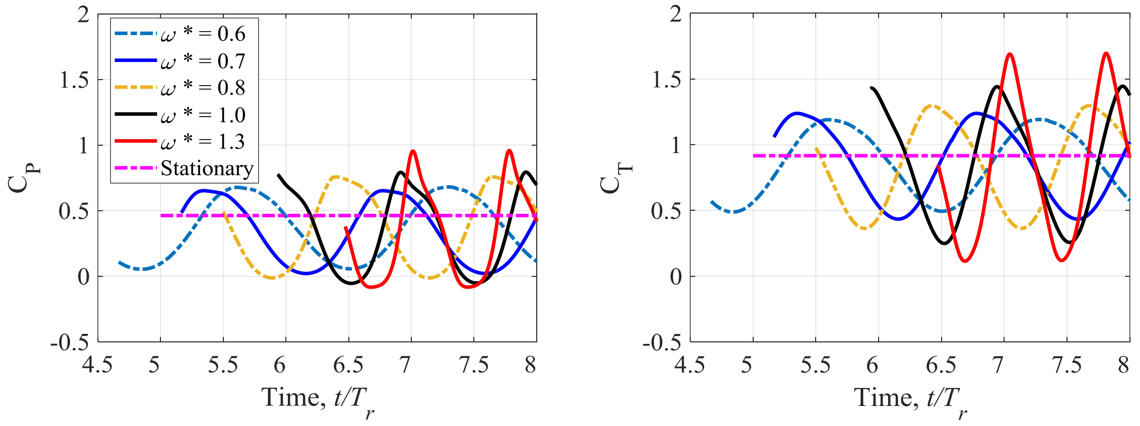

Figure 3-15 Power and thrust coefficients for a floating turbine undergoing a prescribed pendulum motion at $\omega^* = 0.7, 1.0, 1.3$ with a constant $A_0 = 3.0°$ and $\lambda = 4.2$.

In Table 3-2, the mean values of the power coefficient are reduced as the motion frequency is increased. This happens due to the stalling effect, where the rotor lost its lifts due to flow separation, reducing the loading on the blade. The mean thrust coefficient is reduced as the motion frequency is increased, which is typical for a floating turbine undergoing prescribed pendulum motion.

Table 3-2 Mean power and thrust coefficients for a floating turbine undergoing a prescribed pendulum motion at ω^* = 0.7, 1.0, 1.3 with a constant A_0 = 3.0° and λ = 4.2. For the stationary case, the rotor tip speed ratio is also λ = 4.2.

ω^*	$\bar{C}_P$	$\bar{C}_T$	Percentage difference $\bar{C}_P$ [%]	Percentage difference $\bar{C}_T$ [%]
0.6	0.364	0.858	21.38	6.43
0.7	0.334	0.854	27.86	6.87
0.8	0.365	0.846	21.17	7.74
1.0	0.344	0.853	25.71	6.98
1.3	0.320	0.818	30.82	10.80
Stationary	0.463	0.917	-	-

Loading time histories of each blade are presented in Figure 3-16 for all motion frequency cases. For the case of ω^* = 0.7 and 1.3 the loading on each blade shows variation at each motion cycle, where the maximum and minimum loading occurs on different blades at every peak and through. For example, for the ω^* = 0.7 case, blade 3 shows the lowest thrust at t/T_r = 5.4 (the first maximum apparent velocity) while at t/T_r = 6.8 (the second maximum apparent velocity) blade 3 shows the highest. The other two blades also show different variations at each cycle. This is different from the motion amplitude cases presented in the previous sub-chapter (ω^* = 1.0) where all blades show similar trend in every motion cycle. This variation is due to the different azimuth angles of each blade, which happens because the angular velocity of the rotor (rotor rotational speed) differs from that of the pendulum motions.

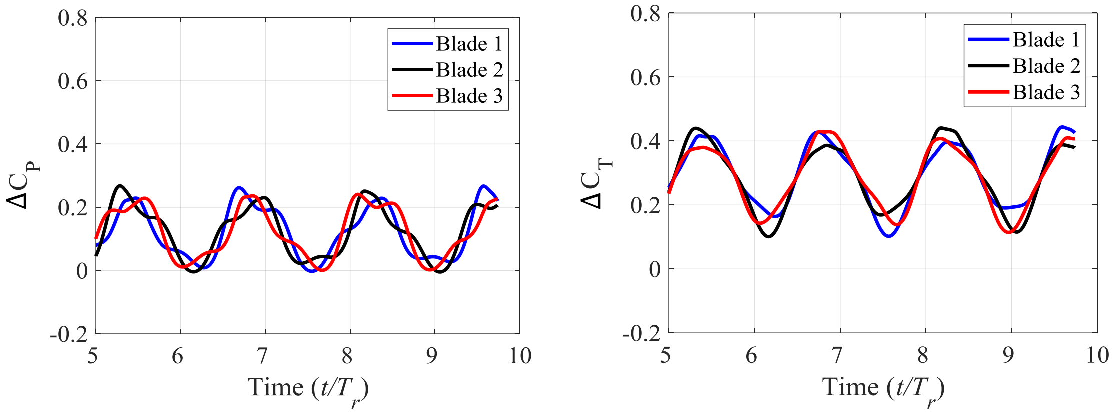

(a) ω^* = 0.7

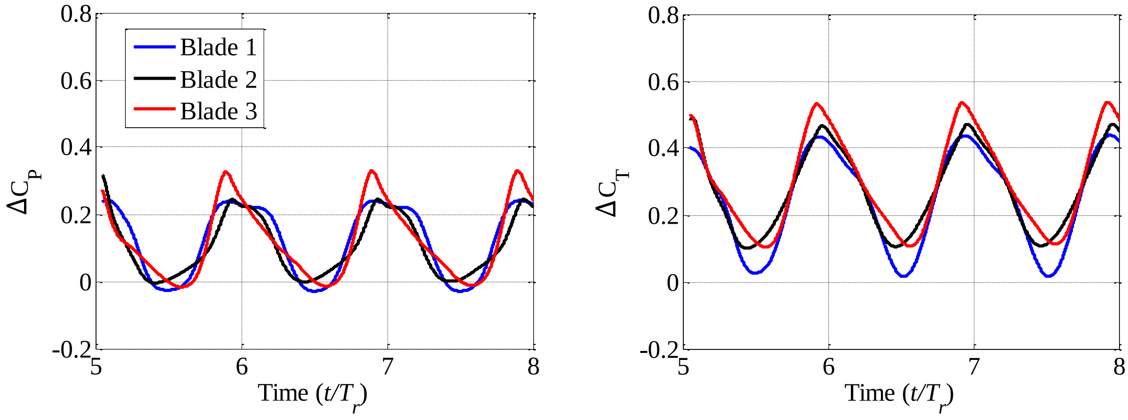

(b) ω^* = 1.0

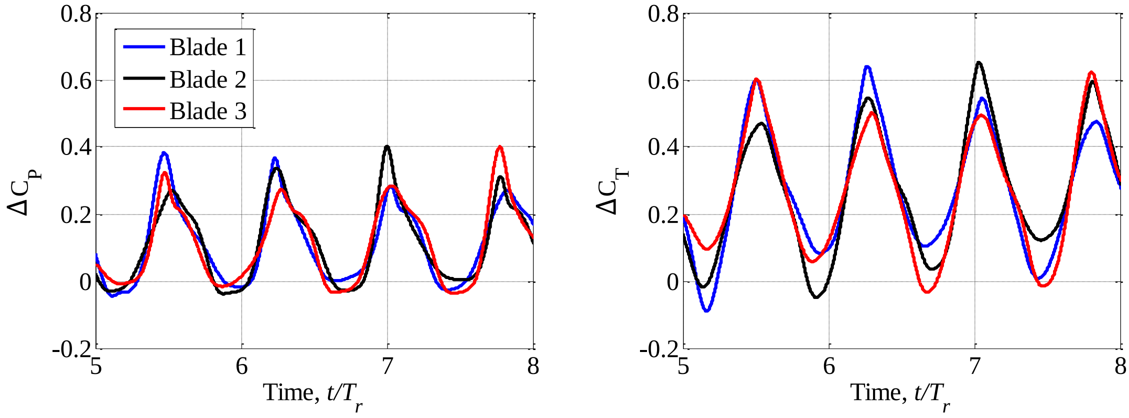

(c) ω^* = 1.3

Figure 3-16 Power and thrust coefficients for each blade, ΔC_P and ΔC_T, respectively, for a floating turbine undergoing a prescribed pendulum motion at ω^* = 0.7, 1.0, 1.3 with a constant A_0 = 3.0° and λ = 4.2.

To explain this from a different perspective, force profiles on blade 1 at two maximum and two minimum apparent velocities are presented in Figure 3-17. Loading on blade 1 shows two different characteristics at two different maximum apparent velocities. At t/T_r = 7.10, flow separation occurs along the blade making the load drops significantly around r/R = 0.4 to 0.9. However, at t/T_r = 7.85 only small change can be observed in the load characteristic indicating only small separation occurs along the blade. It can also be observed that the loading at t/T_r = 6.70 is higher than at t/T_r = 7.45 although at each time steps the apparent velocity is at the minimum. These variations happen due to the difference in the azimuth angle of each blade at both maximums and both minimums, which is caused by the difference in the angular velocity between the rotor rotational speed and the frequency of motion.

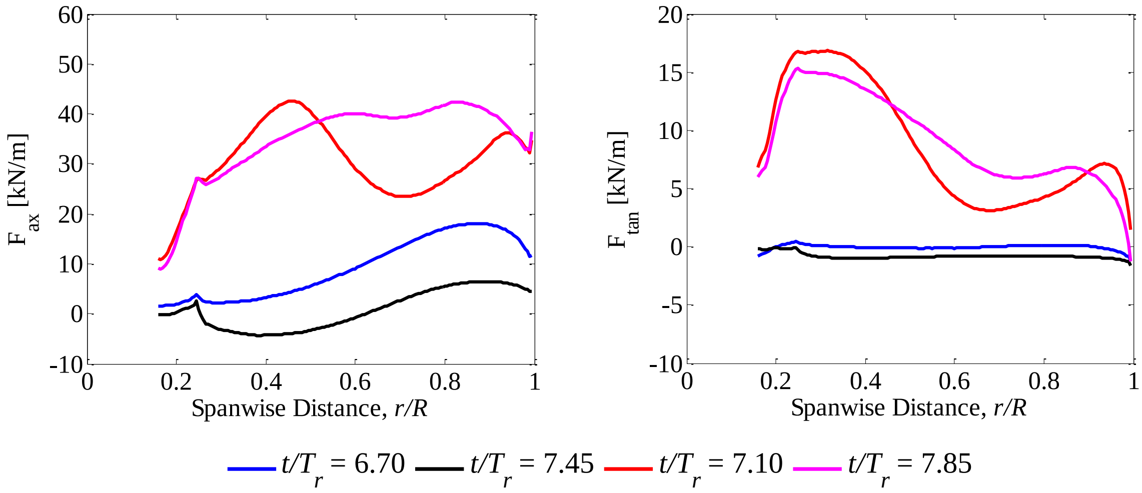

Figure 3-17 Comparison of force profiles at two maximum (t/T_r = 7.10 and 7.85) and two minimum (t/T_r = 6.70 and 7.45) apparent velocity conditions for blade 1 of a rotor undergoing a pendulum motion at ω^* = 1.3 with A_0 = 3.0° operating at λ = 4.2.

Although the frequency of the pendulum motion is increased, there is no significant increase in the maximum power efficiency of the rotor, presented in Figure 3-18. It looks like the power has been capped; the maximum value for each case is similar to that of the mean power coefficient values presented in Table 3-2.

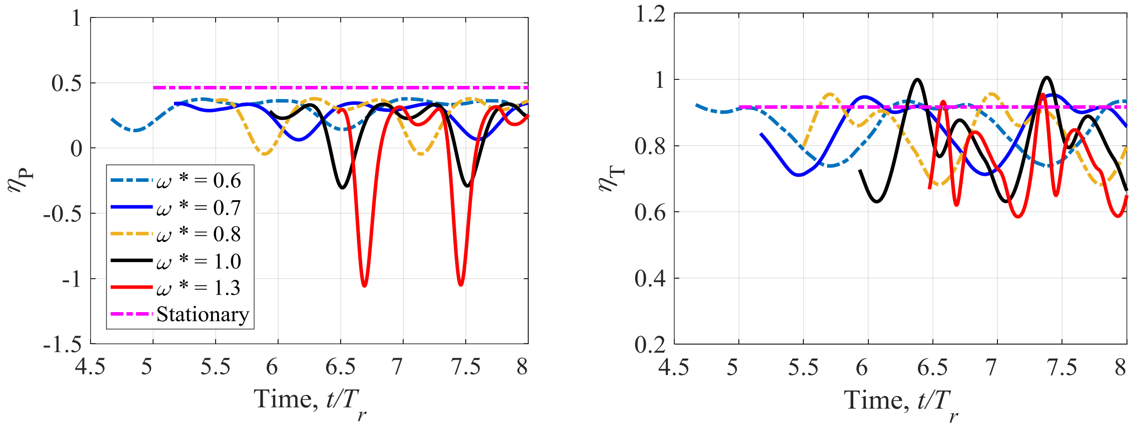

Figure 3-18 Power and thrust efficiencies for a floating turbine undergoing a prescribed pendulum motion at $\omega^* = 0.7$, 1.0, 1.3 with a constant $A_0 = 3.0°$ and $\lambda = 4.2$.

3.7 Effect of rotor rotational speed on a floating turbine undergoing pendulum motion

A rotor undergoing a pendulum motion at $A_0 = 3.0°$ and $\omega^* = 1.0$ was simulated using three different rotor rotational speeds $\omega_r = 0.76$, 0.84, 0.92, and the power and thrust coefficients time histories for all three cases are presented in Figure 3-19. These are typical results for a floating turbine undergoing a prescribed motion, where the amplitude of variation increases as the rotor rotational speed is increased (Wen et al., 2017; Jing et al., 2017; Sun et al., 2017). At the peak of each cycle, where the apparent velocity is at the maximum, the stalling effect is minimized as the rotor spins faster. For a floating turbine operating at a constant rotational speed, the instantaneous tip speed ratio will vary when it oscillates in the pendulum motion. For a stationary turbine, the tip speed ratio is inversely proportional to the free stream velocity. For a floating turbine, the instantaneous tip speed ratio calculation does not depend on the free stream velocity; rather, it depends on the rotor's instantaneous velocity (i.e., the apparent velocity). Hence, the instantaneous tip speed ratio λ_{in} for a floating turbine operating under a fixed rotational speed can be defined as

$$\lambda_{\text{in}}(t) = \frac{R\omega_r}{U_{ap}(t)}.$$

Therefore, at maximum $U_{ap}(t)$ the instantaneous tip speed ratio is not 4.2, but lower than that, and the opposite happens at the minimum $U_{ap}(t)$. So, operating a turbine at a higher than optimal rotational speed will make the rotor operates at near optimum instantaneous tip speed ratio when the apparent velocity goes to the maximum, thus minimizing the flow separation on each blade.

Since the stalling effect was minimized when operating a floating turbine at higher than optimal rotational speed, the rotor can extract more (average) power. Table 3-3 shows the percentage difference between floating and stationary turbines with their respective rotational speed. The rotor can extract more power relative to its rotational speed as the rotational speed increases. This happens due to the flow separation being minimized as the rotational speed is increased.

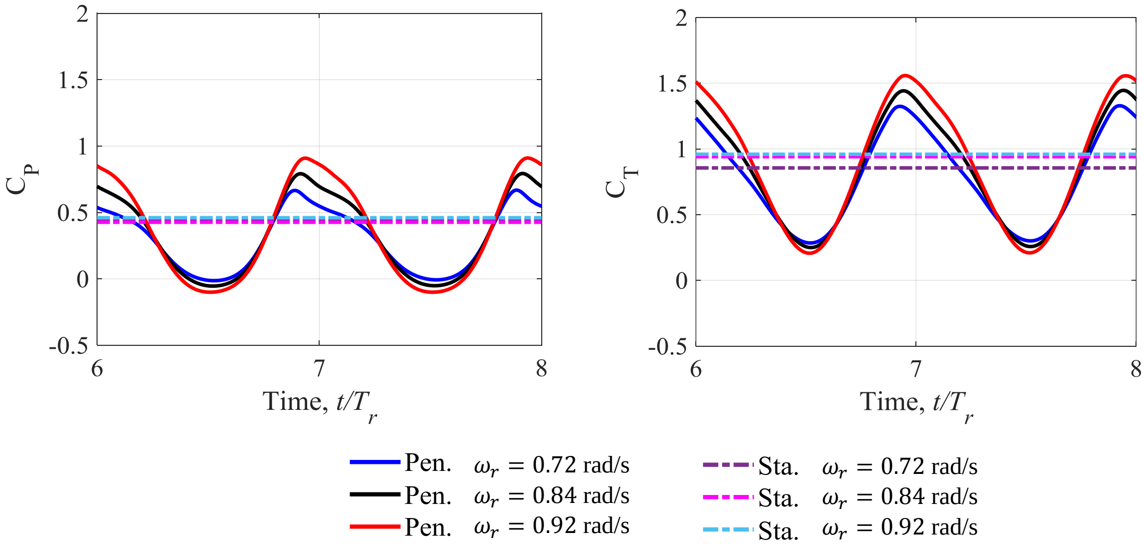

Figure 3-19 Power and thrust coefficients for a stationary (Sta.) and floating turbine undergoing a prescribed pendulum motion (Pen.) over a range of rotor rotational speed with A_0 = 3.0° and ω^* = 1.0.

Table 3-3 Mean power and thrust coefficients for a floating turbine undergoing a prescribed pendulum motion at various rotational speeds with constant A_0 = 3.0° and ω^* = 1.0.

ω_r [rad/s]	$\bar{C}_P$	$\bar{C}_T$	Percentage difference $\bar{C}_P$ [%]	Percentage difference $\bar{C}_T$ [%]
Pendulum 0.72	0.303	0.791	33.502	10.903
Pendulum 0.84	0.344	0.853	25.711	6.975
Pendulum 0.92	0.371	0.909	19.403	5.245
Stationary 0.72	0.455	0.887	-	-
Stationary 0.84	0.463	0.917	-	-
Stationary 0.92	0.461	0.959	-	-

Looking at the loading time histories for each blade presented in Figure 3-20, at each motion cycle’s peak and through, the loading on each blade varies for ω_r = 0.72 and 0.92 rad/s. This happens due to the difference in the azimuth angle of each blade at every motion cycle, which is caused by the difference in the angular velocity between the rotor rotational speed and the motion frequency.

When comparing the force profiles, given in Figure 3-21, on each blade for a floating turbine rotating at ω_r = 0.76 and 0.92 rad/s, at maximum U_{ap} the flow separation is minimized when rotating the rotor at a higher speed. This happens due to the operating tip speed ratio of the turbine. When the apparent velocity increase, the angle of attack will also increase. If the rotor spins at the optimum speed or lower, at maximum U_{ap} the rotor operates at a lower than optimum tip speed ratio condition, and flow separation on the blade surface will occur. If the rotor is rotating faster than the optimum speed, it will operate at a tip speed ratio closer to the optimum condition at high U_{ap} condition.

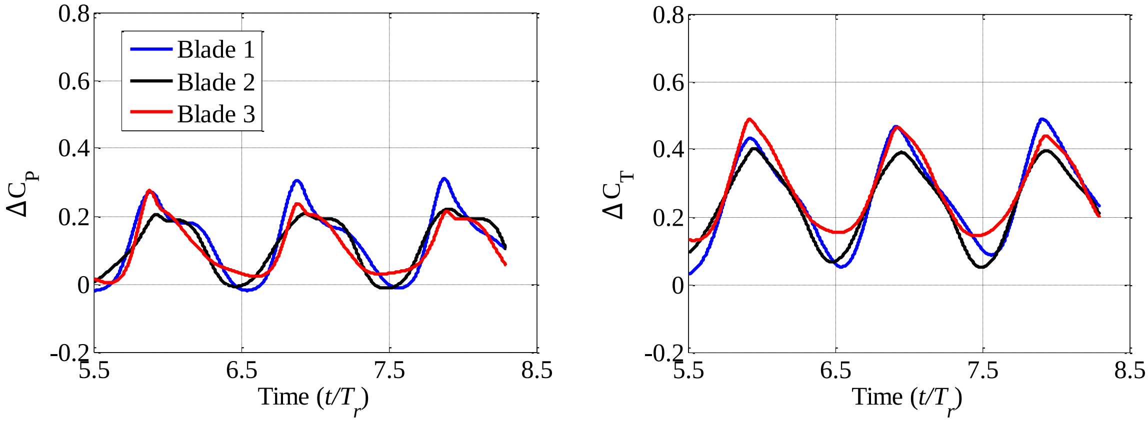

(a) ω_r = 0.76 rad/s

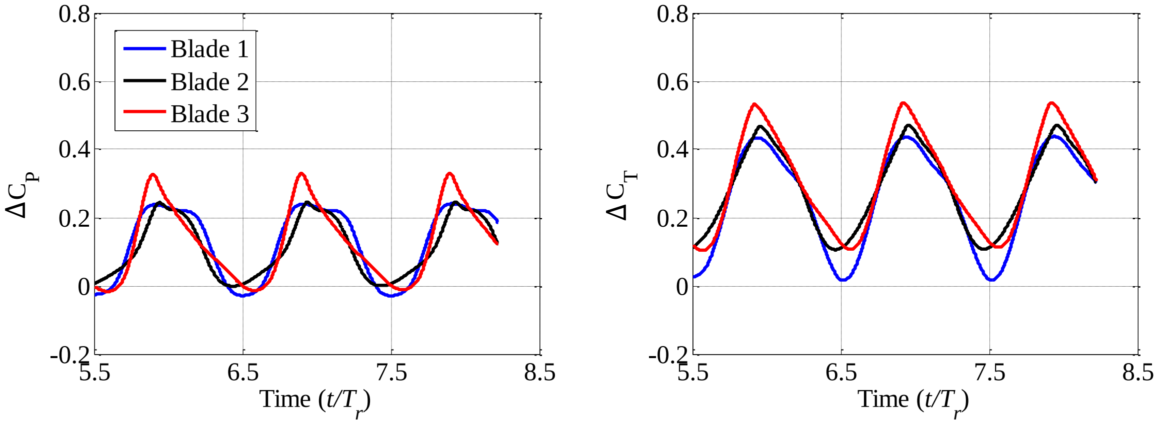

(b) ω_r = 0.84 rad/s

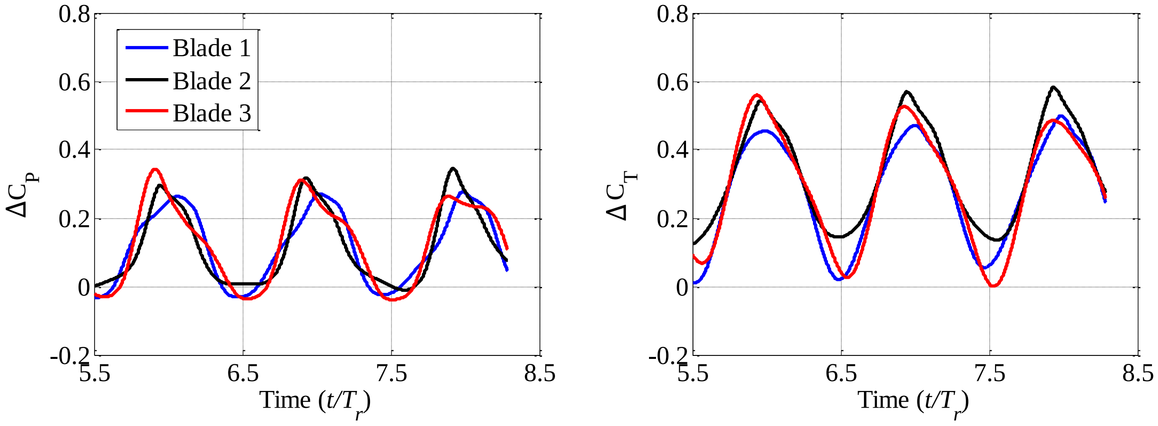

(c) ω_r = 0.92 rad/s

Figure 3-20 Power and thrust coefficients for each blade, ΔC_P and ΔC_T, respectively, for a floating turbine undergoing a prescribed pendulum motion at various rotational speed with a constant A_0 = 3.0° and ω^* = 1.0.

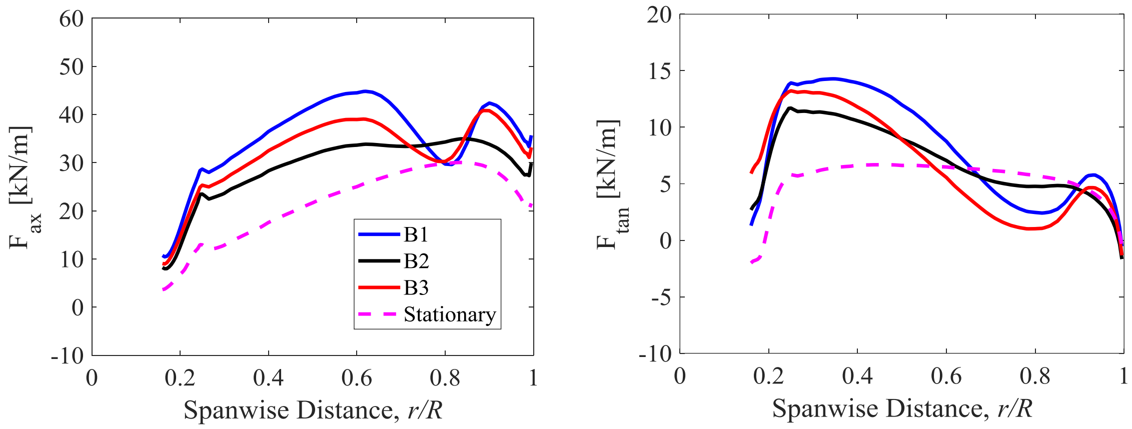

(a) ω_r = 0.76 rad/s at maximum U_{ap}

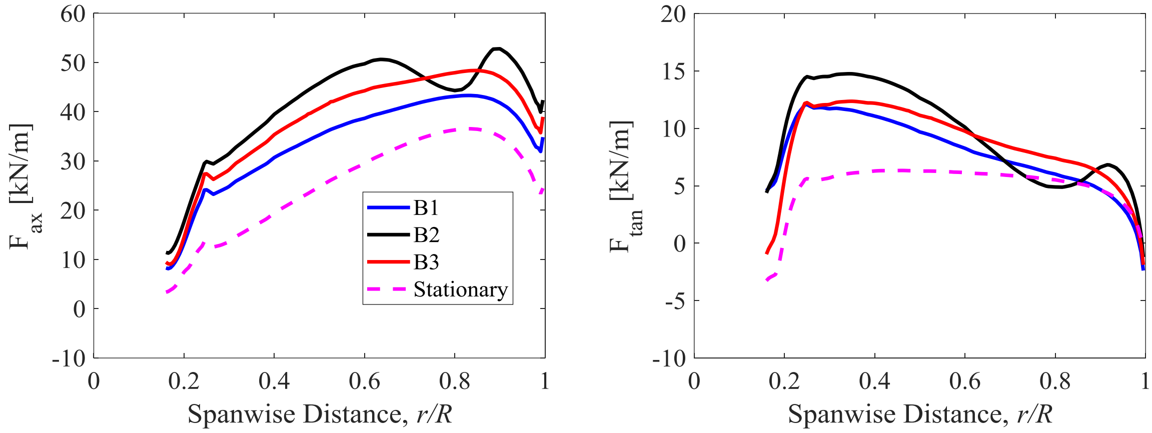

(b) ω_r = 0.92 rad/s at maximum U_{ap}

Figure 3-21 Comparison of axial force profiles at maximum apparent velocity for each blade for a rotor operating at ω_r = 0.76 and 0.92 rad/s while undergoing a pendulum motion with A_0 = 3.0° and ω^* = 1.0.

Contour plots of velocity magnitude on a blade cross-section r/R = 0.8 for two different rotor rotational speed cases are presented in Figure 3-22. Only the data of blade 1 for ω_r = 0.72 and blade 2 for ω_r = 0.92 are presented since both blades show the highest loading among other blades in their respective rotational speed. Visualization of the flow separation is needed to support previous results. Swirling at the suction side of the blade cross-section is more significant in the lower rotational speed case. Therefore, the stalling effect can be minimized for a floating tidal turbine undergoing pendulum motion by increasing the rotor rotational speed. However, the load fluctuation also increases, which contributes to greater fatigue damage.

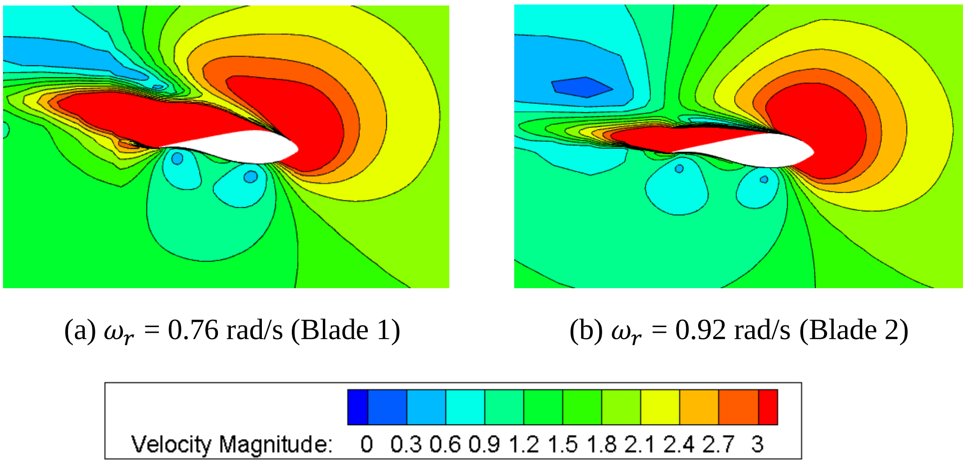
(a) ω_r = 0.76 rad/s (Blade 1) (b) ω_r = 0.92 rad/s (Blade 2)

Figure 3-22 Contour plots of velocity magnitude at r/R = 0.8 for ω_r = 0.76 and 0.92 rad/s at maximum $\mathrm{U_{ap}}$ of a rotor undergoing a pendulum motion at A_0 = 3.0° with ω^* = 1.0.

3.8 Comparison between a floating tidal turbine undergoing pendulum and surge motions

One of the focuses of making a comparative study between the pendulum and surge motions is to investigate how much contribution the horizontal (translational) aspect of the pendulum motion is to the unsteady loading of the rotor. This is because the approximation used in calculating the added mass and damping of the system (more on this in Chapter 5) requires only the translational aspect of the pendulum motion. Besides, a better understanding of the difference in the dynamic loading between the two motions is important for rotor designs to determine which motion contributes more to the fatigue damage on a floating turbine.

To compare two different orientations of motions, one translational and the other rotational, a parameter that can be used as a benchmark is needed to make the study viable. For a floating turbine undergoing surge motion, one amplitude of motion is selected, which is $A^* = {A_0}'/R = 0.1$, where ${A_0}'$ is the surge motion amplitude in meter, and R is the rotor radius. For the pendulum motion, we take the horizontal distance to be the same as the surge motion amplitude, as shown in the sketch of Figure 3-23, where the horizontal amplitude is used as the benchmark parameter between the two motions. At surge motion amplitude A^* = 0.1, the pendulum motion angular displacement is A_0 = 3°. Therefore, these two amplitude parameters were considered in the present study, with a frequency ω^* = 1.0 and rotor rotational speed ω_r = 0.84 rad/s, which corresponds to λ = 4.2.

As explained in Chapter 2, the moving reference frame method was used to model the surge motion. Since the comparison was made with the pendulum motion, the computational domain presented in Figure 3-1 was used to model the floating turbine undergoing surge motion. Both cases have the same computational mesh, blockage ratio, and side boundary conditions. For the surge motion, the inlet and outlet boundaries were set as presented in Chapter 2.

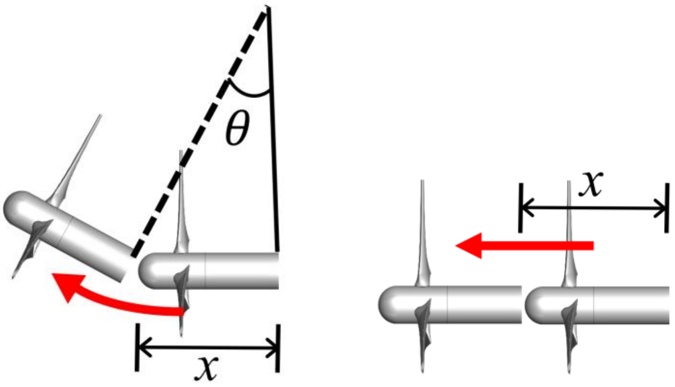

Figure 3-23 Sketch of a floating turbine undergoing pendulum and surge motions (left and right figures, respectively), where *x* refers to the horizontal (in fore-aft direction) amplitude of motions.

The simulation for surge motion was carried out until ∼8 rotor revolutions, and only the data of the last two motion cycles were considered for analysis to ensure stability and convergence. Comparison of the power and thrust coefficients time histories between the pendulum and surge motions are presented in Figure 3-24. Both motions show good agreement for C_P and C_T with the percentage difference of the mean values being less than 1%. Even though the pendulum motion is experiencing a rotational displacement, the amplitude is small with an angle of only 3°. Therefore, these results are expected since the translational amplitude and the frequency of motion for both cases are the same.

Although, when looking at individual blade loading for both motions, there are clear differences between the two. Results of individual blade loading time histories between pendulum and surge motions, presented in Figure 3-25, show that all three blades experience the same loading for the surge motion while each blade experience different loading from one another for the pendulum motion. As explained before, this happens due to the vertical variation of the apparent velocity experienced by the rotor in the pendulum motion. All blades experience the same apparent velocity for surge motion since it is a translational motion in the fore-aft direction.

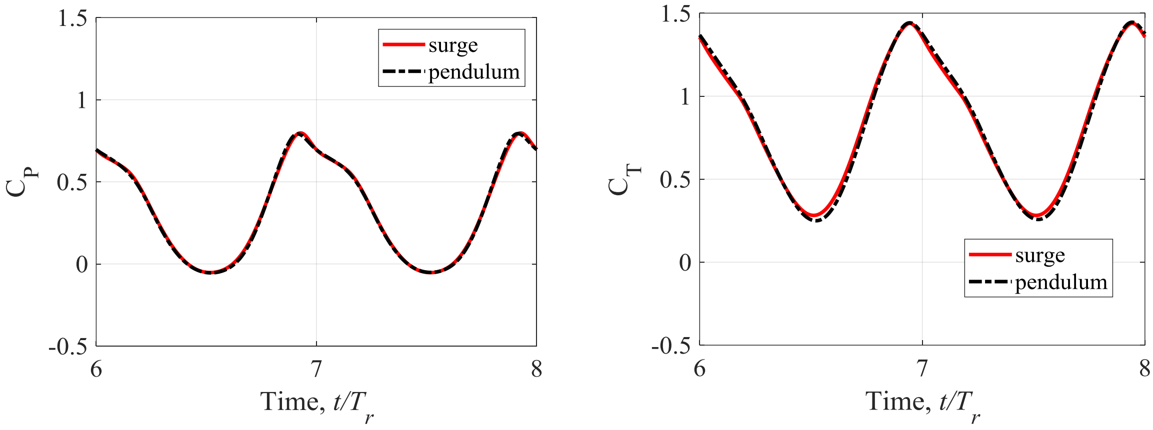

Figure 3-24 Power and thrust coefficients time histories of a floating turbine undergoing pendulum and surge motions.

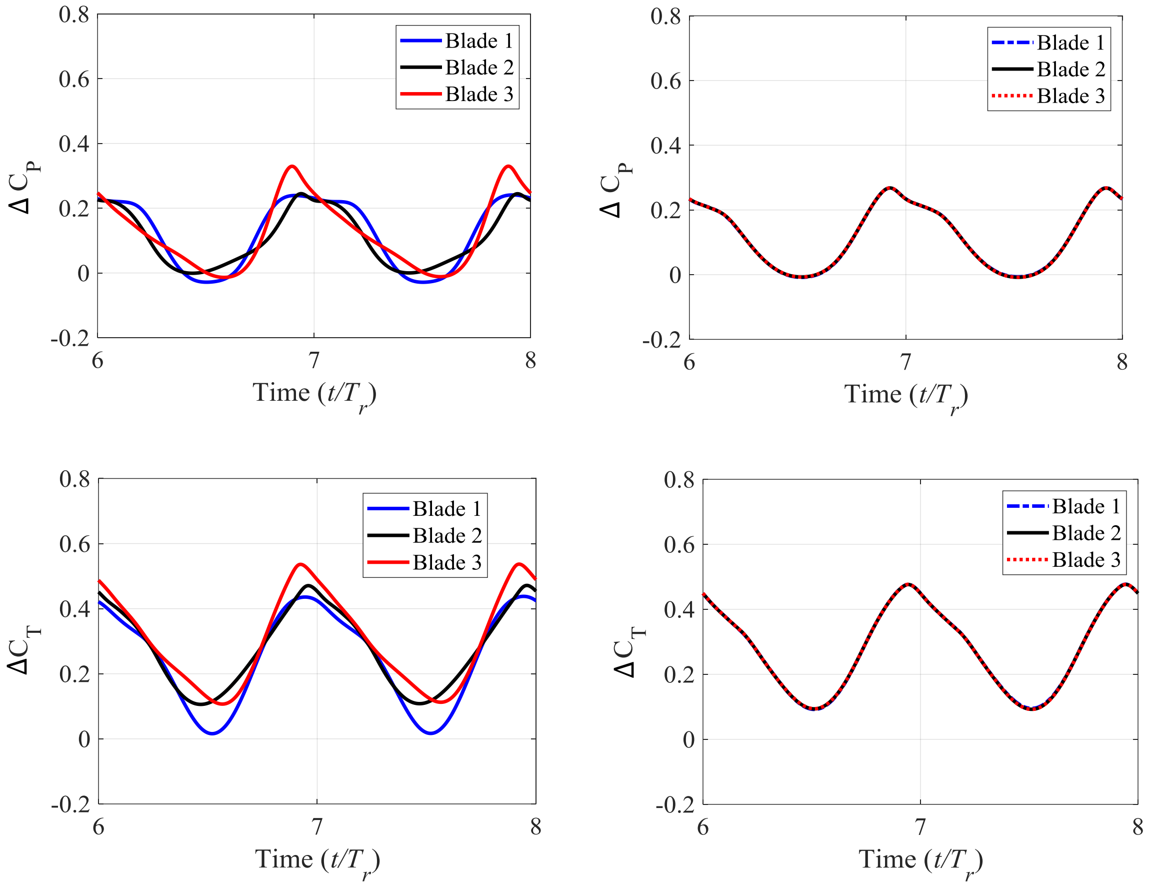

Figure 3-25 Loading time histories of individual blades, ΔC_P and ΔC_T, of a turbine undergoing pendulum (left) and surge (right) motions.

A similar trend can be observed when looking at the axial force profiles of each blade for both cases, which are presented in Figure 3-26. All blades show different variations of axial force profiles for a turbine undergoing pendulum motion at the minimum and maximum apparent velocity. For a surge motion, all blades show almost identical loading at each apparent velocity. Flow separation occurs at all three blades at maximum apparent velocity for a surging turbine while only two blades for pendulum motion turbine. As discussed previously, when the rotor moves forward, an arbitrary point at the rotor plane will experience higher apparent velocity the farther away that point is (radially) from the centre of rotation. The azimuth angle of blade 1 is at 0° (its original position) at maximum apparent velocity, which is experiencing the lowest apparent velocity compared to other blades due to its radial distance from the centre of rotation of the pendulum motion. Although not shown here, the tangential force profiles for both motions have a similar trend as the axial forces.

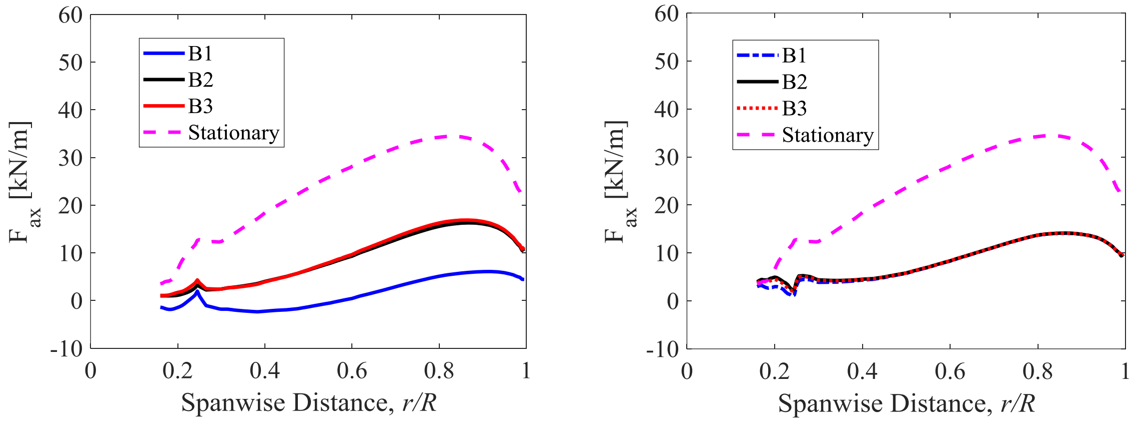

(a) Minimum U_{ap}

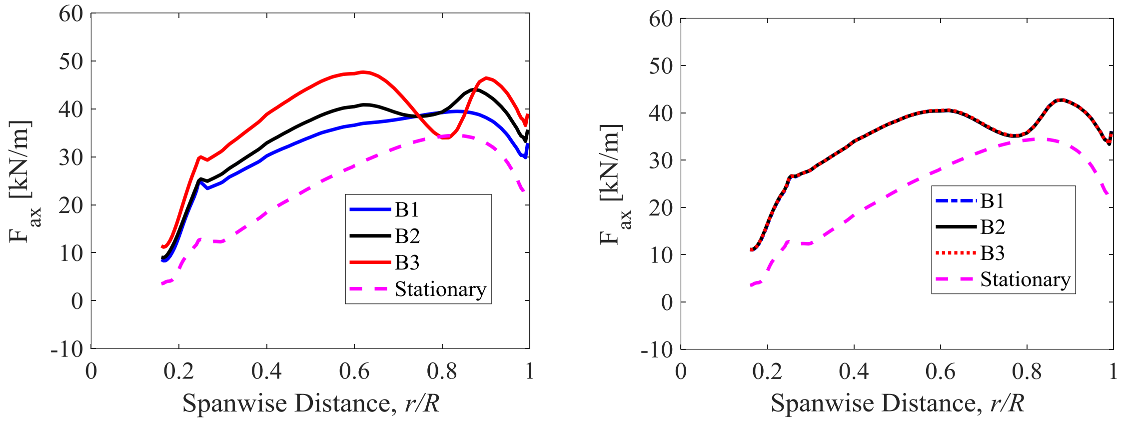

(b) Maximum U_{ap}

Figure 3-26 Axial force profiles at the minimum and maximum apparent velocities of a turbine undergoing pendulum (left) and surge (right) motions.

For a surging turbine, we can make a comparison between the two blockage ratios considered in the present study, B = 0.0982 and 0.01 for the case of $A^* = 0.1$ and $\omega^* = 1.0$. Looking at the C_P and C_T for the high (see Figure 2-21) and low (see Figure 3-24) blockage ratios, it can be observed that both parameters have a slight increase in loading variation amplitude at the higher blockage case. The mean value also increases in the higher blockage case. When comparing forces along the blade for high (Figure 2-37a) and low (Figure 3-26) blockage ratios, at minimum U_{ap}, there is a marginal difference between both blockage ratios.

At the maximum, however, the loading is higher in the high blockage ratio case. From these results, we observed that a higher blockage ratio contributes to higher rotor loading for a surging turbine. This is aligned with the literature, where an increase in the blockage ratio contributes to higher rotor loading (Schluntz & Willden, 2015; Wimshurst & Willden 2016). However, there is a slight difference in the rotor rotational speed (thus, tip-speed ratio) between the two cases compared here ($\lambda = 4.4$ and 4.2 for high and low blockage ratios, respectively). This might affect the rotor loading, where spinning the rotor faster can contribute to an increase in the loading.

3.9 Conclusion

To conclude, this chapter investigates the hydrodynamic loading of a floating tidal turbine undergoing pendulum motion over a range of motion amplitude and frequency. As mentioned in the literature (Tran & Kim, 2015a; Leble & Barakos, 2016; Lienard et al., 2019), and the data presented here, the rotor loading variation is highly in phase with the apparent velocity. The typical result has been shown in the present study for the loading variation. The amplitude of variation increases as the motion amplitude is increased, and the mean power increases while the mean thrust decreases with the increase in motion amplitude. The overall mean power and thrust are significantly lower for the floating turbine compared to the stationary. This might be due to the rotor design used in the present study. Wimshurst & Willden (2016) optimized the blocked rotor design to operate in a high blockage condition (close to blockage ratio B = 20%). The present study uses B = 1%, which significantly affects the performance of the rotor when operating in an unsteady condition, such as oscillating in a pendulum motion. Loading variation for individual blades happens due to the vertical variation of the instantaneous apparent velocity, together with the azimuth angle of each blade at a given time step. The rotor goes into stall at higher motion amplitude and frequency cases due to the loss in lift along the rotor blades, particularly at higher apparent velocity because of the increase in the angle of attack. The floating tidal turbine undergoing pendulum motion operates near the optimum condition twice per motion cycle, where the rotor efficiency is at the maximum at $U_{ap} \approx U_{\infty}$. The rotor enters VRS at higher motion amplitude and frequency when oscillating towards the downstream, increasing the fatigue damage.

In contrast to the literature (Jing et al., 2017; Wang et al., 2017), both mean power and thrust coefficients of the rotor decrease as the motion frequency is increased, which happens due to the loss in lift on rotor blades from stalling effect. When looking into individual blades, they exhibit variation of loading in every motion cycle which happens due to the difference between the rotor rotational speed and the motion frequency (angular velocity). Therefore, different blades will experience the maximum and minimum loading at each motion cycle when the rotor rotational speed and motion frequency are different.

The instantaneous tip speed ratio varies over time for a floating turbine due to the change in the apparent velocity of the rotor; a higher apparent velocity will reduce the instantaneous tip speed ratio and *vice versa* for a lower apparent velocity. Therefore, it is better to increase the speed of rotation (i.e., speed control technique) when operating a floating turbine at a high apparent velocity so that it will operate at an instantaneous tip speed ratio close to its optimum condition. The rotor loading shows a typical result for a turbine undergoing pendulum motion, where the amplitude of loading variation increases as the rotor rotational speed increases. It is typical for the mean power to increase when increasing the rotor rotational speed of a floating turbine oscillating under a prescribed motion. A similar trend has been shown in studies of Jing et al. (2017), Wang et al. (2017), and Sun et al. (2017) for floating tidal turbines undergoing surge and roll motions. However, the mean thrust increased as well, which contradicts the results from the literature. This happens due to the stalling effect being minimized at high apparent velocity when the rotational speed is increased, which increases the mean thrust and the mean power of the floating turbine. As mentioned before, the stalling effect at high apparent velocity can be minimized using the speed control technique.

For a small pendulum motion amplitude, the difference in load variations is non-significant compared to the surge motion with the same horizontal motion amplitude. The difference lies in individual blade loading, where each blade shows different load variations in the pendulum motion while they are the same for surge motion. This can be attributed to the apparent velocity on each blade for both motions, where the vertical apparent velocity varies for the pendulum motion while there is little to no variation for the surge motion.

Chapter 4

Dynamic loading of a floating tidal turbine undergoing heave motion

4.1 Introduction

In most studies involving floating wind or tidal turbines, which are free to oscillate in 6 degrees of freedom (DoF), the heave motion is often neglected due to the small response amplitude variation, thus having minimal impact on the rotor. Pegalajar-Jurado et al. (2016) tested a 1:60 scale model of the DTU 10 MW floating wind turbine supported by a tension-leg platform (TLP) using both experimental and numerical models. The wind turbine was free to oscillate in six degrees of freedom (DoF) under the influence of combined wind and waves conditions. The experiment was conducted at DHI Denmark inside a wave tank size of 20 m x 30 m x 3 m deep. The wind generator with the size of 4 m x 4 m was placed at the top of the wavemaker. The turbine is located 4m downwind from the wind generator. Several probes were placed in the wave tank for various measurements. As for the numerical model, an unsteady BEMT method was used, where the model assumes the turbine as a slender body; therefore, the hydrodynamic force calculation is based on the Morison equation. Added mass matrix was used to accommodate the hydrodynamic coefficient in the calculation, and linear wave theory was used to model waves. The reader can refer to the paper for more information on the experimental and numerical setup. Surge, heave, and pitch motion responses of the floating wind turbine were measured for both the experimental and numerical test cases. Heave shows the least response compared to other motions in both regular and irregular wave conditions. The floating turbine was also tested under various wind speeds. Again, the heave motion shows the smallest magnitude of response for both experimental and numerical tests. A similar trend for the heave motion can be found in literature such as Bagbanci (2011) and Sebastian & Lackner (2013) for numerical studies on floating wind turbines operating under various wind and waves conditions using multiple types of support platforms.

It is common practice for researchers and engineers to consider only DoFs which have significant motion responses, such as surge and pitch motions, in a floating turbine analysis. However, looking deeper into the cases of the papers mentioned in the previous paragraph, we will find that the heave motion is actually very important for a floating tidal turbine. For example, at the rated condition, the wave height used in Pegalajar-Jurado et al. (2016) is 0.069 m for the 1:60 scale model (which translates to 4.14 m for the full-scale model). The result shows that the heave motion height (height = 2 × amplitude) is around 0.03 m, close to half of the wave height. In Bagbanci (2011), he tested a floating wind turbine supported by three different platforms: the ITI energy barge (barge), a spar buoy (spar), and a semi-submersible (semi-sub). The wave height is fixed to 4 m for the rated condition. The heave motion heights are around 4, 1, and 6 m for the barge, spar, and semi-sub, respectively. For the rated condition in Sebastian & Lackner (2013), the wave height is fixed to 2.54 m. This study also tested a floating wind turbine attached to three different platforms: a barge, a spar, and a tension-leg platform (TLP). The heave motion heights, respectively, are around 2, 3, and 0.3 m. These results are based on fully coupled models, showing that the heave motion response is actually quite close to the corresponding wave height, depending on the type of support platform used. For a 20 m diameter tidal turbine (used in the present study), even a small heave motion amplitude can be significant due to the effect from the added mass and damping, which are higher than that of a wind turbine due to the fluid density difference. Besides that, for a floating horizontal axis tidal turbine, exposure to heave motion is non-negligible due to waves that impact the floating support structure. Under a heaving motion, the resultant velocity coming from the vertical and horizontal velocity components exists, leading to an unsteady loading effect. Although considered small in motion response amplitude, the heave motion fluctuation is still damaging and will likely reduce the life span of rotor blades. Therefore, it is crucial to understand the unsteady effect of the heave motion on a floating tidal turbine.

When the frame of reference is fixed to the rotor, we can view a floating tidal turbine undergoing a heave motion as a stationary turbine experiencing a dynamic yawing inflow. Since the author has not managed to find any publication on a heaving (only) turbine, only the literature on yawing turbines will be presented in this thesis.

Lee & Lee (2019) conducted a numerical study on a two-bladed NREL Phase VI wind turbine under yawed inflow conditions. The study uses an in-house code, which was developed using a combination of a non-linear vortex lattice method (to calculate the aerodynamic of the turbine) with the vortex particle method (to model the wake). The reader can refer to the paper for further details on the numerical model. Under the yawed inflow condition, the rotor is experiencing advancing and retreating phases: the advancing phase is where the blade is rotating into the incoming flow, while the retreating phase is where the blade moves away from the inflow. Since a heaving turbine is assumed to have similar dynamics as a turbine undergoing dynamic yawing inflow, it is expected to see the advancing and retreating phase on a heaving turbine. However, the effect would be dynamic compared to static, such as in the paper. The study shows that the loading on the rotor reduces as the yaw angle is increased. This happens due to the reduced impact of the axial flow velocity on the rotor since the effective swept area is reduced as the turbine’s yaw angle is increased. The study also shows that the loading is increased towards the blade tip at the advancing phase, while the opposite happened to the retreating phase. The varying angles of attack around the azimuth position are causing this loading variation, which is due to the change in the effective velocity at the rotor plane. They also investigate the wake skewness on the yawed turbine. They discussed counter-rotating vortices, which occur at the beginning of both advancing and retreating phases, to be the main contributor to wake deflection. The wake in the retreating phase is also shown to have a closer gap between each vortex, showing the effect of the skewed wake. Therefore, unsteady phenomena like the advancing and retreating phases and skewed vortex wake, which will form uneven flow velocity around the rotor plane area, are important considerations that need to be addressed for a heaving tidal turbine. Besides this paper, the reader can also refer to Schepers (1999) for the fundamental explanation of a turbine operating under yawed inflow.

Nowadays, many turbine designs incorporate a yaw control system. This will only be effective for a static yawed inflow or at low yawing frequency cases. In the case of a heaving turbine, which can be viewed as having a dynamic yawing inflow (in the vertical plane rather than horizontal plane), the frequency can be high depending on the interaction between the wave and the floating support platform. For a stationary yawed turbine, the angle of attack changes depending on the azimuth angle of each blade. However, for a heaving turbine case, the angle of attack not only varies depending on the azimuth angle but also the inflow heave angle. This has been shown in the study by Tran & Kim (2015). They conducted a numerical study on a floating wind turbine (the NREL 5 MW turbine) undergoing a dynamic yawing motion. A CFD model which utilized the overset grid mesh method was used to simulate the dynamic yawing motion. Two yawing amplitudes were tested using the same motion frequency. They found that the loading variation increases as the motion amplitude are increased. They also investigate the dynamic wake skewness effect of a yawing turbine. They found that there is an asymmetry in the wake vortices development due to the interaction between the rotating blade (i.e., the effect from the azimuth position) with the dynamic yawing motion. In the study, however, the parameter space used for the dynamic yawing cases is small (only compared two yawing amplitudes), and no frequency variation was tested. Therefore, to capture the effects of unsteady loading of a floating tidal turbine undergoing heave motion, testing a turbine under various motion amplitude and frequency needs to be considered. Furthermore, various rotor rotational speeds on a heaving turbine will also be considered in the present study to improve the analysis in understanding the unsteady loading.

Ye et al. (2020) conducted a CFD study on a wind turbine operating under yawed (fixed angle) and yawing (dynamic angle) conditions. The two-bladed NREL Phase VI wind turbine was used in their simulation. The rotor mesh remains stationary (i.e., rotating around a fixed axis) while a dynamic inflow model was applied at the boundary to simulate the dynamic yawing inflow. Unsteady RANS was used to simulate the flow field surrounding the rotor, with a modified shear stress transport (SST) to model the turbulence. They validated their model with experimental results for a yawed turbine, comparing blade spanwise forces and pressure at several blade cross-sections. The model agrees reasonably well with the experiments. The study mainly focuses on fixed yawed conditions, consistent with other work on this topic. The results mostly revolve around the effect of advancing and retreating phases. Besides that, they investigated the 3-dimensional stall effect. They found that flow separation occurs at the suction side of the blade when it enters the retreating phase (stalling effect), making the loading much lower than the advancing phase. The occurrence of flow separation depends on the yaw angle. As the yaw angle decreases, the occurrence of flow separation moves towards the blade root. They also compared a turbine operating under yawed and yawing conditions and found that the latter has higher loading fluctuation and magnitude. They have not reported any stalling effect for the dynamic yawing case. Therefore, it is important to investigate the stalling effect because of the intermittent occurrence of flow separation along each blade when the rotor oscillates in the heave motion. This can cause serious fatigue damage, particularly around the blade root to mid-section (Ye et al., 2020).

Heave motion is one of the most important degrees of freedom (DoF) motion for a floating tidal turbine since there is no way to avoid this motion using any seakeeping techniques. From the report by Anatec Ltd. (2010), the significant wave height over 20 years at The Fall of Warness tidal site is on average 1 m and is a maximum of around 4 m. Assuming a 20 m diameter rotor to have almost the same heave amplitude as the wave, the range would be around 0.5-2.0 m. Therefore, three heave amplitude ratios $A^* = A_0/R =$ 0.05, 0.10, 0.15 were chosen for the present study to simulate a floating tidal turbine undergoing heave motion, where A_0 is the heave motion amplitude (m), and R is the rotor radius (m). The frequency ratio $\omega^* = \omega_0/\omega_r =$ 0.7, 1.0, 1.3 were chosen based on the wave period range from the tidal site, where ω_0 is the heave motion frequency (rad/s). Three rotor rotational speeds $\omega_r =$ 0.80, 0.88, 0.96 rad/s were chosen in the present study to determine the effect of rotor rotational speed on a heaving turbine.

4.2 Numerical method

In the present study, the heave motion of the rotor is simulated by oscillating the entire domain. This method is quite common for vortex-induced vibration studies, where a cylinder is forced to oscillate in the cross-flow direction to simulate a vibration in the vertical plane. Such a method is presented in Pham et al. (2010) and Akhter & Mysa (2019) for vortex-induced vibration studies on a cylinder. However, these studies neglect the effect of blockage ratio B by using a large computational domain ($B \leq$ 1.0%). Based on research by Schluntz & Willden (2015) and Wimshurst & Willden (2016), where they conducted numerical studies on tidal turbines operating under different blockage ratios, we acknowledge the significance of the blockage ratio to tidal turbine performance. Therefore, there is a limit to using this method for the present study. This is because the aspect ratio on the turbine plane remains the same when the entire domain is moving in the heave motion. However, the aspect ratio will change when the turbine moves in the heave motion while the domain is kept stationary (i.e., via the deforming mesh method). Hence, we need to determine the upper limit of the heaving amplitude to maintain the effect of the aspect ratio at $B = 0.0982$.

4.2.1 Model limitation

As discussed above, we need to determine the limits of the methodology used in the present study (i.e., maintaining the aspect ratio effect for a blockage ratio $B = 0.0982$). For a preliminary test case, a cylinder (as shown in Figure 2-4 in Chapter 2) was chosen to test the limitation of the methodology. A change in reference frame approach, in which the body is held stationary and the flow is pitched towards it, can be used to simulate the flow past a heaving body. This is a common approach used in vortex-induced vibration problems (Pham et al., 2010; Akhter & Mysa, 2019), and these problem setups are mathematically equivalent. In the present problem, the turbine heaves towards a free surface. Treating the free surface as an immovable boundary, the separation between the turbine and the free surface will fluctuate as the turbine heaves. We use the change in frame of reference approach as an approximation to the body heaving in the presence of the free surface and test the limits over which this approach provides a good approximation. We use a cylinder as the test case to test the methodology as this provides a simpler problem without turbine rotation. The cylinder and turbine have similar drag/thrust coefficients and so will develop similar resistances and interactions with boundaries and bypass flows.

The cylinder was oscillated in the heave motion using two different methods: (1) the deforming mesh method; and (2) the oscillating domain method. Method (1) is where the cylinder is physically oscillated in the heave motion by deforming the mesh surrounding the structure. Method (2) is where the entire domain oscillates in heave motion. When using method (2), careful consideration needs to be given to the aspect ratio of the simulation. In method (1), when the cylinder moves into the highest or lowest vertical position, the effect from the aspect ratio becomes significant at higher motion amplitude. This might affect the structural loading on the cylinder where there will be a high and low acceleration region (near the boundary and at the opposite side, respectively), affecting the pressure distribution on the structure. In method (2), however, there will be no change in the aspect ratio since the distance between the cylinder and boundaries remain constant. Therefore, the height of the cylinder's computational domain is equal to that of the turbine, which is $2D$, to maintain the blockage ratio B = 0.0982. This is to determine the upper limit of the aspect ratio, at what amplitude of the heave motion will the structural loading diverges between the two methods.

Three heave amplitudes were chosen, A_0 = 1.0, 2.0, 3.0 m with a constant frequency ω_0 = 0.88 rad/s based on the wave heights and wave period on The Fall of Warness tidal site (Anatec Ltd., 2010). Simulations were carried out until six heave cycles, and the structural loadings of all heave amplitude cases are presented in Figure 4-1, and T_r is the period of one heave cycle. The result diverges between the two methods as the heaving amplitude is increased. Although the difference between the two methods is less than 1.0% for C_Z', the percentage difference of the average peak C_X' are 3.1, 3.9, 4.5% at amplitudes A_0 = 1.0, 2.0, 3.0 m, respectively.

Even though it is incorrect to assume the aspect ratio effect of a cylinder to be the same as a turbine, we can use the result as a baseline for the heaving turbine test case. Therefore, to maintain the effect of blockage ratio B = 0.0982 for the heaving turbine, the amplitude needs to be at the lower range, preferably less than 2.0 m.

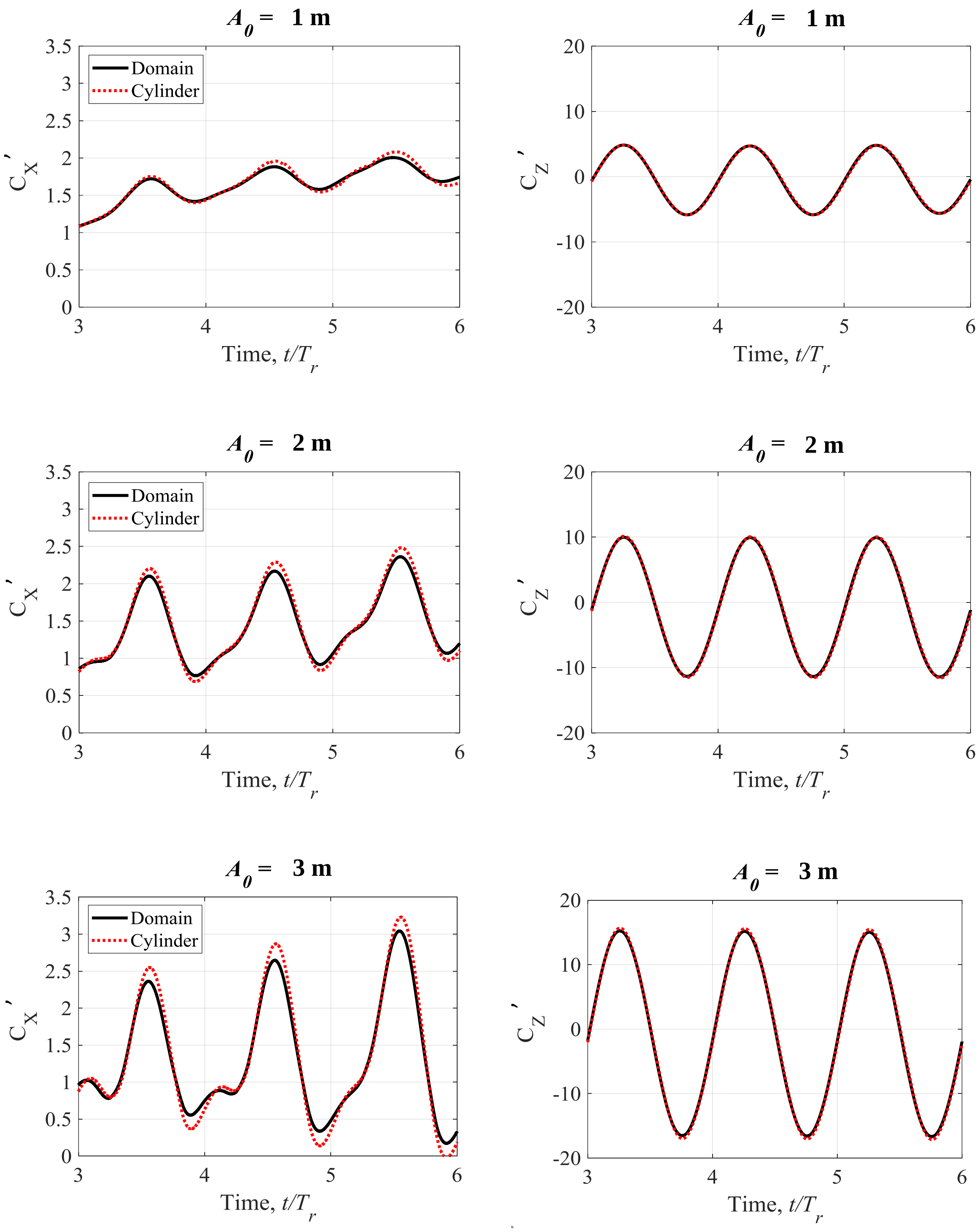

Figure 4-1 Structural loading of a cylinder oscillating in heave motion by method (1) and method (2) i.e., deforming mesh method (red dashed line) and oscillating domain method (solid black line), respectively.

4.3 Flow mechanics of a heaving turbine

To understand the mechanics of a floating tidal turbine undergoing a heave motion, we can look at the rotor as having a turbine with dynamic yawing inflow in the cross-flow direction by fixing the reference frame to the rotor. The vertical flow velocity U_Z' will be in the opposite direction of the rotor velocity U_Z ($U_Z' = -U_Z$). Therefore, theoretically, the heave inflow angle γ will be towards the downward direction when the rotor moves vertically upward, as shown in Figure 4-2, and the effect will be in the opposite when the rotor moves vertically downward. To compare this to a dynamic yawing turbine, in Figure 4-2 when the rotor is moving upward, the rotor will experience something like a positive (or negative depending on the author's definition) yawing with an angle $\gamma_{\mathrm{YAW}} = \gamma$, where the angle is in the vertical plane instead of horizontal. The upper half (azimuth angle ψ from 270° to 90°) of the rotor plane will experience an advancing phase where the blades move into the inflow. The bottom side (ψ from 90° to 270°) of the rotor plane will experience a retreating phase where the blades move away from the inflow.

The displacement $d_Z = A_0 \sin(\omega_0 t)$ of a floating turbine oscillating in heave motion is presented in Figure 4-3 together with the heave velocity and acceleration, $U_Z = A_0 \omega_0 \cos(\omega_0 t)$ and $\dot{\mathrm{U}}_{\mathrm{Z}}$ respectively, for A^* = 0.10 and ω^* = 1.0. T_2 is where the rotor is at the highest vertical position and T_6 is at the lowest, where at both locations the $U_Z = 0$.

As mentioned before, a turbine having a static yawed inflow will experience the advancing phase at the upstream region (blades move into the inflow) and the retreating phase at the downstream region (blades move away from the inflow). However, a floating turbine undergoing heave motion cannot be treated as a quasi-static yawed turbine. Theoretically, when the rotor moves from T_6 to T_2, the upper half of the rotor plane will experience the advancing

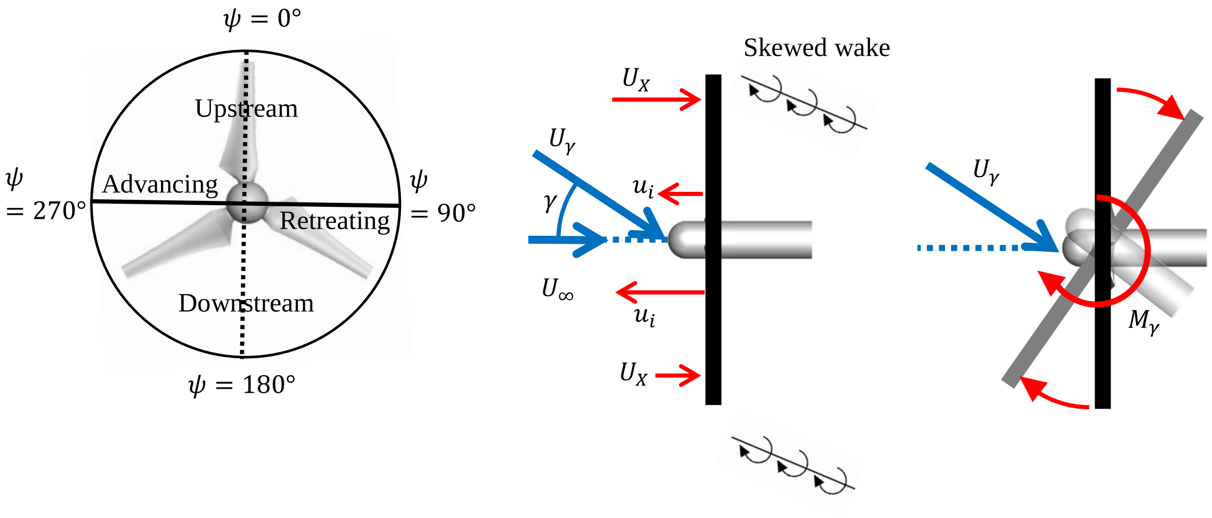

(a) View from inlet (b) Side view (c) Stabilizing moment

Figure 4-2 Effects on a floating tidal turbine undergoing upward heave motion. (a) The solid line separates the upstream and downstream sections, while the dashed line separates the advancing and retreating sections. (b) Flow behaviour of a floating turbine moving in the upward direction, where the induced velocity u_i (near the blade root region) is lower in the advancing phase than retreating. (c) Yaw stabilizing moment M_γ characteristic on a yawed turbine. Effects in these diagrams were exaggerated for visualization purposes.

phase and the lower half, retreating phase. Although looking at the iso-surface of the wake vortices presented in Figure 4-4, it took some time for the wake skewness formation to develop after the rotor starts to move in the upward or downward directions (red and purple dashed lines, respectively). Orange and green solid lines present the downward and upward wake skewness, respectively, showing the wake formation is lagging from the rotor motion. This happens due to the high heave frequency simulated using $\omega^* = 1.0$. This phase lag will be less significant in lower frequency cases (which will be discussed later in this chapter).

To explain the mechanics of the wake skewness development for a floating tidal turbine undergoing heave motion, Figure 4-5 shows the diagram of the wake formation. The turbine will experience the advancing and retreating phases in the upper and lower half, respectively, of the rotor plane when it moves from the middle (original) position to the top position (from

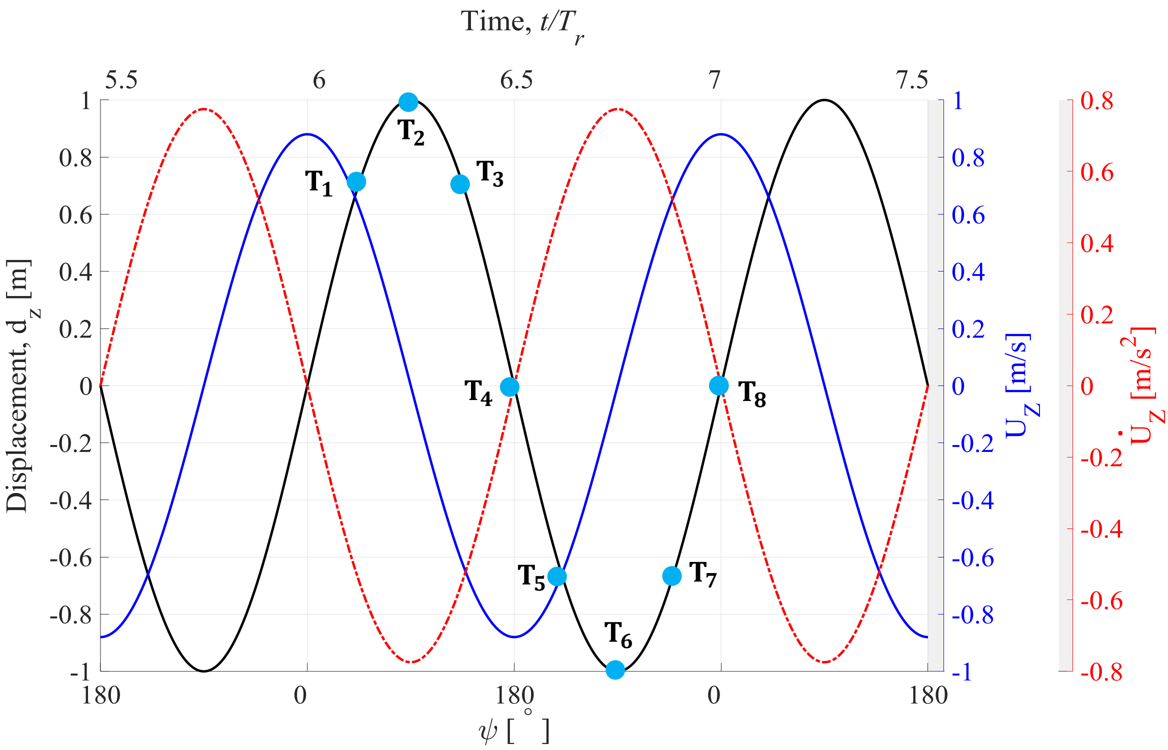

Figure 4-3 Time histories of heave displacement d_Z, velocity U_Z and acceleration $\dot{U}_Z$. The azimuth angle ψ of blade 1 is also given in the *y*-axis of the plot. The negative value shows the opposite direction.

T_8 to T_2) and going back to its original position (from T_2 to T_4) as presented in Figure 4-5(b). The wake iso-surface can be observed based on the orange solid line arrow in Figure 4-4. This is different from the theoretical assumption that we imposed earlier. When the rotor moves from the bottom to top position (from T_6 to T_2) the advancing and retreating phases will switch places (upper to lower half of rotor plane) somewhere around T_8 as presented in Figure 4-5(b). The wake iso-surface can be observed based on the red dashed arrow in Figure 4-4. Aside from the tip vortices skewness, this can also be verified from the vortex build-up near the blade root region in Figure 4-4. However, this will be explained later in this chapter. Therefore, the turbine will experience the advancing and retreating phases at the upper and lower half, respectively, of the rotor plane when it moves from T_8 to T_4. The effect will be the opposite from T_4 to T_8.

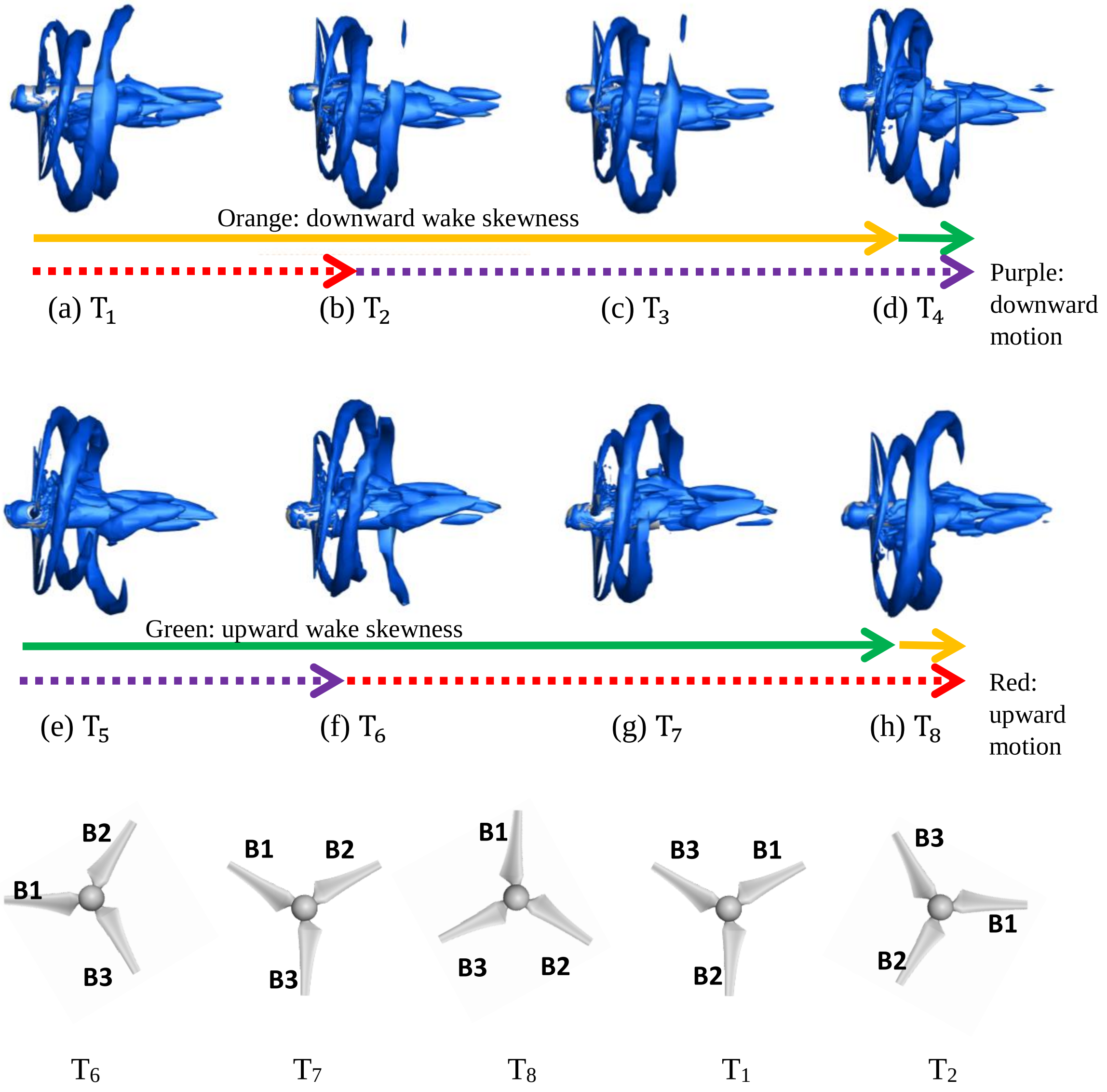

Figure 4-4 Iso-surface of wake vortices of a floating tidal turbine undergoing heave motion at $A^* = 0.15$ and $\omega^* = 1.00$. Bottom figures show the azimuth positions of each blade moving in the upward motion from T_6 to T_2.

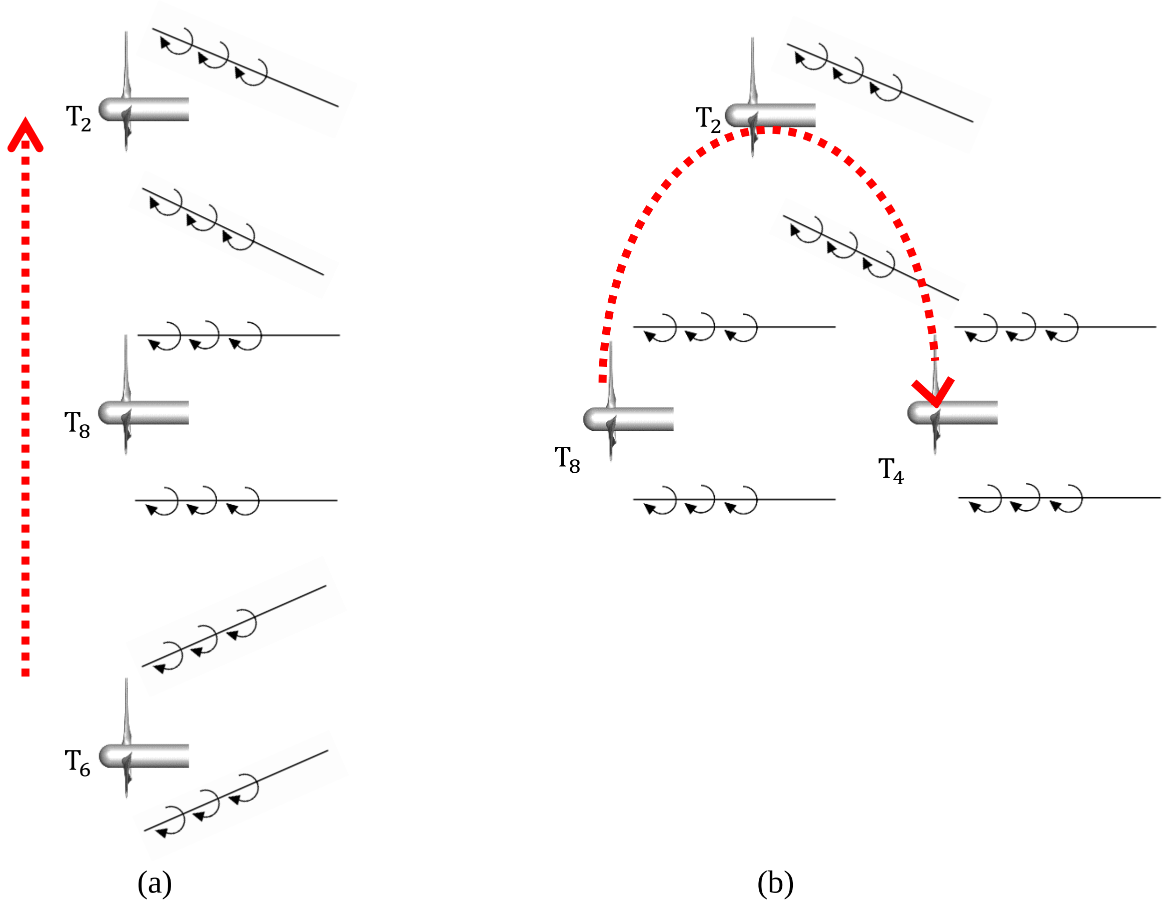

Figure 4-5 Diagram of a floating tidal turbine undergoing heave motion with wake skewness formation: (a) moving upward from bottom to top position; (b) moving upward from middle to top position and moving downward from top to middle position.

4.4 Effect of heave amplitude on turbine performance

Time histories of power and thrust coefficients were presented in Figure 4-6 for three heave motion amplitude cases. The loading variation increase as the heave motion amplitude is increased, which is a common trend for a turbine undergoing a prescribed motion. The mean values of C_P increases while the mean C_T decreases as the heave motion amplitude are increased, as shown in Table 4-1. A similar trend has been shown for other DoF motions, such as the surge motion presented in Chapter 2 and also by Wen et al. (2017), pitch motion by Lienard et al. (2019) and yaw motion by Qiu et al. (2014), Tran & Kim (2015) and Wen et al. (2019), where an increase in the motion amplitude results in an increase in the load variation.

Notice that the maximum loading occurs at every $t/T_r \approx 0.25$ interval. This include timesteps at T_2 and T_6 (see Figure 4-3 and Figure 4-4). As explained above, the wake maximum skewness is fully developed at these two timesteps where the advancing and retreating effects are the most significant.

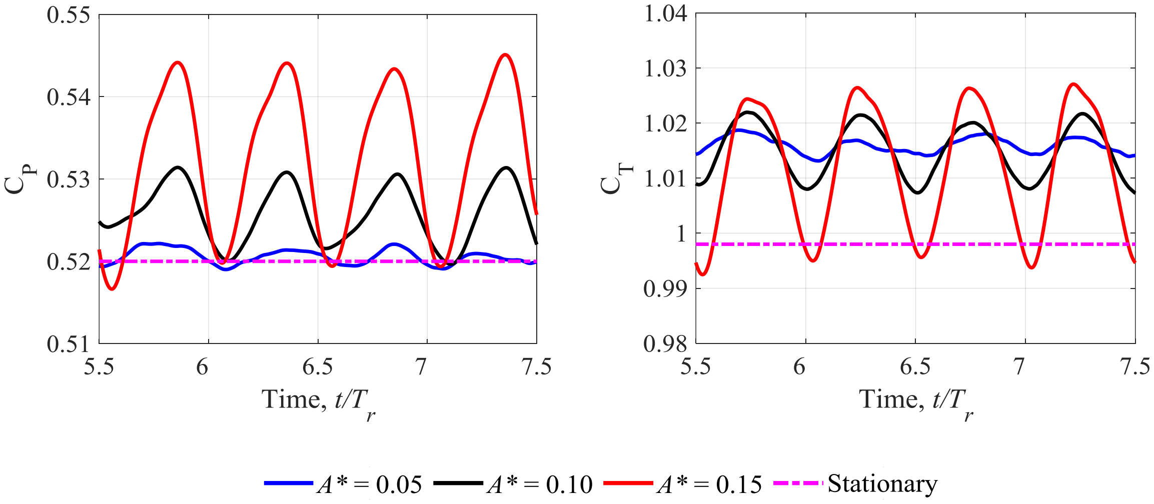

Figure 4-6 Power and thrust coefficients time histories of floating tidal turbine undergoing heave motion at $A^* = 0.05, 0.10, 0.15$ with $\omega^* = 1.0$ and $\lambda = 4.4$.

The mean values of C_T are 1.016, 1.014, and 1.013 for $A^* = 0.05$, 0.10 and 0.15, respectively. This shows that the magnitude of the axial loading on rotor blades decreases while the fluctuation increases as we increase the heave motion amplitude. A similar result has been reported by Lee & Lee (2019), where the magnitude of flap-wise bending moment of the rotor blades decreases while the fluctuation amplitude increase as the inflow yaw angle is increased. The C_P is directly proportional to the torque of the rotor (higher C_P = higher torque). The torque increases as the motion amplitude is increased. This happens due to the increase in the vertical component of the velocity, which affects the tangential loading component (i.e., torque) on the rotor.

Table 4-1 Mean percentage difference of power and thrust coefficients between the heaving and stationary turbines. A negative sign shows the heave cases are lower than the stationary case.

A^*	$\bar{C}_P$	$\bar{C}_T$	Percentage difference $\bar{C}_P$ [%]	Percentage difference $\bar{C}_T$ [%]
0.05	0.521	1.016	0.19	1.77
0.10	0.525	1.014	0.95	1.57
0.15	0.534	1.013	2.62	1.48
Stationary	0.520	0.998	-	-

Looking at individual blade loadings in Figure 4-7, all three blades are out of phase with one another. This happens because of the difference in azimuth angles of each blade while oscillating in the heave motion. A similar trend has been reported for yawing wind turbines by Qiu et al. (2014) and Ye et al. (2020). Notice that blade three always experiences higher loading compared to the other blades. This happens due to the heave motion frequency is equivalent to the rotational speed of the rotor: $\omega_0 = \omega_r$ =0.88 rad/s. At this frequency, blade 3 will always experience the advancing phase. Looking at the wake skewness formation and the azimuth position of blade 3 in Figure 4-4, it is evident that for a floating 3-bladed horizontal axis turbine that has the same heave frequency as the rotor rotational speed, one blade will always experience the advancing phase. This will not happen when the heave frequency and rotor rotational speed differ, as shown later in this chapter. A similar trend has been presented by Wen et al. (2019) for a dynamic yawing turbine where one blade always has higher loading than others when the rotor rotational speed is equal to the yawing frequency.

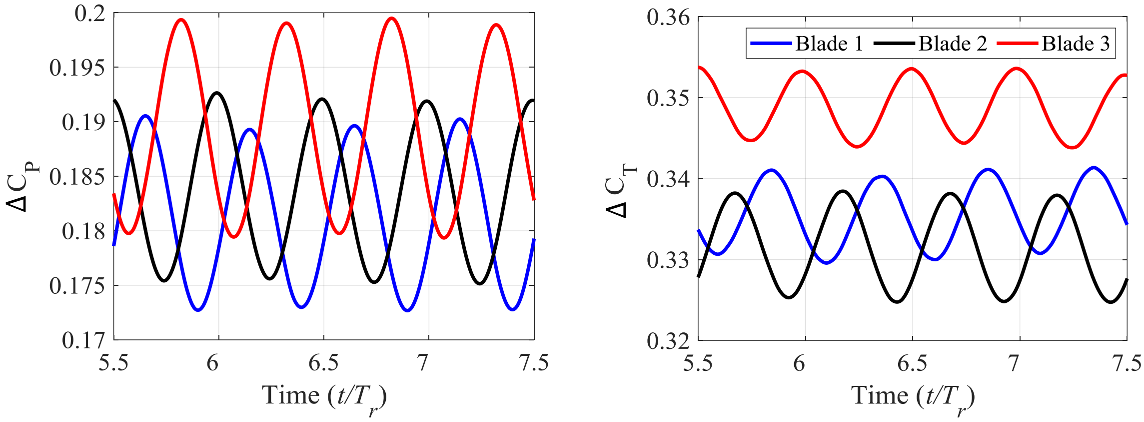

(a) $A^* = 0.05$

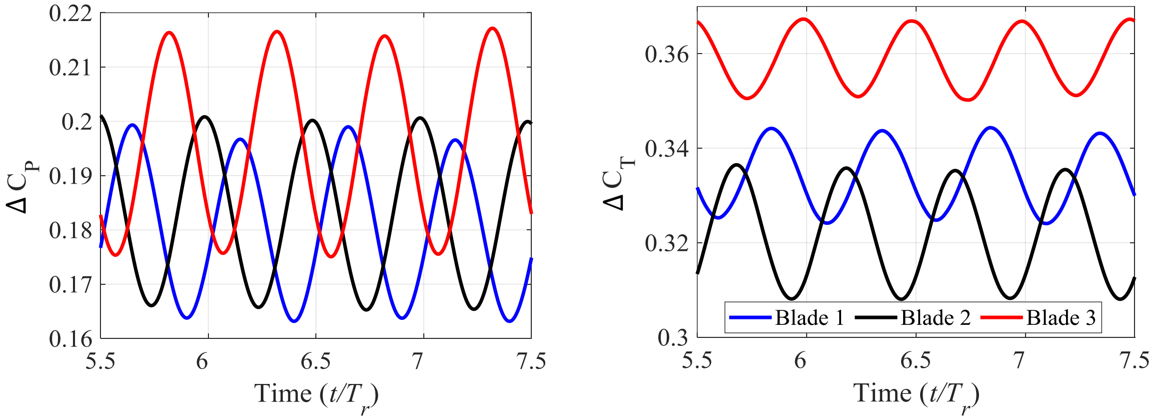

(b) $A^* = 0.10$

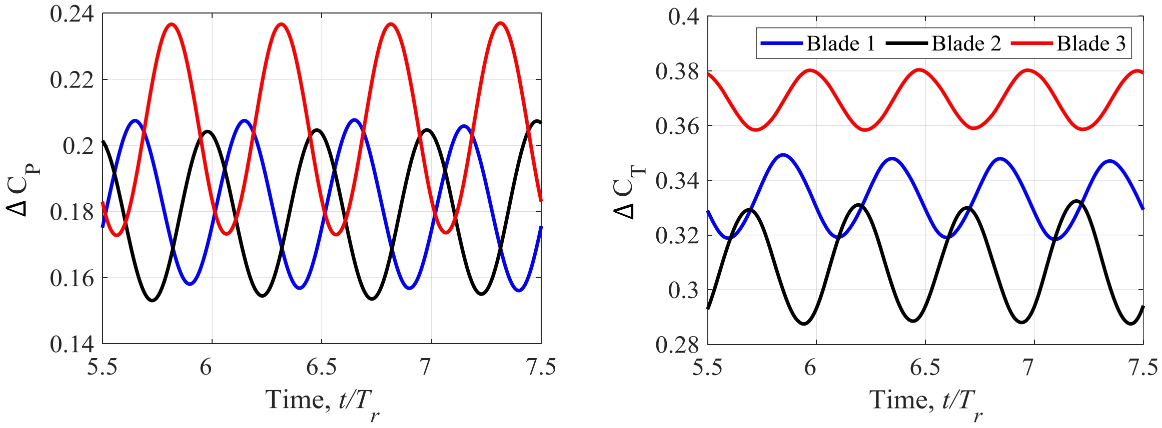

(c) $A^* = 0.15$

Figure 4-7 Individual blade loading time histories for a floating tidal turbine undergoing heave motion at a frequency ratio $\omega^* = 1.0$ at $\lambda = 4.4$.

When we compare the thrust and power coefficients of individual blades in Figure 4-7, they are about ~180° out of phase with one another (compare each blade's C_P and C_T, labelled

ΔC_P and ΔC_T). Since all blades exhibit the same characteristics for all A^* cases, let us focus on blade 3 at $t/T_r = 7.0$ (T$_8$). ΔC_T shows maximum value while ΔC_P is close to the minimum. For a heaving turbine, the torque on the blade which enters the advancing phase will increase due to the skewed inflow, which contains the vertical inflow velocity component U_Z, see Figure 4-8. However, when the heaving angle γ becomes zero (i.e. inflow is in the horizontal direction, such as at positions T$_4$ and T$_8$), the instantaneous inflow velocity only has the horizontal component ($U_Z \approx 0$). This increases the thrust while reduces the torque on the blade. Looking at the spanwise force profiles of blade 3 in Figure 4-9, it experiences an advancing phase at T$_6$ while neutral ($\gamma \approx 0; U_Z \approx 0$) at T$_8$. The thrust is reduced while the torque (represented by the tangential force along the blade) is increased at T$_6$, and the opposite characteristic occurs at T$_8$. The opposite trend can be seen for blade 2 when comparing T$_6$ and T$_8$ since blade 2 almost always experiences the retreating phase. Therefore, it is the skewed instantaneous inflow experienced by the heaving turbine that is causing the thrust and power (torque) to shift phases with one another.

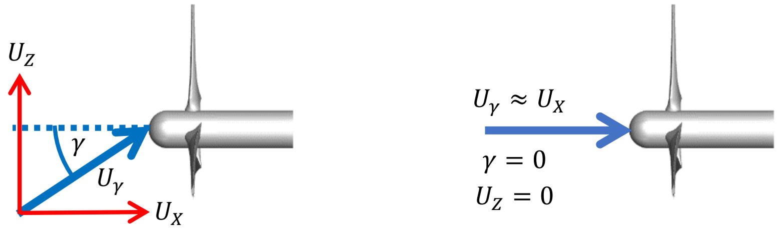

(a) (b)

Figure 4-8 Flow velocity condition at (a) T$_6$ and (b) T$_8$. γ is the heave angle, U_γ is the instantaneous inflow velocity, U_X and U_Z are horizontal and vertical inflow velocity components, respectively.

A yawed turbine will experience the "yaw stabilizing moment" effect where the blade in the advancing phase will have an increase in loading at the outer region (near to tip) and decrease at the inner region (near to root), while the blade in retreating phase will have the opposite effect (Schepers, 1999; Schulz et al., 2017). From a simple perspective, this behaviour implies that the rotor tries to rotate so that the yawed inflow will become normal to the rotor plane (see Figure 4-2(c)). For a heaving turbine moving from T_8 to T_4, the rotor is experiencing something similar. In Figure 4-9, the loading characteristic of a heaving turbine is slightly different from the stationary turbine. Only the A^* = 0.15 case is presented here although all heave amplitude cases exhibit similar trend. For blade 3, which always experience the advancing phase in the case of ω^* = 1.0, the loading is slightly higher towards the blade tip and slightly lower towards the blade root (around $r/R =$ 0.80 and 0.35, respectively). For blade 2, which experienced the retreating phase most of the time, the loading behaviour is the opposite of blade 3. The loading is slightly lower towards the blade tip and slightly higher towards the blade root. Similar trends have been shown in Yu et al. (2013) and Schulz et al. (2017) for a static yawed turbine, where the loading is higher around the blade root and lower at the blade tip when blades are in the retreating phase while opposite behaviour is observed for the advancing phase.

Looking at the velocity magnitude contour plots in Figure 4-10, the intensity of the local flow velocity is higher at $r/R =$ 0.80 and lower at $r/R =$ 0.35 for blade 3 which experience the advancing phase. For blade 2, which is in the retreating phase, the local flow velocity is higher near the blade root and lower towards the blade tip ($r/R =$ 0.35 and 0.80, respectively). These results show the characteristics of yaw stabilizing moment, which occurs due to the advancing and retreating effect from the dynamic yawing inflow. A similar trend has been shown in the study of Schepers (1999) for a static yawed turbine where at the inboard region (around blade root), the local velocity is higher and lower for the retreating and advancing phases, respectively, and the opposite result is shown for the outboard region. However, the effect is not significant for the present study for two reasons: small heave amplitudes were used, and this is an oscillating turbine case where the yaw (or rather, heave) angle changes quickly.

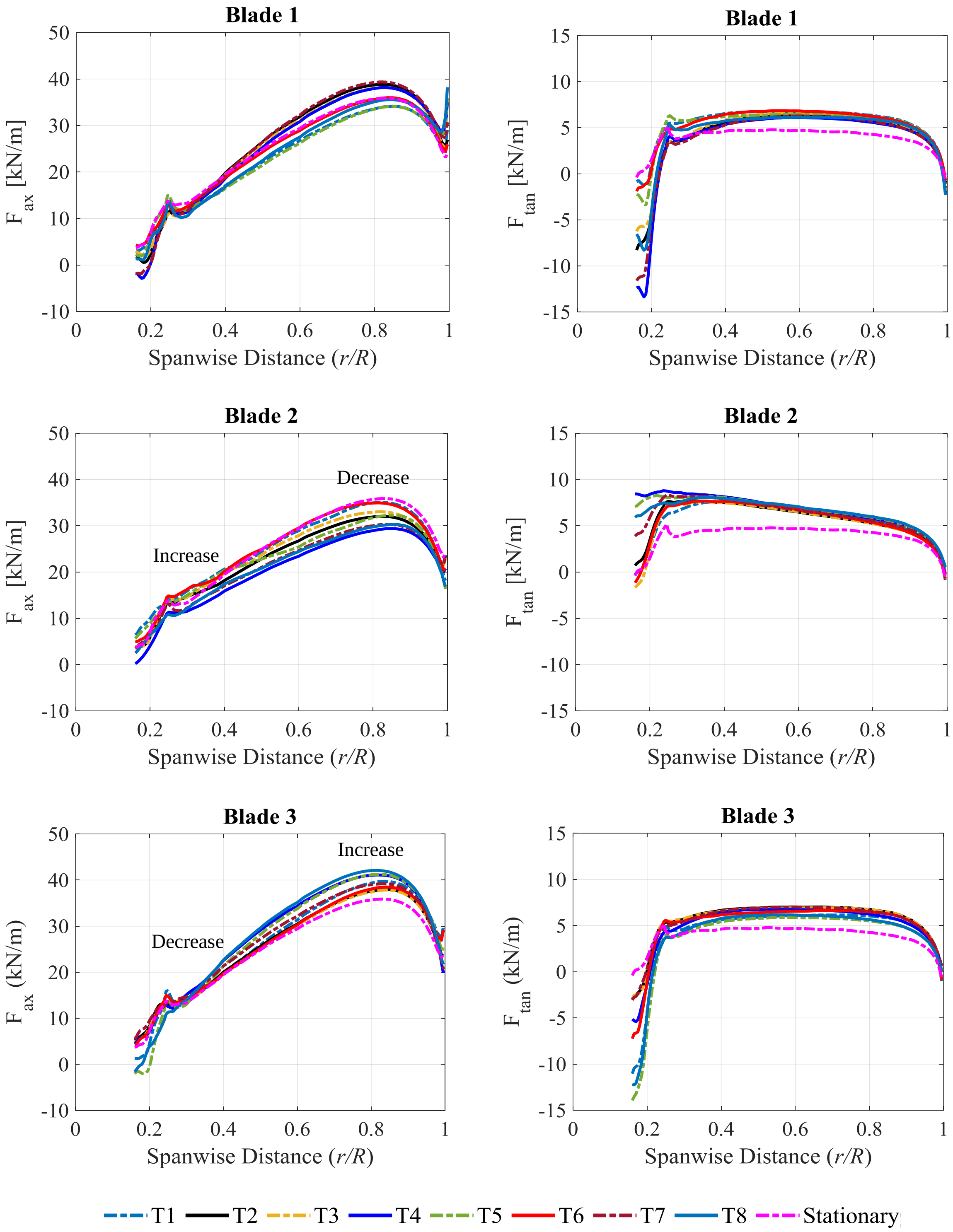

Figure 4-9 Force profiles of a floating tidal turbine undergoing heave motion at $A^{*} = 0.15$.

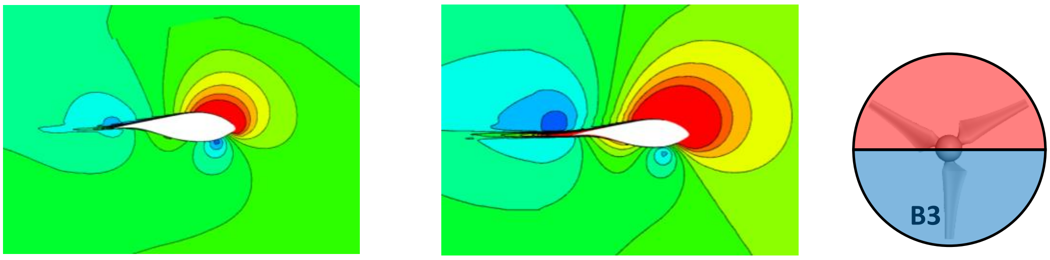

(a) Blade 3, $r/R = 0.35$ at T_7 (b) Blade 3, $r/R = 0.80$ at T_7

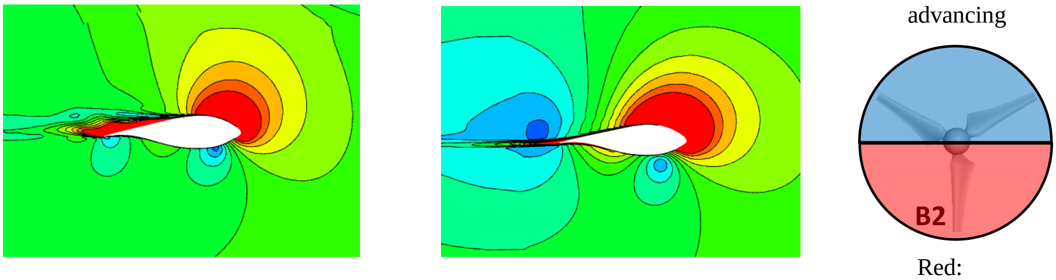

(c) Blade 2, $r/R = 0.35$ at T_1 (d) Blade 2, $r/R = 0.80$ at T_1

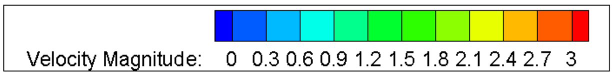

Figure 4-10 Contour plots of velocity magnitude at T_1 and T_7 for blades 2 and 3 cross-sections, respectively, at spanwise distance $r/R = 0.35$ and 0.8 for the case of $A^* = 0.15$.

Looking at the vortex iso-surface presented in Figure 4-4, at T_6, there is a vortex build-up behind blade 2 near the root region at the upper half of the rotor plane. This will increase the induced velocity u_i in this region (refer Figure 4-2 for induced velocity u_i), which causes the increase in the blade loading (Schepers, 1999). Same characteristic can be observed at T_2 but in the opposite (lower half of the rotor plane), which also occurs behind blade 2. In the axial force profiles of blade 2 in Figure 4-9, the loadings are slightly increased at T_2 and T_6 caused by the induced velocity near the blade root region (around r/R = 0.2 to 0.4). Blade 3 always experiences the advancing phase effect due to the heave frequency being the same as the rotor rotational speed. It can be observed that the vortex build-up does not occur (or occurs at a minimal magnitude that it can be neglected) behind blade 3 throughout the entire heave motion cycle. This explains the advancing phase load behaviour of blade 3 in Figure 4-9. On that same note, blade 2 can be observed to constantly experience the retreating phase effect since the vortex build-up always occurs behind this blade for the entire heave motion.

Based on the results presented so far (in this chapter), a heaving rotor experiences the advancing and retreating phases at the upper and lower half, respectively, when it moves in the upward direction. However, the transition from the retreating to advancing phases took place at T_8 when the vortex build-up starts to minimize at the upper side and occurred at the lower side of the rotor plane. This took place at T_4 for the downward motion. Besides this, it can be observed that the near wake skewness tends to neutralize around T_4 and T_8, although this is not significant. Therefore, for a dynamic yawing turbine (or rather, a heaving turbine), the advancing and retreating effect depends on the near wake behaviour as the changes occur at half a cycle of the motion at $\omega^* = 1.0$.

4.5 Effect of heave frequency on turbine performance

Figure 4-11 shows the time histories of a floating turbine undergoing heave motion at a different frequency $\omega^* = 0.7, 1.0, 1.3$ at fixed heave amplitude $A^* = 1.0$ and rotor rotational speed $\omega_r = 0.88$ rad/s. Loading variation increase as the frequency is increased. However, the amplitude of variation reduces as the heave frequency goes above the resonant point (at $\omega^* = 1.3$). The C_P magnitude increase while the C_T magnitude decreases as the heave frequency are increased (see Table 4-2). A similar trend can be seen here as the various heave amplitude cases presented in the previous sub-chapter, which is expected since the motion amplitude will also increase as the frequency is increased.

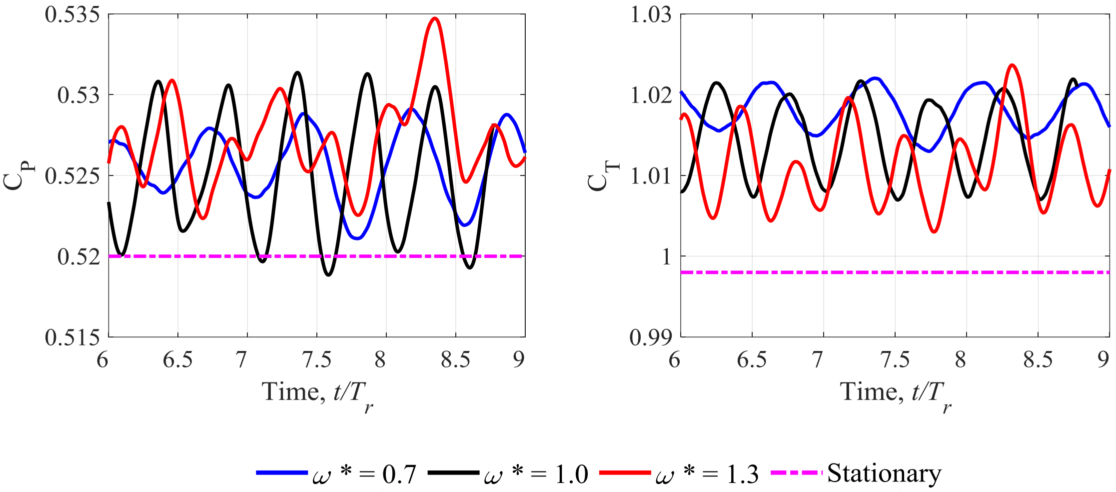

Figure 4-11 Power and thrust coefficients time histories of floating tidal turbine undergoing heave motion at ω^* = 0.7, 1.0, 1.3 with A^* = 0.1 and λ = 4.4.

Figure 4-13 shows the force profiles of a floating tidal turbine undergoing heave motion at a different frequency $\omega^* = 0.7$ and 1.3. The time step markers (T_1 to T_{10} and T_1' to T_{10}') were given in Figure 4-12, showing the rotor heave position and azimuth position of each blade. At time step T_7 and T_7' (see Figure 4-13a), theoretically, blade 1 is experiencing the retreating phase while blades 2 and 3 are in the advancing phase. And looking at the displacements between the two cases, they are not far apart from one another. Therefore, this is a fair comparison for transient simulations conducted in the present study. The same consideration can also be observed for time steps T_3 and T_5' (see Figure 4-13b). Based on force profiles of blades 1 and 3 at time step T_7 and T_7', these two ω^* cases show different effects. For blade 1, $\omega^* = 0.7$ is having the retreating effect while $\omega^* = 1.3$ is having the advancing effect. For blade 3, $\omega^* = 0.7$ is having the advancing effect while $\omega^* = 1.3$ is having the retreating effect. The same pattern can also be observed for time steps T_3 and T_5' when comparing blades 3 to 2 ($\omega^* = 0.7$ and 1.3, respectively) and blades 2 to 1 ($\omega^* = 0.7$ and 1.3, respectively). Results of $\omega^* = 1.3$ is the exact opposite from the theoretical hypothesis that were made earlier. As explained in previous sub-chapter, this is the transient effect of a heaving turbine where the formation of the advancing and retreating phases are lagging compared to the motion at higher heave frequency.

Table 4-2 Mean percentage difference of power and thrust coefficients between the heaving and stationary turbines.

ω^*	$\bar{C}_P$	$\bar{C}_T$	Percentage difference $\bar{C}_P$ [%]	Percentage difference $\bar{C}_T$ [%]
0.7	0.5249	1.0177	0.93	1.93
1.0	0.5251	1.0143	0.97	1.61
1.3	0.5281	1.0121	1.53	1.39
Stationary	0.520	0.998	-	-

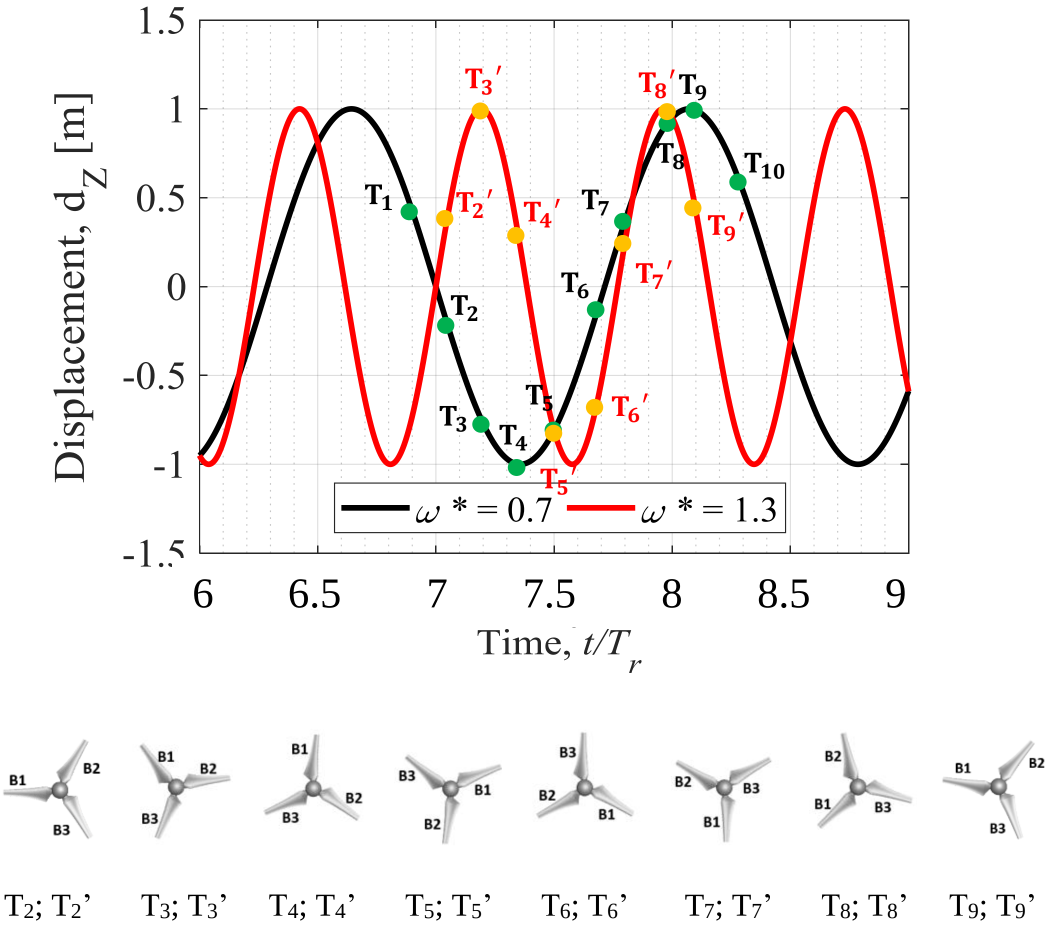

Figure 4-12 Displacements of a heaving turbine at $\omega^* = 0.7$ and 1.3. Bottom figures show azimuth positions at different time steps.

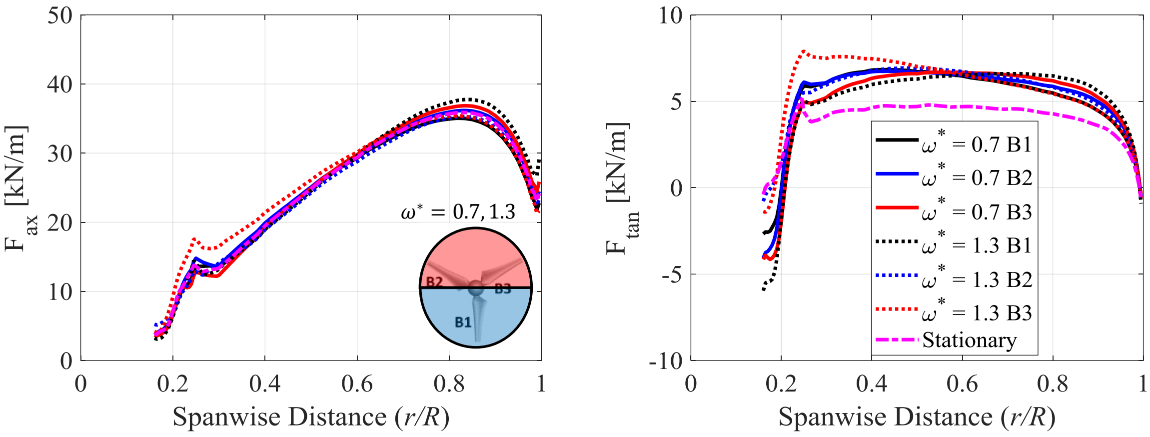

(a) T_7 and T_7' (t = 53 s and 53 s)

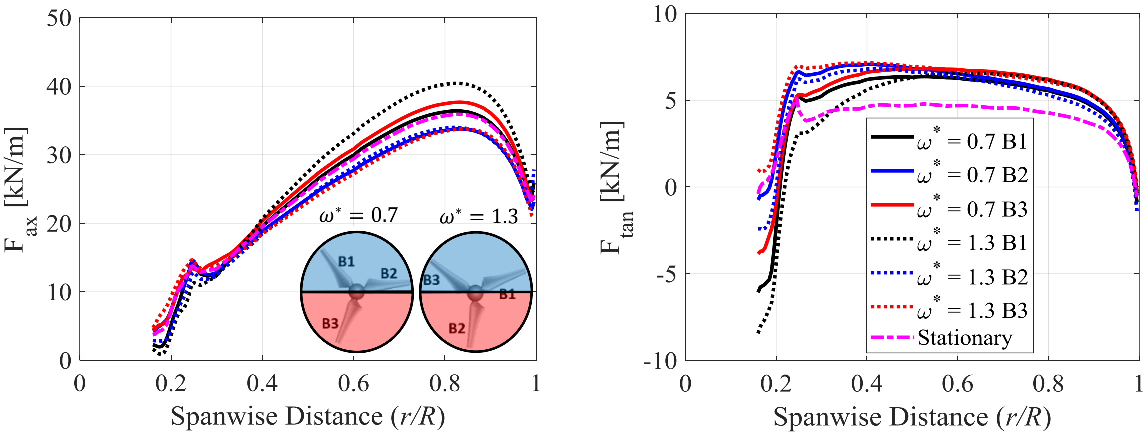

(b) T_3 ($\omega^* = 0.7$) and T_5' ($\omega^* = 1.3$) (t = 49 s and 51 s)

Figure 4-13 Force profiles at different time steps for a floating tidal turbine undergoing heave motion at $\omega^* = 0.7$ and 1.3. Rotor figures: blue is retreating, and red is advancing.

Studies conducted by Yu et al. (2013) and Schulz et al. (2017) on stationary turbines under yawed inflow condition shows that rotor blade loading will increase when it enters the advancing phase and vice versa for the retreating phase. Looking at the individual blade loading time histories presented in Figure 4-14 for the lower frequency case, at time step T_7, the load on blade 1 decreases while blade 3 is increasing, showing that they are experiencing retreating and advancing effects, respectively. However, for the higher frequency case, at time step T_7' blade 1 is increasing while blade 3 is decreasing, showing that they are experiencing advancing and retreating effects, respectively, which is the opposite of what happens to the lower frequency case. These results correspond to the force profiles shown previously, confirming that the advancing and retreating effect formation has a phase lag at high heave frequency. The same trend can also be observed for time steps T_3 and T_5’ when comparing blades 3 to 2 ($\omega^* =$ 0.7 and 1.3, respectively) and blades 2 to 1 ($\omega^* =$ 0.7 and 1.3, respectively).

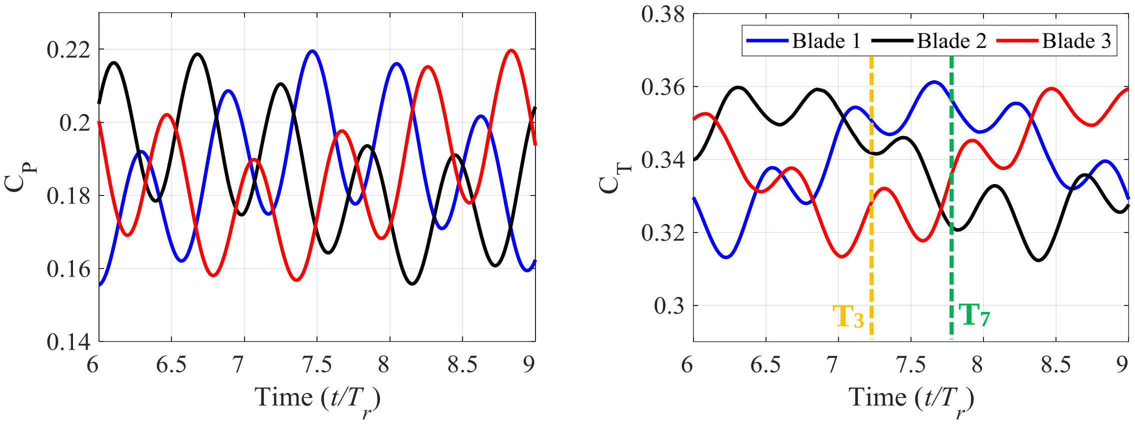

(a) ω^* = 0.7

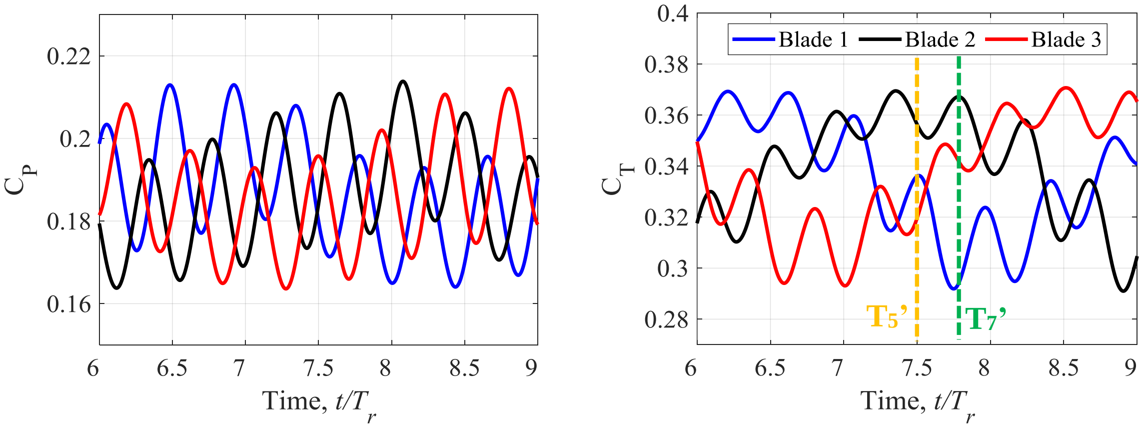

(b) ω^* = 1.3

Figure 4-14 Individual blade loading time histories for a floating tidal turbine undergoing heave motion at constant amplitude A^* = 0.1 and λ = 4.4.

Cross-sections of vorticity magnitude flow field at 0.1D and 0.5D downstream from the rotor plane were presented in Figure 4-15 for the case of $\omega^* =$ 0.7 and 1.3. We can see that the vortex is skewed at the near wake, similar to that of a fixed yawed turbine. Although not shown here, the wake skewness does not extend until the far wake, unlike a fixed yawed turbine, due to the transient nature of dynamic heaving/yawing inflow. At T_7 and T_7’, the rotor is moving upward. It is expected that the wake will be skewed downward. Even though the lower frequency case ($\omega^* = 0.7$) agrees with this hypothesis, the wake skewness of the higher frequency case shows the exact opposite where the wake is skewed upward. As explained previously, this happens due to the rotor heaving too fast for the wake vortex to be properly developed at the expected time step (or expected heave position), thus experiencing a phase lag. The same trend is also shown at T_3 and T_5’.

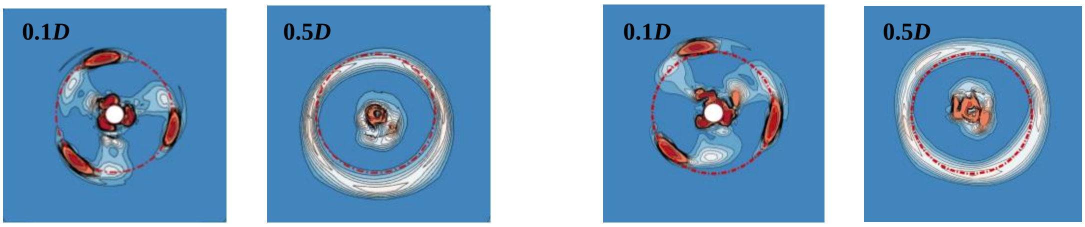

(a) T_7 (b) T_7’

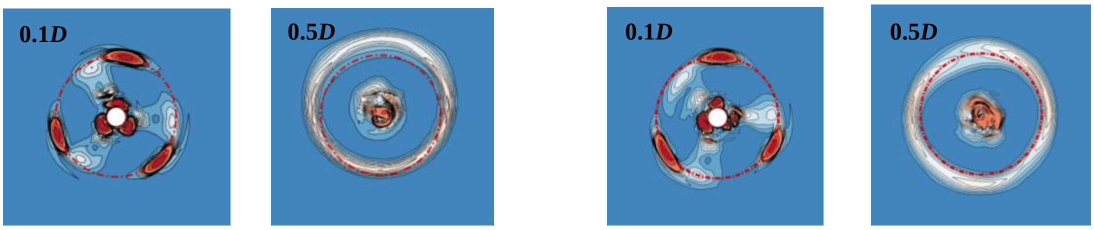

(c) T_3 (d) T_5’

Figure 4-15 Vorticity magnitude (view from upstream) of a floating turbine undergoing an upward heave motion at $\omega^* = 0.7$ (a, c) and 1.3 (b, d). The cross sections, from left to right, are 0.1*D* and 0.5*D* downstream from the rotor plane. The red dashed circular line is the rotor swept area location.

4.6 Effect of rotor rotational speed on a heaving turbine

Figure 4-16 shows the time histories of a floating turbine undergoing heave motion at three rotational speeds at constant heave amplitude $A^* = 0.1$ and frequency $\omega_0 = 0.88$ rad/s. The magnitude of C_T increase as the rotational speed is increased. However, the C_P of $\omega_r = 0.96$ rad/s shows little difference from that of 0.88 rad/s case (refer Table 4-3). For a stationary rotor, it was found that the highest C_P occurs at tip speed ratio $\lambda = 4.4$ (refer Figure 2-8a in Chapter

2), which corresponds to ω_r = 0.88 rad/s and it continues to drop as λ is increased. The C_T however, keep on increasing as the tip speed ratio is increased. Note that for the steady-state simulation results presented in Chapter 2, the tip speed ratio was increased by increasing the rotor rotational speed. Therefore, the results shown in Figure 4-16 is a typical result of a rotor with different operating rotational speeds. In this case, the heave motion does not significantly impact the loading magnitude other than giving a minor fluctuation.

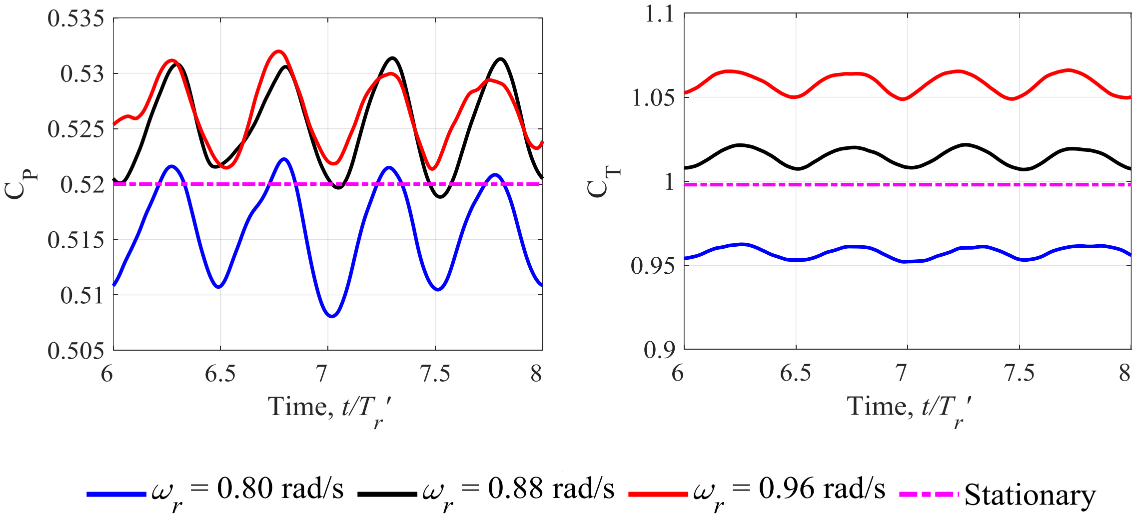

Figure 4-16 Power and thrust coefficients time histories of floating tidal turbine undergoing heave motion at rotor rotational speed ω_r = 0.80, 0.88, 0.96 rad/s with constant A^* = 0.1 and ω_0 = 0.88 rad/s.

Figure 4-17a presents the time histories of power and thrust coefficients of blade 1 at the rotational speed ω_r = 0.96 rad/s of a floating tidal turbine heaving at an amplitude $A^* = 0.1$ and frequency $\omega_0 = 0.88$ rad/s. Looking at both time histories, there are at least two different frequencies for each plot. By plotting the frequency spectrum of C_P using Fast Fourier Transform given in Figure 4-17b, two frequencies are presented which are the frequency of the heave motion and the rotor rotational speed (f = 0.07 and 0.15 Hz, respectively). For the heave frequency, f = 0.07 Hz shows half the motion frequency value. This happens because C_P oscillates twice per heave motion cycle. When the rotor moves from bottom to top position (half a cycle), the loading fluctuation of C_P and C_T completes one cycle. If we compare Figure 4-3 to Figure 4-6 and Figure 4-11 to Figure 4-12, all cases show that one loading cycle (C_P and C_T time histories) is completed within half a cycle of the heave motion. Although not presented here, ω_r = 0.80 rad/s have a similar trend as ω_r = 0.96 rad/s with different frequencies.

Table 4-3 Mean percentage difference of power and thrust coefficients between the heaving and stationary turbines. The negative sign shows the heave cases are lower than the stationary case.

ω_r [rad/s]	$\bar{C}_P$	$\bar{C}_T$	Percentage difference $\bar{C}_P$ [%]	Percentage difference $\bar{C}_T$ [%]
Heave 0.80	0.5156	0.9583	-0.46	1.28
Heave 0.88	0.5251	1.0144	0.97	1.62
Heave 0.96	0.5263	1.0579	0.06	2.07
Stationary 0.80	0.518	0.946	-	-
Stationary 0.88	0.520	0.998	-	-
Stationary 0.96	0.526	1.036	-	-

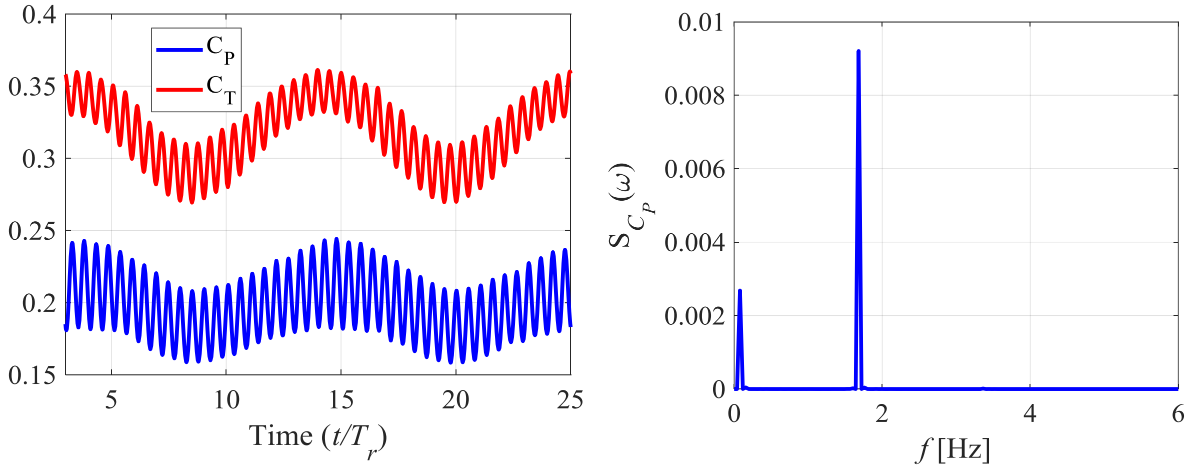

(a)

(b)

Figure 4-17 (a) Power and thrust coefficients time histories of blade 1 for the case of ω_r = 0.96 rad/s. (b) Power coefficient frequency spectrum.

4.7 Conclusion

This chapter presents the findings of the present study for a floating tidal turbine undergoing a heave motion over a range of motion amplitude and frequency, and also different rotor rotational speeds. In conclusion, a floating tidal turbine undergoing heave motion exhibit similar characteristics as a dynamic yawing turbine. The upper half of the rotor experience an advancing phase while the lower half is experiencing the retreating phase while the rotor moves in the upward direction (similar to a yawed turbine), and the effects were reversed when it moves downward.

There is a phase lag of the wake skewness formation, advancing and retreating effects, and the stabilizing moment effect which shows the transient effect of a floating tidal turbine undergoing a heave motion, and the effect is more significant as the heave frequency is increased.

The loading variation amplitude increases as we increase the heave amplitude and frequency, which is typical for a turbine undergoing a heave motion (or dynamic yawing inflow). However, since the parameter space considered in this study is small, the loading variation is not that significant between the cases. Individual blade loading shows phase shifts between each blade and between ΔC_P and ΔC_T. For the former, this happens due to the azimuthal variation affecting the loading. For the latter, this happens due to the variation in the instantaneous skewed inflow which causes the torque and thrust to vary.

Chapter 5

Added mass and damping coefficients

One of the main objectives of the present study is to determine the added mass and damping coefficients that can be used in the fully coupled model. This chapter presents the derivation and calculation of the hydrodynamic coefficients: added mass and damping. The first part explains the derivation of the hydrodynamic forces in phase with the velocity and acceleration of the rotor for surge, heave, and pendulum motions. The second part presents the added mass and damping forces and why these forces cannot be neglected.

5.1 Hydrodynamic forces

We seek to express the fluctuating thrust force, $F_{T,i}(t)$, experienced by a floating turbine undergoing surge, heave, and pendulum motions as the sum of components in phase with the turbine's acceleration and velocity, $F_{TA,i}(t)$ and $F_{TV,i}(t)$ respectively. Thus, we write

$$F_{T,i}(t) \approx \bar{F}_{T,i} + F_{TA,i}(t) + F_{TV,i}(t) \qquad (5.1)$$

where $\bar{F}_{T,i}$ is the mean force component, $F_{TA,i}(t)$ and $F_{TV,i}(t)$ are components in phase with the turbine's fluctuating acceleration and velocity, through which we approximate the dynamic forces experienced by the turbine. The subscript i = 1, 3, 5 refers to the motion surge, heave, and pendulum, respectively (refer to Figure 5-1 for 6 DoF). From the CFD data, it is evident that the dynamic force components are complex. However, as shown in the spectrum of the thrust of the oscillating turbine (in Figure 5-5 in Appendix A at the end of this chapter), the unsteady thrust is dominated by a component at the oscillation frequency. Hence, the leading order components can be approximated through components at the oscillation frequency that is in phase with the turbine's acceleration and velocity, and we, therefore, adopt this simplified approximation to the turbine's loading. In the following stages, we seek to evaluate $F_{TA,i}(t)$ and $F_{TV,i}(t)$, which can be accomplished by minimizing the residual that results from the approximation in equation 5.1.

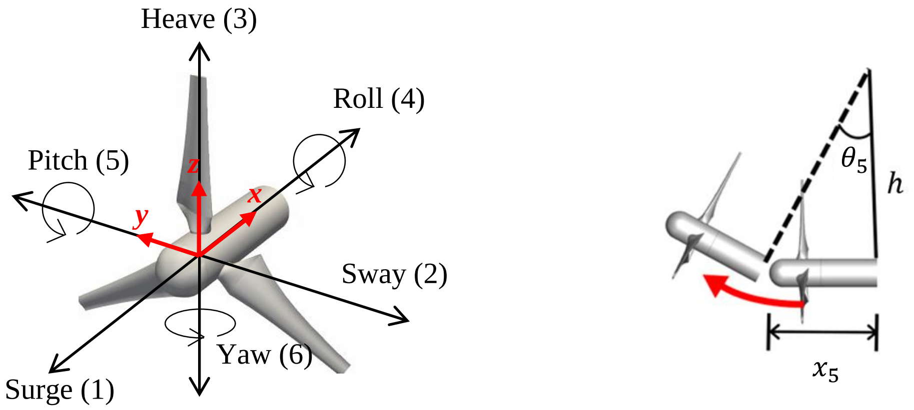

(a) 6 DoF motions

(b) Turbine in the pendulum motion

Figure 5-1 (a) Diagram of 6 DoF motions. Translational motion: surge, sway, and heave. Rotational motion: roll, pitch, and yaw. (b) A turbine moves forward in a pendulum motion, where h is the arm length from the rotor to the COR, θ_5 is the amplitude of the pendulum motion, and x_5 is the horizontal length of the pendulum motion.

Before going into the surge and heave motions, we need to address the condition for the pendulum motion since it is a rotational motion. To calculate the hydrodynamic forces on the floating turbine, we first approximate the amplitude of motion to include only the pendulum's horizontal (translational) motion (see Figure 5-1(b)). This approximation requires that angular motions remain small, which they do in the current investigation ($\theta_{5\,\max} \leq 3.0°$). Thus, we write

$$x_5(t) = h.\tan\theta_5(t)$$

where h is the rotational arm length from the centreline of the turbine nacelle to the centre of pendulum rotation. The pendulum motion is given as

$$\theta_5(t) = \hat{\theta}\sin(\omega_{0,5}t)$$

where $\hat{\theta}$ is the amplitude of motion in degrees and $\omega_{0,5}$ is the frequency of the pendulum oscillation. Therefore,

$$x_5(t) = h\tan(\hat{\theta}\sin(\omega_{0,5}t)).$$

Assuming small angles, we may then approximate

$$\theta_5(t) \approx \tan(\hat{\theta}\sin(\omega_{0,5}t))$$

and

$$x_5(t) \approx h\hat{\theta}\sin(\omega_{0,5}t)$$

which gives us the horizontal displacement, velocity, and acceleration as functions of time

$$x_5(t) \approx h\theta_5(t) \;\; ; \;\; \dot{x}_5(t) \approx h\dot{\theta}_5(t) \;\; ; \;\; \ddot{x}_5(t) \approx h\ddot{\theta}_5(t) \qquad (5.2)$$

in which ($\dot{\phi}$) and ($\ddot{\phi}$) indicate the time derivatives of variable (ϕ).

Considering the fluctuating components only from equation 5.1, we therefore write:

$$\tilde{F}_{T,i}(t) \approx \hat{F}_{A,i}\ddot{x}_i(t) + \hat{F}_V\dot{x}_i(t) \qquad (5.3)$$

where $\hat{F}_{A,i}$ and $\hat{F}_{V,i}$ are amplitudes of components in phase with the turbine motion's acceleration and velocity, respectively. Using the turbine thrust, velocity, and acceleration time histories from CFD simulations, $\hat{F}_{A,i}$ and $\hat{F}_{V,i}$ can be evaluated by minimizing the residual

$$\epsilon_i(t) = \tilde{F}_{T,i}(t) - \hat{F}_{A,i}\ddot{x}_i(t) - \hat{F}_{V,i}\dot{x}_i(t) \qquad (5.4)$$

To minimize the residual squared with respect to $\hat{F}_{A,i}$ and $\hat{F}_{V,i}$, we set the following conditions

$$\frac{\partial}{\partial \hat{F}_{A,i}} \int_{t_1}^{t_2} {\epsilon_i}^2 \, dt = 0 \qquad (5.5a)$$

$$\frac{\partial}{\partial \hat{F}_{V,i}} \int_{t_1}^{t_2} {\epsilon_i}^2 \, dt = 0 \qquad (5.5b)$$

where t_1 and t_2 are the limits of the analysis interval. Substituting equation 5.4 into the constraint equation 5.5, integrating in time, differentiating with respect to $\hat{F}_{A,i}$ and $\hat{F}_{V,i}$, and rearranging, it may be shown that:

$$\hat{F}_{A,i} = \frac{\langle \tilde{F}_{T,i}\ddot{x}_i \rangle \, \langle {\dot{x}_i}^2 \rangle - \langle \tilde{F}_{T,i}\dot{x}_i \rangle \langle \dot{x}_i\ddot{x}_i \rangle}{\langle {\dot{x}_i}^2 \rangle \langle {\ddot{x}_i}^2 \rangle - \langle \dot{x}_i\ddot{x}_i \rangle^2} \qquad (5.6a)$$

$$\hat{F}_{V,i} = \frac{\langle \tilde{F}_{T,i}\dot{x}_i \rangle \, \langle {\ddot{x}_i}^2 \rangle - \langle \tilde{F}_{T,i}\ddot{x}_i \rangle \langle \dot{x}_i\ddot{x}_i \rangle}{\langle {\dot{x}_i}^2 \rangle \langle {\ddot{x}_i}^2 \rangle - \langle \dot{x}_i\ddot{x}_i \rangle^2} \qquad (5.6b)$$

where $\langle \phi \rangle = \int_{t_1}^{t_2} \phi \, dt$ is the time integral of variable ϕ.

It is useful to express the thrust force in equation 5.1 in non-dimensional form by normalization with respect to the freestream dynamic pressure $\frac{1}{2}\rho {U_\infty}^2$ and the turbine area A_D. Therefore, we write the thrust coefficient of a turbine undergoing surge, heave, and pendulum motions as

$$C_{T,i}(t) = \frac{\bar{F}_{T,i}}{\frac{1}{2}\rho U_\infty^2 A_D} + \frac{\hat{F}_{A,i} U_\infty^2}{\frac{1}{2}\rho U_\infty^2 A_D h}\ddot{\eta}_i + \frac{\hat{F}_{V,i} U_\infty}{\frac{1}{2}\rho U_\infty^2 A_D}\dot{\eta}_i \qquad (5.7a)$$

$$C_{T,i}(t) = \bar{C}_{T,i} + C'_{A,i}\ddot{\eta}_i + C'_{V,i}\dot{\eta}_i \qquad (5.7b)$$

in which the non-dimensional parameters of the displacement, velocity, and acceleration of the surge, heave, and pendulum motions can be written as

$$\eta_{1,3} = \frac{x_{1,3}}{D} \quad ; \quad \dot{\eta}_{1,3} = \frac{\dot{x}_{1,3}}{U_\infty} \quad ; \quad \ddot{\eta}_{1,3} = \ddot{x}_{1,3}\frac{D}{U_\infty^2} \qquad (5.8a)$$

$$\eta_5 = \frac{x_5}{h} \quad ; \quad \dot{\eta}_5 = \frac{\dot{x}_5}{U_\infty} \quad ; \quad \ddot{\eta}_5 = \ddot{x}_5\frac{h}{U_\infty^2} \qquad (5.8b)$$

where D is the rotor diameter. Since $D = h = 20$ m, all calculations involving D will be written as h for convenience. Equation 5.7 represents the steady and dynamic non-dimensional thrust acting on the turbine, in which $C'_{A,i}$ and $C'_{V,i}$ represent the forces acting on the turbine in phase with the horizontal component of its acceleration and velocity. $C'_{A,i}$ and $C'_{V,i}$ can be evaluated by first evaluating $\hat{F}_{A,i}$ and $\hat{F}_{V,i}$ from equations 5.6, and then rearrangement of the above to yield:

$$C'_{A,i} = \frac{\hat{F}_{A,i}}{\frac{1}{2}\rho A_D h} \quad ; \quad C'_{V,i} = \frac{\hat{F}_{V,i}}{\frac{1}{2}\rho U_\infty A_D} \qquad (5.9)$$

The non-dimensional forces in phase with the turbine's acceleration and velocity, $C'_{A,i}$ and $C'_{V,i}$ respectively, together with the mean thrust coefficient $\bar{C}_{T,i}$ are presented in Figure 5-2 and Figure 5-3, respectively, over a range of motion amplitude A^* and frequency ω^*. In order to aid in interpretation of the variation of $C'_{A,i}$ and $C'_{V,i}$, it is instructive to consider the magnitudes of the non-dimensional velocity and acceleration. We note:

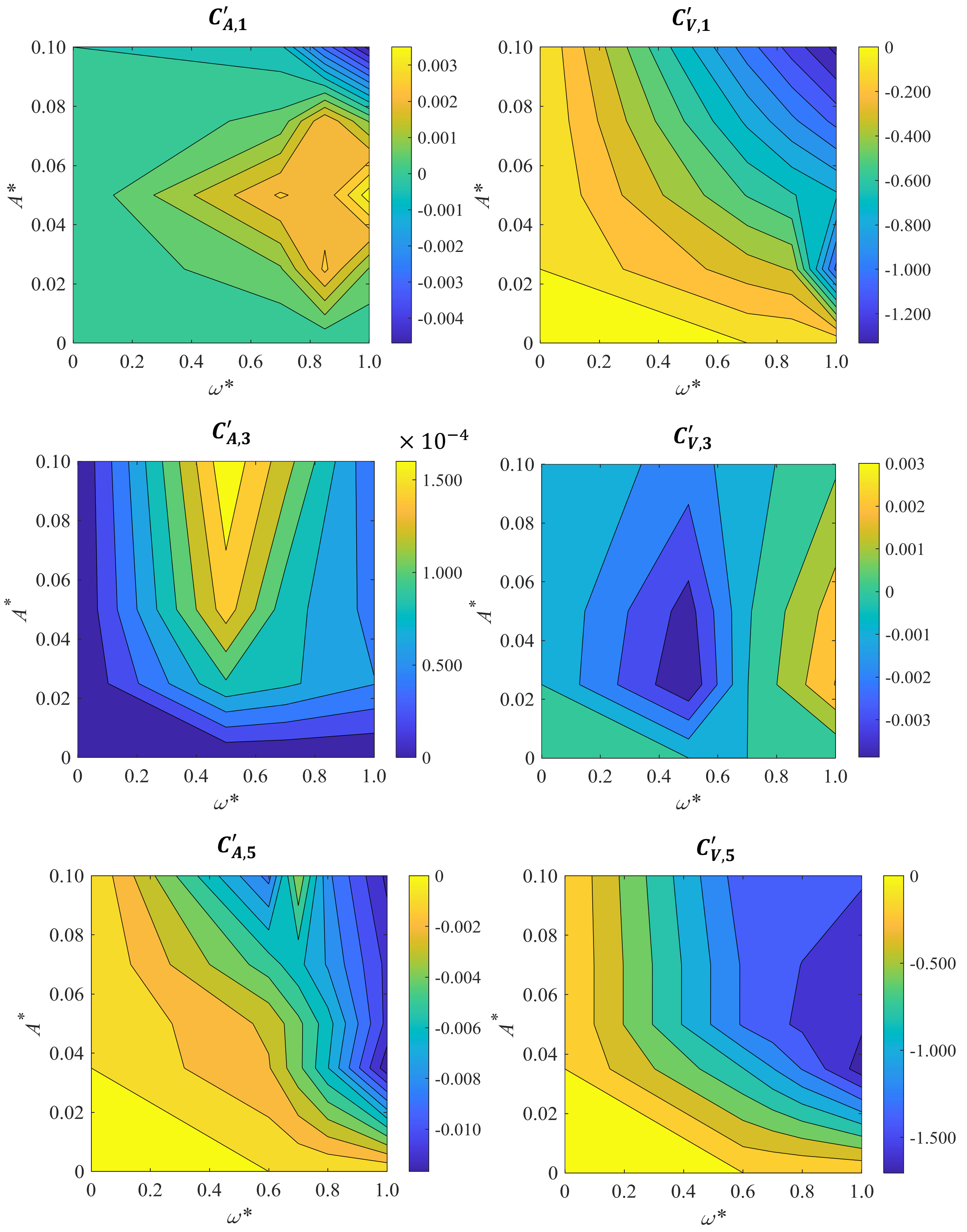

Figure 5-2 $C'_{A,i}$ and $C'_{V,i}$ contour plots over a range of motion amplitudes and frequencies, where $A^* = x_5/R$ for pendulum motion. Values of $A^* = 0.035$, 0.070 and 0.100 corresponds to $\hat{\theta} = 1.0°$, 2.0° and 3.0°, respectively, for pendulum motion.

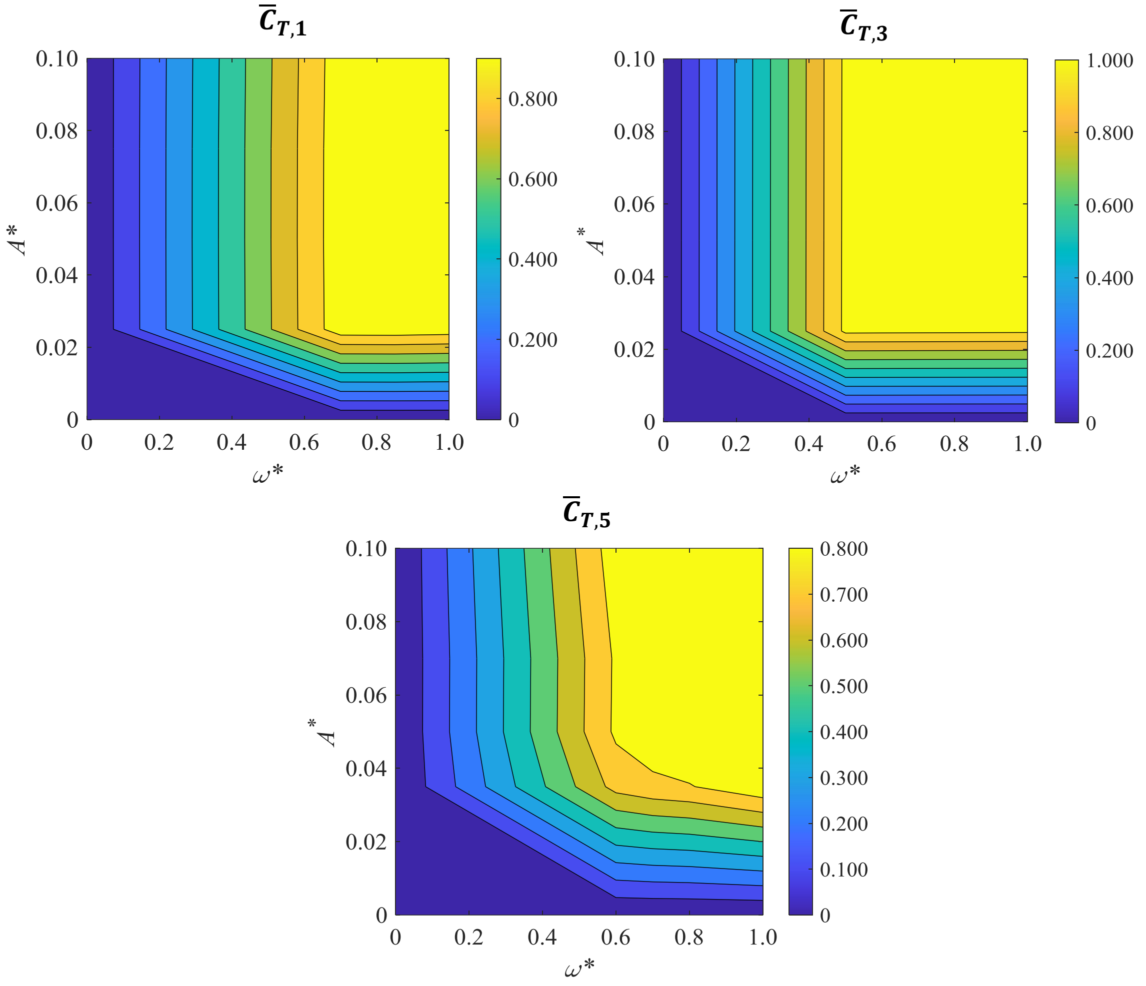

Figure 5-3 $\bar{C}_T$ contour plots over a range of motion amplitudes and frequencies, where $A^* = x_5/R$ for pendulum motion. Values of $A^* = 0.035$, 0.070 and 0.100 corresponds to $\hat{\theta} = 1.0°$, $2.0°$ and $3.0°$, respectively, for pendulum motion.

$$\dot{\eta}_{1,3} = \frac{A_{0\,1,3}\omega_0}{U_\infty}\cos(\omega_0 t) \quad ; \quad \ddot{\eta}_{1,3} = -\frac{DA_{0\,1,3}{\omega_0}^2}{U_\infty^2}\sin(\omega_0 t) \qquad (5.10a)$$

$$\dot{\eta}_P = \frac{h\hat{\theta}\omega_0}{U_\infty}\cos(\omega_0 t) \quad ; \quad \ddot{\eta}_P = -\frac{h^2\hat{\theta}\omega_0^2}{U_\infty^2}\sin(\omega_0 t) \qquad (5.10b)$$

and considering the range of amplitudes $A_{0,1}$ and $\hat{\theta}$, and frequency ω_0 considered in Figure 5-2 and Figure 5-3 for surge and pendulum motions, $|\ddot{\eta}_1|_{max} = 3.87$ and $|\dot{\eta}_1|_{max} = 0.44$, while $|\ddot{\eta}_5|_{max} = 4.05$ and $|\dot{\eta}_5|_{max} = 0.46$. Regarding the magnitude of each coefficient, magnitudes of $C'_{A,1}$ and $C'_{A,5}$ are observed to be small compared to $\bar{C}_{T,1}$ and $\bar{C}_{T,5}$, respectively. However, since both $|\ddot{\eta}_1|_{max}$ and $|\ddot{\eta}_5|_{max} > 1$, the added mass force could become quite significant and cannot therefore be neglected; we consider this further below by exploring the added mass dimensionally for both surge and pendulum motions. Magnitudes of $C'_{V,1}$ and $C'_{V,5}$ are significantly higher than $\bar{C}_{T,1}$ and $\bar{C}_{T,5}$, respectively. Although, both $|\dot{\eta}_1|_{max}$ and $|\dot{\eta}_5|_{max} < 1$, the unsteady force caused by the turbine's velocity of surge and pendulum motions are still significant and will add to the motion damping (as $C'_{V,1}$ and $C'_{V,5} < 0$), and must be included in a fully coupled model of the dynamics of a floating tidal turbine.

For the heave motion amplitude and frequency range of $A_{0,3}$ and ω_0 considered in Figure 5-2 and Figure 5-3, $|\ddot{\eta}_3|_{max} = 3.87$ and $|\dot{\eta}_3|_{max} = 0.44$. Regarding the magnitude of each coefficient, the magnitude of $C'_{A,3}$ is observed to be small compared to $\bar{C}_{T,3}$. Even though $|\ddot{\eta}_3|_{max} > 1$, the magnitude of $C'_{A,3}$ is very small at $O(10^{-4})$ that it can be neglected. The magnitude of $C'_{V,3}$ is significantly lower than $\bar{C}_{T,3}$. Since $|\dot{\eta}_3|_{max} < 1$, the unsteady force caused by the turbine's velocity of heave motion is considered to be very small and can be neglected in a fully coupled model of the dynamics of a floating tidal turbine.

5.2 Added mass and damping

To further explore the significance of the variation of these coefficients, we need to first substitute $C'_{A,i}$ and $C'_{V,i}$ into the turbine's equation of motion. We can represent the system of a floating tidal turbine attached to a compliant floating structure as a spring-damper model with some mass ($\mathcal{M}$), structural damping (δ), and stiffness (κ) due to the hydrostatic stiffness and mooring lines. The equation of motion can be expressed as

$$\mathcal{M}\ddot{x}_i + \delta\dot{x}_i + \kappa x_i = F_{T,i}(t) = \frac{1}{2}\rho U_\infty^2 A_D C_{T,i}(t) \qquad (5.11)$$

By substituting the non-dimensional displacement, velocity, and acceleration, and including the fluctuating force components into the above equation, it can be rewritten as

$$\mathcal{M}\left(\ddot{\eta}_i \frac{U_\infty^2}{h}\right) + \delta(\dot{\eta}_i U_\infty) + \kappa(\eta_i h) = \frac{1}{2}\rho U_\infty^2 A_D \left(\bar{C}_{T,i} + C'_{A,i}\ddot{\eta}_i + C'_{V,i}\dot{\eta}_i\right) \qquad (5.12)$$

We now seek to group terms relating to the turbine's acceleration and terms relating to its velocity and retain the steady forcing on the right-hand side.

$$\left(\mathcal{M}\frac{U_\infty^2}{h} - \frac{1}{2}\rho U_\infty^2 A_D C'_{A,i}\right)\ddot{\eta}_i + \left(\delta U_\infty - \frac{1}{2}\rho U_\infty^2 A_D C'_{V,i}\right)\dot{\eta}_i + \kappa(\eta_i h)$$
$$= \frac{1}{2}\rho U_\infty^2 A_D \bar{C}_{T,i} \qquad (5.13)$$

From the results presented in Figure 5-2 and Figure 5-3, it can be observed that both $C'_{A,5}$ and $C'_{V,5}$ are negative over the motion parameter space investigated. For $C'_{A,1}$ there is a mix of positive and negative values while $C'_{V,1}$ are all negative. When we relate this to equation 5.13, the first term on the left-hand side that includes the influence of $C'_{A,i}$, the turbine forcing in phase with its acceleration acts to increase (or decrease in the case of positive $C'_{A,1}$) the mass of the turbine. Similarly, in the second term on the left-hand side the influence of the turbine is in phase with the structural damping, as $C'_{V,i}$ is negative, thus increasing the overall damping of the system as the magnitude of $C'_{V,i}$ increases. Hence, the pendulum motion of the turbine is self-damping.

Finally, we seek a form of the equation of motion in which the added mass can be readily identified in its dimensional form. By substituting equations 5.8 into 5.13, we may write:

$$\left(\mathcal{M}-\frac{1}{2}\rho h A_D C'_{A,i}\right)\ddot{x}_i+\left(\delta-\frac{1}{2}\rho U_\infty A_D C'_{V,i}\right)\dot{x}_i+\kappa x_i=\frac{1}{2}\rho U_\infty^2 A_D \bar{C}_{T,i} \qquad (5.14a)$$

$$\left(\mathcal{M}+\mathcal{M}_{A,i}\right)\ddot{x}_i+\left(\delta+\delta_{A,i}\right)\dot{x}_i+\kappa x_i=\frac{1}{2}\rho U_\infty^2 A_D \bar{C}_{T,i} \qquad (5.14b)$$

in which the added mass ($\mathcal{M}_{A,i}$) and the added damping ($\delta_{A,i}$) are:

$$\mathcal{M}_{A,i}=-\frac{1}{2}\rho h A_D C'_{A,i}=-\hat{F}_{A,i} \qquad (5.15a)$$

$$\delta_{A,i}=-\frac{1}{2}\rho U_\infty A_D C'_{V,i}=-\hat{F}_{V,i} \qquad (5.15b)$$

When a submerged structure accelerates in a fluid, kinetic energy must be imparted to the surrounding fluid so that it moves with it. This ‘surrounding fluid’ can be thought of as an additional mass $\mathcal{M}_{A,i}$ that must be accelerated together with the structure. Based on the results presented in Figure 5-4 and equation 5.15, the added mass $\mathcal{M}_{A,i}$ increases as the motion amplitude and frequency are increased, and more mass must be accelerated with the turbine. It is instructive to note the magnitude of the added mass is $O(10^4)$ kg, which although smaller is not negligible compared to the mass of a typical commercial tidal turbine, circa 1.5×10^5 kg for a 20 m diameter turbine (SIMEC Atlantis Energy, 2016).

The fluid added mass acts to increase the actual mass of the system and reduce the system’s effective natural frequency. From equation 5.14b, we can see that the effective natural frequency ω_N of the combined fluid and structural system may be found from

$$\omega_{N,i}^2=\frac{\kappa}{\left(\mathcal{M}+\mathcal{M}_{A,i}\right)} \qquad (5.16)$$

From this relationship, the effective natural frequency squared is inversely proportional to the total effective mass ($\mathcal{M} + \mathcal{M}_{A,i}$) of the oscillating structure. Based on the results obtained from the CFD simulations, for which $\mathcal{M}_{A,i} > 0$, the effective natural frequency must be less than $\omega_n = \sqrt{\kappa/\mathcal{M}}$ which is the natural frequency of the structure alone. Further, we may write the ratio of natural frequencies as

$$\left(\frac{\omega_{N,i}}{\omega_n}\right)^2 = \left(1 + \mathcal{M}_{A,i}/\mathcal{M}\right)^{-1} \qquad (5.17)$$

So that if, for instance, in the pendulum motion case, we estimate $\mathcal{M}_{A,5}$ to be 10% of $\mathcal{M}$ (e.g., for $\hat{\theta} = 2.0°$ and $\omega^* = 0.8$, then $\mathcal{M}_{A,5} = 1.5 \times 10^4$ kg with an assumed turbine mass of $\mathcal{M} = 1.5 \times 10^5$ kg), then the effective natural frequency is reduced 5% below that without considering the turbine's added mass. Clearly, the added mass of the turbine allows a bandwidth of effective natural frequencies that would enable a turbine in the pendulum motion to resonate at frequencies up to 10% (for the parameter space investigated here $\mathcal{M}_{A,5} \leq 3.0 \times 10^4$ kg), below the structure's natural frequency. A similar estimation can be made for the surge motion case, although the effect will be the opposite for the negative $\mathcal{M}_{A,1}$.

It is instructive to rewrite equation 5.17 as

$$\left(\frac{\omega_{N,i}}{\omega_n}\right)^2 = \left(1 + C_{A,i}/m^*\right)^{-1} \qquad (5.18)$$

in which $C_{A,i} = \mathcal{M}_{A,i}/\rho V$ is the added mass coefficient and expresses the ratio between the fluid added mass and an effective displaced fluid mass of the rotor, and $m^* = \mathcal{M}/\rho V$ is the rotor's mass ratio which is likely around or a little greater than 1 as tidal turbines are designed to be neutrally buoyant or a little heavier than the water they displace. To define the displaced fluid mass, we choose a representative fluid volume as the rotor swept area multiplied by the streamwise thickness of the rotor. We take the thickness to be the axial projection of the rotor blade at its root (thickness $= c_{root} \sin \beta_{root}$; where c_{root} is the chord length at the blade root and β_{root} is the geometric twist angle at the blade root). The contour scale of $C_{A,i}$ is also included in Figure 5-4, with the variation in $C_{A,i}$ clearly being the same as that for $\mathcal{M}_{A,i}$ with different magnitude.

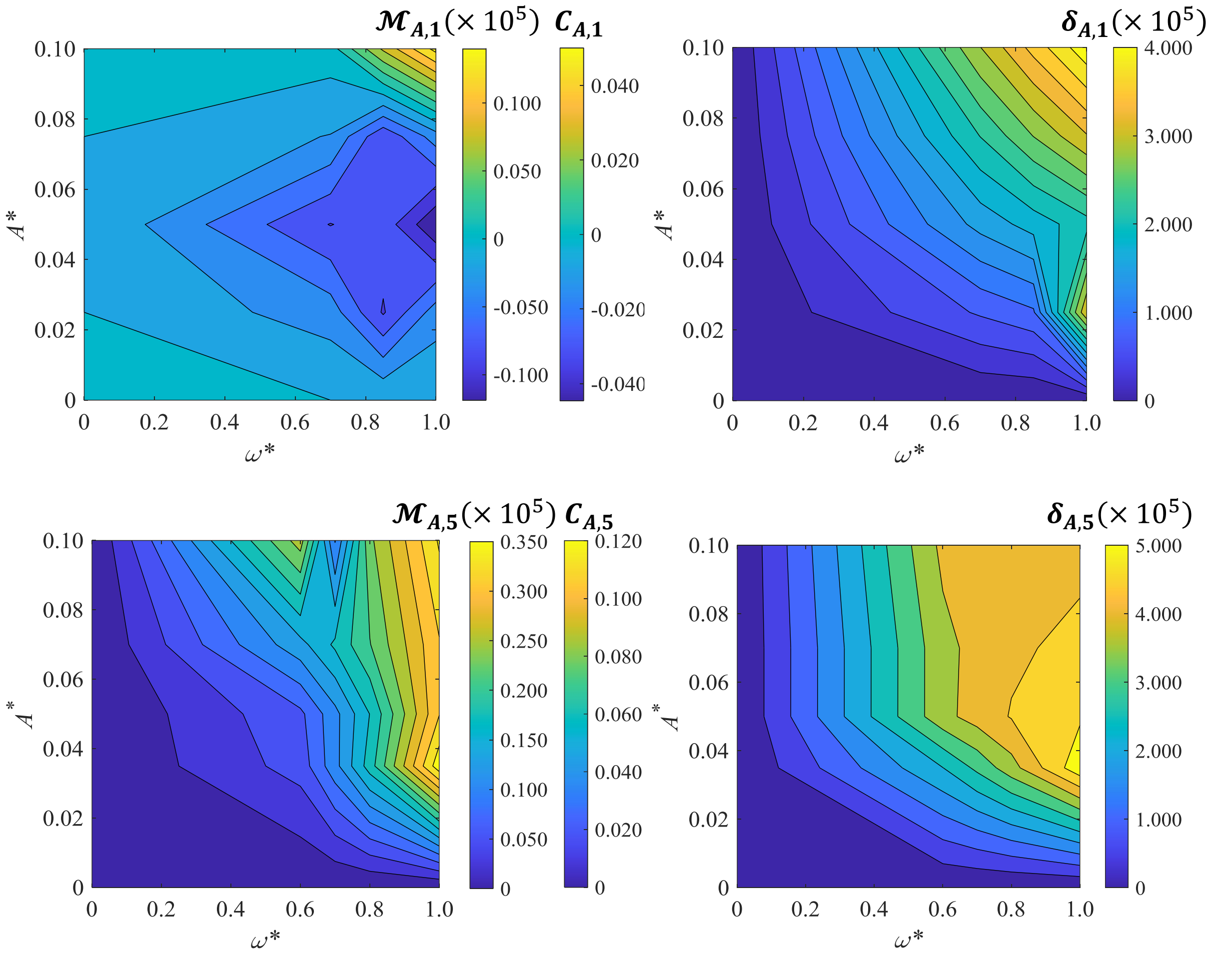

Figure 5-4 Added mass, $\mathcal{M}_{A,i}$, added mass coefficient, $C_{A,i} = \mathcal{M}_{A,i}/\rho V$, and hydrodynamic damping, $\delta_{A,i}$, contour plots over a range of motion amplitudes and frequencies for a floating tidal turbine undergoing surge and pendulum motions. Values of $A^* = 0.035$, 0.070 and 0.100 corresponds to $\hat{\theta} =$ 1.0°, 2.0° and 3.0°, respectively, for the pendulum motion.

For a body oscillating through a fluid, there is an additional hydrodynamic force, the added damping, that contributes to its unsteady loading. When a floating structure in otherwise still water is perturbed into motion, it will oscillate, and that oscillation will decay over time due to the damping forces within the system which act to extract energy from the body's motion. Based on the simulation results presented in Figure 5-4 and equation 5.15, the added damping $\delta_{A,i}$ increases as the amplitude and frequency of pendulum motion are increased. This demonstrates that the surrounding fluid acts to damp the turbine's motion, and further that the magnitude of this hydrodynamic damping generally increases with motion frequency and amplitude. Thus, we expect that the surge and pendulum motions of a turbine will be naturally damped and, therefore, stable.

Similar trends in the variation of the added mass and damping are shown in the studies of Jing et al. (2017) and Wang et al. (2017) for a floating tidal turbine oscillating in prescribed surge and roll motions. The variation of $\mathcal{M}_{A,i}$ and $\delta_{A,i}$ through the oscillation parameter space will be used to model the fluctuating force components of a fully coupled model of a floating tidal turbine in later analysis presented in the next chapter.

5.3 Conclusion

In conclusion, the added mass and damping forces of a floating tidal turbine undergoing prescribed motions were extracted and detailed derivations are provided in this chapter. Contour plots of the hydrodynamic forces were plotted and based on the data trend, it is possible to construct functions to calculate the added mass and damping forces as functions of the motion amplitude and frequency, which theoretically can be readily applied to a conventional model, such as the BEMT. This should be the main focus of future work for the author. The importance of added mass and damping on a floating tidal turbine were shown in this chapter. It was estimated that the added mass would be around 10% of the turbine mass which acts to increase the overall mass of the rotor, while the introduction of the added damping will increase the overall damping of the entire system which therefore will be affecting the motion (and thus, loading) of the floating turbine.

Appendix A

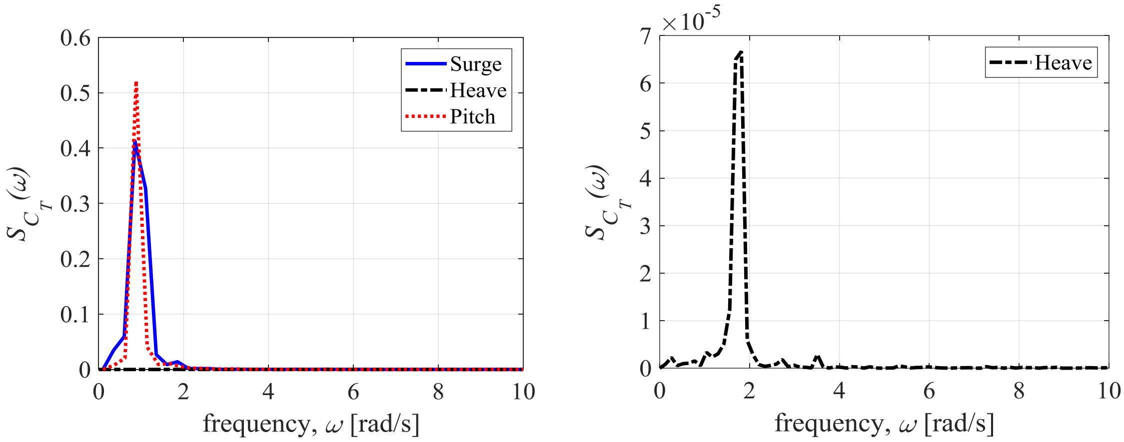

Figure 5-5 Frequency spectra of thrust coefficients of a floating turbine undergoing surge, heave, and pendulum (pitch) motions oscillating at $A^* = 0.1$ and $\omega^* = 1.0$. The spectra of surge and pitch motion cases show the peak occurs at the motion frequency (~0.88 rad/s). For the heave motion case this occurs at ~1.76 rad/s, which happen because of the double oscillation within one motion cycle, as explained in Chapter 4.

Chapter 6

Multi-degree of freedom model of a floating tidal turbine

6.1 Introduction

A fully coupled dynamic model is essential to simulate a floating offshore tidal turbine in understanding the multi-degree of freedom (multi-DoF) effect on the device's performance. In addition to this, an actual floating turbine operates under this condition rather than a single DoF motion. Therefore, it is considered better to simulate as close to the actual condition as possible. Previous studies, such as Vaal et al. (2006), Micallef & Sant (2015), Jing et al. (2017), and many others, have investigated the uncoupled motion of floating offshore turbines. For example, Guo et al. (2018) developed a model that couples the support platform's motion to the floating offshore tidal turbine. They calculated the 6-DoF motion from the support platform and used it as inputs to a BEMT model to calculate the turbine's aerodynamic based on these motions. However, they did not input the turbine load back into the system dynamic model, making it an uncoupled model.

Liu et al. (2017) developed a 3-DoF fully coupled model for a floating offshore wind turbine. They use the sliding mesh method to model the pitch motion while deforming the outer domain mesh to simulate surge and heave motions. Although this method is considered to be effective in modelling a floating offshore turbine, the high computational cost is needed to run simulations using both sliding mesh and deforming mesh methods at the same time while running a blade resolved simulation. Furthermore, high mesh volume is needed to consider the water surface region, especially around the support platform. It is crucial to develop a computationally cost-effective model while maintaining most of its accuracy. This is because researchers and engineers need to be able to run routine simulations for dynamic and transient cases, such as floating tidal turbines operating under various sea conditions, without sacrificing more time.

The NREL FAST code, first developed by Jonkman et al. (2007), is an all-around wind turbine code that can model the combined aero-hydrodynamic of a floating turbine operating under waves. FAST uses the Blade element momentum theory (BEMT) to calculate the turbine loading, which is widely considered a good theory to model a turbine even though it neglects the radial component effect. However, FAST code did not include the added mass since the code is developed primarily for wind turbine applications (see Murray et al. (2018) for more detail), for which the added mass effect can be neglected due to the low fluid density of air. However, this assumption cannot be accepted in modelling a tidal turbine since the fluid density is relatively high. To put this into perspective, we assume the turbine mass $\mathcal{M} = 1.5 \times 10^5$ kg. We then define the displaced fluid mass as ρV, where ρ is the fluid density (kg/m^3) and V is the displaced fluid volume (m^3). The displaced volume is assumed to be the rotor swept area multiplied by the thickness of the rotor. The thickness can be calculated as $t_R = c_{root} \sin \beta_{root}$; where c_{root} is the chord length at the blade root and β_{root} is the geometric twist angle at the blade root. The rotor's mass ratio $m^* = \mathcal{M}/\rho V$ to water is around 0.7 while to air is 590. The percentage difference is more than 100% between the two displaced fluid masses. And note that in the previous chapter, the added mass is estimated to be around 10% of the rotor mass, which is quite high considering a 20 m diameter rotor. Therefore, the added mass cannot be neglected as it is deemed critical to the force calculation on a floating tidal turbine. The added damping is also an important coefficient that needs to be considered since they are a magnitude higher than the added mass, as shown in the previous chapter.

Lake et al. (2021) collected field data on a floating tidal turbine at the Falls of Lora in Connel, Scotland. They recorded strain on a rotor blade attached to a floating platform operating under flood and ebb sea state, with parked and generating conditions. The platform used, PLAT-I, consists of three floating hulls that can support 4 SCHHOTTEL Instream Turbines (SITs). For their test, however, only one turbine has all 3 blades installed, with strain gauges attached to only one blade. No blades were installed on the other three turbines. The reader can refer to their paper for more detail on the test design and setup. They found that the loading on the turbine is higher in the generating compared to the parked conditions in the ebb sea state. The result suggests that rotor thrust and torque (hence, power) have a direct correlation to the blade level strain. However, data from blade level strain are more reliable at higher frequency load fluctuation cases compared to the former parameters. They also mentioned that this might happened due to the dampening effect coming from the presence of the turbine and the platform itself.

Recently, Brown et al. (2019) developed a fully coupled model of a floating tidal turbine, which uses an actuator disc model as an approximation to calculate the turbine loading. Using an actuator disc model minimizes the computational cost by a huge margin compared to a blade resolved turbine. The model has been validated with an experimental work by Xie et al. (2019), where a 0.33 m diameter porous disc is attached underneath a catamaran floating platform based on the Modular Tidal Generator (MTG) design concept, conducted inside an ocean basin at the University of Plymouth. Chain mooring lines were used to anchor the whole system in both experiment and numerical studies. The numerical model predicts the surge, heave, and pitch motions of the turbine quite well. The turbine load also shows good agreement with the experimental results for a fixed turbine. However, when the floating turbine is operating under a moored condition, the result diverges from the experiment. The numerical model underpredicts the loading variation amplitude in the wave-only case with an error of up to 250%. It also overpredicts the mean thrust load for the wave-current case with no mention of the error percentage. They conclude that the error is due to the static catenary approach of the mooring model and the actuator disc theory not being able to accurately predict the loading from the non-uniform inflow. Therefore, the present study seeks to improve this model to include the added mass and damping forces into the loading calculation. This is to determine whether these hydrodynamic forces can actually improve the model's accuracy. The methodology will be further explained later in this chapter.

Modifications to include the hydrodynamic forces into the existing model of Brown et al. (2020) will be presented in this chapter. The impact of including the added mass and damping forces will be verified with the original model and the blade resolved simulation results. Besides that, analyses of the floating tidal turbine over a range of waves-only and wave-current cases will also be addressed, including the comparison between single and multi-DoF motions (3 DoF – surge, heave, and pitch).

This chapter will start with the numerical method used in the present study, focusing on developing the actuator disc model, followed by the wave generation and relaxation and the mooring lines model. This is followed by consideration of the model optimization process, including mesh sensitivity test, wave decay test, and actuator disc model verification. Having established the model, the chapter focuses on the effect of both waves only and wave-current conditions on the fully coupled model. The final part of the chapter examines the floating turbine operating under various wave frequencies.

6.2 Numerical method

This subchapter will discuss the modifications to Brown et al.'s (2019) actuator disc model to include the added mass and damping forces into the thrust calculation. Further, this section presents the wave generation toolbox waves2foam used to generate and dampen the waves inside the computational domain, as well as the mooring lines model used in the present study.

6.2.1 Actuator disc model

The fully coupled model of a floating tidal turbine used in the present study was developed by Brown et al. (2019) within the open-source code OpenFOAM. The model was built based on an existing solver within OpenFOAM (interFoam), which models two-phase flows using the volume of fluid (VOF) method.

The model first appeared in Ransley et al. (2016), where it was validated against commercial software Ansys AQWA and OrcaFlex. The study conducted a numerical validation of a floating tidal turbine attached to a support barge design based on the Modular Tide Generator Ltd. design concept. Unlike in Brown et al. (2019), the mooring line model in the study uses a look-up table from a matrix produced from OrcaFlex, which was included in the equation of motion in the form of additional force. The time series of the surge, heave, and pitch motions were plotted against the result of Ansys AQWA under various wave-current conditions (neap and spring tidal current, with following and opposing directions to the incoming waves). In the study, Ansys AQWA only provides the upper and lower limit of the motion amplitude. The heave motion shows good agreement with AQWA. However, the pendulum motion only shows good agreement under the following tidal current condition while it overpredicts the motion amplitude under the opposing condition. The surge motion amplitude was overpredicted in all conditions. The front and rear mooring lines time histories were plotted against that of OrcaFlex using two wave steepness. For the high wave steepness case, the front mooring tension amplitude underpredicts the load while the rear overpredicts them. For the low wave steepness case, variations of the mean load exist between the mooring lines with OrcaFlex results. The rotor loading time series are also presented. The loading variation and mean values increases in the following tidal current condition while decreases in the opposing. However, these results were not validated against any commercial software.

They further tested the model using a cylindrically shaped support platform (cylinder axis perpendicular to the tidal current direction) with an actuator disc model under various sea state conditions to provide a test case in modelling a fully coupled model of a floating tidal turbine (Brown et al., 2020). The diameter of the support platform is 12 m, and a height of 3 m, with a 4 m diameter actuator disc attached underneath, was simulated inside a numerical wave tank with a 20 m water depth and 1.5 times the wavelength in length (m). They verified the model using the platform only (without moorings and actuator disc) against a Linear Potential Theory (LPT) model. The model's surge, heave, and pendulum motions show good agreement with the LPT model, especially in the lower wave frequency cases. In the wave-only case (with moorings and actuator disc), the rotor thrust increases as the wave frequency increase towards the natural frequency. A similar trend was also reported for the pitch motion displacement, signifying that the pitch motion is the main contributor (compared to surge and heave motions) to the rotor thrust. Response amplitude operators (RAOs) of the surge, heave, and pitch motions for the wave-current condition were also plotted over a range of wave frequency and tidal current speed. The result shows a substantial increase in the RAOs for the wave-current condition compared to wave-only cases (up to 50% increase). In the study, the model was tested using a small wave height (H

= 0.3 m at the inlet) and a low tidal current speed ($U_\infty \leq 0.5$ m/s). Although this is an excellent test case for the model, higher wave heights and faster tidal current speeds are needed to determine the robustness of the model.

A 6-DoF fully coupled model, first developed by Ransley et al. (2016) and further improved by Brown et al. (2019), is a versatile model which can model a floating tidal turbine operating under combined wave-current conditions. The turbine is approximated by an actuator disc model, with the turbine load **T** imposed over the computational disc through a Gaussian distribution. The Gaussian weighting distribution here refers to the volume of the disc which occupies the mesh, where the user needs to input the thickness and the area of the disc pre-simulation. The model will maintain this volume (the position will vary based on the platform motion, which can move in 6 DoF motion) throughout the simulation. For more detail on the Gaussian weighting distribution, the reader can refer to Brown et al. (2019) and Brown et al. (2020). The load **T**, approximated as a drop in the momentum at the turbine plane, is included in the Reynold Averaged Navier-Stokes equation (RANS)

$$\frac{\partial(\rho \mathbf{u})}{\partial t} + \nabla.(\rho \mathbf{u}\mathbf{u}) = -\nabla p + \nabla^2(\mu \mathbf{u}) + \rho \mathbf{g} + \mathbf{T} \qquad (6.1)$$

where ρ is the fluid density (two-phase fluid), $\mathbf{u} = (u, v, w)$, and $\mathbf{g}$ is the acceleration due to gravity.

In Ransley et al.'s (2019) model the axial induction factor a, which represents the reduction in axial flow velocity at the disc plane, is used to calculate an approximation to the thrust on the rotor. The rotor flow is assumed to be quasi-steady so that the thrust coefficient can be assumed constant, but with the thrust force still varying dynamically with the square of the instantaneous relative velocity of the flow to the turbine. An assumed induction factor is used to provide the thrust coefficient, $C_T = 4a(1-a)$, and is held fixed throughout the simulation to maintain constant C_T. This simple model may have limitations for accuracy in both the mean and dynamic components of the rotor thrust; improvements to the representation of the floating tidal turbine's static and dynamic thrust components will be discussed later in this chapter. In their model, only the component of **T** normal to the turbine plane is considered in the turbine load model.

$$\mathbf{T}.\boldsymbol{n}_{\mathbf{axial}} = T = C_T \frac{1}{2} \rho {U_R}^2 A_D \qquad (6.2a)$$

$$\mathbf{T}.\boldsymbol{n}_{\mathbf{axial}} = T = \big(4a(1-a)\big) \frac{1}{2} \rho \left(\frac{U_T}{1-a}\right)^2 A_D \qquad (6.2b)$$

where $\boldsymbol{n}_{\mathbf{axial}}$ is the unit normal vector to the rotor plane, the effective relative free stream velocity (far enough ahead of the rotor so not affected by its presence) $U_R = U_T/(1-a)$ and $U_T = \boldsymbol{U_T}.\boldsymbol{n}_{\mathbf{axial}}$ is the local instantaneous velocity at the rotor plane relative to the rotor (i.e., including body motions and wave kinematics), which can be readily determined from the actuator disc model in the simulation through

$$\boldsymbol{U_T} = \left(\frac{1}{V}\sum_{j=1}^{N} \boldsymbol{u_j} V_j W_j\right) - \mathbf{v}_{\boldsymbol{hub}} \qquad (6.3)$$

in which the summation is over the number of cells N containing the actuator disc, V is the total weighted volume of those cells, $\boldsymbol{u_j}$ is the velocity in cell *j*, V_j is the volume of the cell *j*, and W_j is the weighting of the cell *j* which follows a Gaussian weighting distribution. $\mathbf{v}_{\boldsymbol{hub}}$ is the velocity of the turbine hub, so that $\boldsymbol{U_T}$ is the velocity of the flow relative to the turbine in the frame of reference of the turbine itself. Further details on the model can be found in Ransley et al. (2016) and Brown et al. (2019, 2020). Note that in equation 6.2 it is implicitly assumed that $U_R > U_T > 0$ so that the flow is restricted to cases in which the relative flow velocity is in the positive sense through the rotor.

Starting with the quasi-steady model presented in equation 6.2b, we now include additional forces associated with dynamic effects. We assume that the dynamic force components resulting from motions in each DoF are independent of each other and hence that we can include them through summation over the DoF's.

$$T = C_T \frac{1}{2} \rho {U_R}^2 A_D + \sum_{i=1}^{6} \hat{F}_{A,i}(A_i^*, \omega_i^*) \dot{U}_{\mathrm{dyn},i} + \hat{F}_{V,i}(A_i^*, \omega_i^*) U_{\mathrm{dyn},i} + \Delta \bar{T}_i(A_i^*, \omega_i^*) \tag{6.4}$$

in which $\hat{F}_{A,i}$ and $\hat{F}_{V,i}$ are the magnitudes of the added mass and damping associated with the acceleration and velocity of the moving rotor in each *i* DoF. The subscript $i = 1 \ldots 6$ refers to each of the motions in surge, sway, heave, roll, pitch, and yaw, respectively, and A_i^* and ω_i^* are the rotor (non-dimensional) motion amplitude and frequency in the relevant DoF. U_{dyn} is the effective dynamic velocity associated with the rotor's relative velocity due to the platform motion and waves. $\Delta \bar{T}_i$ is the difference between the mean thrust of the stationary turbine and the turbine oscillating in the *i* DoF.

To improve the representation of the actuator disc, we first consider the quasi-steady part of equation 6.4, i.e. ignoring the dynamic force terms within the summation. In the same manner as Brown et al. (2019), we assume that this quasi-steady component of the thrust of a floating tidal turbine is dependent on the effective relative free stream velocity U_R, which contains contributions to the flow velocity from the tidal current, waves, and the motion of the floating support platform. As can be seen from equation 6.2b, Ransley et al.'s (2016) model require the specification of the induction factor a to calculate the rotor thrust. To eliminate the requirement to specify the axial induction factor in the calculation, we instead represent the axial thrust force through the local force coefficient C_X, in which the thrust force is non-dimensionalized based on the local relative flow speed U_T as $C_X = T/\frac{1}{2}\rho {U_T}^2 A_D$.

$$C_T \frac{1}{2}\rho {U_R}^2 A_D = C_T \left(\frac{U_R}{U_T}\right)^2 \frac{1}{2}\rho {U_T}^2 A_D = C_X \frac{1}{2}\rho {U_T}^2 A_D \qquad (6.5)$$

The local force coefficient, $C_X = C_T(U_R/U_T)^2$, can be determined in advance from steady flow rotor simulations, in which C_X is parameterized based on the instantaneous relative tip-speed ratio $\lambda_R = R\omega_r/U_{R,\text{steady}}$, or alternatively can be parameterized in terms of the instantaneous local tip-speed ratio $\lambda_T = R\omega_r/U_{T,\text{steady}}$. R is the rotor radius, ω_r is its rotational speed and we use the subscript *steady* to denote flow speeds measured or set in precursor steady current flow simulations. In a dynamic moving platform simulation the relative flow speed at the actuator disk $U_T = \boldsymbol{U_T}.\boldsymbol{n}_{\textbf{axial}}$ may be readily determined from the simulation, following which λ_T and the quasi-steady contribution to the rotor thrust can be found as $C_X(\lambda_T)\frac{1}{2}\rho {U_T}^2 A_D$, using the pre-determined variation of $C_X(\lambda_T)$. In a similar manner the induction factor in the precursor simulations, $\tilde{a}$, may also be parameterized as a function of the instantaneous local tip-speed ratio λ_T. The induction factor may be evaluated from analysis of the precursor simulation flowfield through $\tilde{a}(\lambda_T) = 1 - \left(U_{T,\text{steady}}/U_{R,\text{steady}}\right)$. Note that $\tilde{a}$ is not required to evaluate the quasi-steady force components, but it is useful to define here and will be later used for dynamical force component evaluation.

The representation of the turbine thrust can be further improved from an assumed steady-state representation by including the simulated hydrodynamic forces acting on a moving turbine. Based on research by Jing et al. (2017), Wang et al. (2017), Fontanella et al. (2018), and Osman & Willden (2020b) on floating offshore wind and tidal turbines, the thrust on a floating turbine contain dynamic components in addition to the quasi-steady component. Recall that Brown et al.'s model only considers the quasi-steady contribution to C_T while including a dynamically varying local flow velocity and ignores dynamic effects associated with the rate of change of inflow velocity and hence added mass and damping effects. We now seek to develop a model that includes these additional dynamic components.

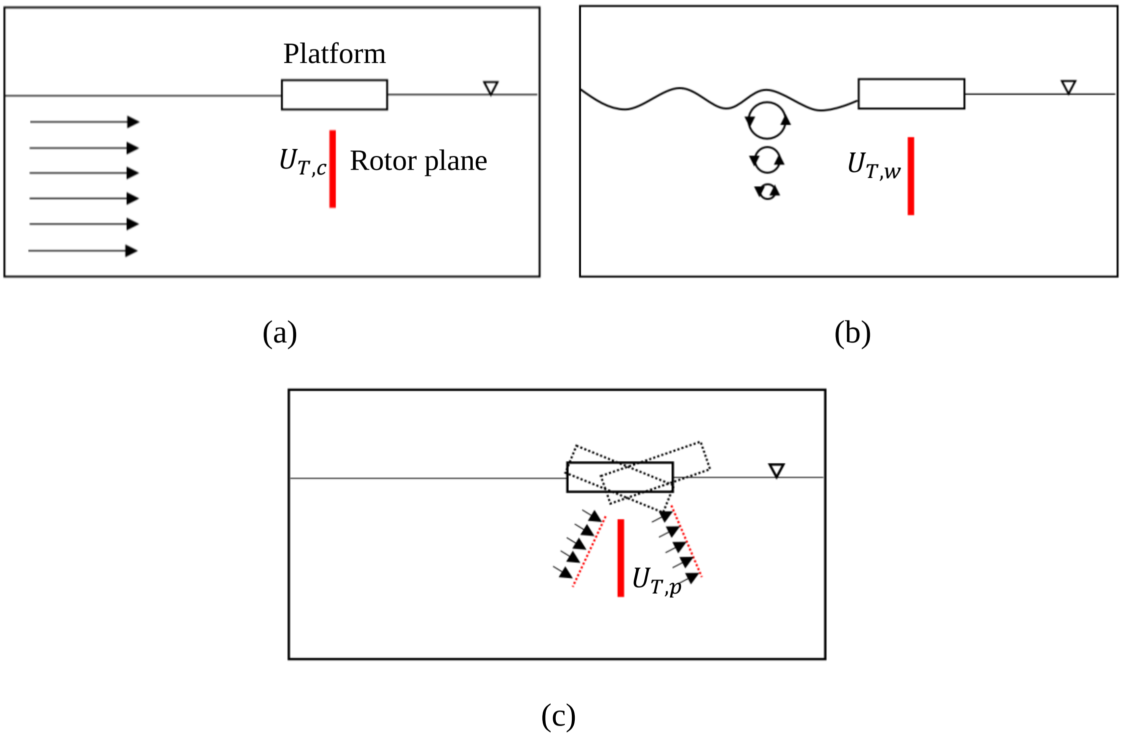

(a) (b)

(c)

Figure 6-1 Three velocities components of U_T captured at each cell at the actuator disc area. (a) shows the stationary platform (and thus, turbine) operating in moving water (from the tidal current); (b) shows the stationary platform operating in moving water (from the wave-induced velocity); (c) shows the moving platform (and thus, turbine) operating in still water.

For simplicity, we restrict ourselves to motions of the platform and turbine in the vertical plane containing the current direction. Further, we restrict our analysis to cases where the wave propagation direction is the same as the current direction. Hence, partly based on the literature (Vaal et al. 2006, Micallef & Sant 2015, Fontanella et al. 2018, and Wen et al. 2019) and the results of added mass and damping forces calculated in the previous chapters, and the chosen restriction to the vertical plane of motion, we consider fluctuating components from three motions (surge, heave, pitch) in the present representation of the thrust force in equation 6.4. Although the heave motion hydrodynamic forces were found to be significantly smaller than those in surge and pitch motions, we retain them in the multi-DoF platform model for completeness.

By substituting equation 6.5 into 6.4, we can present the thrust load as having quasi-steady and a summation of imposed hydrodynamic loading components.

$$T = C_X(\lambda_T)\frac{1}{2}\rho U_T^2 A_D + \sum_{i=1,3,5} \hat{F}_{A,i}(A_i^*, \omega_i^*)\dot{U}_{\mathrm{dyn},i} + \hat{F}_{V,i}(A_i^*, \omega_i^*)U_{\mathrm{dyn},i} + \Delta\bar{T}_i(A_i^*, \omega_i^*) \quad (6.6)$$

We can view a stationary turbine operating under wave conditions as having the same added mass and damping as a floating turbine undergoing, say, a surge motion by fixing the frame of reference to the rotor plane (Keulegan & Carpenter, 1958), as presented in Chapter 2 of this thesis. Therefore, we can combine the effect of added mass and damping from the platform motion and waves. We can achieve that by introducing U_{dyn} in equation 6.6. To evaluate U_{dyn}, we assume that the effective relative velocity at the rotor plane U_T contains components of three combined velocities (refer to Figure 6-1 for visualizations): velocity from tidal current $U_{T,c}$, wave-induced velocity $U_{T,w}$, and relative velocity due to the platform motion $U_{T,p}$ (note that this is defined in the direction opposite to platform motion).

$$U_T = \boldsymbol{U_T}.\boldsymbol{n}_{\mathbf{axial}} = \left(\boldsymbol{U_{T,c}} + \boldsymbol{U_{T,w}} + \boldsymbol{U_{T,p}}\right).\boldsymbol{n}_{\mathbf{axial}} \quad (6.7a)$$

$$\boldsymbol{U_{T,\mathrm{dyn}}} = \boldsymbol{U_T} - \boldsymbol{U_{T,c}} = \boldsymbol{U_{T,w}} + \boldsymbol{U_{T,p}} \quad (6.7b)$$

$$\boldsymbol{U}_{\mathbf{dyn}} = \frac{\boldsymbol{U_{T,\mathrm{dyn}}}}{1-\tilde{a}} = \boldsymbol{U_w} + \boldsymbol{U_p} \quad (6.7c)$$

The effective dynamic velocity at the rotor plane $\boldsymbol{U_{T,\mathrm{dyn}}}$, which is given in equation 6.7b, is a relative velocity at the rotor plane consisting of contributions from the wave velocity and the velocity due to platform motion. The effective velocity due to tidal current at the rotor plane $\boldsymbol{U_{T,c}} = \boldsymbol{U_c}(1-\tilde{a})$, where $\boldsymbol{U_c}$ is the tidal current velocity, i.e., $\boldsymbol{U_c} =$ (2, 0,

0) m/s for the present study, and $\tilde{\alpha}$ is determined from the precursor simulations as a function of the instantaneous local tip-speed ratio λ_T.

We next assume that the induction factor for the dynamical components is the same as that of the quasi-steady components. This allows us to evaluate the relative upstream dynamic velocity $\boldsymbol{U}_{\mathbf{dyn}}$, from the dynamic velocity at the turbine plane $\boldsymbol{U}_{\mathbf{T,dyn}}$, see equation 6.7c, which is itself evaluated from equation 6.7b as the difference between total and current only velocities at the rotor plane.

Equation 6.6 can be extremely complicated to model since the velocity and acceleration are associated with the combined waves and platform motions in 3 DoF. The difficulty comes in integrating the non-linear relationship between the platform motion's velocity amplitude and the wave velocity amplitude, thus evaluating the added mass and damping. For simplicity, the present study only considers the hydrodynamic parameters of the pendulum motion since it is the dominant motion of a floating tidal turbine operating under waves conditions. Therefore, we approximate equation 6.6 as

$$\begin{aligned} T = \; & C_X(\lambda_T)\frac{1}{2}\rho U_T^2 A_D + \hat{F}_{A,pen}(A_{pen}^*, \omega_{pen}^*)\dot{U}_{\mathrm{dyn}} + \hat{F}_{V,pen}(A_{pen}^*, \omega_{pen}^*)U_{\mathrm{dyn}} \\ & + \Delta\bar{T}_{pen}(A_{pen}^*, \omega_{pen}^*) \end{aligned} \tag{6.8}$$

Note that the hydrodynamic parameters (added mass and damping) depend on the amplitude and frequency of an effective pendulum motion that encapsulates all dynamic velocity components (platform motion and wave kinematics). U_{dyn} is the velocity of that effective pendulum motion, $\dot{U}_{\mathrm{dyn}}$ is the acceleration of that motion which can be evaluated from time derivatives of U_{dyn}. We next seek to use U_{dyn} and $\dot{U}_{\mathrm{dyn}}$ to evaluate the amplitude of effective pendulum motion, A_{pen}. We assume the normal component of $U_{\mathrm{dyn}} =$

$\boldsymbol{U}_{\mathbf{dyn}}.\boldsymbol{n}_{\mathbf{axial}}$ has a sinusoidal behaviour, consisting of the combined effective velocities from waves and platform motion.

$$x_{\text{effective motion}}$$

$$= A_{pen}\sin\left(\omega_{pen}t + \phi\right)$$

$$= A_{pen}\left\{\cos\left(\omega_{pen}t\right)\sin\phi + \sin\left(\omega_{pen}t\right)\cos\phi\right\} \tag{6.9a}$$

$$-U_{\text{dyn}} = \dot{x}_{\text{effective motion}}$$

$$= A_{pen}\,\omega_{pen}\left\{-\sin\left(\omega_{pen}t\right)\sin\phi + \cos\left(\omega_{pen}t\right)\cos\phi\right\} \tag{6.9b}$$

$$-\dot{U}_{\text{dyn}} = \ddot{x}_{\text{effective motion}}$$

$$= -A_{pen}\,\omega_{pen}^{2}\left\{\cos\left(\omega_{pen}t\right)\sin\phi + \sin\left(\omega_{pen}t\right)\cos\phi\right\} \tag{6.9c}$$

ϕ is an arbitrary phase angle. We assume that the platform responds at the wave frequency, ω_{pen}. Having extracted U_{dyn} from the simulation and computed $\dot{U}_{\text{dyn}}$ as a time derivative, we can evaluate ϕ and A_{pen} using equations 6.9b and 6.9c above. This provides $A_{pen}^{*} = A_{pen}/R$, and $\omega_{pen}^{*} = \omega_{pen}/\omega_{r}$, which are then used to evaluate the added mass and damping $\hat{F}_{A,pen}$ and $\hat{F}_{V,pen}$ and the mean thrust force $\Delta\bar{T}_{pen}$, respectively, from the look-up table given in the previous chapter, unless otherwise specified.

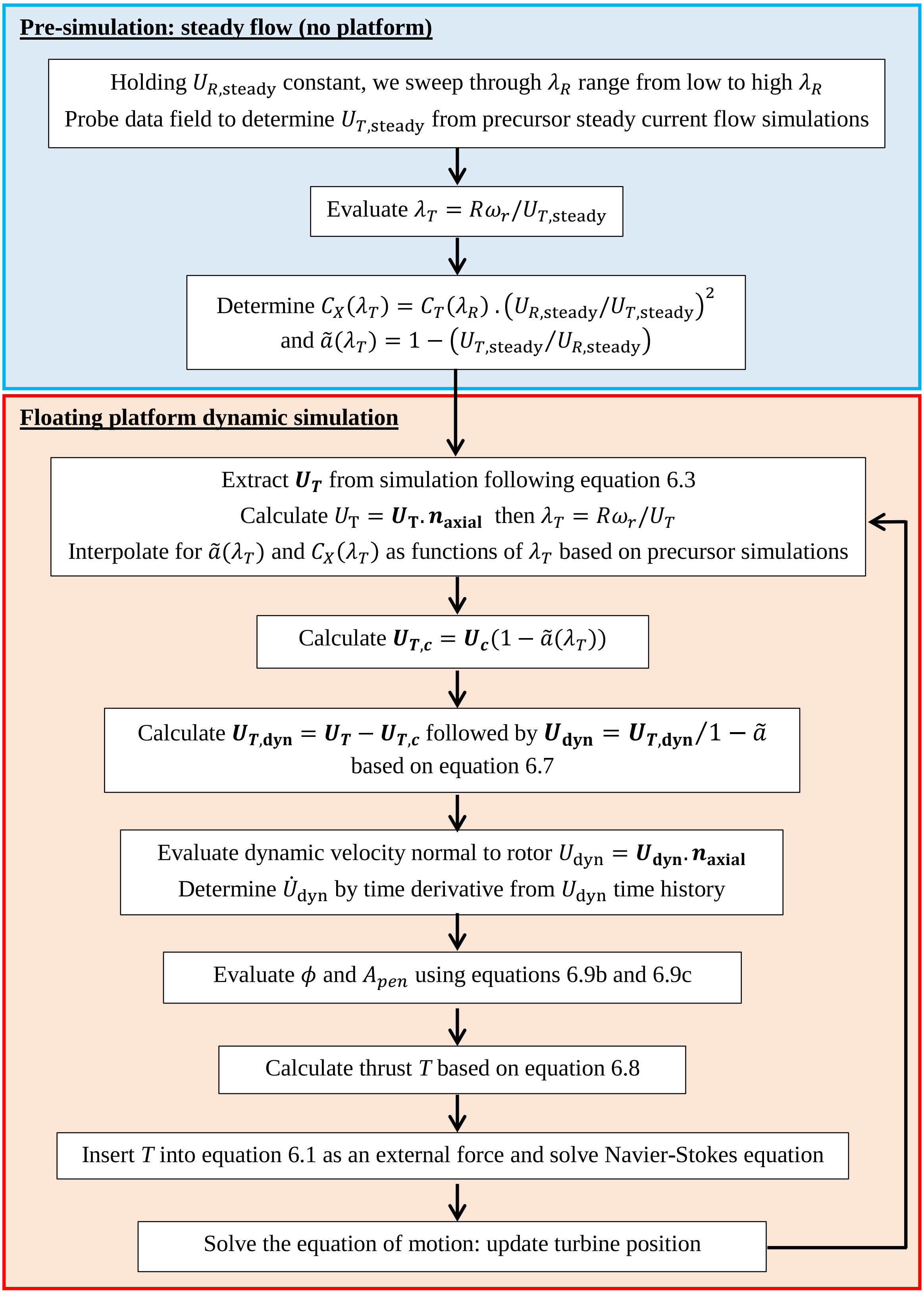

Figure 6-2 Summary of the computational process based on the model derivation.

6.2.2 Wave generation and relaxation zone

Waves2foam, first introduced by Jacobsen et al. (2012), was used as the primary solver in the present study to model the waves, relaxation zones, and the two-phase simulation. Waves2foam solves the two-phase fluids Reynolds averaged Navier-Stokes (RANS) equations in Cartesian coordinates. The relaxation zone introduced in this toolbox is used to minimize the wave reflection from the outlet boundary and eliminate wave reflection within the domain to not interfere with the wavemaker boundary (at the inlet). Waves2foam has been widely used and validated in the OpenFOAM community for wave generation under various seakeeping cases, including floating tidal turbines and wave energy devices. Therefore, it will not be discussed in detail in the present study. In general, the solver is versatile. It can model rectangular and circular wave tanks; it can model regular, irregular, and solitary waves, including tidal current; it can also model relaxation zones that act as wave dampers. The reader can refer to Jacobsen et al. (2012) and the waves2foam manual for more information regarding the model.

The floating tidal turbine's computational domain is given in Figure 6-3 (note that figures are not to scale). The size of the wave tank (front cross-section) is $5D \times 6D$, with water depth of 50 m based on the depth at the Fall of Warness tidal site (Anatec Ltd., 2010). Half a wavelength λ' is adequate for the inlet relaxation zone since the wave reflection will not be interfering with the incoming waves since the wave tank size is large enough and the wave will be coming from one direction only, and the outlet relaxation zone with the size of $2\lambda'$ was required to minimize the reflection and dampened the waves at the outlet, based on studies by Ransley et al. (2016) and Brown et al. (2020). The actuator disc will be hanging below the floating platform, as shown in Figure 6-3, and the support mast (or support tower) will be neglected in the present study to eliminate other unsteady variations which can interfere with the actuator disc loading. Table 6-1 shows the platform dimensions and other parameters, together with the actuator disc and mooring lines used in the present study unless otherwise specified. The present study uses regular waves (first-order) under various wave heights *H* and periods *T*.

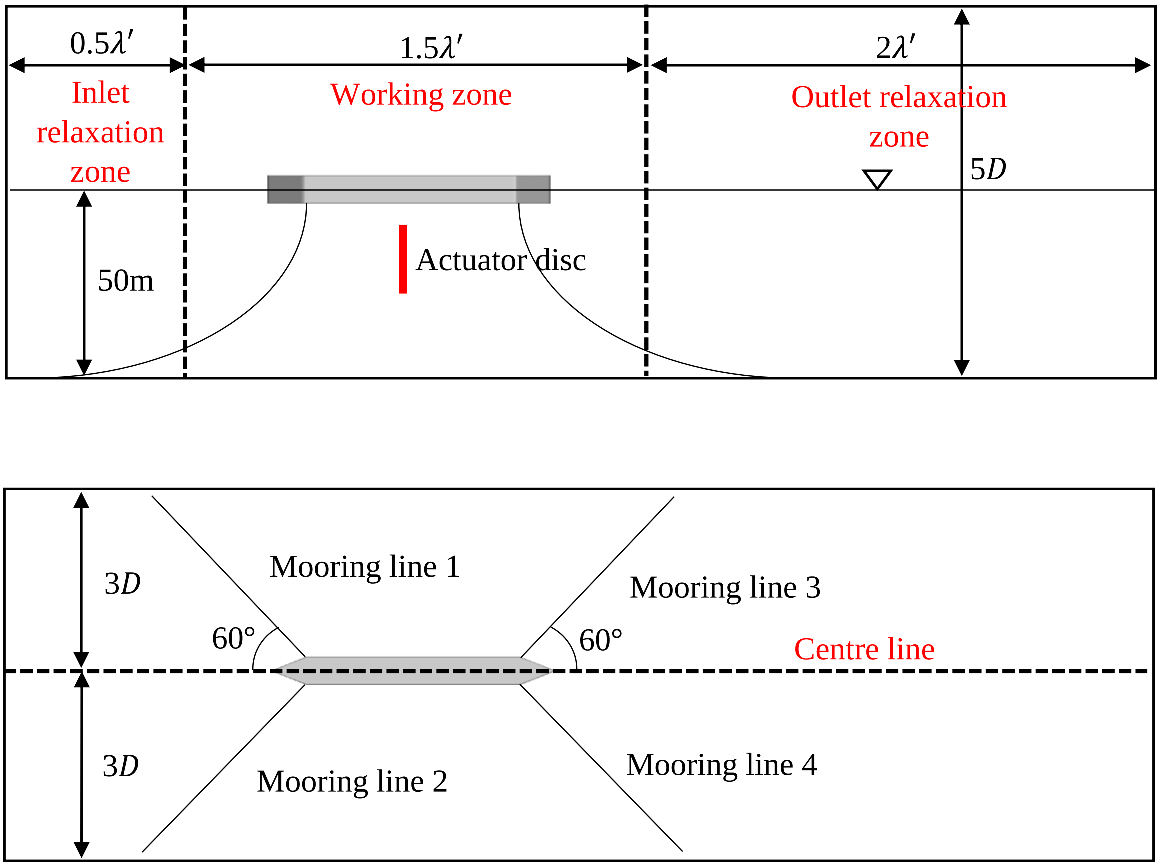

Figure 6-3 Computational domain of the floating platform: top is the side view (*x*-*z* plane); bottom is the top view (*x*-*y* plane).

6.2.3 Floating motion in OpenFOAM

OpenFOAM has the capability to model a floating body moving in all six DoF motions (refer to Figure 5-1 in Chapter 5 for the motion). However, only three DoF (surge, heave, and pitch) were considered in the present study. The body motion is modelled by calculating the forces acting on the floating structure. These forces can be categorized into two: fluid flow and external. The fluid flow force comes from the impact of the fluid on the floating structure, such as the pressure, buoyancy, and viscous forces. The external force is forces originating from outward sources, such as mooring lines, gravity, and, in this case, turbines. Then the linear and angular acceleration, velocity, and displacement of the floating body were determined based on these forces. The reader can refer to Ekedahl (2009) and Urquhart (2016) for a more detailed explanation of the six DoF mesh motion in OpenFOAM, including equations and model setup. In this chapter, the mesh deformation method was used to move the mesh (i.e. the floating platform). This is a different approach to the mesh motion technique used compared to previous chapters due to the nature of the model (fluid-structure interaction rather than prescribed motion) and the three DoF motions considered. Since the accuracy and stability of the simulation decreases when the surrounding mesh is skewed from the mesh deformation, it is important to construct a mesh that can maintain a good level of accuracy and stability while minimizing the computational cost. Therefore, a mesh sensitivity test was conducted in the following sub-chapter to determine the optimal mesh volume which considers these aspects of the simulation.

6.2.4 Mooring lines model

Bruinsma (2016) explains the three states of mooring lines available in the waves2foam toolbox: simple state, resting state, and hanging state. These are catenary-type moorings. The simple state is defined as the touchdown point being the same as the anchor point, while the resting state is where some portion of the mooring lines lies on the seabed, the anchor point is (horizontally) longer than the touchdown point. The hanging state is defined when the anchor point of the mooring line is located right below the attachment point of the platform, such as a typical design of a tension leg platform.

The simple state is chosen in the present study using (solid) chain mooring lines with zero dampings and elasticity. The mooring line force is defined as

$$F_T = m_{sub} g \left(\frac{s^2 - d^2}{2d} + l \right) \qquad (6.10)$$

where m_{sub} is mass of the submerged mooring line, g is the acceleration due to gravity, s is the length of the mooring line, d and l are the horizontal and vertical distances between the anchor point to the attachment point of the floating platform. The mooring lines are attached to each end of the platform, at 60° apart from the centre line of the domain, as shown in Figure 6-3. The model neglects environmental forces acting on the mooring lines, such as forces from tidal currents and waves.

Table 6-1 Parameters used in the present study for the floating tidal turbine system.

Section	**Parameter**	
Platform:		
	Total length [m]	24.0
	Width [m]	2.4
	Height [m]	2.4
	Initial draft [m]	1.2
	Mass (with turbine) [kg]	177,807.0
	Moment of inertia I_{xx} [kg.m^2]	80,940,426.7
	Moment of inertia I_{yy} [kg.m^2]	81,609,581.3
	Moment of inertia I_{zz} [kg.m^2]	81,614,159.7
Rotor:		
(Actuator	Diameter [m]	20.0
disk)	Disk thickness [m]	0.7
Mooring:		
	Mass per length [kg/m]	43.2
	Total length [m]	80.0

6.3 Model optimization

This subchapter is divided into three sections. The first section explains the mesh sensitivity test. Comparisons between six mesh volumes were carried out to determine the suitable mesh size to be used in the present study. The second section examines the wave decay test at various locations inside the computational domain. The last section will discuss the model verification of the modified actuator disc (present study) to the blade resolve CFD result under prescribed surge and pitch motions.

6.3.1 Mesh sensitivity test

For a fluid-structure interaction study of a floating body involving waves, adequate cell size is critical to ensure the accuracy of the simulation. Some of the cell sizes used in previous studies involving floating objects under wave conditions (wave energy converter, ships, floating object, etc.) are presented in Table 6-2, where the cell size presented is located around the floating object and the water surface. It is crucial to develop a mesh that maintains computational accuracy while minimizing the cost. Therefore, a mesh sensitivity test was conducted to determine the most suitable minimum cell size for the present study.

Six different mesh sizes were tested. The minimum cell size for each mesh is presented in Table 6-3. The computational mesh cross-section is illustrated in Figure 6-4. Only the mesh in the water level area is modified for each mesh volume. Very coarse mesh is used towards the outlet relaxation zone, the sides, and the top of the domain to minimize the computational cost. The mesh below the floating platform is purposely made fine to cater to the actuator disc model. Regular 1st order waves with a wave height H = 1.0 m (at the inlet) and a period T = 7.14 s (corresponds to $\omega^* = 1$) were used to simulate the waves with no tidal current.

Table 6-2 Cell sizes used in the literature to simulate floating objects in waves. ϕ refers to the parameter used to measure the cell size. The cell size here refers to the water surface area and surrounding a floating object used in each study.

Literature	Cell size [m]	Direction	ϕ of present study [m]	Cell size based on ϕ [m]
Kim (2011)	150 cells per λ'	Not mention	λ' = 80	0.533
Yu & Li (2011)	< $\lambda'/80$	x	λ' = 80; H = 1	<1.0
	$H/20$	z		0.05
Fleming (2014)	$0.1c_{0.8R}$	z	$c_{0.8R}$ = 1.23	0.123
Ransley et al. (2016)	0.0625	Not mention	-	-
Ransley et al. (2017)	0.025	Not mention	-	-
Jin et al. (2018)	0.01	Not mention	-	-
Windt et al. (2019)	1332 cells per λ' (0.075)	x	λ' = 80; H = 1	0.06
	20 cells per H (0.075)	z		0.05
Brown et al. (2020)	0.1	x, y, z	-	-

Table 6-3 Mesh sensitivity test for the present study using six mesh volumes with different cell lengths and heights.

Mesh	Minimum cell length x [m]	Minimum cell width y [m]	Minimum cell height z [m]	Total cell volume [$\times 10^6$]
1	0.1	0.1	0.1	27.7
2	0.1	0.1	0.05	37.5
3	0.1	0.1	0.025	62.1
4	0.05	0.1	0.1	43.3
5	0.025	0.1	0.1	67.8
6	0.05	0.1	0.05	91.4

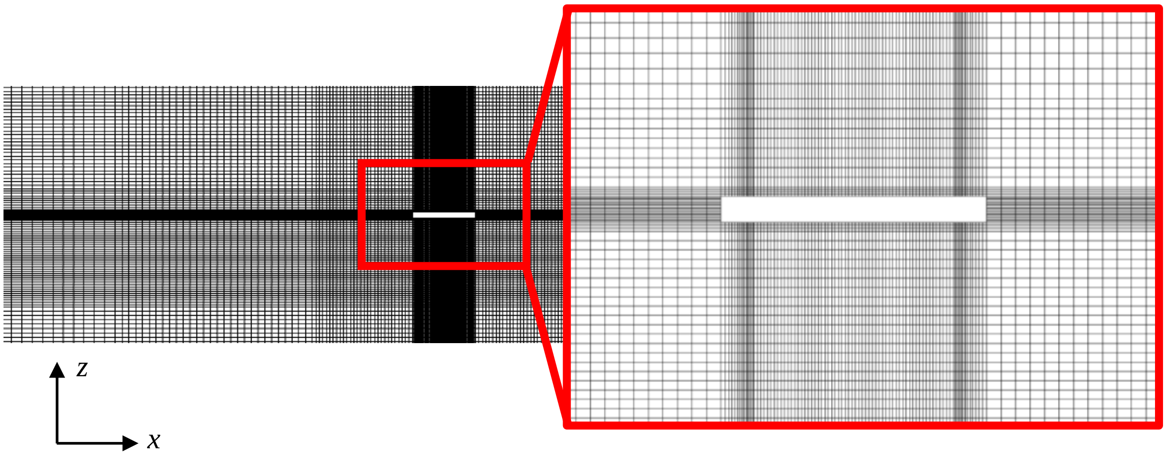

Figure 6-4 Computational domain mesh cross-section of the floating support platform. The platform is located at the centre of the domain (in both *y* and *z* directions).

Table 6-4 Percentage difference of motion amplitudes between different mesh volumes. Motion amplitudes were averaged based on the data of the last 6 cycles. Negative values show the amplitude of other meshes is higher than mesh 6.

Motion	Mesh	Amplitude [m; °]	Percentage difference [%]
Surge	1	0.387	15.692
	2	0.377	18.701
	3	0.423	5.820
	4	0.428	4.489
	5	0.457	-2.162
	6	0.447	-
Heave	1	0.387	15.685
	2	0.377	18.699
	3	0.423	5.815
	4	0.428	4.517
	5	0.457	-2.172
	6	0.447	-
Pitch	1	1.139	9.106
	2	1.096	13.336
	3	1.546	-19.627
	4	1.256	-1.115
	5	1.334	-6.861
	6	1.242	-

Simulations were conducted for ~14 wave periods using each mesh listed in Table 6-3. Data from the last 6 cycles were averaged and the comparison between them is shown in Table 6-4. Mesh 6 was taken as the finest mesh for the present study, and percentage differences were calculated by comparing with this mesh. Looking at mesh 2 and 4, the difference with mesh 6 is higher when the mesh is refined vertically. A similar trend has been shown for mesh 3 and 5 for refinement in vertical and horizontal directions, respectively. Therefore, for this particular wave height and frequency, accuracy can be increased by refining the mesh horizontally as to vertically. For translational motion, mesh 5 shows good agreement with mesh 6 with a percentage difference of ~2%. For rotational motion (pitch), mesh 4 shows a better agreement than mesh 5. Since mesh 4 has a lower volume than mesh 5, the former is chosen for the present study to minimize the computational cost while maintaining acceptable accuracy.

6.3.2 Wave decay test

Waves degeneration, or decay, is a natural process where the amplitude becomes smaller as they travel over a distance farther away from the wave generating point (for example, the wave generator flaps at the end of a wave tank). For non-breaking waves, this happens because of wave energy dissipation or dampening due to the material of the fluid and the boundaries of the channel. This form of wave energy loss is known as viscous damping. For nonturbulent flows the energy loss due to viscous effects can be classified as follows: energy loss at the boundary layer interface, the internal damping of each homogenous fluid layer, at the sidewalls and the bottom of the wave tank (Leone et al., 1982; Troy & Koseff, 2006; Zago et al., 2021). For a numerical study, not enough mesh resolution in the wave area is another possibility that Fleming (2014) pointed out in his thesis which causes the wave to decay, where it can cause the information transfer between cells to be less accurate, as it travels downstream of the numerical wave tank.

The wave decay test is important to determine the wave condition at the centre of the wave tank since this is where the floating platform and the turbine are located. Therefore, it will be beneficial to know the flow condition that will be imposed on the floating turbine to make a better analysis of the entire system. Fleming (2014) study the effects of waves on a bottom fixed tidal turbine, where he conducted a wave decay test using two wave heights and frequencies. He found that the wave decay rate is less significant when varying the wave frequency but increase by 0.7% when using higher wave height. Troy & Koseff (2006) studied the viscous damping for progressive waves in a rectangular channel using numerical models and experiments. They found that the rate of wave decay becomes larger in higher wave frequency cases, which is the opposite of Fleming's (2014) findings.

In the present study, simulations were carried out on a fixed platform until ~12 wave periods, using H = 1, 2, 3 m and ω^* = 0.7, 1.0, 1.3. Four wave gauges are placed at 8D, 6D, 4D, 2D upstream from the centre of the wave tank. Wave heights at every wave gauge and rates of decay are presented in Table 6-5. The result shows that the effect is reversed from that found in Fleming (2014). The increase in wave height marginally affects the rate of decay, while the increase in wave frequency (or decrease in wave period) significantly affects the rate of decay. A similar trend was found in Troy & Koseff (2006) where the rate of wave decay increases as the wave frequency is increased. At wave frequency ω^* = 1.0 the rate of decay increases to ~50% when the wave travels from x_1 to x_4, and it gets even worse at a higher wave frequency.

Even when using the finest mesh (not shown here), the wave decay is still ~50% at ω^* = 1.0. This might be due to the size of the wave tank used in the present study. A similar trend can be found in an experimental work done by Brown et al. (2021), where the wave height generated by the wavemaker becomes smaller as the wave frequency is increased. Therefore, the motion response of the floating platform (to that extent, the floating tidal turbine) is expected to become smaller as the wave frequency is increased due to the rate of wave decay.

Table 6-5 Rate of decay of waves used in the present study under various wave height H and frequency ω^*. The location x_i refers to the horizontal distance in the *x*-direction, where subscript 1, 2, 3, 4 refers to the distance 8*D*, 6*D*, 4*D*, 2*D*, respectively, upstream from the centre of the numerical tank (0, 0, 0). The negative sign refers to an increase in the wave height.

ω^*	H at inlet [m]	H at x_1 [m]	H at x_2 [m]	H at x_3 [m]	H at x_4 [m]	Rate of decay x_{1-2} [%]	Rate of decay x_{2-3} [%]	Rate of decay x_{3-4} [%]	Rate of decay x_{1-4} [%]
0.7	1.0	0.99	0.95	0.92	0.85	4.0	3.2	7.6	14.1
1.0	1.0	0.96	0.79	0.64	0.49	17.7	18.9	23.4	48.9
1.3	1.0	0.86	0.41	0.27	0.23	52.0	34.1	14.8	73.2
1.0	2.0	1.90	1.62	1.44	1.00	14.7	11.1	30.5	47.3
1.0	3.0	2.95	2.70	2.41	1.47	8.4	10.7	39.0	50.1

6.3.3 Actuator disc model verification

It is important to verify the actuator disc model used in the present study against the 3-dimensional blade resolved simulations to determine the level of improvements of the present model. The case of a surging turbine oscillating at amplitude A^* = 0.1 with frequecies ω^* = 0.7, 1.0, 1.3 rotating at a constant rotor rotational speed of 0.88 rad/s was compared to the modified actuator disc model in the present study. The computational domain is similar to that of the blade resolved surge motion in Chapter 2. The turbine is replaced with an actuator disc at the centre of the domain, as presented in Figure 6-5. Similar boundary conditions were applied in the actuator disc model as in the surge motion cases presented in

Chapter 2, which uses the moving reference frame. Similar to the rotor, the actuator disc has a 20 m diameter. Note that the added mass $\hat{F}_A$, damping $\hat{F}_V$ and the mean thrust force $\Delta\bar{T}$ of the surge motion were used in the model (refer to equation 6.8), which was presented in the previous chapter.

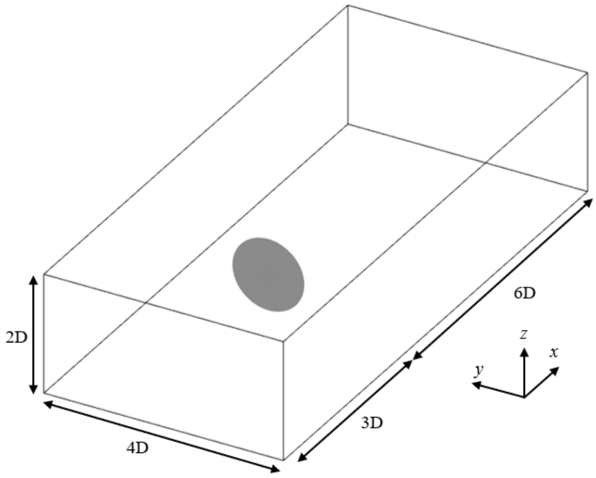

Figure 6-5 Diagram of an actuator disc computational domain. The domain is similar to that of the rotor, with a blockage ratio B = 0.0982.

The time histories of thrust coefficient are presented in Figure 6-6 for a turbine oscillating in the surge motion. The present actuator disc model is compared with the 3-dimensional blade resolved simulation and the original model of Brown et al. (2020). Note that in the present study, Brown's model refers to the simulation done by the author in the present study using Brown et al.'s (2020) original model. Dashed lines present the average value of thrust coefficients of the last two surge cycles. Brown et al.'s (2020) original model overpredict the thrust by an average of ~30%, while the present study's model underpredicts the loading by less than 1.0% compared to the blade resolved. Thus, there is a significant improvement in using the modified actuator disc model in terms of the average value when simulating the surge motion. However, the maximum and minimum values are still being underpredicted by the actuator disc model, especially in the lower frequency case, although these are significantly minimized compared to the original model.

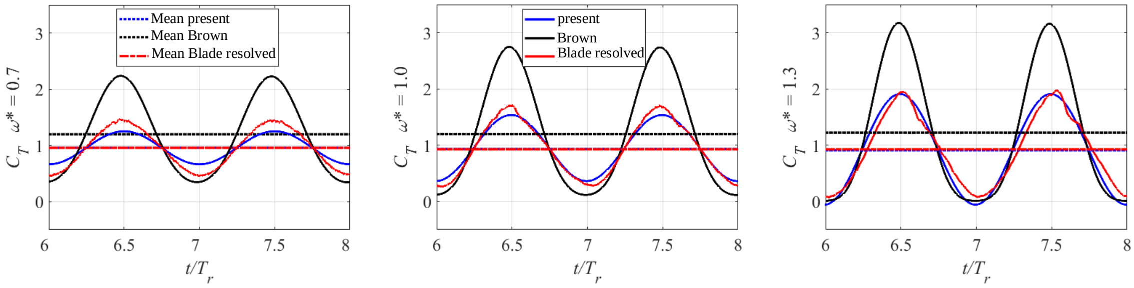

Figure 6-6 Thrust coefficient time histories of a rotor and actuator discs undergoing prescribed surge motion at $\omega^* = 0.7$, 1.0, 1.3. The 3-dimensional blade resolved (rotor) model was compared to the present actuator disc model and the actuator disc model by Brown et al. (2020). The time is normalized with the period of one surge cycle in their respective frequency.

Since the fully coupled model includes the pendulum motion, we need to test the actuator disc model in a rotational oscillation condition. This is to ensure that the actuator disc can accurately represent the turbine in a fully coupled model. Brown et al.'s (2020) original model include a "rotating actuator disc" mode, which continuously rotates the actuator disc around the desired axis, where the centre of rotation (COR) is located at the centre of the disc. Even though this is a useful mode to have on such a model, it does not represent a pendulum-like motion of a floating tidal turbine. Therefore, modifications to the model were made in the present study to include the transformation matrix to simulate the pendulum motion.

$$\mathrm{T}_y.\mathrm{R}_\theta.\mathrm{T}_{-y} \qquad (6.11)$$

$$\mathrm{T}_y = \begin{bmatrix} 1 & 0 & 0 & dx \\ 0 & 1 & 0 & dy \\ 0 & 0 & 1 & dz \\ 0 & 0 & 0 & 1 \end{bmatrix}; \quad \mathrm{T}_{-y} = \begin{bmatrix} 1 & 0 & 0 & -dx \\ 0 & 1 & 0 & -dy \\ 0 & 0 & 1 & -dz \\ 0 & 0 & 0 & 1 \end{bmatrix}; \quad \mathrm{R}_\theta = \begin{bmatrix} \cos\theta & 0 & \sin\theta & 0 \\ 0 & 1 & 0 & 0 \\ -\sin\theta & 0 & \cos\theta & 0 \\ 0 & 0 & 0 & 1 \end{bmatrix}$$

where dx, dy, dz are distances between the COR and the turbine hub. Equation 6.11 is included in the model to calculate the turbine hub position. For the pendulum motion, a similar computational domain from Chapter 3 was used (with the blockage ratio B = 1.0%).

The turbine mesh was replaced with an actuator disc, and all boundary conditions remain the same as the blade resolved cases in Chapter 3.

The time histories of thrust coefficient are presented in Figure 6-7 for a turbine undergoing a prescribed pendulum motion. The present study's model overpredicts the loading by ~14% compared to the blade resolved at lower frequencies, and the prediction becomes better in the higher frequency case. Again, the loading fluctuation amplitudes are still being underpredicted by the actuator disc model, especially in the lower frequency case. Brown et al.'s (2020) model overpredict the loading by ~16% at a lower frequency and decreases to ~9% at higher frequency case. Further improvements are needed to accurately represent the rotor using an actuator disc model undergoing a rotational motion. For instance, improving the calculation of the added mass and damping forces in the previous chapter to include the angular component instead of only taking into account the translational component of the pendulum motion.

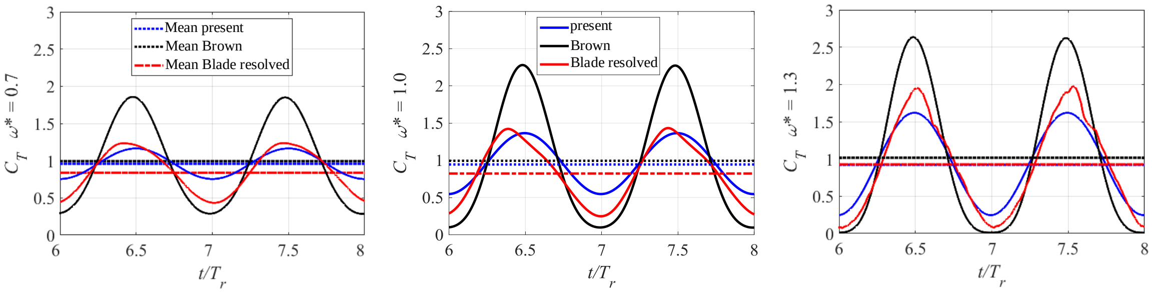

Figure 6-7 Thrust coefficient time histories of a rotor and actuator discs undergoing prescribed pendulum motion at $\omega^* = 0.7, 1.0, 1.3$. The 3-dimensional blade resolved (rotor) model was compared to the present actuator disc model and the actuator disc model by Brown et al. (2020). The time is normalized with the period of one pendulum motion cycle in their respective frequency.

The result shows that the modified actuator disc model works well in the surge motion, comparable to that of the blade resolved simulation. Significant improvement is shown when compared with the original model. Some upgrades are needed to simulate an actuator disc oscillating in a rotational (pendulum) motion, focusing on lower frequency cases. However, the study conducted here is only of a single DoF motion. The coupled motion will have a more complex movement, and the unsteady loading of a floating tidal turbine is expected to be more severe when operating under this condition.

6.4 The fully coupled model

This section explains some of the results and relationships between parameters involved in the new model. Only results for the case of $H = 1.0$ m and $\omega^* = 1.0$ are shown as a representation in this entire section, as other cases exhibit similar trends and to ease with the explanation. Both wave-only and wave-current conditions were presented in this section with a constant tidal current velocity (at the inlet) $U_\infty = 2.0$ m/s.

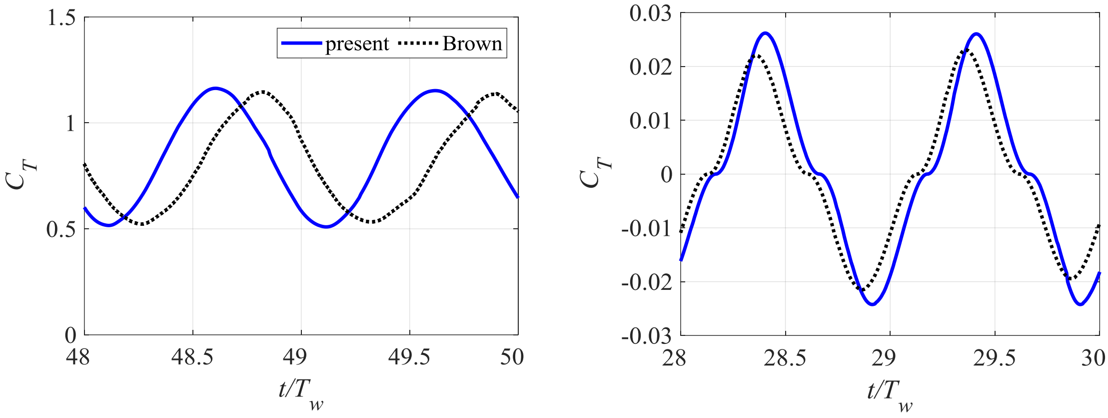

Figure 6-8 Thrust coefficient time histories of a floating tidal turbine for Brown's model and the present model for wave-only (right) and wave-current (left) cases for $\omega^* = 1.0$ and $H = 1.0$ m with rotor rotational speed of 0.88 rad/s.

Figure 6-8 shows the comparison of the thrust coefficient time series between the present model and Brown’s model for wave-only and wave-current conditions. Note that in the present study, Brown’s model refers to the simulation done by the author in the present study using Brown et al.'s (2020) original model. The thrust coefficient in the wave-only condition is normalized using $\frac{1}{2}\rho {U_\infty}^2 A_D$ where $U_\infty = 2.0$ m/s although there is no tidal current flow. The reason for this is to make the normalization process consistent with the wave-current condition for comparability.

In Figure 6-8, the present model shows a slightly higher loading variation amplitude compared to Brown's model, which happens due to the additional forces included in the thrust calculation (i.e., the hydrodynamic components). The phase difference between the two models is caused by the additional hydrodynamic forces introduced in equation 6.8. This trend is different from the single DoF motion results presented previously, where Brown's model predicts higher loading variation than the present model when compared to the blade resolved data. This might be from the difference in the pitch amplitude used in these two studies; the single DoF uses a fixed amplitude $A^* = 0.1 = A_0 = 3.0^{\circ}$ while the 3 DoF model (i.e., the fully-coupled model) only produced $A_0 \approx 1.3^{\circ}$ (refer to Figure 6-10 for the motion response of the platform). Besides this, there may be a slight difference in the actual frequency of oscillation in the 3 DoF model since there is a phase difference between the wave and the platform motion, which comes from the turbine model and mooring lines. Other than that, this might be due to the fluid-structure interaction effect, including structural damping, mooring lines load, a phase difference between waves and platform motion, which does not appear in the prescribed single DoF motion case presented previously.

Figure 6-9 shows the C_T and velocity components normalized with their respective maximum values for wave-current and wave-only cases for $\omega^* = 1.0$ and H = 1.0 m with a constant rotor rotational speed $\omega_r = 0.88$ rad/s for the present model. Note that for the wave-current case, C_T and U_T were averaged at the last 6 motion cycles of the data, and the entire data was subtracted based on their respective average values for presentation

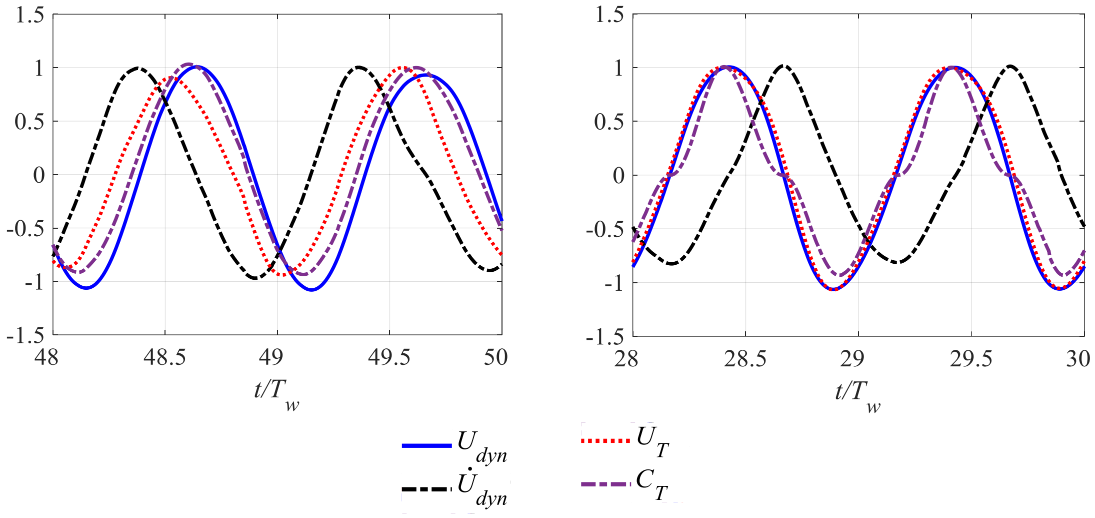

Figure 6-9 Normalized (with their respective maximum values) parameters time histories of a floating tidal turbine for the present model for wave-only (right) and wave-current (left) cases for $\omega^* = 1.0$ and H = 1.0 m with rotor tip-speed ratio of 4.4.

purposes. For the wave-current case, the C_T is influenced by the U_T and U_{dyn} (C_T phase shifts in between the two velocities). By referring to equation 6.8, the C_T is dominated by the quasi-steady term (which is in phase with U_T) and the added damping force (which is in phase with U_{dyn}). The influence of the added damping is considered to be minimal since the C_T has a huge phase difference with the $\dot{U}_{dyn}$ (which is in phase with the added mass, according to equation 6.8). Besides this, the added mass and ΔT is one magnitude lower than the added damping (refer to Chapter 5 for the range of added mass, damping, and ΔT used in the present study). For the wave-current case, U_T and U_{dyn} have different phase angles. This happens due to the inclusion of tidal current velocity $U_{T,c}$, which minimally fluctuates based on the induction factor $\tilde{a}$. Looking at the wave-only case, there is no difference in the phase angle between U_T and U_{dyn} since $U_{T,c} = 0$. For the wave-only case, C_T is also highly dominated by the quasi-steady term and the added damping force term.

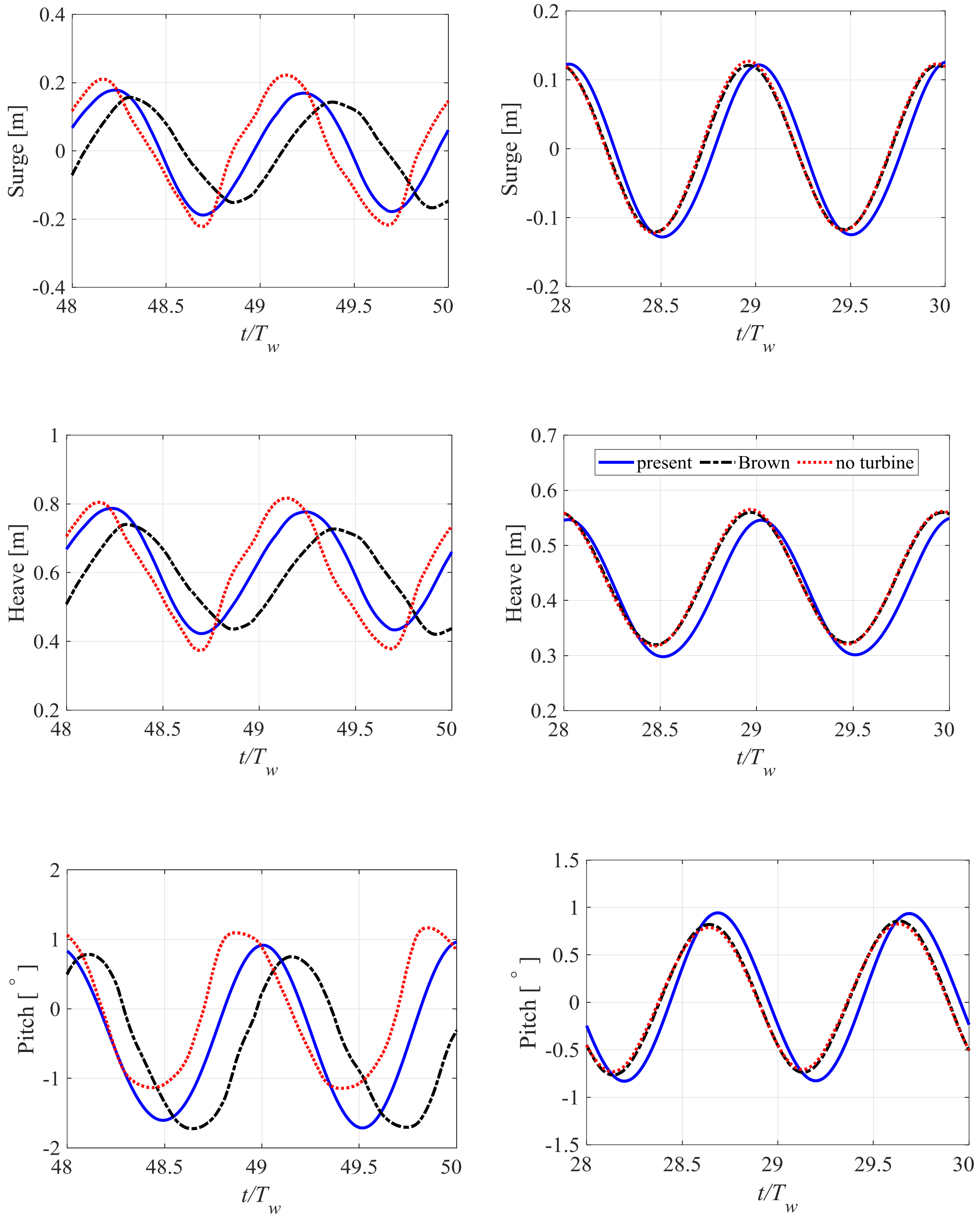

Figure 6-10 Motion response time histories of a floating tidal turbine for the no turbine case, Brown's model, and the present model for wave-only (right) and wave-current (left) cases for $\omega^* = 1.0$ and $H = 1.0$ m with rotor tip-speed ratio of 4.4.

Figure 6-10 shows the time histories of motion response of the floating platform with and without the turbine for wave-only and wave-current conditions. The surge motion was averaged at the last 6 motion cycles of the data, and the entire data was subtracted based on their respective average values. This is to eliminate the offset from its original position due to the (downstream) drift of the floating platform, following a similar method by Brown et al. (2020).

For the translational motion (surge and heave) for the wave-current condition, the presence of the turbine reduces the motion amplitude of the platform. This happens due to the dampening effect coming from the turbine (Brown et al., 2021). Although the no turbine case has a higher surge motion response amplitude, the mean surge motion response of the present model is 24% higher, and Brown's model is 21% higher than the no turbine case. This happens due to the increase of the overall surface area below the water surface, which increases the downstream drag of the platform.

The pitch motion amplitude increases with the presence of the turbine. This happens due to the lever arm effect from the turbine, where the platform tends to pitch because of the added flow resistance coming from the turbine. For the pitch motion response, the negative sign shows that the platform pitches backwards i.e., counter-clockwise based on the Cartesian coordinate system. In Figure 6-10 it can be observed that the platform is pitching slightly backward with the presence of the turbine since it provides additional resistance to the system.

Compared to the wave-only conditions, the overall motion response increases with the presence of tidal current. This result is expected since the flow velocity (and hence the pressure) is increased. Furthermore, the turbine increases the underwater surface area which makes the motion response much more significant with the tidal current. The reason heave motion also increased with the presence of tidal current is because the mooring lines are restricting the surge motion even more due to the increase in the flow velocity, implying that the mooring is no longer only resisting the vertical motion but also the horizontal, and this gives more freedom for the platform to move vertically (Brown et al., 2020).

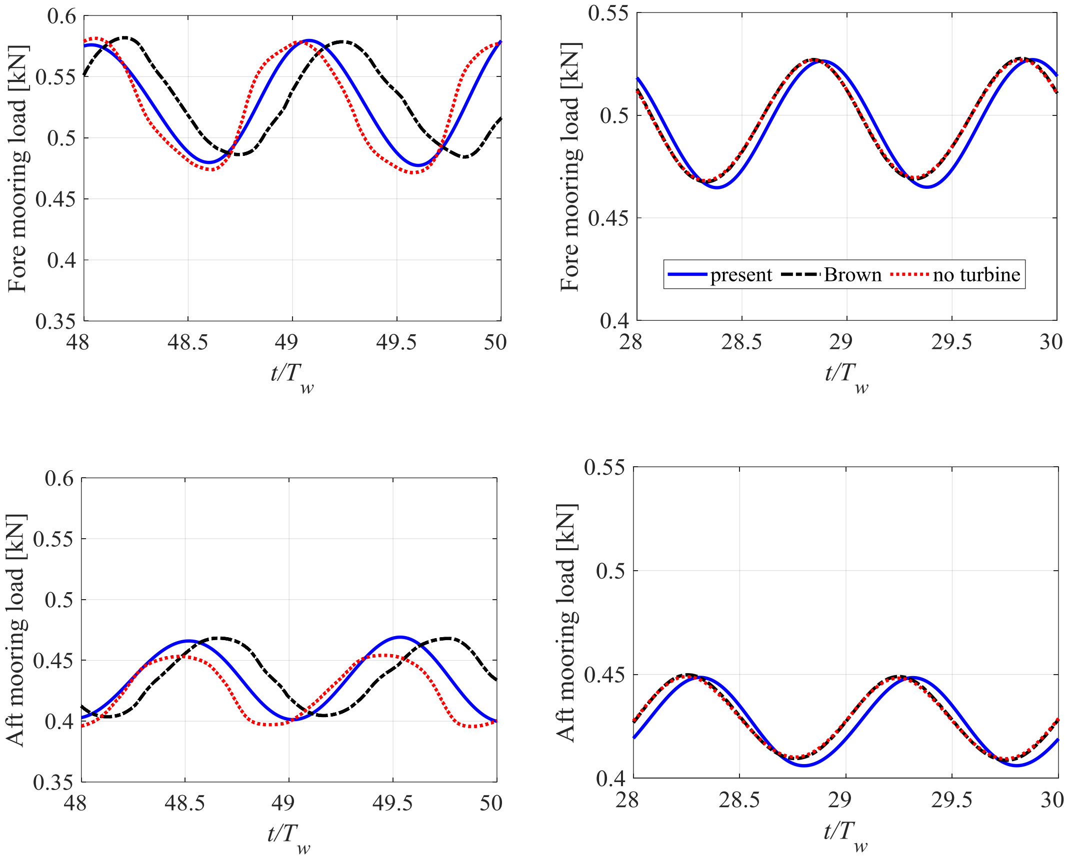

Figure 6-11 Mooring tension time histories of a floating tidal turbine for the no turbine case, Brown's model, and the present model for wave-only (right) and wave-current (left) cases for $\omega^* = 1.0$ and $H = 1.0$ m with rotor tip-speed ratio of 4.4.

Figure 6-11 shows the time histories of the front and rear mooring lines loading for the floating tidal turbine operating under wave-only and wave-current conditions for the case of $\omega^* = 1.0$. The increase in the fore mooring tension is because of the horizontal drift downstream due to the drag resistance of the floating platform. It is surprising to see there is little to no difference between with and without turbine cases for the front mooring load. The presence of the turbine was supposed to increase the overall horizontal surface area and hence increase the drag, especially in the wave-current condition. Although the mean values marginally increase with the presence of the turbine (will be shown in the next section in Figure 6-13), they are insignificant since the tidal current used in the present study is considered high ($U_\infty = 2.0$ m/s) compared to previous studies such as Brown et al. (2019), Brown et al. (2020), and Brown et al. (2021) (with $U_\infty < 1.0$ m/s). The increase in the loading amplitude of the aft mooring tension with the turbine present is due to the increase in the pitching motion response.

6.5 Operation under various wave frequencies

This section compares the present model with Brown's model under various wave frequencies, with and without the presence of the turbine, under wave-only and the combined wave-current conditions. Note that the present study uses a constant wave height H = 1.0 m and a constant tidal current velocity (at the inlet) $U_\infty = 2.0$ m/s for the wave-current condition.

Figure 6-12 shows the response amplitude operators (RAOs) of the surge, heave, and pitch motions of the floating platform with and without the presence of the turbine for the wave-only and combined wave-current conditions. The motion amplitude was normalized with the wave amplitude at the inlet for the calculation of RAOs. Simulations were run for around 20 to 30 wave periods for wave-current and wave-only cases, respectively, and the RAOs were calculated based on the last 6 motion cycles (i.e., 6 wave periods) of the data. The surge motion was averaged at the last 6 motion cycles of the data, and the entire data was subtracted based on their respective average values. This is to eliminate the offset from its original position due to the (downstream) drift of the floating platform caused by waves. For the combined wave-current condition, a fixed platform with a constant tidal current velocity $U_\infty = 2.0$ m/s at the inlet was simulated for $t = 200$ seconds (simulation time) before introducing the waves (and allowing the platform to freely move in the 3 DoF motions), following the step used in Brown et al. (2020).

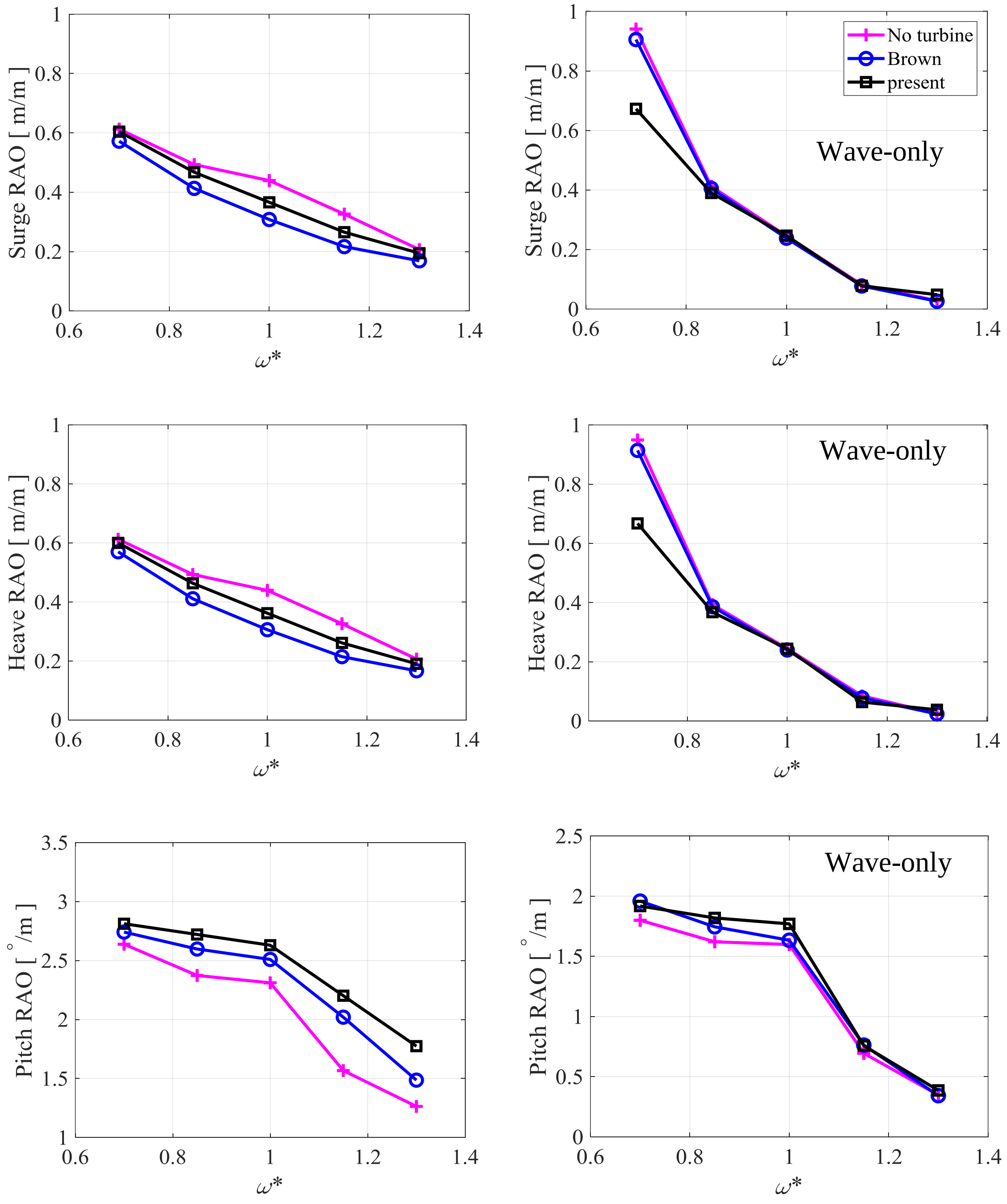

Figure 6-12 Response amplitude operator (RAO) for the wave-current (left) and wave-only (right) conditions with *H* = 1.0 m and rotor tip-speed ratio of 4.4.

A study done by Brown et al. (2021) on a floating tidal turbine operating under various waves conditions, found that for translational motion responses (surge and heave), there are only tiny differences between with and without turbine cases for the wave-only condition. This might be due to the small waves used in their study and the absence of tidal current which produces lower thrust on the rotor. Looking at the motion response between the no turbine and Brown's model in Figure 6-12, the translational RAOs have little to no difference. The motion response of the present model shows good agreement with the no turbine case for the translational motion, although there were slight differences in the RAOs at the lower wave frequency case. However, for the pitch motion, the present model has slightly higher RAOs than the no turbine and Brown's model cases. The surge RAO is lower than the no turbine case at the lowest wave frequency case, and it becomes closer to the no turbine case as the wave frequency is increased. A similar trend can be observed for the heave motion. The RAO is higher for Brown's model is because of the high loading variation at the lower wave frequency case (see Figure 6-14) which also triggers the increase in the front mooring loads (see Figure 6-13). Both the present and Brown's models have lower translational RAOs than the no turbine case, although the present model has significantly lower RAOs. As discussed before, the turbine model is dampening the translational motion, hence lowering the translational RAOs.

When U_{dyn} is positive, the damping force becomes negative and *vice-versa* when U_{dyn} is negative. The C_T is in-phase with U_T, and since $U_{T,c}$ is zero for the wave-only case, U_{dyn} is also in-phase with C_T (C_T in-phase with U_T, which is the quasi-steady term, and U_{dyn}, the added damping term). So when C_T is positive, the added damping is reducing the (positive) force, while it reduces the (negative) force when C_T is negative.

However, this is not the case for the pitch motion. The pitch RAO of the present model is consistently higher than the no turbine case, which happens due to the lever arm effect with the presence of the turbine. Looking at the mooring lines tension in Figure 6-13, the front mooring line tension amplitude of variation is higher for the no turbine case compared to the present model for the wave-only condition at lower wave frequency. This shows that the platform (for the no turbine case) is oscillating in a much higher surge amplitude and hence, producing higher surge RAO compared to the present model at lower wave frequency. The reason for the reduction in RAOs with the increase in wave frequency is the rate of wave decay. Wave height reduces more significantly, from the inlet to the centre of the wave tank, as the wave frequency is increased, as shown in Table 6-5 in section 6.3.2.

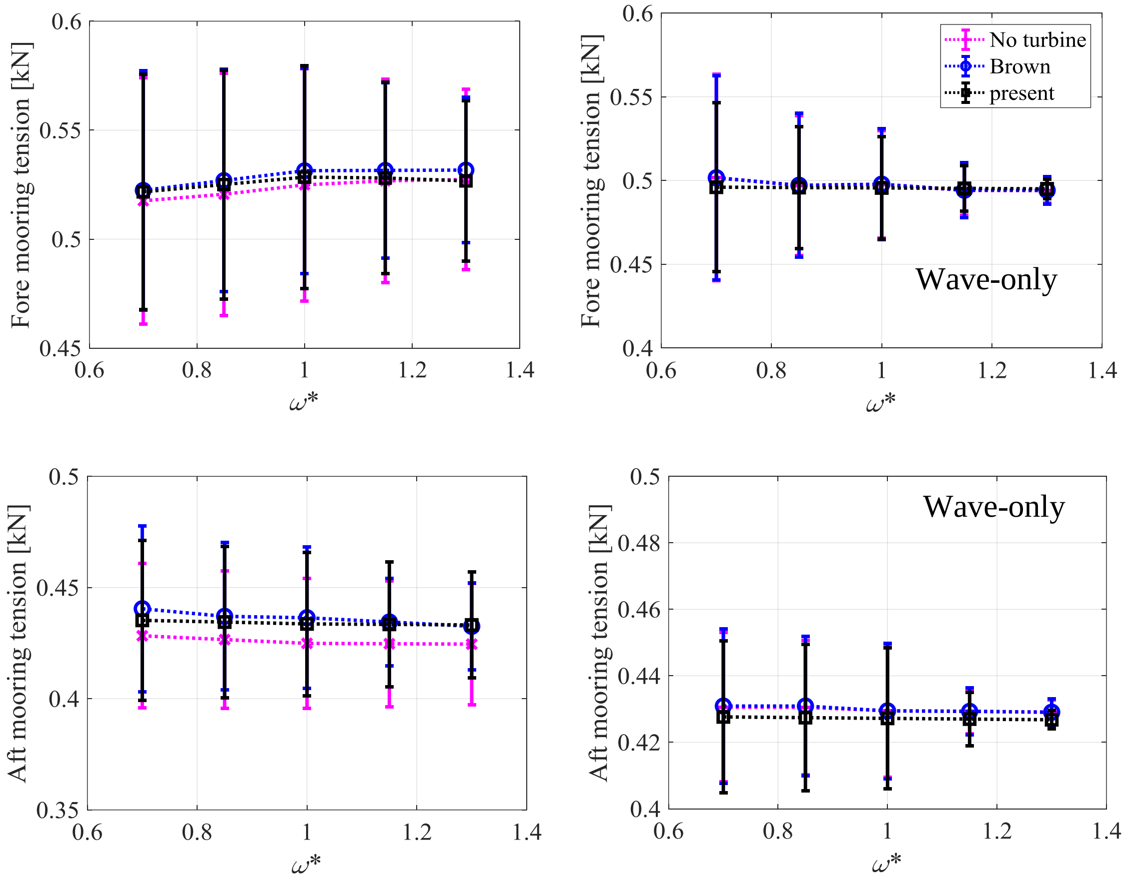

Figure 6-13 Mooring tensions for the wave-current (left) and wave-only (right) conditions with *H* = 1.0 m and rotor tip-speed ratio of 4.4.

For the wave-current condition, both models (present and Brown) predict lower RAOs for the translational motion compared to the no turbine case. This happens due to the dampening effect from the turbine and the mooring lines when simulating under the wave-current conditions considered in the present study. The increase in RAOs at lower wave frequency might be from the non-linear effects of the wave-current interaction (Brown et al., 2021). For the translational motion, RAOs of the wave-current condition are lower than wave-only at lower wave frequency case, but the result became the opposite as the wave frequency is increased. A similar trend was presented in Brown et al. (2020), where they conclude that the changes were caused by the effect of the wave-current combination, which shifts the peak frequency of the motion from the wave-only condition.

The effect from the drag of the platform can be seen in the mooring tension, where the fore mooring is higher than the aft mooring, as presented in Figure 6-13. For the fore mooring tension in the wave-only condition, at the lower wave frequency case, the present model has a lower amplitude than the no turbine case, with (almost) the same mean value. However, the amplitude and magnitude of the loading decrease as the wave frequency is increased for the no turbine case (and also Brown's model). The mean values of the present model remain (almost) the same although the wave frequency is increased. This is unexpected since the RAOs for both surge and pitch decrease as the wave frequency is increased, although the loading variation does decrease with the increase in frequency for the wave-only condition. The aft mooring tension amplitude of the present model increases (slightly) compared to the no turbine case in the wave-only condition because of the increase in the pitch RAOs.

Brown et al. (2021) found that the mean loading of the entire system (the combined drag loading of the platform and turbine load) is significantly increased with the presence of the turbine in the combined wave-current condition. With the presence of tidal current, the turbine will increase the drag of the entire system due to the increase in the underwater surface area. This increases the mooring line tension with the presence of a turbine. This can be observed in the wave-current case in Figure 6-13, where the mean mooring load increases with the presence of a turbine. The loading amplitude, however, decreases with the presence of the turbine. This happens because of the dampening effect coming from the turbine (Brown et al., 2020).

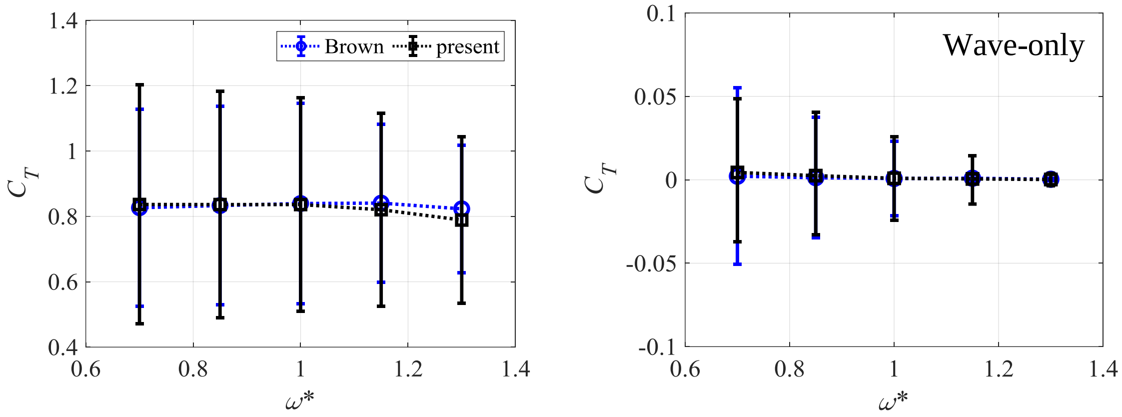

Figure 6-14 Thrust coefficients for the wave-current (left) and wave-only (right) conditions with *H* = 1.0 m and rotor tip-speed ratio of 4.4.

Figure 6-14 shows the comparison of the thrust coefficient between Brown's model and the present model for wave-current and wave-only conditions under various wave frequencies. In Brown et al. (2020), they found that the waves (which trigger the platform motion) cause the power and thrust to fluctuate but the average values remain zero for wave-only cases. A similar trend can be observed in the present study where the mean values of all cases are (close to) zero for the wave-only condition for the present model, except for the lowest wave frequency case. This happens due to the shear flow profile from waves which can increase the pressure at the water depth near the turbine (Brown et al., 2021). The loading variation decreases as the wave frequency are increased because of the increase in the wave's rate of decay. In high wave frequency cases, waves become smaller when they reached the centre of the wave tank and thus having a small impact on the platform motion. Besides this, the flow velocity shear profile due to waves also becomes less significant as the frequency is increased.

For the wave-current case, the result in Figure 6-14 shows that the mean C_T at lower wave frequency has little to no change between the two models, but the present model predicts a slightly lower mean C_T at higher wave frequency. The present model predicts higher loading amplitude compared to Brown's model. This shows that the hydrodynamic forces increase the loading fluctuation while having a marginal impact on the mean value. Previously in section 6.3.3, the present model reduces the loading variation and mean value to become closer to blade resolved data for a turbine oscillating under prescribed motions in constant flow velocity $U_\infty = 2.0$ m/s. In Figure 6-14, the mean C_T increases closer to the steady-state C_T value presented in Figure 2-9 in Chapter 2.

6.6 Conclusion

The present study modifies (the quasi-steady part of) the actuator disc model of Brown et al. (2020) while adding in the dynamic component. The dynamic component includes the added mass and damping forces (which corresponds to the turbine's acceleration and velocity, respectively), and ΔT. The model's detailed derivation from Brown et al.'s (2020) original model has also been presented.

Model verification for a turbine undergoing surge and pitch motions has been conducted between actuator disc models with blade resolved CFD data from chapters 2 and 3. The present model manages to verify well against the blade resolved data. Although, the present model is yet to be validated against any experimental or numerical work from literature. This should be the main focus for future work. Therefore, it is incorrect to assume that the present model has any improvement from the original. We can only assume that it has improved the model based on the results of the present study.

Comparison between the present model with Brown's original model has been carried out and presented in this chapter, for a multi-DoF simulation of a floating tidal turbine. The hydrodynamic forces have a significant impact on the motion response of the overall system, where the present model has shown having a significant difference in RAOs compared to Brown's model. These additional forces are also shown to have increased the loading variation on the floating turbine, which could potentially increase the fatigue damage to the overall system.

Chapter 7

Conclusion

Unsteady loading of a floating tidal turbine, from single to multi degrees of freedom (DoFs) motions, has been presented in this thesis. First, 3-dimensional blade resolved CFD simulations of a tidal turbine undergoing surge, heave, and pendulum motions were analyzed. Next, derivation and calculations of the added mass and damping coefficients were presented, which can be used as a reference to simulate a fully coupled model of a simplified rotor using an actuator disc model. Finally, modifications to an existing fully coupled model are derived, introducing the hydrodynamic effects from waves and floating platform motion. This model has been verified with the single DoF motion results, and analyses of the coupled model were presented. This chapter summarizes some of the key findings of the present study, followed by some recommendations of future work related to the present study.

7.1 Summary and key findings

This section presents the summary of the result chapters of the thesis, highlighting each chapter's key findings.

7.1.1 Rotor undergoing the surge motion

The moving reference frame was used to simulate the surging motion of the turbine to minimize the computational cost. The turbine undergoes prescribed surging motion over a range of motion amplitude, frequency, and rotor rotational speed. The data shows that the mean thrust decreases while the mean power increases as the surging amplitude and frequency are increased, which is a typical result found in studies of floating wind turbines undergoing surge motion. However, at maximum amplitude and frequency cases, the mean power decrease. This happens because of the stalling effect experienced by the turbine. At higher motion amplitude and frequency, the apparent velocity increases when the rotor moves in the upstream direction, thus increasing the effective angle of attack. The flow along the blade starts to separate when the effective angle of attack increases to a point where it passes the stall angle.

Increasing the rotor rotational speed reduces the stalling effect by increasing the tip-speed ratio close to its optimum condition when the rotor moves into the upstream direction (i.e., maximum apparent velocity). The angle of attack on the blade increases as the apparent velocity goes to the maximum. Therefore, by increasing the rotational speed (to the correct value), the angle of attack can be reduced to its optimum condition, thus minimizing the stalling effect.

Besides this, the rotor transition into a propeller state when it moves into the downstream direction at higher motion amplitude and frequency. This happens due to the fixed rotor rotational speed applied in the simulation. The apparent velocity decreases as the rotor moves downstream towards its own wake, further reducing the effective angle of attack into negative values. This causes the lift to appear at the pressure side instead of the suction side of the blade, turning it into a propeller.

7.1.2 Rotor undergoing the pendulum motion

Unlike the surge motion, the pendulum motion is modelled in the inertial reference frame using the sliding mesh method. The blockage ratio is increased to 1.0% due to the model limitation. Similar to the surge motion, the loading variation is in phase with the apparent velocity. The mean power and thrust are significantly lower than the stationary case when the rotor undergoes the pendulum motion over a range of motion amplitude and frequency. This might be due to the rotor design where it was designed to operate in a highly blocked condition, where in this case, it operates under a much lower blockage ratio.

A comparative study was conducted between surge and pendulum motions under the same operating condition. Results show that the rotor loading variation is quite similar between the two cases. The difference lies in the individual blade loading, where power and thrust time histories show each blade is out of phase when undergoing the pendulum motion and has different loading magnitude at the minimum and maximum. However, all blades have the same loading (in both magnitude and variation) for the surge motion. Each blade also shows different magnitudes of flow separation when the rotor moves upstream (at maximum apparent velocity) in the pendulum motion. These variations can be attributed to the difference in the azimuthal apparent velocity (and hence, angles of attack) at each blade which does not occur for surge motion.

7.1.3 Rotor undergoing the heave motion

For the heave motion, we can view it as a rotor operating under a dynamic yawing inflow condition. The rotor experience alternating advancing and retreating phases just like in the yawing condition. Like the pendulum motion, each blade experiences different loading throughout the time history due to the azimuthal variations of the apparent velocity. Besides this, effects of advancing and retreating phases were shown, including the skewed dynamic wake due to the heaving motion. There is a phase lag in the wake skewness formation and the advancing and retreating effect in the high motion frequency case. Even though the loading variation is tiny compared to surge and pendulum motions, the fatigue damage caused by the constant switching between advancing and retreating phases cannot be ignored.

7.1.4 Fully coupled model of a floating tidal turbine

A detailed derivation of the dynamic actuator disc, which is a modification of the original model by Brown et al. (2020), is presented in this thesis. The present study model modifies the quasi-steady component of the rotor thrust by using the local force coefficient C_X, determined from precursor steady flow simulations, instead of relying on induction factors. The model also introduces the hydrodynamic forces (added mass, damping, and averaged thrust difference) to integrate the dynamic force component into the floating tidal turbine system. The model was verified with blade resolved simulations, and comparisons with the original model were analyzed for an actuator disc undergoing surge and pendulum motions.

Effects of wave-only and combined wave-current conditions on a fully coupled model were simulated under various wave frequencies and results were presented in the previous chapter. The present model predicts lower thrust amplitude but higher mean loading compared to the original model, mainly due to the modification to the quasi-steady term and the inclusion of the hydrodynamic components into the thrust calculation in equation 6.8.

7.2 Future work

It would be interesting to make a comparative study between the inertial and moving (non-inertial) reference frame for the surge motion case. In this thesis, we compared a surging cylinder using the moving reference frame and deforming mesh method (i.e., the inertial frame of reference). The result shows that both methods agree quite well. However, this study does not take into account the rotor rotation, whether there is any difference in both frames of reference used in the present study. There might be some differences between the two reference frames when a rotation is included in the simulation, even though it is just a translational motion. The inertial reference frame can be simulated using a modified solver in OpenFOAM to include the combination of sliding mesh and deforming mesh methods, as presented in Jing et al.'s (2017) study. Theoretically, the methodology of this new solver will have the ability to deform the outer domain mesh to simulate the surging motion for the middle and inner domain, while the inner domain (the rotor mesh) rotates using the sliding mesh method.

Earlier in this project, the author has tried using the moving reference frame method to simulate the heave motion by including the necessary changes to the momentum equation and boundary conditions. However, the boundary conditions settings are not straightforward as the surge motion and errors occur during the simulation where the vertical flow does not entirely escape the boundaries. Instead, it interferes with the incoming flow from the opposite vertical direction, creating vortices at the boundaries and causing the flow field to scramble, hence terminating the simulation. The author has spent considerable time and resources building the code yet still met with failures. However, this method has proven to be effective in modelling a translational motion inside a moving fluid, as in the surge motion case. Therefore, the code development of this methodology will be revisited and completed in the future. Although, this method is no different from the one used in this thesis to simulate the heaving motion, and it is expected to yield similar (or close to) the present study's results. In order to take into account the fluctuation of aspect ratio at the top and bottom of the domain as the rotor oscillates in the heave motion, a new solver needs to be developed, using a similar methodology as the one presented in the previous paragraph (combined deforming and sliding mesh methods). Theoretically, by using this new method, it is expected that the dynamics of a heaving turbine will be different from that of a yawing turbine.

There is an idea to develop a modified solver that combines free surface with sliding mesh method for the pendulum motion case. Through this solver, it is possible to increase the blockage ratio without having to re-mesh the computational domain, modify the frame of reference, deforming the mesh, or using the overset grid method. First, however, this will introduce the free surface effect on the floating turbine undergoing pendulum motion. From that, it is possible to test all three motions under the free surface effect (without waves).

Besides this, simulating a floating turbine undergoing each motion under shear flow conditions is one of the interesting ideas to investigate. It is expected to see some periodic changes (which may have several frequencies in the spectra) to individual blade loading due to the combined shear flow profile and the turbine motions. Secondly, simulating a floating tidal turbine under waves conditions while oscillating in their respective DoF motions is one of the more challenging yet exciting topics to investigate. Theoretically, it is possible to have different hydrodynamic loading in terms of the added mass and damping than the ones presented in this thesis. Besides this, it is expected to see azimuthal variation due to the shear flow profile coming from waves.

For the fully coupled model, due to the limited range of parameter space, the present model is limited to using only the range provided by the look-up tables. Therefore, it is crucial to develop an empirical model to interpolate the range of parameters used in the present model, such as C_X, λ_T, and $\tilde{\alpha}$. It is also important to include the calculation of extracted power in the present model. Since this is an actuator disc model, we may use approximations, such as induction factors, to determine the power. Although, this can be improved by introducing a dynamic coefficient, just like the C_X used for thrust, to improve the quasi-steady assumption.

References

Afgan, I., McNaughton, J., Rolfo, S., Apsley, D. D., Stallard, T., & Stansby, P. (2013). Turbulent flow and loading on a tidal stream turbine by LES and RANS. *International Journal of Heat and Fluid Flow*, *43*, 96–108.

Akhter, M. Z., & Mysa, R. C. (2019). Prescribed motion flow dynamics. *Journal of Mechanical Science and Technology, 33*(1), 289–297.

Anatec Ltd. (2010). Navigation Risk Assessment Update Fall of Warness. *Technical Report, 01* (A2343-EMEC-NRA-1).

Arcos, F. Z. De, Vogel, C. R., & Willden, R. H. J. (2020). Extracting angles of attack from blade-resolved rotor CFD simulations. *Wind Energy, 23*, 1868–1885.

Bagbanci, H. (2011). Dynamic Analysis of Offshore Floating Wind Turbines. *Technical Report, Centre for Marine Technology and Engineering (CENTEC).*

Bertagnolio, F., Sorensen, N., Johansen, J., & Fuglsang, P. (2001). Wind turbine airfoil catalogue. (Denmark. Forskningscenter Risoe. Risoe-R; No. 1280(EN))

Bonfiglio, L., Brizzolara, S., & Chhryssostomidis, C. (2011). Added mass and damping of oscillating bodies: a fully viscous numerical approach. *Recent Advances in Fluid Mechanics, Heat & Mass Transfer and Biology*, *1*, 210–215.

Brown, S. A., Ransley, E. J., & Greaves, D. M. (2020). Developing a coupled turbine thrust methodology for floating tidal stream concepts : Verification under prescribed motion. *Renewable Energy*, *147*, 529–540.

Brown, S. A., Ransley, E. J., Xie, N., Greaves, D. M., Johanning, L., & Guerrini, E. (2019). Validation of a Coupled CFD Model for Evaluating Floating Tidal Systems. *International Society of Offshore and Polar Engineers (ISOPE), 1.*

Brown, S. A., Ransley, E. J., Xie, N., Monk, K., Angelis, G. M. De, & Nicholls-lee, R. (2021). On the impact of motion-thrust coupling in floating tidal energy applications. *Applied Energy*, *282*(PB), 116246.

Brown, S. A., Ransley, E. J., Zheng, S., Xie, N., Howey, B., & Greaves, D. M. (2020). Development of a fully nonlinear, coupled numerical model for assessment of floating tidal stream concepts. *Ocean Engineering*, *218* (February), 108-253.

Bruinsma, N. (2016). Validation and Application of a Fully Nonlinear Numerical Wave Tank. *Master thesis, Science in Offshore and Dredging Engineering, Delft University of Technology*, 144.

Burton, T., Sharpe, D., Jenkins, N., & Bossanyi, E. (2001). Wind energy handbook. *Jon Wiley & Sons, Ltd.*

Castro-Santos, L., & Diaz-Casas, V. (2015). Sensitivity analysis of floating offshore wind farms. *Energy Conversion and Management*, *101*, 271–277.

Chen, H., & Christensen, E. D. (2016). Computation of added mass and damping coefficients of a horizontal circular cylinder in openfoam. *Proceedings of the ASME 2016 35th International Conference on Ocean, Offshore and Arctic Engineering OMAE2016*, 1–8.

DECC. (2009). National Renewable Energy Action Plan for the United Kingdom Article 4 of the Renewable Energy Directive. *Department of Energy and Climate Change - Technical Report*, 1–160.

Draper, S., & Nishino, T. (2014). Centred and staggered arrangements of tidal turbines. *Journal of Fluid Mechanics*, *739* (March), 72–93.

Ekedahl, E. (2009). 6-DOF VOF-solver without Damping in OpenFOAM. *Technical Report*, 1–20.

Fleming, C. (2014). Tidal turbine performance in the offshore environment. *PhD thesis, University of Oxford*.

Fontanella, A., Bayati, I., & Belloli, M. (2018). Linear coupled model for floating wind turbine control. *Wind Engineering*, *42*(2), 115–127.

Guo, X., Yang, J., Lu, W., & Li, X. (2018). Dynamic responses of a floating tidal turbine with 6-DOF prescribed floater motions. *Ocean Engineering*, *165* (February), 426–437.

Hansen, M. H., Gaunaa, M., & Madsen, H. a. (2004). A Beddoes-Leishman type dynamic stall model in state-space and indicial formulations. *Riso National Laboratory*, *Ris{ø}-R-1354(EN)*, 7–35.

Jacobsen, N., Fuhrman, D., & Fredsoe, J. (2012). A wave generation toolbox for the open-source CFD library: OpenFoam. *International Journal for Nuemrical Methods in Fluids*, *70*, 1073–1088.

Jasak, H. (1996). Error Analysis and Estimation for the Finite Volume Method with Applications to Fluid Flows. *PhD Thesis, University of London*.

Javanmard, E., Mansoorzadeh, S., & Mehr, J. A. (2020). A new CFD method for determination of translational added mass coefficients of an underwater vehicle. *Ocean Engineering*, *215* (August), 107-857.

Jeffcoate, P., & Cresswell, N. (2018). Field Performance Testing of a Floating Tidal Energy Platform-Part 2: Load Performance. *4th Asian Wave and Tidal Energy Conference*.

Jin, S., Patton, R. J., & Guo, B. (2018). Viscosity effect on a point absorber wave energy converter hydrodynamics validated by simulation and experiment. *Renewable Energy*, *129*, 500–512.

Jing, F., Wang, S. qi, Sheng, Q. hu, Ma, Y., & Zhang, L. (2017). The effects of surge motion of the floating platform on hydrodynamics performance of horizontal-axis tidal current turbine. *Journal of Marine Science and Technology (Japan)*, *22*(2), 259–269.

Johnson, W. (2004). Model for vortex ring state influence on rotorcraft flight dynamics. *AHS International 4th Decennial Specialists' Conference on Aeromechanics, December 2005*, 839–899.

Jonkman, J. M. (2009). Dynamics of offshore floating wind turbines-model development and verification. *Wind Energy, 12*(5), 459–492.

Jonkman, J. M., & Buhl, M. L. (2007). Development and verification of a fully coupled simulator for offshore wind turbines. *Collection of Technical Papers - 45th AIAA Aerospace Sciences Meeting*, *4* (January), 2510–2534.

Jost, E., Klein, L., Leipprand, H., Lutz, T., & Krämer, E. (2018). Extracting the angle of attack on rotor blades from CFD simulations. *Wind Energy, 2018, 21*, 807-822.

Keulegan, G. H., & Carpenter, L. H. (1958). Forces on cylinders and plates in an oscillating fluid. *Journal of Research of the National Bureau of Standards*, *60* (5), 423–440.

Kim, S. P. (2011). CFD as a seakeeping tool for ship design. *International Journal of Naval Architecture and Ocean Engineering*, *3* (1), 65–71.

Lake, T., Hughes, J., Togneri, M., Williams, A. J., Jeffcoate, P., Starzmann, R., Kaufmann, N., & Masters, I. (2021). Strain gauge measurements on a full scale tidal turbine blade. *Renewable Energy*, *170*, 985–996.

Leble, V., & Barakos, G. (2016). Forced pitch motion of wind turbines. *Journal of Physics: Conference Series*, *753*(2).

Lee, H., & Lee, D. J. (2019). Wake impact on aerodynamic characteristics of horizontal axis wind turbine under yawed flow conditions. *Renewable Energy*, *136*, 383–392.

Leone, C., Segur, H., & Hammack, J. L. (1982). Viscous decay of long internal solitary waves. *Physics of Fluids*, *25*(6), 942–944.

Li, L., Sherwin, S. J., & Bearman, P. W. (2002). A moving frame of reference algorithm for fluid/structure interaction of rotating and translating bodies. *International Journal for Numerical Methods in Fluids*, *38* (2), 187–206.

Lienard, C., Boisard, R., Daudin, C. (2019). Aerodynamic behavior of a floating offshore wind turbine. *AIAA Scitech 2019*, Jan 2019, San Diego, United States.

Liu, Y., Xiao, Q., Incecik, A., Peyrard, C., & Wan, D. (2017). Establishing a fully coupled CFD analysis tool for floating offshore wind turbines. *Renewable Energy*, *112*, 280–301.

McAdam, R. A., Houlsby, G. T., Oldfield, M. L. G., & McCulloch, M. D. (2010). Experimental testing of the transverse horizontal axis water turbine. *IET Renewable Power Generation*, *4* (6), 510–518.

McNaughton, J. (2013). *Turbulence modelling in the near-field of an axial flow turbine using Code_Saturne*. *PhD thesis, University of Manchester,* 205.

Meneghini, J., & Bearman, P. (1995). Numerical simulation of high amplitude oscillatory flow about a circular cylinder. *Journal of Fluid and Structures*, *9*, 435–455.

Menter, F. R. (1994). Two-equation eddy-viscosity turbulence models for engineering applications. *AIAA Journal*, *32*(8), 1598–1605.

Micallef, D., & Sant, T. (2015). Loading effects on floating offshore horizontal axis wind turbines insurge motion. *Renewable Energy*, *83*, 737–748.

Murray, R. E., Thresher, R., & Jonkman, J. (2018). Added-mass effects on a horizontal-axis tidal turbine using FAST v8. *Renewable Energy (2018).*

Nachtane, M., Tarfaoui, M., Goda, I., & Rouway, M. (2020). A review on the technologies, design considerations and numerical models of tidal current turbines. *Renewable Energy*, *157*, 1274–1288.

Orbital Marine Power Ltd. (2018). Orbital Marine Power (Orkney) plc. Orbital O2 2MW Tidal Turbine. *Technical Report* (2018).

Osman, M. H. B., & Willden, R. H. J. (2020a). Unsteady loading of a floating tidal turbine oscillating in a pendulum motion. *Developments in Renewable Energies Offshore*, 571–581.

Osman, M., Willden, R. H. J., & Vogel, C. R. (2020b). The effects of surge motion on floating horizontal axis tidal turbines. *International Marine Energy Journal*, *3*(2), 45–54.

Ouro, P., Harrold, M., Stoesser, T., & Bromley, P. (2017). Hydrodynamic loadings on a horizontal axis tidal turbine prototype. *Journal of Fluids and Structures*, *71*, 78–95.

Pegalajar-Jurado, A., Hansen, A. M., Laugesen, R., Mikkelsen, R. F., Borg, M., Kim, T., Heilskov, N. F., & Bredmose, H. (2016). Experimental and numerical study of a 10MW TLP wind turbine in waves and wind. *Journal of Physics: Conference Series*, *753*(9).

Pham, A. H., Lee, C. Y., Seo, J. H., Chun, H. H., Kim, H. J., Yoon, H. S., Kim, J. H., Park, D. W., & Park, I. R. (2010). Laminar flow past an oscillating circular cylinder in cross flow. *Journal of Marine Science and Technology*, *18*(3), 361–368.

Qiu, Y. X., Wang, X. D., Kang, S., Zhao, M., & Liang, J. Y. (2014). Predictions of unsteady HAWT aerodynamics in yawing and pitching using the free vortex method. *Renewable Energy*, *70*, 93–106.

Ransley, E. J., Brown, S. A., Greaves, D. M., Hindley, S., Weston, P., & Guerrini, E. (2016). Coupled RANS-VOF modelling of floating tidal stream concepts. *In Proceedings of the 2nd International Conference on Offshore Renewable Energy (CORE)*, *9*.

Ransley, E. J., Greaves, D., Raby, A., Simmonds, D., & Hann, M. (2017). Survivability of wave energy converters using CFD. *Renewable Energy*, *109*, 235–247.

Rockel, S., Camp, E., Schmidt, J., Peinke, J., Cal, R. B., & Hölling, M. (2014). Experimental study on influence of pitch motion on the wake of a floating wind turbine model. In *Energies* (Vol. 7, Issue 4).

Rodrigues, S. F., Teixeira Pinto, R., Soleimanzadeh, M., Bosman, P. A. N., & Bauer, P. (2015). Wake losses optimization of offshore wind farms with moveable floating wind turbines. *Energy Conversion and Management*, *89*, 933–941.

Sant, T., Bonnici, D., Farrugia, R., & Micallef, D. (2006). Measurements and modelling of the power performance of a model floating wind turbine under controlled conditions. *Renewable Energy*, *December 2005*, 163–177.

Schepers, G. (1999). An engineering model for yawed conditions , developed on basis of wind tunnel measurements. *American Institute of Aeronautics & Astronautics*, 164–174.

Schulz, C., Letzgus, P., Lutz, T., & Kramer, E. (2017). CFD study on the impact of yawed inflow on loads, power and near wake of a generic wind turbine. *Wind Energy*, *20* (July 2016), 253–268.

Sebastian, T., & Lackner, M. (2013). Characterization of the unsteady aerodynamics of offshore floating wind turbines. *Wind Energy*, *March 2012*, 1–20.

Sebastian, T., & Lackner, M. A. (2012). Development of a free vortex wake method code for offshore floating wind turbines. *Renewable Energy*, *46*, 269–275.

Sebastian, Thomas, & Lackner, M. (2012). Analysis of the induction andwake evolution of an offshore floating wind turbine. *Energies*, *5* (4), 968–1000.

Shen, X., Chen, J., Hu, P., Zhu, X., & Du, Z. (2018). Study of the unsteady aerodynamics of floating wind turbines. *Energy*, *145*, 793–809.

Shen, X., Hu, P., Chen, J., Zhu, X., & Du, Z. (2018). The unsteady aerodynamics of floating wind turbine under platform pitch motion. *Proceedings of the Institution of Mechanical Engineers, Part A: Journal of Power and Energy*, *232*(8), 1019–1036.

Shirasawa, K., Tokunaga, K., Iwashita, H., & Shintake, T. (2016). Experimental verification of a floating ocean-current turbine with a single rotor for use in Kuroshio currents. *Renewable Energy*, *91*, 189–195.

SIMEC Atlantis Energy. (2016). AR1500 tidal turbine. *Technical Report*, 1–6. https://www.atlantisresourcesltd.com/wp/wp-content/uploads/2016/08/AR1500-Brochure-Final-1.pdf

Speziale, C. G. (1989). Theoretical and Computational Fluid Dynamics Turbulence Modeling in Noninertial Frames of Reference. *Theoretical and Computational Fluid Dynamics*, 3–19.

Starzmann, R., Goebel, I., & Jeffcoate, P. (2018). Field Performance Testing of a Floating Tidal Energy Platform-Part 1: Power Performance. *4th Asian Wave and Tidal Energy Conference*.

Stewart, W. (1959). Helicopter Behaviour in the Vortex-Ring Conditions. *Aeronautical Research Council, Reports & Memoranda*, *3117*.

Sun, K., Zhang, J. hua, Zhang, L., & Wang, S. qi. (2017). The effects of roll motion of the floating platform on hydrodynamics performance of horizontal-axis tidal current turbine. *Journal of Marine Science and Technology (Japan)*, *22* (2), 259–269.

Tran, T., Kim, D., & Song, J. (2014). Computational fluid dynamic analysis of a floating offshore wind turbine experiencing platform pitching motion. *Energies*, *7* (8), 5011–5026.

Tran, T. T., & Kim, D. H. (2015a). The aerodynamic interference effects of a floating offshore wind turbine experiencing platform pitching and yawing motions. *Journal of Mechanical Science and Technology*, 29 (2), 549–561.

Tran, T. T., & Kim, D. H. (2015b). The platform pitching motion of floating offshore wind turbine: A preliminary unsteady aerodynamic analysis. *Journal of Wind Engineering and Industrial Aerodynamics*, *142*, 65–81.

Tran, T. T., & Kim, D. H. (2016). A CFD study into the influence of unsteady aerodynamic interference on wind turbine surge motion. *Renewable Energy*, *90*, 204–228.

Troy, C. D., & Koseff, J. R. (2006). The viscous decay of progressive interfacial waves. *Physics of Fluids*, *18*(2).

Uihlein, A., & Magagna, D. (2016). Wave and tidal current energy - A review of the current state of research beyond technology. *Renewable and Sustainable Energy Reviews*, *58*, 1070–1081.

Urquhart, M. (2016). A tutorial of the sixDofRigidBodyMotion library with multiple bodies. *Technical Report*, 1–19.

Vaal, J. B. de, Hansen, M. O. L., & Moan, T. (2006). Effect of wind turbine surge motion on rotor thrust and induced velocity. *Renewable Energy*, *December 2005*, 163–177.

Wang, K., Sun, K., Sheng, Q. hu, Zhang, L., & Wang, S. qi. (2016). The effects of yawing motion with different frequencies on the hydrodynamic performance of floating vertical-axis tidal current turbines. *Applied Ocean Research*, *59*, 224–235.

Wang, S. qi, Sun, K., Xu, G., Liu, Y. tao, & Bai, X. (2017). Hydrodynamic analysis of horizontal-axis tidal current turbine with rolling and surging coupled motions. *Renewable Energy*, *102*, 87–97.

Wen, B., Dong, X., Tian, X., Peng, Z., Zhang, W., & Wei, K. (2018). The power performance of an offshore floating wind turbine in platform pitching motion. *Energy*, *154*, 508–521.

Wen, B., Tian, X., Dong, X., Peng, Z., & Zhang, W. (2017). Influences of surge motion on the power and thrust characteristics of an offshore floating wind turbine. *Energy*, *141*, 2054–2068.

Wen, B., Tian, X., Dong, X., Peng, Z., Zhang, W., & Wei, K. (2019). A numerical study on the angle of attack to the blade of a horizontal-axis offshore floating wind turbine under static and dynamic yawed conditions. *Energy*, *168*, 1138–1156.

Wen, B., Tian, X., Zhang, Q., Dong, X., Peng, Z., Zhang, W., & Wei, K. (2019). Wind shear effect induced by the platform pitch motion of a spar-type floating wind turbine. *Renewable Energy*, *135*, 1186–1199.

Whelan, J. I., Graham, J., & Pierø, J. (2009). Inertia Effects on Horizontal Axis Tidal-Stream Turbines. *Proceedings of the 8th European Wave and Tidal Energy Conference, Uppsala, Sweden*, 586–591.

Wilcox, D. C. (1988). Reassessment of the Scale-Determining Equation for Advanced Turbulence Models. *AIAA Journal*, *26*(11), 1299–1310.

Willcox, D. C. (1993). Turbulence Modeling for CFD. *Technical Report*, DCW Industries, Inc., California.

Wimshurst, A. (2018). Tip Flow Corrections for Horizontal Axis Wind and Tidal Turbine Rotors. *PhD Thesis, University of Oxford*.

Wimshurst, A, & Willden, R. (2016). Computational analysis of blockage designed tidal turbine rotors. *Progress in Renewable Energies Offshore*, 587–600.

Wimshurst, Aidan, Vogel, C., & Willden, R. (2018). Cavitation limits on tidal turbine performance. *Ocean Engineering*, *152* (December 2017), 223–233.

Windt, C., Davidson, J., & Schmitt, P. (2019). On the Assessment of Numerical Wave Makers in CFD Simulations. *Journal of Marine Science and Engineering*, *7*(47).

Xie, N., Ransley, E. J., Brown, S., Greaves, D., Nicholls-Lee, R., Johanning, L., Weston, P., & Guerrini, E. (2019). Wave tank experiments of a floating, tidal-stream energy device. *Advances in Renewable Energies Offshore - Proceedings of the 3rd International Conference on Renewable Energies Offshore, RENEW 2018*, *October*, 203–207.

Ye, Z., Wang, X., Chen, Z., & Wang, L. (2020). Unsteady aerodynamic characteristics of a horizontal wind turbine under yaw and dynamic yawing. *Acta Mechanica Sinica/Lixue Xuebao*, *36* (2), 320–338.

Yu, D., You, J., & Kwon, O. (2013). Numerical investigation of unsteady aerodynamics of a Horizontal-axis wind turbine under yawed flow conditions. *Wind Energy*, *16* (July 2012), 711–727.

Yu, Y., & Li, Y. (2011). Preliminary results of a RANS simulation for a floating point absorber wave energy system in extreme wave conditions. *Proceedings of the ASME 30th International Conference on Ocean, Offshore and Arctic Engineering OMAE2011*, *2009* (October), 1–8.

Zago, V., Schulze, L. J., Bilotta, G., Almashan, N., & Dalrymple, R. A. (2021). Overcoming excessive numerical dissipation in SPH modeling of water waves. *Coastal Engineering*, *170* (May), 104018.